Inhomogeneous charge states and electronic transport in manganites

M. Yu. Kagan*

P. L. Kapitza Institute for Physical Problems, Russian Academy of Sciences 2 Kosygina St., 117334 Moscow, Russia

K. I. Kugel and A. L. Rakhmanov

Institute of Theoretical and Applied Electrodynamics, Russian Academy of Sciences 13/19 Izhorskaya St., 127412 Moscow, Russia

D. I. Khomskii

Laboratory of Applied and Solid State Physics, Materials Science Center, University of Groningen Nijenborgh 4, 9747 AG Groningen, The Netherlands

(Submitted February 9, 2001)
Fiz. Nizk. Temp. **27**, 815–825 (August 2001)

We analyze the interplay between charge ordering, magnetic ordering, and the tendency toward phase separation and its importance for the physics of manganites. A simple model of charge ordering is considered. It takes into account both the Coulomb repulsion at neighboring sites responsible for charge ordering and the essential magnetic interactions. It is shown explicitly that at any deviation from half-filling ($n \neq 1/2$) the system is unstable with respect to phase separation into charge-ordered regions with $n = 1/2$ and metallic regions with smaller electron or hole density. A possible structure of this phase-separated state (metallic droplets in a charge-ordered matrix) is discussed. We construct the phase diagram reproducing the main features observed in real manganites. Based on the same physical picture, we also derive explicit expressions for the dc conductivity and noise power in the phase-separated state. It is shown that the noise spectrum has a nearly $1/f$ form in the low-frequency range.
 [DOI: 10.1063/1.1399195]

1. INTRODUCTION

The problem of charge ordering in magnetic oxides has attracted the attention of theorists since the discovery of the Verwey transition in magnetite at the end of thirties [1]. Recently this problem has been reexamined in a number of papers in connection with the colossal magnetoresistance in manganites; see, e.g., Refs. 2–4. The mechanisms stabilizing the charge-ordered (CO) state may be different: the Coulomb repulsion of charge carriers or the electron–lattice interaction leading to the effective repulsion of electrons at the nearest-neighbor sites. In all cases, charge ordering can arise in systems with mixed valence if the electron bandwidth is sufficiently small-large electron kinetic energy stabilizes the homogeneous metallic state. In the simplest bipartite lattice, the class which includes the colossal-magnetoresistance manganites of the type $R_{1-x}A_xMnO_3$ (R=La, Pr; A=Ca, Sr) or layered manganites $R_{2-x}A_xMnO_4$, $R_{2-2x}A_{1+2x}Mn_2O_7$, the optimum conditions for the formation of the CO state exist for doping $x=1/2$. At this value of x the concentrations of Mn^{3+} and Mn^{4+} are equal, and a simple checkerboard arrangement is possible. The most remarkable experimental fact here is that even at $x \neq 1/2$ (in the underdoped manganites, $x<1/2$) only the simplest version of charge ordering is experimentally observed, with an alternating checkerboard structure of occupied and empty sites in the basal plane.[5]

Then the natural question arises: how could we redistribute the extra or missing electrons in the case of arbitrary doping level, keeping the superstructure the same as for $x=1/2$? To answer this question, the experimentalists introduced the concept of an incipient charge-ordered state corresponding to the distortion of long-range charge ordering by microscopic metallic clusters.[6] In fact, the existence of such a state implies a kind of phase separation. Note that the phase separation scenario in manganites is very popular now.[7–10] Nowadays, there is a growing evidence suggesting that an interplay between the charge ordering and the tendency toward phase separation plays an essential role in the physics of materials with colossal magnetoresistance.

In this paper we consider a simple model which allows us to clarify the situation at arbitrary doping. We include in this model both the Coulomb repulsion of electrons on neighboring sites and the magnetic interactions responsible for the spin ordering of manganites. After demonstrating the instability of the system toward phase separation in certain ranges of doping, we consider the simplest form of the phase separation-the formation of metallic droplets in an insulating matrix, and we estimate the parameters of such droplets and construct the phase diagram illustrating the interplay between charge ordering, magnetic ordering, and phase separation.

Based on this model, we also calculate the conductivity and noise spectral power of the system in the phase-separated state, taking into account the electron jumps from one droplet to another. The concentration range not too close to the percolation transition to the metallic state is considered. The relation of these results to the giant $1/f$ noise observed in the phase-separated manganites[11] is discussed.

2. A SIMPLE MODEL FOR CHARGE ORDERING

Let us consider a simple lattice model for charge ordering:

$$\hat{H}=-t\sum_{\langle i,j\rangle} c_i^+ c_j+V\sum_{\langle i,j\rangle} n_i n_j-\mu\sum_i n_i, \tag{1}$$

where t is the hopping integral, V is the nearest-neighbor Coulomb interaction (similar *nn* repulsion can be also obtained via interaction with breathing-type optical phonons); μ is the chemical potential, and c_i^+ and c_j are one-electron creation and annihilation operators, $n_i=c_i^+ c_i$. The symbol $\langle i,j\rangle$ denotes the summation over the nearest-neighbor sites. Here, for simplicity, we omit the spin indices. We also assume the absence of double occupancy in this model due to the strong on-site repulsion between electrons.

Models of the type (1) with the *nn* repulsion being responsible for the charge ordering are the most popular ones for describing this phenomenon; see, e.g., Refs. 2, 4, 12–14 and references therein. Hamiltonian (1) captures the main physical effects; if necessary, one can add to it some extra terms, which we will also do below.

In the main part of our paper we will always speak about electrons. However, in application to real manganites we will mostly have in mind less-than-half-doped (underdoped) systems of the type $R_{1-x}A_xMnO_3$ with $x<1/2$. Thus, for a real system one has to substitute *holes* for our *electrons*. All the theoretical treatment definitely remains the same (from the very beginning we could define operators c and c^+ in (1) as the operators for holes); we hope that it will not lead to any misunderstanding.

We consider below the simplest case of square (2D) or cubic (3D) lattices, where for $x=1/2$ the simple two-sublattice ordering would take place. As mentioned in the Introduction, this is the case in layered manganites, whereas the ordering in 3D perovskite manganites is like this only in the basal plane, the ordering being ''in-phase'' in the c direction. To account for this behavior, apparently a more complicated model would be necessary.

For the case $n=1/2$, model (1) has been analyzed in many papers; we follow the treatment of Ref. 12 (see also Ref. 10). As mentioned above, the Coulomb repulsion [the second term in (1)] stabilizes the charge ordering in the form of a checkerboard arrangement of occupied and empty sites, whereas the first term (band energy) opposes this tendency. At arbitrary values of electron density n, we shall at first consider a homogeneous CO solution and use the same ansatz as in Ref. 12, namely

$$n_i=n[1+(-1)^i\tau]. \tag{2}$$

Such an expression implies doubling of the lattice periodicity, with local densities $n_1=n(1+\tau)$ and $n_2=n(1-\tau)$ at neighboring sites. Note that at $n=1/2$ for a general form of electron dispersion without nesting, the CO state exists only at sufficiently strong repulsion $V>2t$.[12] For finite values of $V/2t$ the order parameter $\tau<1$, and the ordering in general is not complete, i.e., the average electron densities n_i differ from zero or one even at $T=0$.

We use the same coupled Green function approach as in Ref. 12, which leads to the following spectrum:

$$E+\mu=Vnz\pm\sqrt{(Vn\tau z)^2+t_k^2}=Vnz\pm\omega_k. \tag{3}$$

The spectrum defined by (3) resembles the spectrum of a superconductor, and hence the first term under the square root is analogous to the square of the superconducting gap. In other words, we can introduce the charge-ordering gap by the formula $\Delta=Vn\tau z$. It depends upon density not only explicitly, but also via the density dependence of τ.

Hence, we get

$$\omega_k=\sqrt{\Delta^2+t_k^2}. \tag{4}$$

Note that there is one substantial difference between the spectrum of the charge ordered state (4) and superconducting state, namely, here for $n\neq 1/2$ the chemical potential does not appear under the square root in (4), in contrast to the spectrum of a superconductor, where $\omega_k=[(t_k-\mu)^2+\Delta^2]^{1/2}$. Thus, the problem of the uniform CO state is reduced to a self-consistent determination of the gap Δ and chemical potential μ as functions of charge density n and temperature:

$$2n=\int\frac{d^3\mathbf{k}}{\Omega_{BZ}}[f_F(\varepsilon_{k-})+f_F(\varepsilon_{k+})],$$

$$1=\frac{Vz}{2}\int\frac{d^3\mathbf{k}}{\Omega_{BZ}}\frac{1}{\omega_k}[f_F(\varepsilon_{k-})-f_F(\varepsilon_{k+})], \tag{5}$$

where $f_F(\varepsilon_{k\pm})=1/(\exp\{\varepsilon_{k\pm}/T\}+1)$ are the Fermi distribution functions, and Ω_{BZ} is the volume of the first Brillouin zone. The first equation in (5) determines the chemical potential and the second one gives the gap Δ. For low temperatures $T\to 0$ and $n\leqslant 1/2$ it is reasonable to assume that $\mu-Vnz$ is negative. Hence $f_F(\omega_k-\mu+Vnz)=0$, and $f_F(-\omega_k-\mu+Vnz)=\theta(-\omega_k-\mu+Vnz)$ is the step function.

It is easy to see that for $n=1/2$ the system of equations (5) yields identical results for all $-\Delta\leqslant\mu-Vnz\leqslant\Delta$. From this point of view, $n=1/2$ is a point of indifferent equilibrium. For infinitely small deviations from $n=1/2$, that is, for densities $n=1/2-0$, the chemical potential should be defined as $\mu=-\Delta+Vz/2=Vz/2(1-\tau)$. If we consider the strong-coupling case $V\gg 2t$ and assume a constant density of states inside the band, then for a simple cubic lattice we have $\tau=1-(2W^2/3V^2z^2)$, and hence

$$\mu=\frac{W^2}{3Vz}, \tag{6}$$

where $W=2zt$ is the bandwidth. Note that for density $n=1/2$ a charge-ordering gap Δ appears for an arbitrary interaction strength V. This is due to the existence of nesting in our simple model. In the weak coupling case $V\ll 2t$ and with perfect nesting, we have $\Delta\sim W\exp\{-W/Vz\}$, and τ is exponentially small. For $zV\gg W$ or, accordingly, for $V\gg 2t$: $\Delta\approx Vz/2$ and $\tau\to 1$. As mentioned above, for a general form of electron dispersion without nesting, charge ordering exists only if the interaction strength V exceeds a certain critical value of the order of the bandwidth W.[12] Further on, we restrict ourselves only to the physically more instructive case of strong coupling $V\gg 2t$.

Now let us consider the case $n=1/2-\delta$, where $\delta\ll 1$ is a deviation of the density from $n=1/2$. For this case $\mu=\mu(\delta,\tau)$, and we have two coupled equations for μ and τ. As a result,

$$\mu(\delta)\approx Vnz(1-\tau)-\frac{4W^2}{Vz}\delta^2\approx\frac{W^2}{3Vz}+\frac{4W^2}{3Vz}\delta+O(\delta^2). \tag{7}$$

Correspondingly, the energy of a charge-ordered state is as follows:

$$E_{CO}(\delta)=E_{CO}(0)-\frac{W^2}{3Vz}\delta-\frac{2W^2}{3Vz}\delta^2+O(\delta^3), \tag{8}$$

where $E_{CO}(0)=-W^2/6Vz$ is the energy of charge order for density n precisely equal to 1/2 and $|E_{CO}(0)|\ll W$. At the same time, the charge-ordering gap Δ is given by:

$$\Delta\approx\frac{Vz}{2}\left[1-2\delta-\frac{2W^2}{3V^2z^2}(1+4\delta)\right]. \tag{9}$$

For $n>1/2$ the energy of the charge-ordered state starts to increase rapidly due to the large contribution from the Coulomb repulsion (the upper Verwey band is partially filled for $n>1/2$). Contrary to the case $n<1/2$, for $n>1/2$ each extra electron put into the checkerboard CO state will necessarily have occupied nearest-neighbor sites, increasing the total energy by $Vz|\delta|$. As a result, we have for $|\delta|=n-1/2>0$

$$E_{CO}(\delta)=E_{CO}(0)+\left(Vz-\frac{W^2}{3Vz}\right)|\delta|-\frac{2W^2}{3Vz}\delta^2+O(\delta^3). \tag{10}$$

Accordingly, the chemical potential has the form

$$\mu(\delta)=Vz-\frac{W^2}{3Vz}-\frac{4W^2}{3Vz}|\delta|+O(\delta^2). \tag{11}$$

It undergoes a jump equal to Vz for $\tau\to1$. Note that the gap Δ is symmetric for $n>1/2$ and is given by

$$\Delta\approx\frac{Vz}{2}\left[1-2|\delta|-\frac{2W^2}{3V^2z^2}(1+4|\delta|)\right].$$

We could make the whole picture symmetric with respect to $n=1/2$ by shifting all the one-electron energy levels and the chemical potential by $Vz/2$, i.e., defining $\mu'=\mu-Vz/2$. In terms of μ', relations (7), and (11) can be written as:

$$\mu'=-\frac{Vz}{2}+\frac{W^2}{3Vz}+\frac{4W^2}{3Vz}\delta,\quad n<\frac{1}{2};$$

$$\mu'=\frac{Vz}{2}-\frac{W^2}{3Vz}-\frac{4W^2}{3Vz}|\delta|,\quad n>\frac{1}{2}.$$

Similar to the situation in semiconductors, here $\mu'=0$ precisely at the point $n=1/2$, i.e., the chemical potential lies in the middle of the band gap (see Fig. 1). At densities $n=1/2-0$, the chemical potential $\mu'=-Vz/2$ coincides with the upper edge of the filled Verwey band.

3. PHASE SEPARATION

Let us now check the stability of the charge-ordered state. At densities close to $n=1/2$, the dependence of the energy on charge density will have the form illustrated in Fig. 2.

This figure is clearly indicative of possible instability of the charge-ordered state. Indeed, the most remarkable implication of (7)–(11) is that the compressibility κ of the homogeneous charge-ordered system is negative for densities different from 1/2,

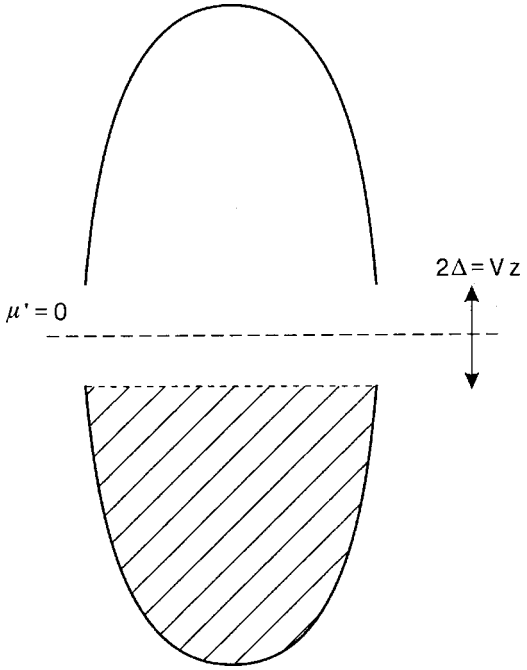

FIG. 1. Band structure of the model (1) at $n=1/2$. The lower Verwey band is completely filled. The upper Verwey band is empty. The chemical potential $\mu'=0$ lies in the middle of the band gap of width 2Δ.

$$\frac{1}{\kappa}\propto\frac{d\mu}{dn}=\frac{d\mu}{d\delta}=\frac{d^2E}{d\delta^2}=-\frac{4W^2}{3Vz}<0, \tag{12}$$

where $\delta=1/2-n$. This is a manifestation of the tendency toward phase separation characteristic of the charge-ordered system with $\delta\neq0$. The presence of a kink in $E_{CO}(\delta)$ [cf. Eqs. (8), (10)] implies that one of the states into which the system might separate would correspond to the checkerboard CO state with $n=1/2$, whereas the other would have a certain density n' smaller or larger than 1/2. This conclusion resembles that of Ref. 3 (see also Refs. 9 and 15), although the detailed physical mechanism is different. The possibility of phase separation in the model (1) away from half-filling was also reported earlier[13] for the infinite-dimensional case. Below we concentrate our attention on the situation with $n<1/2$ (underdoped manganites); the case $n>1/2$ apparently has certain special properties—the existence of stripe phases etc.,[16] the detailed origin of which is not yet clear.

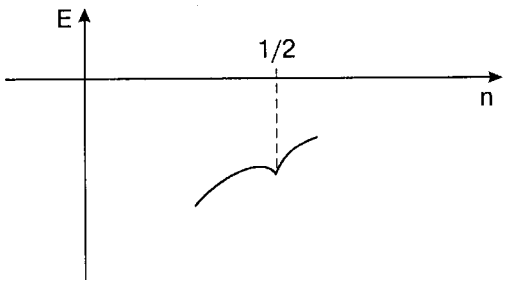

FIG. 2. Energy of the charge-ordered state versus charge density at $n\to1/2$.

It is easy to understand the physics of phase separation in our case. As follows from (9), the CO gap decreases linearly with the deviation from half-filling. Correspondingly, the energy of the homogeneous CO state increases rapidly, and it is more favorable to ''extract'' extra holes from the CO state, putting them into one part of the sample, while creating the ''pure'' checkerboard CO state in the other part of it. The energy cost of such a redistribution of holes is overcompensated by the energy benefit provided by the better charge ordering.

The long-range Coulomb forces would, however, prevent the full phase separation into large regions containing all the extra holes and the pure $n=1/2$ charge-ordered region. This energy cost can be avoided by forming finite metallic clusters with a smaller number of electrons instead of one big metallic phase with many electrons. The limiting case would be a set of spherical droplets, each containing one electron. This state is similar to magnetic polarons (''ferrons'') considered in the problem of phase separation in doped magnetic insulators.[7,15,10]

We present below an estimation of the characteristic parameters of these droplets. The main aim of this treatment is to demonstrate that the state constructed in such a way will have lower energy than the homogeneous state, even if we treat these droplets rather crudely and do not optimize all their properties. In particular, we will make the simplest assumption that the droplets have sharp boundaries and that the charge-ordered state outside these droplets is not modified in their vicinity. This state can be treated as a variational one: if we optimize the structure of the droplet boundary, its energy would only decrease.

The energy (per unit volume) of the droplet state with a concentration n_d of the droplets can be written in total analogy with the ferron energy in the double-exchange model (see Refs. 10 and 15). This yields

$$E_{\text{droplet}}=-tn_d\left(z-\frac{\pi^2a^2}{R^2}\right)-\frac{W^2}{6Vz}\left[1-n_d\,\frac{4}{3}\,\pi\left(\frac{R}{a}\right)^3\right]. \tag{13}$$

Here a is the lattice constant and R is the droplet radius. The first term in (13) corresponds to the kinetic energy benefit of electron delocalization inside the metallic droplets, and the second term describes the charge ordering energy in the remaining insulating part of the sample.

Minimization of the energy in (13) with respect to R gives

$$\frac{R}{a}\approx\left(\frac{2V}{t}\right)^{1/5}. \tag{14}$$

The critical concentration n_{dc} corresponds to the configuration where metallic droplets start to overlap, i.e., where the volume of the CO phase [the second term in (13)] tends to zero. Hence,

$$n_{dc}=\frac{3}{4\pi}\left(\frac{a}{R}\right)^3\propto\left(\frac{t}{V}\right)^{3/5}. \tag{15}$$

Actually, one should include the surface energy contribution to the total energy of the droplet. The surface energy should be of the order of W^2R^2/V. For large droplets, this contribution is small compared to the term $\propto R^3$ in (13); it would also be reduced for a ''soft'' droplet boundary. It is easy to show that even in the worst case of a small droplet (of the order of several lattice constants) with a sharp boundary, R/a acquires a factor $1-0.2(t/2V)^{1/5}$ related to the surface contribution. Thus the corrections related to the surface would not exceed about 20% of the bulk value. That is why we will ignore this term below.

By comparing (8) with (13), we see that for deviations from half-filling $0<\delta\leqslant\delta_c=1/2-n_{dc}$, the energy of the phase-separated state is always lower than the energy of the homogeneous charge-ordered state. Thus the energy of a phase-separated state with droplets corresponds to global minima of the energy for all $0<\delta\leqslant\delta_c$. This justifies our conclusion about phase separation into a charge-ordered state with $n=1/2$ and a metallic state with small spherical droplets.

Note also that for $n>1/2$ the compressibility of the charge-ordered state is again negative, $1/\kappa=d^2E/d\delta^2=-4W^2/3Vz<0$, and has the same value as for the case $n<1/2$. As a result, it is again more favorable to create a phase-separated state for these densities. However, as we have said, the nature of the second phase with $n>1/2$ is not quite clear at present, and we shall therefore not consider this case here.

4. AN EXTENDED MODEL

Now we can extend the model discussed in the previous Sections by taking into account the essential magnetic interactions. In manganites, besides the conduction electrons in e_g bands, there exist also practically localized t_{2g} electrons, which we now include in our consideration. The corresponding Hamiltonian has the form

$$\hat{H}=-t\sum_{\langle i,j\rangle,\sigma}c_{i\sigma}^{+}c_{j\sigma}+V\sum_{\langle i,j\rangle}n_in_j-J_H\sum_i\mathbf{S}_i\boldsymbol{\sigma}_i$$
$$+J\sum_{\langle i,j\rangle}\mathbf{S}_i\mathbf{S}_j-\mu\sum_i n_i. \tag{16}$$

In comparison to (1), the additional terms here corresponds to the strong Hund-rule on-site coupling J_H between the localized spins $\mathbf{S}$ and the spins of conduction electrons σ, and to the relatively weak Heisenberg antiferromagnetic (AFM) exchange J between neighboring local spins. In real manganites, the AFM ordering of the CE type in the CO phase is determined not only by the exchange of localized t_{2g} electrons but to a large extent by the charge- and orbitally ordered e_g electrons themselves. For simplicity, we ignore this factor here and assume that the superexchange interaction is the same both in the CO and in the metallic phases.

It is physically reasonable to consider this model in the limit

$$J_HS>V>W>JS^2.$$

In the absence of the Coulomb term, this is exactly the conventional double-exchange model (see, e.g., Refs. 7 and 15). The large Hund's term favors the metallicity in the system, since the effective bandwidth in our problem depends upon the magnetic order. Therefore, the estimate for the critical concentration here is different from (15). As in Ref. 15 the

metallic droplets will be ferromagnetic (FM) due to the double exchange. The energy of this state has the form:

$$E=-tn_d\left(z-\frac{\pi^2a^2}{R^2}\right)-\frac{W^2}{6Vz}\left[1-\frac{4}{3}\pi\left(\frac{R}{a}\right)^3 n_d\right]$$
$$+zJS^2\frac{4}{3}\pi\left(\frac{R}{a}\right)^3 n_d-zJS^2\left[1-\frac{4}{3}\pi\left(\frac{R}{a}\right)^3 n_d\right]. \quad (17)$$

The last two terms in (17) describe, respectively, the energy cost of the Heisenberg AFM exchange inside the FM metallic droplets and the energy benefit from it in the AFM insulating part of the sample. Minimization with respect to the droplet radius [as in (13)] yields:

$$\frac{R}{a}\propto\left(\frac{t}{V}+\frac{JS^2}{t}\right)^{-1/5}. \quad (18)$$

Note that for $t/V\ll JS^2/t$, formula (18) gives just the same estimate for the radius of a FM metallic droplet $R/a\sim(t/JS^2)^{1/5}$ as in Refs. 7 and 15.

In the opposite limit, when $t/V\gg JS^2/t$, we recover the same result $R/a\sim(V/t)^{1/5}$ as in (14). Finally, the critical concentration n_c is estimated as follows

$$n_c\propto\left(\frac{t}{V}+\frac{JS^2}{t}\right)^{3/5}. \quad (19)$$

As a result, taking into account also the tendency toward phase separation at very small values of n,[7–10,15] we come to the following phase diagram for the extended model (cf. Ref. 10):

1. At $0<n<(JS^2/t)^{3/5}$ it corresponds to phase separation into a FM metal embedded in an AFM insulating matrix. To minimize the Coulomb energy, it may be again favorable to split this metallic region into droplets with an average radius given by (18) with $t/V=0$, each droplet containing one electron and kept apart from one another.

2. At $(JS^2/t)^{3/5}<n<(t/V+JS^2/t)^{3/5}<1/2$, the system is a FM metal.

Of course, we need a window of parameters to satisfy the inequality on the right-hand side. In actual manganites where $t/V\sim1/2-1/3$ and $JS^2/t\sim0.1$, these conditions upon n are not necessarily satisfied. Experiments suggest that this window is present for $La_{1-x}Ca_xMnO_3$, but it is definitely absent for $Pr_{1-x}Ca_xMnO_3$ (Ref. 10).

3. Finally, at $(t/V+JS^2/t)^{3/5}<n<1/2$, we have phase separation in the form of FM metallic droplets inside an AFM charge-ordered matrix.

This phase diagram is in good qualitative agreement with many available experimental results for real manganites,[17–20] in particular with the observation of small-scale phase separation close to 0.5 doping.[21] Note also that our phase diagram has certain similarities with the phase diagram obtained in Refs. 22 and 23 for the problem of spontaneous ferromagnetism in doped excitonic insulators.

5. CONDUCTIVITY OF THE PHASE–SEPARATED STATE

Let us consider an insulating antiferromagnetic sample of volume V_s in an electric field **E**. The total number of magnetic polarons in the volume is N, and thus their spatial density is $n=N/V_s$. As was mentioned before, the number of polarons is assumed to be equal to the number of charge carriers introduced by doping. Neglecting the conductivity of the insulating phase, we assume that charge carriers are located only within the droplets. Charge transfer can thus occur either due to the motion of droplets or due to electron tunneling. The former mechanism is less effective because of the large effective mass of magnetic polarons and their possible pinning by crystal lattice defects. We therefore neglect the contribution of polaron motion.

A magnetic polaron in the ground state contains one electron. As a result of a tunneling process, droplets with more than one electron are created, and some droplets become empty. If the energy of an empty droplet $E(0)$ is taken to be zero, the energy of a droplet with one electron can be estimated as $E(1)\sim t(a/R)^2$. This is essentially the kinetic energy of an electron localized in a sphere of radius R. In the same way, the energy of two-electron magnetic polaron $E(2)\sim2E(1)+U$, with U being the interaction energy of the two electrons. In all these estimates, we have disregarded the surface energy, which is expected to be small (see the previous Section). Thus, $E(2)+E(0)>2E(1)$, and the creation of two-electron droplets is associated with an energy barrier of the order of $A\equiv E(2)-2E(1)\sim U$. It is clear that the interaction energy U of two electrons in one droplet is determined mainly by the Coulomb repulsion of these electrons, and hence $A\sim e^2/\varepsilon a$, where ε is the static dielectric constant, which in real manganites can be rather large ($\varepsilon\sim20$). We assume below that the mean distance between the droplets is $n^{-1/3}\gg R$ (the droplets do not overlap). Then A is larger than the average Coulomb energy $e^2n^{1/3}/\varepsilon$. Since the characteristic value of the droplet radius R is of the order of 10 Å, we have $A/k_B\sim1000$ K, and $A>k_BT$ in the case under study. In the following, we assume that the temperature is low, $A\gg k_BT$, and we do not consider the possibility of the formation of droplets with three or more electrons.

Let us denote the numbers of single-electron, two-electron, and empty droplets as N_1, N_2, and N_3, respectively. According to our model, $N_2=N_3$, $N_1+2N_2=N$, and N is constant. Before turning to the conductivity, we evaluate the thermal averages of N_1 and N_2. To this end, we note that the number p_N^m of possible states with m two-electron droplets and m empty droplets is equal to $C_N^mC_{N-m}^m$, where C_N^m are the binomial coefficients. Since the created pairs of droplets are independent, we write the partition function in the form

$$Z=\sum_{m=0}^{N/2}P_N^m\exp(-m\beta),\quad \beta=A/k_BT. \quad (20)$$

Approximating the sum by an integral and using Stirling's formula for the factorials, we get

$$Z=\int_0^{N/2}dm\exp\left[-m\beta-N\ln\left(1-\frac{2m}{N}\right)\right.$$
$$\left.+2m\ln\left(\frac{N}{m}-2\right)\right].$$

Calculating Z in the saddle-point approximation, and subsequently evaluating the statistical average of N_2 in the same way, i.e.,

$$\overline{N}_2 = Z^{-1}\sum_{m=0}^{N/2} m P_N^m \exp(-m\beta) = -\frac{\partial}{\partial\beta}\ln Z, \tag{21}$$

we easily obtain

$$\overline{N}_2 = N\exp(-A/2k_BT),$$

$$\overline{N}_2 = N - 2\overline{N}_2 = N[1-2\exp(-A/2k_BT)]. \tag{22}$$

Within the framework of the proposed model, the electron tunneling occurs via one of the following four processes illustrated in Fig. 3:

(i) In the initial state we have two droplets in the ground state, and after tunneling in the final state we have an empty droplet and a droplet with two electrons;

(ii) an empty droplet and a two-electron droplet in the initial state transform into two droplets in the ground state (two droplets with one electron);

(iii) a two-electron droplet and a single-electron droplet exchange their positions by transferring an electron from one droplet to the other;

(iv) an empty droplet and a single-electron droplet exchange their positions by transferring an electron from one droplet to the other.

In the linear regime, all these processes contribute to the current density j independently, $j = j_1 + j_2 + j_3 + j_4$. The contributions of the first two processes are

$$j_{1,2} = en_{1,2}\left\langle \sum_i v_{1,2}^i \right\rangle, \tag{23}$$

where $n_{1,2} = N_{1,2}/V_s$ are the densities of the single- and two-electron droplets, and $\langle ... \rangle$ stands for statistical and time averages. Factors $n_{1,2}$ correspond to electron tunneling from a single-electron droplet (process (i)) or two-electron (ii) droplet. The summation in (23) is performed over all of the magnetic polarons on which the electron can tunnel—one-electron droplets for process (i) and empty droplets for process (ii). Finally, the components of the average electron velocity $\langle v_{1,2}^i \rangle$ along the direction of the electric field are obviously found as:[24]

$$\left\langle \sum_i v_{1,2}^i \right\rangle = \left\langle \sum_i \frac{r^i \cos\theta^i}{\tau_{1,2}(r^i,\theta^i)} \right\rangle, \tag{24}$$

where r^i and θ^i are the electron tunneling length (the distance between the droplets) and the angle between the electric field and the direction of motion, respectively, and

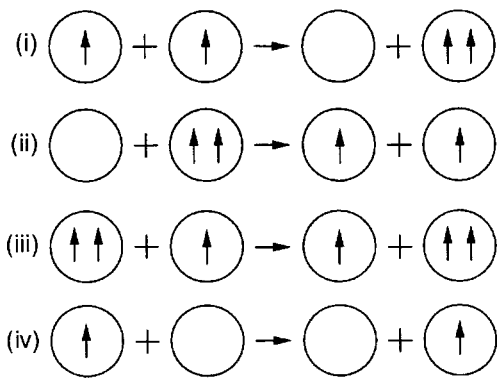

FIG. 3. Elementary tunneling processes.

$\tau_{1,2}(r^i,\theta^i)$ are characteristic times associated with the tunneling processes. The relation between $\tau_1(r,\theta)$ and $\tau_2(r,\theta)$ can be found from the following considerations. Near equilibrium, the number of two-electron droplets excited per unit time is equal to the number of decaying two-electron droplets. We thus have the detailed-balance relation,

$$\frac{\overline{N}_1^2}{\tau_1(r,\theta)} = \frac{\overline{N}_2^2}{\tau_2(r,\theta)}, \tag{25}$$

where we have taken into account that the probability of formation of a two-electron droplet is proportional to the total number N_1 of single-electron states multiplied by the number of available hopping destinations, which also equals N_1. Similarly, the probability of decay of a two-electron droplet is proportional to $N_2N_3 = N_2^2$. Relation (25) implies that $\tau_2(r,\theta) = \tau_1(r,\theta)\exp(-A/k_BT)$. Then we can write the conventional expression for the tunneling times[24] in the form

$$\tau_{1,2}(r,\theta) = \omega_0^{-1}\exp\left(\frac{r}{l} \pm \frac{A}{2k_BT} - \frac{eEr\cos\theta}{k_BT}\right), \tag{26}$$

where l and ω_0 are the characteristic tunneling length and magnon frequency, and we have taken into account the contribution of the external electric field to the tunneling probability.

To perform the averaging, we assume that the centers of the magnetic polarons are randomly positioned in space, and the average distance $n^{-1/3}$ between them is much larger than the droplet radius R. Both assumptions seem to be perfectly justified far below the percolation threshold. Then the averaged sum in (23) is essentially the space average of v^i, multiplied by the number of droplets available for hopping (N_1 for process (i) and N_2 for process (ii)). Expanding in the small parameter $eEl/k_BT \ll 1$, we obtain

$$\left\langle \sum_i v_{1,2}^i \right\rangle = \frac{eE\omega_0}{k_BT} N_{1,2} e^{-A/2k_BT}\langle r^2\cos^2\theta e^{-r/l}\rangle_V,$$

$$\langle ... \rangle_V = V_s^{-1}\int ... d^3r. \tag{27}$$

In (27) the electric field is outside the averaging. Rigorously speaking, this means that the characteristic hopping length l is larger than the interdroplet distance $n^{-1/3}$, and our approach is valid only when the droplet concentration is not too small. Substituting (27) into (23) and performing the integration, we find

$$j_{1,2} = \frac{32\pi e^2 E\omega_0 l^5 n_{1,2}^2}{k_BT}\exp(\mp A/2k_BT). \tag{28}$$

In processes (iii) and (iv) the free energy of the system is not changed after the tunneling, and we write the characteristic times as:

$$\tau_{3,4}(r,\theta) = \omega_0^{-1}\exp(r/l - eEr\cos\theta/k_BT). \tag{29}$$

The contribution of these two processes to the current is calculated similarly to that of (i) and (ii). For process (iii) the number of magnetic polarons from which the electron may tunnel is N_2, whereas the number of accepting droplets is N_1. In the same way, for process (iv) these numbers are N_1 and $N_3 = N_2$, respectively. Consequently, the factors $n_{1,2}^2$ in (28) are replaced by n_1n_2,

$$j_{3,4}=\frac{32\pi e^2 E\omega_0 l^5 n_1 n_2}{k_B T}. \tag{30}$$

From (28) and (30) we now obtain the dc conductivity $\sigma=j/E$,

$$\sigma=\frac{32\pi e^2\omega_0 l^5}{kT}[2n_1n_2+n_1^2 e^{-A/2k_BT}+n_2^2 e^{A/2k_BT}]. \tag{31}$$

In this Section, we are only interested in the average conductivity; fluctuations give rise to noise and are considered in Sec. 6. Using (22), we find that all the four processes illustrated in Fig. 3 give identical contributions to the conductivity; for $A\gg k_BT$ the average conductivity (for which we retain the notation σ) reads

$$\sigma=\frac{128\pi e^2 n^2\omega_0 l^5}{k_BT}\exp(-A/2k_BT). \tag{32}$$

We see that the conductivity increases with temperature as $\sigma(T)\propto T^{-1}\exp(-A/2k_BT)$, which is typical for tunneling systems (see, e.g., Ref. 24).

6. 1/*f* NOISE POWER

Recently, Podzorov *et al.*[11] reported the observation of a giant $1/f$ noise in perovskite manganites in the phase-separated regime. Generally, systems with distributed hopping lengths are standard objects which exhibit $1/f$ noise (for review, see Refs. 25 and 26). The purpose of this Section is to study low-frequency noise within the framework of the model used to calculate the conductivity in Sec. 5 and to show that it indeed has a $1/f$ form.

Starting from Ohm's law $U=IL/\sigma S$ (where L and S are the sample length and cross section, respectively) and assuming that the measuring circuit is stabilized ($I=$const), we can express the voltage noise at the frequency ω, which we denote $\langle\delta U^2\rangle_\omega$, in the following way:

$$\langle\delta U^2\rangle_\omega=U_{dc}^2\frac{\langle\delta\sigma^2\rangle_\omega}{\sigma^2}, \tag{33}$$

where U_{dc} is the time-averaged voltage, and $\langle\delta\sigma^2\rangle_\omega$ is the spectrum of conductivity fluctuations.

If we disregard possible fluctuations of the temperature in the system, the only sources of fluctuations in our model are those of the occupation number n_1 and n_2. Using the conservation law $n_1+2n_2=n$, we find from (31):

$$\delta\sigma=\sigma\frac{\delta n_2}{n_2}[1-2\exp(-A/2k_BT)]. \tag{34}$$

Now we need to find the fluctuation spectrum $\langle\delta n_2^2\rangle_\omega$. Taking into account that two-electron droplets decay via process (ii), we can write the relaxation equation in the usual form[27]

$$\delta\dot n_2=-\frac{\delta n_2}{\tau(r)},\quad \tau(r)=\omega_0^{-1}\exp(r/l-A/2k_BT), \tag{35}$$

where we have neglected the effect of the electric field. The fluctuation spectrum then reads[27]

$$\langle\delta n_2^2\rangle_\omega=\langle\delta n_2^2\rangle_T\left\langle\sum_i\frac{2\tau(r^i)}{1+\omega^2\tau^2(r^i)}\right\rangle$$
$$=8\pi\overline{n_2}\langle\delta n_2^2\rangle_T\int_0^\infty\frac{\tau(r)}{1+\omega^2\tau^2(r)}r^2dr, \tag{36}$$

where $\langle\delta n_2^2\rangle_T$ is the thermal average of the variation of n_2, and the summation is performed over the "empty droplet–two-electron droplet" pairs, with r_i being the distance between the sites in a pair.

We are interested below in the frequency range

$$\tilde\omega_0\exp(-L_s/l)\ll\omega\ll\tilde\omega_0,$$
$$\tilde\omega_0\equiv\omega_0\exp(A/2k_BT), \tag{37}$$

where L_s is the smallest of the sample sizes. In this case, with logarithmic accuracy we obtain for $A\gg k_BT$

$$\langle\delta U^2\rangle_\omega=U_{dc}^2\frac{\langle\delta n_2^2\rangle_T}{\overline{n_2}}\frac{4\pi^2 l^3}{\omega}\ln^2\left(\frac{\tilde\omega_0}{\omega}\right). \tag{38}$$

Thus, in a wide range of sufficiently low frequencies (37) the noise power spectrum for our system has almost $1/f$ form.

The variation $\langle\delta n_2^2\rangle_T=V_s^{-2}(\overline{N_2^2}-\overline{N_2}^2)$ is easily found in the same way as in (22),

$$\langle\delta n_2^2\rangle_T=\frac{\overline{n_2}}{2V_s}. \tag{39}$$

Combining this with (38), we write the final expression for the spectral density of noise for $A\gg k_BT$ in the form

$$\alpha=\frac{\langle\delta U^2\rangle_\omega V_s\omega}{U_{dc}^2}=2\pi^2 l^3\ln^2\left(\frac{\tilde\omega_0}{\omega}\right). \tag{40}$$

It is remarkable that the noise spectrum in our model has a $1/f$ form down to very low frequencies. This is due to the fluctuations in the occupation numbers of droplets, associated with the creation and annihilation of extra electron–hole pairs. This mechanism of $1/f$ noise is specific to our model and is not present in standard hopping conduction.[28]

Let us estimate the numerical value of the parameter α, which is the standard measure of the strength of $1/f$ noise. This parameter is proportional to the third power of l. Simple estimates reveal that, in general, l is of the order of or higher than R. Assuming again that the excitation energy is of the order of the Coulomb energy $A\sim e^2/R\varepsilon$, taking ω_0 to be of the order of the Fermi energy inside the droplets (which means $\hbar\omega_0\sim 300$ K for $n<n_c$), and estimating the tunneling length l as being $l\geqslant 2R\sim 20$ Å, we arrive to the conclusion that the parameter α is of the order $\alpha\approx 10^{-17}-10^{-16}\,\mathrm{cm}^3$ for $T<A/k_B$ and $\omega\sim 1$ Hz–1 MHz. This value of α is several orders of magnitude higher than in ordinary semiconducting materials (see Refs. 25 and 26). Such a large magnitude of the noise can be attributed to the relatively low height of the potential barrier A and to the relatively large tunneling length l. Formally, it is also related to the large value of the logarithm squared in (40).

7. CONCLUSIONS

Summarizing, we have shown that the narrow-band system, which has the checkerboard charge ordering at $n=1/2$

(corresponding to the doping $x=0.5$) is unstable toward phase separation away from half-filling ($n\neq 1/2$). It separates into regions with the ideal charge ordering ($n=1/2$) and other regions in which extra electrons or holes are trapped. The simplest form of these metallic regions could be spherical metallic droplets embedded in the charge-ordered insulating matrix. Simple considerations have allowed us to estimate the size of these droplets and the critical concentration, or doping $x_c=1/2-\delta_c$, at which the metallic phase would occupy the whole sample and the CO phase would disappear. Taking the magnetic interactions into account does not change these conclusions but somewhat modifies the characteristic parameters of the metallic droplets.

The long-range Coulomb interaction may also modify the results, but we do not expect any qualitative changes. For realistic values of the parameters, the size of metallic droplets is still microscopic (about 10–20 Å), and the excess charge in them will be rather small.

The picture obtained corresponds rather well to the known properties of 3D and layered manganites at close to (less than) half doping, $x\leqslant 1/2$. Our treatment is also applicable to other systems with charge ordering, such as cobaltites[29] and nickelates.[30] It would be interesting to study them for charge carrier concentrations different from the commensurate ''checkerboard'' one.

A number of important problems still remain unsolved (the origin of the ''in-phase'' ordering in perovskite manganites in the c direction, the detailed description of inhomogeneous states in the overdoped regime $x>1/2$, the behavior at finite temperature). Nevertheless, in spite of the simplifications made, our model seems to capture the essential physics underlying the interplay between phase separation and charge ordering in transition-metal oxides.

Even in our oversimplified model we get reasonable behavior of resistivity for underdoped manganites. Moreover, we have shown that $1/f$ noise appears in the framework of our model in a natural way. The phase separation ensures a large magnitude of the noise power as compared with homogeneous materials. Of course, a more sophisticated theory should include both the ferromagnetic structure of the droplet and the antiferromagnetic structure of the insulating matrix. This can lead us to a physics resembling that observed in the process of spin-assisted tunneling, which attracts a considerable interest nowadays (see, e.g., Ref. 31).

The work was supported by INTAS (grants 97-0963 and 97-11954), the Russian Foundation for Basic Research (projects 00-02-16255 and 00-15-96570), and by the Russian-Dutch Program for Scientific Cooperation. M.Yu.K.acknowledges the support of the Russian President Program (grant 96-15-9694).

*E-mail: kagan@kapitza.ras.ru

[1] E. Verwey, Nature (London) **144**, 327 (1939); E. Verwey and P. W. Haayman, Physica (Amsterdam) **8**, 979 (1941).
[2] T. Mutou and H. Kontani, Phys. Rev. Lett. **83**, 3685 (1999).
[3] J. van den Brink, G. Khaliullin, and D. I. Khomskii, Phys. Rev. Lett. **83**, 5118 (1999).
[4] G. Jackeli, N. B. Perkins, and N. M. Plakida, Phys. Rev. B **62**, 372 (2000).
[5] Z. Jirák, S. Krupička, Z. Šimša, M. Dlouha, and S. Vratislav, J. Magn. Magn. Mater. **53**, 153 (1985).
[6] A. Arulraj, A. Biswas, A. K. Raychaudhuri, C. N. R. Rao, P. M. Woodward, T. Vogt, D. E. Cox, and A. K. Cheetham, Phys. Rev. B **57**, R8115 (1998); M. Uehara, S. Mori, C. H. Chen, and S.-W. Cheong, Nature (London) **399**, 560 (1999).
[7] E. L. Nagaev, Usp. Fiz. Nauk **166**, 833 (1996) [Sov. Phys. Usp. **39**, 781 (1996)].
[8] A. Moreo, S. Yunoki, and E. Dagotto, Science **283**, 2034 (1999).
[9] D. Arovas and F. Guinea, Phys. Rev. B **58**, 9150 (1998).
[10] D. I. Khomskii, Physica B **280**, 325 (2000).
[11] V. Podzorov, M. Uehara, M. E. Gershenson, T. Y. Koo, and S.-W. Cheong, Phys. Rev. B **61**, R3784 (2000).
[12] D. I. Khomskii, *Preprint of the P. N. Lebedev Physics Institute*, No. 105 (1969).
[13] G. S. Uhrig and R. Vlamink, Phys. Rev. Lett. **71**, 271 (1993).
[14] P. Pietig, R. Bulla, and S. Blawid, Phys. Rev. Lett. **82**, 4046 (1999).
[15] M. Yu. Kagan, D. I. Khomskii, and M. V. Mostovoy, Eur. Phys. J. B **12**, 217 (1999).
[16] S. Mori, C. H. Chen, and S.-W. Cheong, Nature (London) **392**, 473 (1998).
[17] N. A. Babushkina, L. M. Belova, A. N. Taldenkov, E. A. Chistotina, D. I. Khomskii, K. I. Kugel, O. Yu. Gorbenko, and A. R. Kaul, J. Phys.: Condens. Matter **11**, 5865 (1999).
[18] M. Hennion, F. Moussa, G. Biotteau, J. Rodríguez-Carvajal, L. Pinsard, and A. Revcolevscki, Phys. Rev. Lett. **81**, 1957 (1998).
[19] G. Allodi, R. De Renzi, G. Guidi, F. Licci, and M. W. Pieper, Phys. Rev. B **56**, 6036 (1997).
[20] I. F. Voloshin, A. V. Kalinov, S. E. Savel'ev, L. M. Fisher, N. A. Babushkina, L. M. Belova, D. I. Khomskii, and K. I. Kugel, JETP Lett. **71**, 106 (2000).
[21] Y. Moritomo, A. Machidas, S. Mori, N. Yamamoto, and A. Nakamura, Phys. Rev. B **60**, 9220 (1999).
[22] L. Balents and C. M. Varma, Phys. Rev. Lett. **84**, 1264 (2000).
[23] V. Barzykin and L. P. Gor'kov, Phys. Rev. Lett. **84**, 2207 (2000).
[24] N. F. Mott and E. A. Davis, *Electronic Processes in Non-Crystalline Materials*, Clarendon Press, Oxford (1979).
[25] P. Dutta and P. M. Horn, Rev. Mod. Phys. **53**, 497 (1981).
[26] Sh. M. Kogan, *Electronic Noise and Fluctuations in Solids*, Cambridge University Press, Cambridge (1996).
[27] L. D. Landau and E. M. Lifshitz, *Statistical Physics, Pt. 1*, Butterworth-Heinemann, Oxford (1980).
[28] Sh. M. Kogan and B. I. Shklovskii, Fiz. Tekh. poluprovodn. **15**, 1049 (1981) [Sov. Phys. Semicond. **15**, 605 (1981)].
[29] Y. Moritomo, M. Takeo, X. J. Liu, T. Akimoto, and A. Nakamura, Phys. Rev. B **58**, R13334 (1998).
[30] J. A. Alonso, J. L. García-Múñoz, M. T. Fernández-Díaz, M. A. G. Aranda, M. J. Martínez-Lope, and M. T. Casais, Phys. Rev. Lett. **82**, 3871 (1999).
[31] *Tunneling in Complex System*, edited by S. Tomsovic, World Scientific Singapore (1998).

This article was published in English in the original Russian journal. Reproduced here with stylistic changes by AIP.

SUPERCONDUCTIVITY, INCLUDING HIGH TEMPERATURE SUPERCONDUCTIVITY

Magnetic flux trapping and frozen magnetoresistance in bismuth-containing high-temperature superconducting films

A. A. Sukhanov* and V. I. Omel'chenko

Institute of Radio Engineering and Electronics, Russian Academy of Sciences, pl. Vvedenskogo d.1, 141190 Fryazino, Moscow District, Russia

(Submitted March 5, 2001)
Fiz. Nizk. Temp. **27**, 826–830 (August 2001)

Hall-probe and magnetoresistance studies of trapped magnetic fields are carried out on Bi-containing high-T_c superconducting films obtained by magnetron sputtering. It is shown that the trapped magnetic fields are alternating in sign in the plane of the film on a characteristic scale of less than 50 μm. The temperature dependence of the frozen magnetoresistance and trapped magnetic fields is investigated. It is found that heating the films causes the trapped magnetic fields and frozen magnetoresistance to decrease to zero at a temperature substantially lower than the temperature at which the magnetoresistance vanishes, and for trapping after cooling in zero field a maximum appears on the curve of the trapped magnetic fields versus the trapping temperature. The experimental data are discussed and compared with the results of calculations in the model of superconducting loops, making it possible to determine the form and parameters of the distribution function of the loops over critical fields and the temperature dependence of the critical fields.
[DOI: 10.1063/1.1399196]

INTRODUCTION

In the study of the hysteretic magnetic properties of granulated high-T_c superconductors (HTSCs), which are Josephson media with a large dispersion of the parameters of the weak links,[1] measurements of the trapped magnetic fields (TMFs) by means of Josephson interferometers and Hall probes are widely used.[2–4]

However, in the region of the superconducting transition these granulated HTSCs contain not only superconducting regions but also normal regions and a normal simply connected cluster, as a consequence of which the magnetic fields trapped in the superconducting regions, being closed through the normal regions of the sample, should be of alternating sign in this plane and cannot be observed by the usual methods. At the same time, these sign-varying trapped magnetic fields, by destroying the superconductivity of the weak links of the percolation channels, must give rise to an additional resistance.

Therefore, investigation of the magnetoresistance due to the trapped magnetic fields, or frozen magnetoresistance, a phenomenon which is well known to experimenters,[5] is an efficient method of obtaining information about the trapped magnetic fields in the region of the superconducting transition in granulated HTSCs and in microscopically inhomogeneous HTSC samples with an extended superconducting transition.

In this study we have used Hall probes and measurements of the frozen magnetoresistance to investigate the features of the magnetic flux trapping in Bi-HTSC films obtained by magnetron sputtering, and here we discuss the experimental data in the framework of various trapping models and compare them with the results of calculations in the superconducting loops (rings) model.[6,7]

EXPERIMENT

Measurements were made on Bi-HTSC films 3 μm thick, obtained by magnetron sputtering of a ceramic target of nominal composition $Bi_2Sr_2Ca_2Cu_3O_{10-y}$ on Polikor (Al_2O_3) substrates with a subsequent brief (3–5 min) annealing in air at $T=820-860\,^{\circ}$C.

The resistive superconducting transition in the resulting films begins at a temperature $T_{c0}=83$ K, which attests to the presence of an appreciable fraction of the 2-2-1-2 phase in them.

Measurements of the trapped magnetic fields in these films by means of Hall probes with dimensions of the working region 0.15×0.45 mm on an apparatus with a sensitivity of 0.1 Oe showed that the trapped fields averaged over the area of the probe (i.e., the measured values) were less than 0.1 Oe in the temperature interval 4–80 K for inducing fields $H_i<500$ Oe.

At the same time, the magnetron-sputtered Bi-HTSC films exhibited a rather large frozen magnetoresistance, and that was used to study the trapped magnetic fields.

The most suitable films for studying the temperature dependence of the trapped magnetic fields and frozen magnetoresistance turned out to be those having an extended resistive transition, with a temperature T_f at completion of the transition equal to 5–40 K. The largest values of the trapped magnetic fields and frozen magnetoresistance were obtained when the plane of the films was perpendicular to the magnetic field.

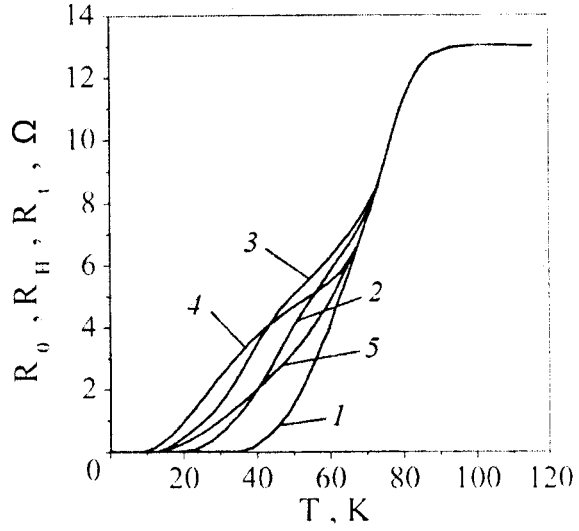

FIG. 1. Typical temperature dependence of the resistance of a Bi-HTSC magnetron film 3 μm thick, 3 mm wide and 8 mm long. R_0 is the resistance in zero field (*1*), $R_H(T,H)$ is the resistance in external magnetic fields of 40 Oe (*2*) and 95 Oe (*3*); $R_t(T,H_i,T_t)$ is the resistance in the trapped magnetic field for $H_i=200$ Oe and $T_t=5$ K in the FC (*4*) and ZFC (*5*) regimes.

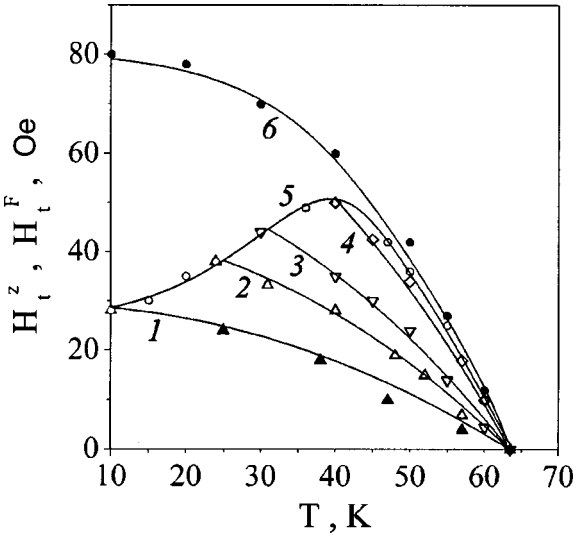

FIG. 2. Temperature dependence of the effective values of the trapped magnetic fields. The symbols represent the experimental data, and the solid lines the curves calculated in the superconducting-loops model. The functions $H_t^Z(T)$ on heating from different trapping temperatures T_t [K]: 10 (*1*), 25 (*2*), 30 (*3*), and 40 (*4*). The dependence of the trapped magnetic fields on the trapping temperature (*5*) (ZFC regime). The function $H_t^F(T)$ obtained in the case of trapping by cooling in a field (*6*) (the FC regime); $H_i=200$ Oe.

Figure 1 shows the typical temperature dependence of the resistance R_0 of a 3-μm-thick Bi-HTSC film in zero field (curve *1*), the resistances $R_H(H)$ in external magnetic fields of 40 and 95 Oe (curves *2* and *3*), and the resistances $R_t(H_i,T_t)$ in a trapped magnetic field (curves *4* and *5*). These last two curves were obtained as the film was heated after trapping at $T_t=5$ K in the field cooling (FC) regime (cooling in a field $H_i=200$ Oe) and in the zero-field cooling (ZFC) regime (applying a field pulse of amplitude $H_i=200$ Oe after cooling in zero field).

A characteristic feature of the curves shown in Fig. 1 is that the temperature at which the trapped magnetic fields and, hence, the frozen magnetoresistance vanish, T_{tm}, is considerably lower than the limiting temperature T_m at which the magnetoresistance vanishes. For the films studied here these temperatures have the values $T_{tm}=62-64$ K and $T_m=72-78$ K.

The curves of $R_t(T,H_i,T_t)$ and $R_H(T,H)$ cross at temperatures where the decaying trapped fields have the same effect on the resistance as do external fields of 40 and 95 Oe.

This means that in these magnetron films the local trapped fields that govern the magnetoresistance are at least 2–3 orders of magnitude greater than the mean fields, the highest possible value of which is set by the sensitivity of the Hall measurements (0.1 Oe).

This leads to what we think is an important conclusion: the trapped magnetic fields in the Bi-HTSC films studied here are not only highly nonuniform but also vary in sign. The characteristic scales of the nonuniformities here must be much smaller than the size of the probe (0.45×0.15 mm) and clearly cannot exceed 50 μm.

The fact that the frozen magnetoresistance and trapped magnetic fields did not change when the width of the films was decreased to 100 μm confirms the given upper limit on the size of the nonuniformity of the trapped magnetic fields.

As a characteristic of the sign-varying trapped fields we introduce the concept of an effective value of the frozen magnetoresistance. We shall assume that the effective value of a nonuniform trapped magnetic field is equal to the external field that would have the same effect on the resistance of the sample as do the frozen magnetic fields.

By measuring the temperature dependence of the frozen magnetoresistance and the field dependence of the magnetoresistance at different temperatures and using the condition

$$R_t(T,H_i,T_t)=R_H(T,H_t),$$

we determine how the effective values of the frozen magnetoresistance $H_t(T,H_i,T_t)$ depend on the temperature, inducing field, and trapping temperature.

Figure 2 shows the temperature dependence of the effective values of the trapped magnetic fields in the case of trapping by a field pulse $H_i=200$ Oe (the ZFC regime) at different trapping temperatures T_t (curves *1–4*) and in the FC regime for trapping by cooling to 10 K in a field $H_i=200$ Oe (curve *6*). Curve *5* is the envelope of the family of curves *1–4*, i.e., the dependence of the trapped magnetic fields on the trapping temperature for the ZFC regime.

The curves shown in Fig. 2 have the following characteristic features: the presence of a maximum on the curve of the effective trapped field as a function of trapping temperature for the ZFC regime, a slow decline of the trapped magnetic fields with decreasing temperature in the low-temperature region, vanishing of the trapped magnetic fields in all cases at a single temperature $T_{tm}=63$ K which is lower than the temperature at which the magnetoresistance appears ($T_m=72$ K).

DISCUSSION OF RESULTS

The results presented above cannot be explained in terms of the trapping models ordinarily used — the critical-state (Bean) model,[8] and the model of pinned Abrikosov vortices.[9]

Indeed, the Bean model describes the magnetic properties of the samples only after a complete transition to the superconducting state, when their resistance has already gone to zero. According to the model of pinned Abrikosov vortices, on the other hand, the magnetic flux trapping should occur at temperatures higher than the temperature T_m at which magnetoresistance appears, when a considerable fraction of the granules have already undergone transition to the superconducting state, and therefore, contrary to experiment, the temperature regions in which the frozen magnetoresistance and magnetoresistance exist should coincide.

At the same time, our results can be explained consistently in the model of superconducting loops (rings),[7,6] according to which the trapped magnetic fields in granulated HTSCs are due to magnetic flux trapping in a system of superconducting loops formed by the superconducting granules and the Josephson weak links connecting them. Such a system is characterized by a wide set of weak links and, hence, a dispersion of the superconducting loops with respect to critical fields and temperatures.

On the basis of the superconducting-loops model, one can give the following picture of the change in the state of a granulated film as the temperature is lowered. In the temperature interval $T_m<T<T_{c0}$ individual granules with high T_c's undergo transition to the superconducting state. Accordingly, and in agreement with the curves of Fig. 1, the resistance of the film decreases, and magnetoresistance and magnetic flux trapping are essentially nonexistent. At lower temperatures Josephson weak links sensitive to magnetic fields $\sim 1-100$ Oe arise between granules. Besides the additional drop in resistance due to the formation of superconducting channels, this gives rise to magnetoresistance. As the temperature is lowered further, closed superconducting loops are formed. In these loops (or ''rings'') a trapping of magnetic flux occurs, leading to the onset of frozen magnetoresistance due to the destruction of the weak links of the superconducting channels.

The superconducting-loops model gives not only a qualitative explanation of the experimental results but also a good quantitative description of the temperature dependence of the trapped magnetic fields.

We shall assume that the effective values of the trapped magnetic fields are proportional to the average (with respect to modulus) magnetic fields produced by the system of superconducting rings (the effective-medium approximation).

In the case of trapping by a pulse of amplitude H_i (the ZFC regime), trapping occurs, according to the superconducting-loops model, only in rings whose critical fields H_c are less than H_i, and the value of the field trapped in each of the rings is equal to the critical field; thus the average trapped fields are described by the integral[7]

$$H_t^Z(H_i,T_t,T)=A\int_0^{H_c^*(T)}H_c f(H_c)dH_c, \tag{1}$$

where $T\geqslant T_t$, $f(H_c)$ is the distribution function of the rings with respect to critical fields, the upper limit of the integral in (1) is determined by the temperature dependence of the critical fields and the condition $H_c^*(T_t)=H_i$, and the coefficient A takes into account the geometric factors and the demagnetizing factor.

In the FC regime, when trapping is effected by cooling in a magnetic field and its removal at T_t, trapping occurs in all the rings, but in those with $H_c<H_i$ the trapped fields are equal to H_c, while in those with $H_c>H_i$ they are equal to H_i; consequently, the average trapped fields are given by[7]

$$H_t^F(H_i,T_t,T)=A\left[\int_0^{H_i}H_c f(H_c)dH_c+H_i\int_{H_i}^{\infty}f(H_c)dH_c\right]. \tag{2}$$

As we see from Fig. 2, the magnetic fields trapped in the ZFC regime at low inducing fields decrease with decreasing trapping temperature T_t. It follows from this and an analysis of expression (1) that the distribution function $f(H_c)$ should have a pronounced maximum which shifts to larger H_c as the temperature is lowered.

To describe the $H_t(T)$ curves obtained, we used a great diversity of distribution functions of the rings with respect to critical fields and different kinds of temperature dependence of the critical fields. However, good agreement with the experimental data could be achieved only for a normal (Gaussian) distribution

$$f(H_c)\propto\exp(-(H_c-H_{cm})^2/2\Delta H_c^2) \tag{3}$$

and the following form of temperature dependence of the critical fields of the rings:

$$H_{cm}(T)=H_{cm}^*\left[1-\left(\frac{T}{T_{tm}}\right)^2\right]. \tag{4}$$

We note that the function (4) gives a good description of the temperature dependence of the critical currents of Josephson contacts that act as superconducting shorts[10] and bridges of variable thickness and a length that is small or comparable to the effective correlation length.[11,12] The distribution function of the critical currents of a system of such Josephson contacts is determined by the dispersion relation of the parameters of the bridges or shorts.

The calculated curves are shown by the solid lines in Fig. 2. The adjustable parameters used to fit the family of 6 curves in Fig. 2 are the mean value of the critical field H_{cm} and the standard deviation ΔH_c, which equalled 215 and 74.5 Oe, respectively, at $T\to 0$.

Thus the observed features of the trapping of magnetic fields in Bi-HTSC films obtained by magnetron sputtering—in particular, the appearance of sign-varying trapped magnetic fields and a narrower temperature existence region of the frozen magnetoresistance and trapped magnetic fields as compared to that in which magnetoresistance is observed—find a consistent explanation in the superconducting-loops model, which also gives good quantitative agreement for the temperature dependence of the effective trapped fields. We have shown that the distribution of weak links over critical fields obeys a normal distribution law, and the temperature dependence of the critical fields is described approximately by a quadratic expression close to the typical dependence for short Josephson bridges.

We thank V. B. Sandomirskii for helpful discussions and A. V. Tuzhikov for assistance in preparing the magnetron films.

*E-mail: sukh@ms.ire.rssi.ru

[1] E. Z. Meĭlikhov, Usp. Fiz. Nauk **163**, 27 (1993) [Phys. Usp. **36**, 129 (1993)].
[2] D. M. Ginsberg (Ed.), *Physical Properties of High Temperature Superconductors I* [World Scientific, Singapore (1989); Mir, Moscow (1990)].
[3] Yushung He, C. M. Muirhead, and W. F. Vinen, Phys. Rev. B **53**, 12441 (1996).
[4] H. Darhmaoui, J. Jung, J. Talvacchio, M. A.-K. Mohamed, and L. Friedrich, Phys. Rev. B **53**, 12330 (1996).
[5] K. Y. Chen and Y. J. Qian, Physica C **159**, 131 (1989).
[6] Kh. R. Ozmanyan, V. B. Sandomirskii, and A. A. Sukhanov, Supercond. Sci. Technol. **3**, 255 (1990).
[7] A. A. Sukhanov and V. I. Omel'chenko, Fiz. Nizk. Temp. **27**, 826 (2001) [Low Temp. Phys. **27**, 609 (2001)].
[8] C. P. Bean, Rev. Mod. Phys. **36**, 31 (1964).
[9] G. Blatter, M. V. Feigel'man, W. B. Geshkenbein *et al.*, Rev. Mod. Phys. **66**, 1125 (1994).
[10] I. O. Kulik and A. N. Omel'yanchuk, JETP Lett. **21**, 96 (1975).
[11] K. K. Likharev, Pis'ma Zh. Tekh. Fiz. **2**, 29 (1976) [Sov. Tech. Phys. Lett. **2**, 12 (1976)].
[12] K. K. Likharev and B. T. Ul'rich, *Systems with Josephson Contacts* [in Russian], Izd. MGU, Moscow (1978), Ch. 28.

Translated by Steve Torstveit

Superconducting gap and pair breaking in $CeRu_2$ studied by point contacts

A. V. Moskalenko,* Yu. G. Naidyuk, and I. K. Yanson

B. Verkin Institute for Low Temperature Physics and Engineering of the National Academy of Sciences of Ukraine, 47 Lenin Ave., Kharkov 61103, Ukraine

M. Hedo, Y. Inada, and Y. Ōnuki

Graduate School of Science, Osaka University, Toyonaka 560-0043, Japan

Y. Haga and E. Yamamoto

Advanced Science Research Center, Atomic Energy Research Institute of Japan, Tokai, Ibaraki 319-1195, Japan

(Submitted March 15, 2001)
Fiz. Nizk. Temp. **27**, 831–834 (August 2001)

The superconducting gap in a $CeRu_2$ single crystal is investigated by point contacts. BCS-like behavior of the gap Δ in the temperature range below T_c^* ($T_c^* < T_c$, where T_c is the critical temperature) is established, indicating the presence of a gapless superconductivity region (between T_c^* and T_c). The pair-breaking effect of paramagnetic impurities, supposedly Ce ions, is taken into consideration using the Scalski–Betbeder–Matibet–Weiss approach based on Abrikosov–Gorkov theory. It allows us to recalculate the superconducting order parameter Δ^α (in the presence of paramagnetic impurities) and the gap Δ^p (in the pure case) for the single crystal and for the previously studied polycrystalline $CeRu_2$. The value $2\Delta^p(0) \approx 2$ meV, with $2\Delta^p(0)/k_B T_c \approx 3.75$, is found in both cases, indicating that $CeRu_2$ is a "moderate" strong-coupling superconductor. © *2001 American Institute of Physics.* [DOI: 10.1063/1.1399197]

INTRODUCTION

The superconducting gap Δ of $CeRu_2$ has been evaluated by point-contact Shottky tunneling (PCT),[1] break-junction tunneling (BJT),[2] point contact spectroscopy (PCS),[3] and scanning tunneling microscope (STM) experiments.[4] The necessity of new PCS experiments is due to the discrepancy between the results obtained by different experimental methods. From the PCT measurements $2\Delta(0)/k_B T_c$ is estimated as 6.6 ± 0.6, while the BJT experiments yielded $2\Delta(0)/k_B T_c = 4.4$. These values are remarkably larger than our previous PCS result 3.1 ± 0.1,[3] which is more consistent with the recent tunneling data $2\Delta(0)/k_B T_c = 3.3$.[4] The measurements of the superconducting gap were performed by different methods and on samples of different quality. In this paper we present a comparison of the superconducting gap behavior of samples with different quality studied by a single method. We also propose a procedure for Δ correction based on taking pair-breaking effects into account, which results in almost equal gap values for both samples.

EXPERIMENT AND RESULTS

We have studied the superconducting gap in single crystal $CeRu_2$ samples by measuring dV/dI for S–c–N (here S is a superconductor, c is a constriction, and N is a normal metal) point contacts. The single crystal was grown by the Czochralski pulling method in a tetra-arc furnace. Its residual resistivity ratio (RRR) is 120, residual resistivity $\rho_0 = 1\ \mu\Omega \cdot$cm, and $T_c = 6.3$ K. The polycrystalline $CeRu_2$ studied in Ref. 3 had $RRR = 14$, $\rho_0 = 31.5\ \mu\Omega \cdot$cm, and $T_c = 6.2$ K, that is, it had much lower quality. The point-contact characteristics presented were obtained on cleaved surface of $CeRu_2$ for both samples.[1)] The samples were cleaved in air at room temperature. The PCs were prepared by touching this surface with the edge of an Ag or Cu counterelectrode, which were cleaned by chemical polishing. The experimental cell with the sample and counterelectrode was immersed directly in liquid ^{4}He to ensure good thermal coupling. The measurements were carried out in the temperature range 1.7–6.7 K. The differential resistance dV/dI of the PCs was recorded versus the bias voltage using a standard lock-in amplifier technique, modulating the direct current I with a small 480 Hz ac component.

The Blonder, Tinkham, and Klapwijk (BTK) theory[5] is commonly used to describe the behavior of the current-voltage characteristics of clean S–c–N microconstrictions. As in our previous publication,[3] here we have used this model, which takes into account the Andreev reflection on the S–N interface,[5] to fit the measured $dV/dI(V)$ curves of PCs. According to the theory[5] a maximum at zero bias voltage and a double-minimum structure around $V \sim \pm\Delta/e$ on the dV/dI curves manifests the Andreev reflection process with a finite barrier strength parameter Z. This structure follows from the equations for the current-voltage characteristics

$$I(V) \sim \int_{-\infty}^{\infty} T(E)[f(E-eV) - f(E)]dE, \tag{1}$$

$$T(E) = \frac{2\Delta^2}{E^2 + (\Delta^2 - E^2)(2Z^2+1)^2}, \quad |E| < \Delta,$$

$$T(E)=\frac{2|E|}{|E|+\sqrt{E^2-\Delta^2}(2Z^2+1)},\quad |E|>\Delta,$$

where $f(E)$ is the Fermi distribution function. The broadening of the quasiparticle density of states $N(E,\Gamma)$ in the superconductor was taken into account according to Dynes *et al.*:[6]

$$N(E,\Gamma)=\mathrm{Re}\left\{\frac{E-i\Gamma}{\sqrt{(E-i\Gamma)^2-\Delta^2}}\right\}, \tag{2}$$

where Γ is the broadening parameter.

In Fig. 1a a series of experimental $dV/dI(V)$ curves of PCs based on the $CeRu_2$ single crystal are presented along with the fitted ones for different temperatures. The good agreement between experimental and theoretical curves allowed us precisely to determine Δ along with its temperature dependences from calculations according to (1), (2). The average value of the gap Δ of the $CeRu_2$ single crystal extracted from the fit for 5 PCs is (0.83 ± 0.07) meV, with $2\Delta(0)/k_BT_c^*=3.23\pm0.23$ and $T_c^*=(5.9\pm0.2)$ K. The maximum $\Delta(0)$ was 0.95 meV and $T_c^*=6.1$ K, where T_c^* is the extrapolated temperature at which the gap drops to zero (see Fig. 1b). The temperature dependence of the superconducting gap extracted from the curves in Fig. 1a is presented in Fig. 1b and has a BCS-like behavior as in the polycrystalline sample.[3] The extrapolated critical temperature T_c^* for single crystal is higher and the gapless region is smaller than in the polycrystalline sample.[3] The gap value (averaged for 5 PCs as well) grew from (0.51 ± 0.07) meV for the polycrystal to the value indicated above for the single crystal of $CeRu_2$. This has a natural explanation considering the difference in the quality of the samples. The contacts made on the more perfect single-crystal $CeRu_2$ exhibited better superconducting properties than those with the polycrystal.

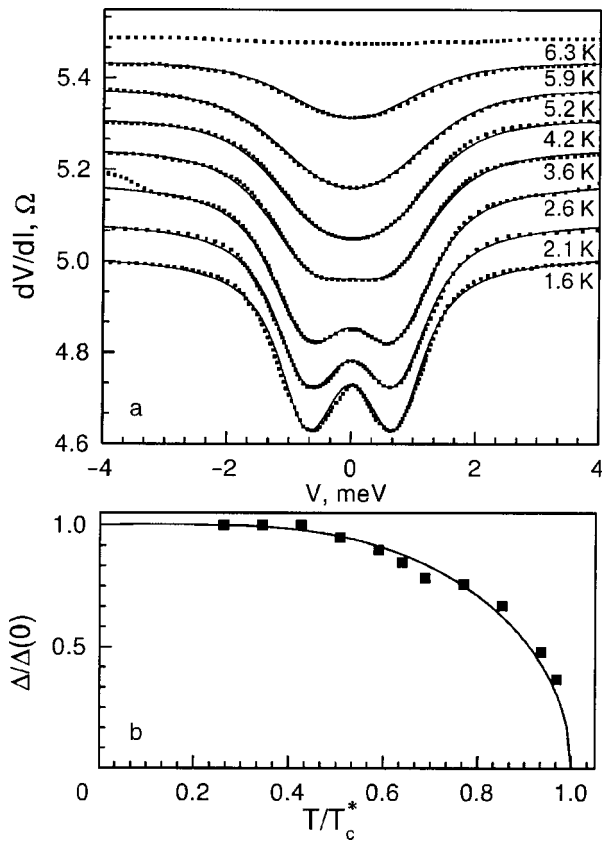

FIG. 1. Temperature dependence of the experimental $dV/dI(V)$ curves (squares) for a $CeRu_2$–Ag point contact with $R_N=5\ \Omega$ along with the fit using Eqs. (1), (2) with $\Gamma\cong0.13$ meV and $Z=0.43$ (solid lines). The curves are shifted vertically for clarity (a). Temperature dependence of the superconducting gap Δ extracted from the fit in Fig. 1a. $\Delta(0)=0.79$ meV and $T_c^*=6.1$ K, with $2\Delta(0)/k_BT_c^*=3.05$. The solid line is the BCS curve (b).

In our previous paper[3] the presence of a region of gapless superconductivity in $CeRu_2$ between T_c^* and T_c was proposed to explain why $T_c^*\neq T_c$. The gap was assumed to be suppressed by the local magnetic moments, presumably Ce, distributed randomly in the contact region. That is, because of the lower purity (quality) of the polycrystal some of the Ce ions could be impurities.

The well-known Abrikosov–Gorkov (AG) theory of a superconductor containing paramagnetic (PM) impurities[7] has been considered for explaining a gapless state in $CeRu_2$. The theory describes a situation when in the presence of PM impurities the gap Δ in the excitation energy spectrum drops to zero at a transition temperature T_c^* although the material is still a superconductor in the sense of having pair correlations. The transition temperature T_c^* is lower than the critical temperature T_c, and a range of temperatures between T_c^* and T_c where Δ is zero for any value of the impurity concentration exists. The Scalski–Betbeder-Matibet–Weiss (SBMW) approach[8] based on AG theory allows us to take into account a pair breaking caused by spin-exchange scattering. As a measure of this effect produced by PM impurities the inverse collision time for exchange scattering $\alpha=\hbar/\tau_{ex}$ was used. The advantage of the SBMW approach is the natural way in which the distinction between the energy gap Δ and the order parameter Δ^α arises when the effect of PM impurities on the density of states is taken into account. The SBMW theory allows us to calculate the order parameter Δ^α of a superconductor with PM impurities by transformation of the original expression (4.8) from Ref. 8:

$$\Delta(T,\alpha)=\Delta^\alpha(T,\alpha)\left[1-\left(\frac{\alpha}{\Delta^\alpha(T,\alpha)}\right)^{2/3}\right]^{3/2}$$

into the following form:

$$\Delta^\alpha(T,\alpha)=\Delta(T,\alpha)\left[1+\left(\frac{\alpha}{\Delta(T,\alpha)}\right)^{2/3}\right]^{3/2}. \tag{3}$$

In (3) the pair-breaking parameter α is unknown. It was determined from the T_c^*/T_c^p and $\Delta(0)/\Delta^p(0)$ versus $\alpha/\Delta^p(0)$ curves (the superscript p indicates a pure superconductor; we also suppose that $T_c^p\equiv T_c$) shown in Fig. 2. The value of T_c^* was taken from the experimental temperature dependence of Δ as the value extrapolated according to the BCS theoretical curve (see Fig. 1b). Then $\alpha/\Delta^p(0)=\beta$ corresponding to T_c^*/T_c^p was determined for the particular point contact, and $\Delta(0)/\Delta^p(0)=\gamma$ at the value of $\alpha/\Delta^p(0)=\beta$ determined was specified. The $\Delta(0)$ value was taken from a fit of the experimental curve. Thus we obtained $\Delta^p(0)=\Delta(0)/\gamma$ and, hence, $\alpha=\Delta^p(0)\beta=\Delta(0)\beta/\gamma$. The order parameter $\Delta^\alpha(0)$ was found from (3) to be (0.99 ± 0.05) meV for the single crystal and (0.87 ± 0.1) meV for the polycrystal. Figure 3 shows the results of the calculations of $\Delta^\alpha(T)$ from (3). The

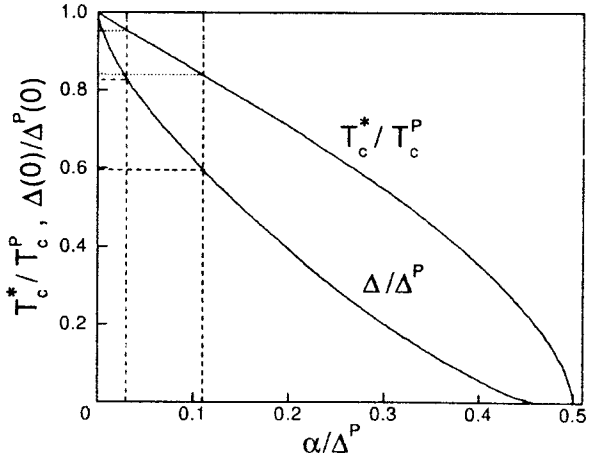

FIG. 2. The T_c^*/T_c^p and $\Delta(0)/\Delta^p(0)$ versus $\alpha/\Delta^p(0)$ curves from Ref. 8. The dashed vertical lines indicate $\alpha/\Delta^p(0)=\beta=0.03$ for the single crystal from Fig. 1 and $\beta=0.11$ for the polycrystal from Fig. 1 in Ref. 3 as determined using the experimental values of T_c^*/T_c^p (dotted horizontal lines). The dashed horizontal lines show the $\Delta(0)/\Delta^p(0)=\gamma$ determined values.

temperature dependences of the parameter Δ^α both for the purer sample and for the less perfect one have behavior close to the BCS curve.

The order parameter $\Delta^p(0)$ of the pure superconductor can be determined from Fig. 2 using the value of γ or calculated from the expression (3), (5) of Ref. 8:

$$\ln\left(\frac{\Delta^\alpha(0,\alpha)}{\Delta^p(0)}\right)=-\frac{\pi}{4}\frac{\alpha}{\Delta^\alpha(0,\alpha)},$$

which transforms into

$$\Delta^p(0)=\Delta^\alpha(0,\alpha)\exp\left\{\frac{\pi}{4}\frac{\alpha}{\Delta^a(0,\alpha)}\right\}.$$

The value of $\Delta^p(0)$ has less scatter in comparison with $\Delta^\alpha(0)$ and is about (1.02 ± 0.05) meV with $2\Delta^p(0)/k_BT_c=3.8\pm0.2$ for the single crystal and $\Delta^p(0)=(0.99\pm0.13)$ meV with $2\Delta^p(0)/k_BT_c=3.7\pm0.5$ for the polycrystal.

DISCUSSION AND CONCLUSIONS

As was shown earlier[3,4] and in this paper the temperature dependence of Δ in $CeRu_2$ has a BCS-like behavior, but with a lower critical temperature T_c^*. Because of the difference in T_c^* for the samples of different quality we can conclude that in the cleaner one the influence of impurities on the superconductivity is also weaker. Pair-breaking effects in the contact area can be caused by the randomly distributed local magnetic moments. It was noted by Joseph *et al.*[9] that a Ce-rich solid solution is present as a second phase in $CeRu_2$ in an amount up to 10% in the samples of low quality. This means that pair-breaking effects and gapless superconductivity in the compound more probably are connected with the influence of Ce impurities. Calculations based on the SBMW approach gave very close values of $\Delta^p(0)$ and $2\Delta^p(0)/k_BT_c$ for poly- and single crystals. This supports our assumptions about the influence of paramagnetic impurities on superconductivity in $CeRu_2$ and gives a method of Δ correction. This method of recovering the superconducting parameters from point-contact $dV/dI(V)$ characteristics can theoretically be improved by including in the BTK fit a density of states modified by the pair-breaking effect.

The investigations were carried out in part with the help of equipment donated by Alexander von Humboldt Stiftung (Germany).

*E-mail: amoskalenko@ilt.khakov.ua

[1)]The sample size was about $1\times1\times5$ mm.

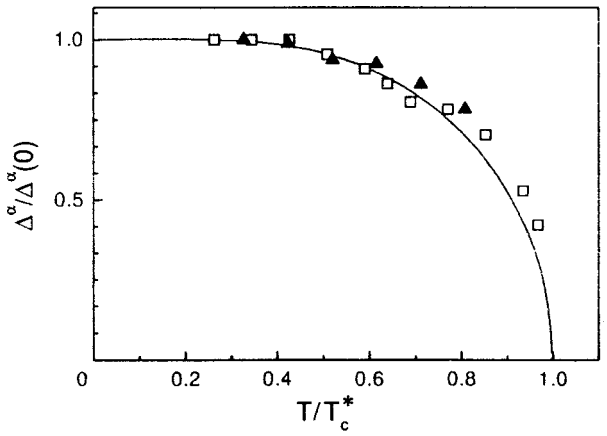

FIG. 3. Temperature dependences of the order parameter $\Delta^\alpha(T)$ for the single-crystal sample from Fig. 1 (open squares) and for the polycrystalline sample from Fig. 1 in Ref. 3 (triangles).

[1] W. Schmitt and G. Guntherodt, J. Magn. Magn. Mater. **47–48**, 542 (1985).
[2] T. Ekino, H. Fujii, T. Nakama, and K. Yagasaki, Phys. Rev. B **56**, 7851 (1997).
[3] Yu. G. Naidyuk, A. V. Moskalenko, I. K. Yanson, and C. Geibel, Fiz. Nizk. Temp. **24**, 495 (1998); [Low Temp. Phys. **24**, 374 (1998)].
[4] H. Sakata, N. Nishida, M. Hedo, K. Sakurai, Y. Inada, Y. Onuki, E. Yamamoto, and Y. Haga, J. Phys. Soc. Jpn. **69**, 1970 (2000).
[5] G. E. Blonder, M. Tinkham, and T. M. Klapwijk, Phys. Rev. B **25**, 4515 (1982).
[6] R. C. Dynes, V. Narayanamurti, and J. P. Garno, Phys. Rev. Lett. **21**, 1509 (1978).
[7] A. A. Abrikosov and L. P. Gorkov, Zh. Éksp. Teor. Fiz. **39**, 1781 (1961) [JETP **12**, 1243 (1961)].
[8] S. Skalski, O. Betbetiber-Matibet, and P. R. Weiss, Phys. Rev. **136**, A1500 (1964).
[9] R. R. Joseph, K. A. Gschneidner, Jr., and D. C. Koskimaki, Phys. Rev. B **6**, 3286 (1972).

This article was published in English in the original Russian journal. Reproduced here with atylistic changes by AIP.

Mesoscopic multiterminal Josephson structures. I. Effects of nonlocal weak coupling

M. H. S. Amin

D-Wave Systems Inc., 320-1985 W. Broadway, Vancouver, B.C., V6J 4Y3 Canada

A. N. Omelyanchouk*

B. Verkin Institute for Low Temperature Physics and Engineering of the National Academy of Sciences of Ukraine, 47 Lenin Ave., Kharkov 61103, Ukraine

A. M. Zagoskin

D-Wave Systems Inc., 320-1985 W. Broadway, Vancouver, B.C., V6J 4Y3 Canada; Physics and Astronomy Dept., The University of British Columbia, 6224 Agricultural Rd., Vancouver, B.C., V6T 1Z1, Canada

(Submitted March 15, 2001)
Fiz. Nizk. Temp. **27**, 835–844 (August 2001)

We investigate nonlocal coherent transport in ballistic four-terminal Josephson structures (in which bulk superconductors (terminals) are connected through a clean normal layer, e.g., a two-dimensional electron gas). Coherent anisotropic superposition of macroscopic wave functions of the superconductors in the normal region produces phase slip lines (2D analogs to phase-slip centers) and time-reversal symmetry breaking 2D vortex states in it, as well as such effects as phase dragging and magnetic flux transfer. The tunneling density of local Andreev states in the normal layer is shown to contain peaks at the positions controlled by the phase differences between the terminals. We obtain the general dependence of these effects on the controlling supercurrent/phase differences between the terminals of the ballistic mesoscopic four-terminal SQUID. © *2001 American Institute of Physics.* [DOI: 10.1063/1.1399198]

1. INTRODUCTION

Multiterminal Josephson junctions[1,2] generalize the usual (two-terminal) Josephson junctions[3] to the case of weak coupling between several massive superconducting banks (terminals). Compared with two-terminal junctions, such systems have additional degrees of freedom and the corresponding set of control parameters, preset transport currents, and (or) applied magnetic fluxes. As a result, the current- or voltage-biased and the magnetic flux-driven regimes can be combined in one multiterminal microstructure.

One of the implementations of multiterminal coupling is a system of short, dirty microbridges going from a common center to separate massive superconductors. The theory of this kind of multiterminals was derived in Refs. 4 and 5 within the phenomenological Ginzburg–Landau scheme (Aslamazov and Larkin model[6]). This approach is valid for temperatures T near the critical temperature T_c and for the local case, when the characteristic spatial scale is larger then the coherence length $\xi_0 \sim \hbar v_F / T_c$. The stationary states and the dynamical behavior of the microbridge-type multiterminals have been studied for different microstructures, a four-terminal SQUID controlled by the transport current, and weakly coupled superconducting rings (see the review of theoretical and experimental results in Refs. 7 and 8).

The Josephson effect in mesoscopic weak links with direct conductivity (S–N–S junctions, ballistic point contacts) exhibits specific features[9,10] which are absent in conventional dirty microconstrictions near T_c (Ref. 6). As in normal metal mesoscopic structures,[11] the electrodynamics of supercurrents in mesoscopic Josephson junctions is nonlocal. The supercurrent density depends on the spatial distribution of the superconducting order parameter at all points of the mesoscopic weak-link region. The coherent current flow is carried by the Andreev states[12] formed inside the weak link. A nonlocal nature of mesoscopic supercurrents was demonstrated by Heida *et al.*,[13] who investigated mesoscopic S-2DEG-S (superconductor–two-dimensional electron gas–superconductor) Josephson junctions. They measured $2\Phi_0$ periodicity of the critical current instead of the standard Φ_0 ($\Phi_0 = hc/2e$ is the magnetic flux quantum). A theory of this effect was developed in Refs. 14 and 15.

The present-day level of nanofabrication technology has made it possible to realize multiterminal mesoscopic Josephson junctions, similar to the 2-terminal junction studied in Ref. 13. A microscopic theory of the mesoscopic ballistic Josephson multiterminals was derived in Ref. 16. It is valid for arbitrary temperatures $0 < T < T_c$ and describes the nonlocal coherent current states in the system. The effects of nonlocal coupling, such as phase dragging and magnetic flux transfer, were obtained in Ref. 17.

In the present paper we continue the study of quantum interference effects, which are related to the nonlocality of weak coupling, in mesoscopic multiterminals. The paper consists of two parts. In first part (Article I) the effects of nonlocal coupling in mesoscopic multiterminal structures are studied. The general properties of Josephson multiterminals are described in Sec. 2. Section 3 gives the results concerning the current distribution and density of states inside a weak link. In Sec. 3 we study properties of four-terminal SQUID which are specific to the mesoscopic case. In the second part (Article II) a superconducting phase qubit based

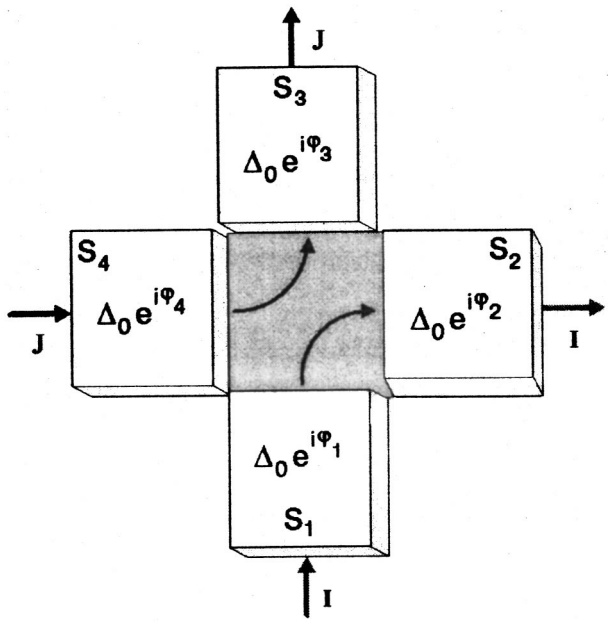

FIG. 1. Mesoscopic four-terminal Josephson junction with "parallel" implementation of the supercurrents. The four bulk superconducting regions, $S_1 \ldots S_4$, are weakly coupled through the thin layer of normal metal (2DEG), represented by the shaded area.

on a mesoscopic multiterminal junction is proposed and investigated.

2. MESOSCOPIC FOUR-TERMINAL JUNCTION

System description

In a mesoscopic 4-terminal junction, bulk superconductors (terminals) are weakly coupled to each other through a clean two-dimensional normal metal layer (2D electron gas), as is shown in Fig. 1. The pairs of terminals can be incorporated in bulk superconducting rings or in circuits with preset transport currents. In Fig. 2 we show two such configurations. The first one (Fig. 2a) presents two superconducting rings, each interrupted by a Josephson junction, which are at the same time weakly coupled to each other. The second configuration (Fig. 2b), combines a current- (or voltage-) biased junction and a flux-driven junction in the ring. We call this configuration the four-terminal SQUID controlled by the transport current.

The state of the ith terminal S_i $(i=1,...,4)$ is determined by the phase φ_i of the complex off-diagonal potential $\Delta_0 \exp(i\varphi_i)$. The superconducting banks induce an order parameter Ψ in the normal metal region (shaded area in Fig. 1).

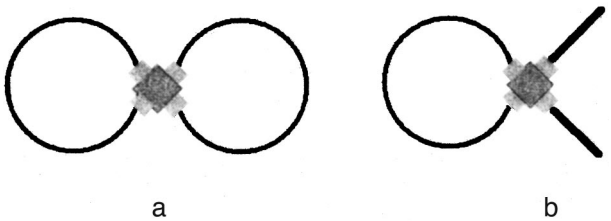

FIG. 2. Superconducting microstructures based on mesoscopic four-terminal Josephson junctions (a). Two weakly coupled superconducting rings (b). Mesoscopic four-terminal SQUID.

Inside this mesoscopic, fully phase-coherent weak link, the supercurrent density $j(\rho)$ at point ρ depends *nonlocally* on the values of the induced order parameter Ψ at all points ρ'. In turn, the order parameter $\Psi(\rho)$ depends on the phases φ_i. The total current I_i flowing into the ith terminal depends on the phases φ_j of all the banks and has the form:[16]

$$I_i=\frac{\pi\Delta_0}{e}\sum_{j=1}^{4}\gamma_{ij}\sin\left(\frac{\varphi_i-\varphi_j}{2}\right)\tanh\left[\frac{\Delta_0\cos((\varphi_i-\varphi_j)/2)}{2T}\right]. \tag{1}$$

In the case of two terminals Eq. (1) reduces to the formula for ballistic point contacts[10] with γ_{12} equal to the Sharvin conductance.

Expression (1) corresponds to the case of a small junction, when the linear dimensions of the N layer are smaller than the coherence length $\xi\sim\hbar v_F/\Delta_0$ (for the case of arbitrary junction dimensions see Ref. 16). We are focusing here on the small junction case because the effects of nonlocality are most pronounced in this situation. The geometry dependent coefficients γ_{ij} denote the coupling between the partial Josephson currents in ballistic two-terminal S_i-S_j weak links.

Equation (1) is simplified when $T\approx 0$, or when $T\approx T_c$. In the $T=0$ limit, it becomes

$$I_i=\frac{\pi\Delta_0(0)}{e}\sum_{j=1}^{4}\gamma_{ij}\sin\left(\frac{\varphi_i-\varphi_j}{2}\right)\mathrm{sign}\left[\cos\left(\frac{\varphi_i-\varphi_j}{2}\right)\right]. \tag{2}$$

Near T_c, on the other hand, the order parameter is small, $\Delta_0\to 0$, and one can write

$$I_i=\frac{\pi\Delta_0^2(T)}{4eT_c}\sum_{j=1}^{4}\gamma_{ij}\sin(\varphi_i-\varphi_j). \tag{3}$$

Equations (2) and (3) are qualitatively similar, differing in the magnitude of critical currents and in the shape of the current–phase relations $(\sin\varphi/2)$ sign $[\cos(\varphi/2)]$ and $\sin\varphi$). For definiteness, in the following we will consider the case $T\sim T_c$, keeping in mind that the results hold qualitatively at low temperatures as well.

For the Josephson coupling energy of the junction, E_J, which is related to the supercurrents I_i (3) through $I_i=(2e/\hbar)\partial E_J/\partial\varphi_i$, we have

$$E_J(\varphi_i)=\frac{\hbar}{2e}\frac{\pi\Delta_0^2(T)}{4eT_c}\sum_{j<k}\gamma_{jk}[1-\cos(\varphi_j-\varphi_k)]. \tag{4}$$

Expression (1) for the supercurrents I_i looks similar to Buttiker's multiprobe formula[18]

$$I_i=e\sum_j T_{ij}(\mu_i-\mu_j), \tag{5}$$

which relates the currents to the voltage drops between terminals in a mesoscopic normal metal multiterminal system. The similarity reflects the above-mentioned nonlocality of mesoscopic transport on a scale of $\xi_T\sim\hbar v_F/T$ (in the ballistic limit we are considering). The essential difference between (1) and (5) is that, unlike the Josephson currents of (1), the normal currents of (5) can flow only out of equilibrium; while the current–phase relation in (1) is periodic, the current-bias dependence of (5) certainly is not.

Circuit implementations of four-terminal junction. Nonlocal weak coupling

The current-phase relations (3) determine the behavior of the system in the presence of transport currents and/or the diamagnetic currents induced by the magnetic fluxes through the closed superconducting rings. It is necessary to distinguish two types of circuit implementation of the mesoscopic 4-terminal junction.[17] The first one, is the ''crossed'' or ''transverse'' implementation, when the total current in one circuit goes in and out through one pair of opposite banks in Fig. 1, and in the second circuit-through the other pair. In the ''parallel'' implementation, shown in Fig. 1, the currents I and J flow through pairs of adjacent banks. In this case, nonlocal coupling of currents inside the mesoscopic N layer results in the peculiar effect of ''dragging'' of the phase difference between one pair of terminals by the phase difference between another pair of terminals.[17] In the following, we consider the ''parallel'' implementation and study the manifestations of the phase dragging effect.

The coefficients γ_{ij} in (3), (4) depend on the geometry of the weak link (the shape of the N layer) and on the transparency of S–N interfaces. In general we have $\gamma_{ij}=\gamma_{ji}$ and $\gamma_{ii}=0$. For the case of parallel implementation, the elements γ_{12} and γ_{34} are related to the critical currents of the individual subjunctions S_1–S_2 and S_3–S_4, respectively. The matrix

$$\hat{\gamma}_{\text{coupl}}=\begin{pmatrix}\gamma_{13} & \gamma_{14}\\ \gamma_{23} & \gamma_{24}\end{pmatrix} \tag{6}$$

describes the coupling between these two junctions. The properties of the system (in particular, the existence of phase dragging) qualitatively depends on whether $\det(\hat{\gamma}_{\text{coupl}})$ is equal to zero or not (see Appendix). In the case of a conventional nonmesoscopic 4-terminal Josephson junction the coefficients γ_{ij} factorize, $\gamma_{ij}\sim(1/R_i)(1/R_j)$, where R_i are the normal resistances of the dirty microbridges.[7] This yields $\det(\hat{\gamma}_{\text{coupl}})\equiv 0$, which we call local coupling. On the other hand, in a mesoscopic system, even in the completely symmetric case of an $a\times a$ square N layer and ideal transparency ($D=1$) of the N–S_i interfaces, the coefficients γ_{ij} are given by:[17]

$$\gamma_{12}=\gamma_{34}=\gamma_0,\quad \hat{\gamma}_{\text{coupl}}=\gamma_0\begin{pmatrix}\sqrt{2} & 1\\ 1 & \sqrt{2}\end{pmatrix}, \tag{7}$$

$$\gamma_0=\frac{e^2 p_F a}{\sqrt{2}\hbar^2\pi^2}\left(1-\frac{1}{\sqrt{2}}\right),$$

with $\det(\hat{\gamma}_{\text{coupl}})\neq 0$. In a more general case than the completely symmetric one (Eq. (7)), we can write γ_{ij} in the form

$$\gamma_{34}=\kappa\gamma_{12},\quad \hat{\gamma}_{\text{coupl}}=\gamma_0\begin{pmatrix}p & q\\ q & p\end{pmatrix}. \tag{8}$$

This corresponds to a square N layer with different transparencies for junctions S_1–S_2 and S_3–S_4 and/or with different widths of the superconductor banks connected to the normal layer. In our numerical calculations we will use the simple form (7), i.e., $\kappa=1$, $p=\sqrt{2}$, $q=1$.

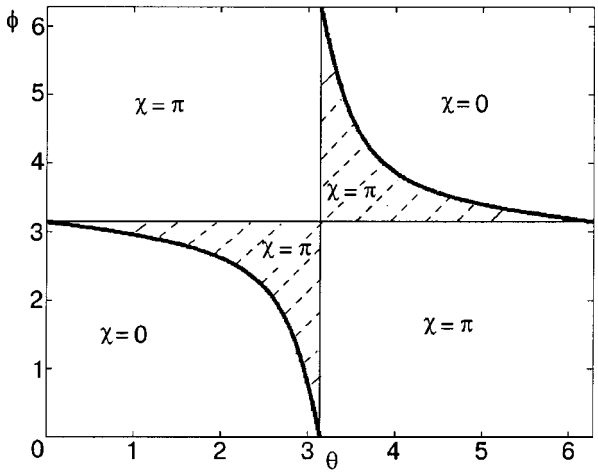

FIG. 3. Phase diagram for the phase difference χ in the (θ, ϕ) plane. The solid curve separates the regions with $\chi=0$ and $\chi=\pi$. The hatched region is absent in the case of local coupling.

Current–phase relations. The phase dragging effect

Let us introduce the new variables:

$$\varphi_2-\varphi_1=\theta,\ \ \varphi_3-\varphi_4=\phi,$$

$$\frac{1}{2}(\varphi_1+\varphi_2)=\alpha,\ \ \frac{1}{2}(\varphi_4+3)=\beta,$$

$$\alpha-\beta=\chi,\ \ \alpha+\beta=\gamma. \tag{9}$$

Without loss of generality, we can choose the phase γ equal to zero ($\Sigma_j\phi_j=0$). For the circuit implementation shown in Fig. 1, we have

$$I=I_2=-I_1,\quad J=I_3=-I_4. \tag{10}$$

In terms of the phase differences (9) the currents I and J have the form

$$I=\sin\theta+\left[(p+q)\sin\frac{\theta}{2}\cos\frac{\phi}{2}+(p-q)\cos\frac{\theta}{2}\sin\frac{\phi}{2}\right]\cos\chi, \tag{11}$$

$$J=\kappa\sin\phi+\left[(p+q)\sin\frac{\phi}{2}\cos\frac{\theta}{2}+(p-q)\cos\frac{\phi}{2}\sin\frac{\theta}{2}\right]\cos\chi. \tag{12}$$

All the γ's (8) are normalized by γ_{12}, and the currents I and J are measured in units of $I_0=\pi\gamma_{12}\Delta_0^2(T)/4eT_c$.

From the equation of current conservation (10), it follows that the phase χ in Eqs. (11) and (12) can take only two values, 0 or π. Minimization of E_J (4) with respect to χ also gives $\chi=0$ or π, depending on the equilibrium values of θ and ϕ (see Appendix):

$$\cos\chi=\operatorname{sign}\left[(p+q)\cos\frac{\phi}{2}\cos\frac{\theta}{2}-(p-q)\sin\frac{\phi}{2}\sin\frac{\phi}{2}\right]. \tag{13}$$

The current–phase relations (11) and (12) with the condition (13) are invariant under the transformation $\theta\to\theta+2\pi n$, and $\phi\to\phi+2\pi k$. The 2π periodicity of observable quantities is sustained by the ''hidden'' variable phase χ. In Fig. 3 the phase diagram for χ in the (θ, ϕ) plane is presented. The solid line separates the regions with $\chi=0$ and

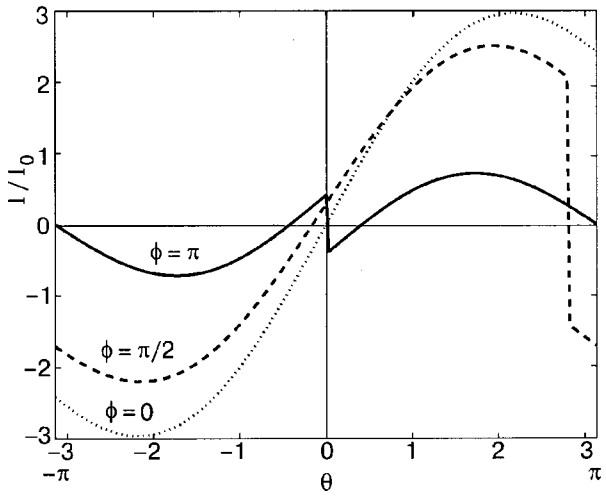

FIG. 4. Current–phase relations I for different values of ϕ.

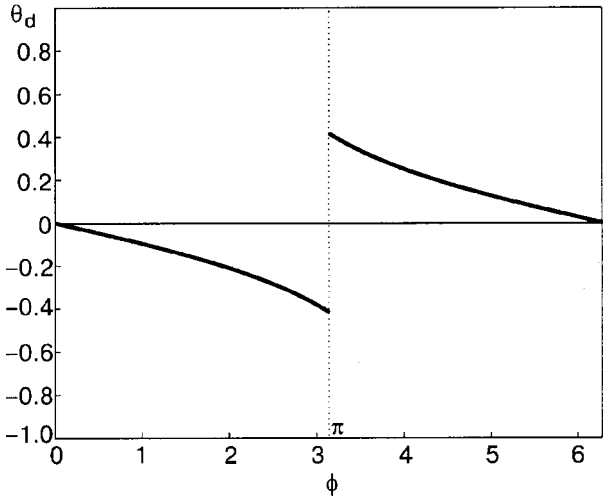

FIG. 5. The dragged phase θ_d between terminals S_1–S_2, at zero transport current I, as a function of the phase difference ϕ between the other pair of terminals S_3–S_4.

$\chi=\pi$. When the state of the system (θ, ϕ) crosses this line, a jump in χ occurs. Corresponding jumps take place in current-phase relations (11) and (12). The current $I(\theta)$ (11) is shown in Fig. 4 for several values of the phase ϕ. Note that the function $I(\theta)$ has jumps, which for $\phi\neq 0$, are not located at $\theta=\pm\pi$, as they would be in conventional 4-terminal junctions. The jump in χ means slippage of the phase θ (or ϕ). In the case of two-terminal or conventional 4-terminal junction the phase-slip events occur at phase difference equal to $\pi(2n+1)$, $n=0,\pm1,\pm2,...$ In one-dimensional structures slippage of the phase occurs at phase-slip centers (PSC), i.e., points where the order parameter equals zero. In our case of a 2D mesoscopic 4-terminal weak link, the analog of the PSC are phase-slip lines in the normal metal region. They appear when the state (θ, ϕ) of the system belongs to the hatched region in Fig. 3. This region, which is absent in the local coupling case (it actually coincides with the lines $\theta=\pi$, $\phi=\pi$), we call the ''frustrated'' region for phases θ and ϕ. For states inside this region, the distribution of the supercurrent in the weak link contains 2D vortex states (see below).

Nonlocal weak coupling leads to the phase dragging effect.[17] One notices that if $p\neq q$ then putting $\theta=0$ in (11) results in a nonzero value of the current I:

$$I=(p-q)\sin\frac{\phi}{2}\,\mathrm{sign}\left(\cos\frac{\phi}{2}\right). \tag{14}$$

This current is absent in conventional 4-terminal junctions or mesoscopic four-terminal junctions with crossed implementation at which $p=q$ (i.e., $\det(\hat{\gamma}_{\mathrm{coupl}})=0$).

Similarly, if we set $I=0$ in (11), we find a nonzero solution for θ, which again vanishes when $p=q$. This solution $(\equiv\theta_d)$ is a function of ϕ and is plotted versus ϕ in Fig. 5. The influence of the phase of one side of the mesoscopic 4-terminal junction on the phase of the other side is what we call the phase dragging effect. This effect is one of the important characteristics of the junction with parallel implementation.

In general the current-phase relations are asymmetric, $I(-\theta)\neq -I(\theta)$, unlike in conventional cases. In another words, the presence of a phase difference ϕ on the terminals S_4-S_3 breaks the time reversal symmetry for the Josephson junction S_1-S_2. It also follows from expression (11) that $I(\theta)$ is not only a function of $|\phi|$, as in conventional junctions, but also depends on the sign of ϕ. The phase dragging has an analog in the normal metal mesoscopic multiterminals described by formula (5); the normal current flowing through one pair of terminals induces a voltage difference between the other ones.[18]

3. CURRENT DISTRIBUTION AND LOCAL DENSITY OF STATES INSIDE THE MESOSCOPIC WEAK LINK

The coupling through the normal layer determines the behavior of the Josephson weak links S_1-S_2 and S_4-S_3. On the other hand, the properties of the normal layer itself depend on the phase differences θ and ϕ across the junctions. The phases θ and ϕ can be controlled by external magnetic fluxes through the rings (Fig. 2a). In this Section we present the results of numerical calculations for the current density distribution $j(\rho)$ and density of local Andreev levels $N(\epsilon)$ inside the mesoscopic 4-terminal weak link. The expressions for $j(\rho)$ and $N(\epsilon)$ as functionals of $\{\varphi_1,\varphi_2,\varphi_3,\varphi_4\}$ were obtained in Ref. 16 by solving the Eilenberger equations.[19]

Figure 6 illustrates the effect of phase dragging. Two sets of phases $(\theta=-0.42,\ \phi=\pi)$ and $(\theta=0.42,\ \phi=\pi)$ correspond to zero value of the current I (11) (see Fig. 4) and opposite directions of the current J (12). In the absence of the current from terminal S_1 to terminal S_2, a phase difference across the junction S_1-S_2 exists.

When the phases θ and ϕ lie in the ''frustrated'' region of the diagram of Fig. 3 (hatched area), the current distribution $j(\rho)$ contains 2D vortex states. They are shown in Fig. 7 for states $(\theta=\pi-0.2,\ \phi=\pi-0.2)$ and $(\theta=\pi+0.2,\ \phi=\pi+0.2)$. In both cases, the order parameter $\Psi(\rho)$ vanishes along the diagonal $x=y$, and its phase drops by π when crossing this 2D phase-slip line.

The Andreev scattering processes on the S_i-N interfaces lead to the appearance of energy levels with energies ϵ inside the gap Δ_0, $|\epsilon|<\Delta_0$, in the normal metal. The local

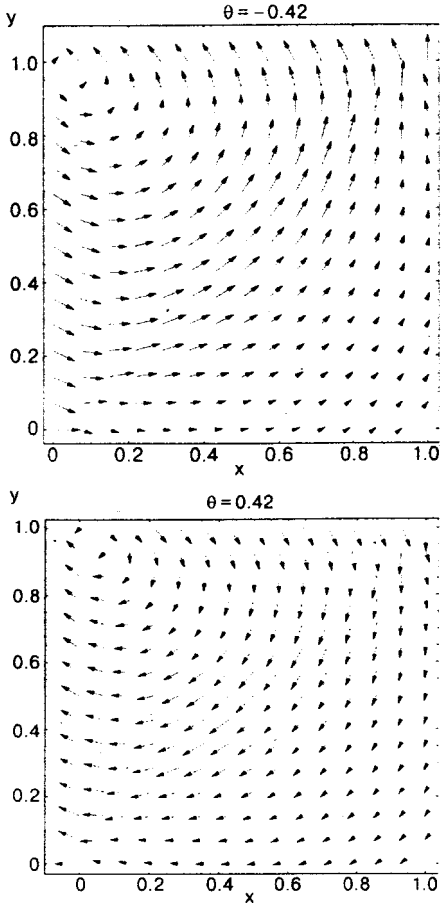

FIG. 6. Distribution of the current density inside the normal layer for phase $\phi=\pi$ and two values of the phase θ at which the current $I=0$ (Fig. 4).

density of electron states in the normal layer is given by the formula

$$\mathcal{N}(\epsilon,\rho)=N(0)\langle \mathrm{Re}\, g(\omega=-i\epsilon,\rho,\mathbf{v}_F)\rangle_{\mathbf{v}_F}. \tag{15}$$

($g(\omega,\rho,v_F)$ is the Eilenberger Green's function). We have studied the dependence of the density of states, averaged over area of the N layer, $N(\epsilon)$, on the phases θ and ϕ. This tunneling density of states can be measured by a scanning tunneling microscope. It contains the spikes whose intensity and position on the energy axes are controlled by the phases θ and ϕ. The results are shown in Fig. 8 (the δ-function singularities in $N(\epsilon)$ are smeared by introducing a small damping $\Gamma=0.01\Delta_0$).

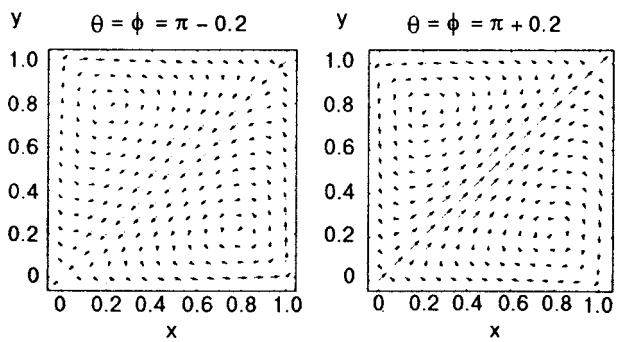

FIG. 7. The vortexlike distributions of the current inside the weak link when θ and ϕ are inside the frustrated region.

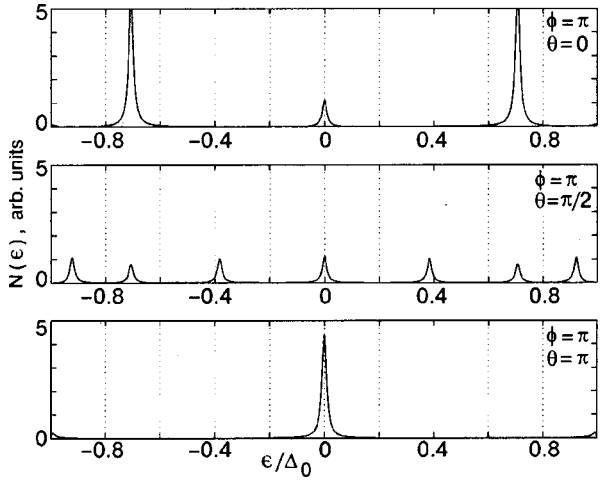

FIG. 8. Density of states, $N(\epsilon)$, averaged over the normal region for different values of θ and ϕ.

4. MESOSCOPIC FOUR-TERMINAL SQUID

In this section we consider the four-terminal SQUID configuration (Fig. 2b). The conventional 4-terminal SQUID has been studied in detail in Ref. 5, wherein the steady-state domain and dynamical properties of the system were calculated. Here we are interested in the specific features of the mesoscopic case reflected in the current-phase relations (11), (12). As we have seen in the previous Section, the nonlocal coupling ($p\neq q$) leads to the phase dragging effect. This dragged phase can induce in the ring a transferred magnetic flux which depends on the transport current. Conversely the magnetic flux state in the ring influences the behavior of the Josephson junction in the current circuit.

When the terminals 3 and 4 are short-circuited by a superconducting ring with self-inductance L, the phase ϕ is related to an observable quantity, the magnetic flux Φ threading the ring $\phi=(2e/\hbar)\Phi$. The current J circulating in the ring is given by $J=(\Phi^e-\Phi)/L$, where Φ^e is the external magnetic flux threading the ring. From (11) and (12) we have

$$I=\sin\theta+\left[(p+q)\sin\frac{\theta}{2}\cos\frac{\Phi}{2}+(p-q)\cos\frac{\theta}{2}\sin\frac{\Phi}{2}\right]\cos\chi, \tag{16}$$

$$\frac{\Phi^e-\Phi}{\mathcal{L}}=\sin\Phi+\frac{1}{\kappa}\left[(p+q)\sin\frac{\Phi}{2}\cos\frac{\theta}{2}+(p-q)\cos\frac{\Phi}{2}\sin\frac{\theta}{2}\right]\cos\chi, \tag{17}$$

where the fluxes Φ,Φ^e are measured in units $\hbar/2e$, and $\mathcal{L}=(2e/\hbar)LI_0\kappa$ is the dimensionless self-inductance. The parameter $\kappa=\gamma_{34}/\gamma_{12}$ is the ratio of the critical currents of the subjunctions 3–4 and 1–2. The limiting cases of $\kappa\to\infty$ and $\kappa\to 0$ correspond to the autonomous SQUID and the current-biased Josephson junction, respectively.

The transport current I and the external flux Φ^e are the external control parameters. The corresponding Gibbs potential for the 4-terminal SQUID takes the form

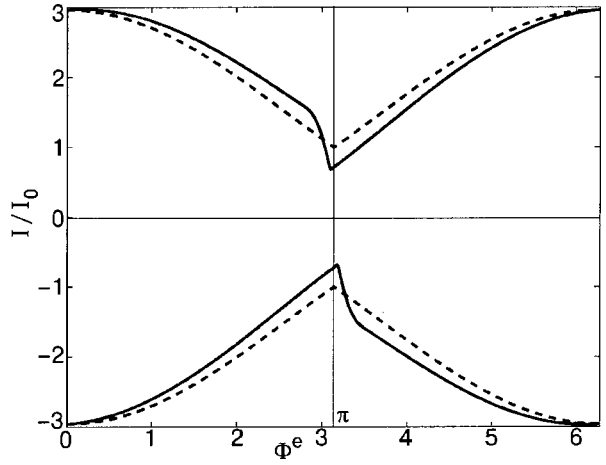

FIG. 9. The steady-state domain for a mesoscopic four-terminal SQUID in the plane (I,Φ^e) of the control parameters (solid curve). The dashed curve corresponds to conventional four-terminal SQUIDs.

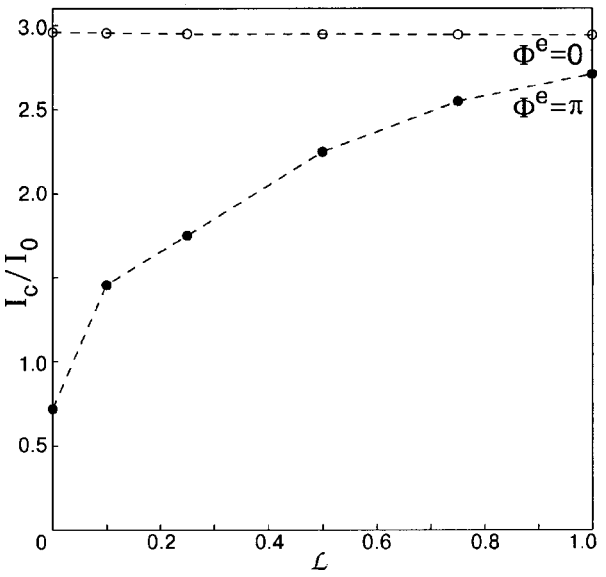

FIG. 10. The critical current I_c between the superconductors S_1 and S_2 as a function of $\mathcal{L}$ for $\Phi^e=0$ and π.

$$U(\Phi,\theta;I,\Phi^e)=\frac{\kappa(\Phi-\Phi^e)^2}{2\mathcal{L}}-I\theta-\cos\theta-\kappa\cos\Phi-2\times\left[(p+q)\cos\frac{\theta}{2}\cos\frac{\Phi}{2}-(p-q)\sin\frac{\theta}{2}\sin\frac{\Phi}{2}\right]\cos\chi. \tag{18}$$

The last three terms in Eq. (18) are the Josephson coupling energy (4) in terms of the variables θ, Φ, and χ. The minimization of U with respect to χ gives the expression (13) for $\cos\chi$, with ϕ replaced by Φ. At given values of the control parameters I and Φ^e, relations (16) and (17) [together with Eq. (13)] determine the set of possible states of the system $\{\theta,\Phi\}$, among which we should choose those that correspond to the local minima of the potential U, Eq. (18).

Let us consider the effect of the magnetic flux state of the ring on the behavior of the current-driven junction. The critical current I_c of the junction depends on the applied magnetic flux Φ^e. In the simplest case of small self-inductance $\mathcal{L}\ll 1$, we can neglect the difference between Φ and Φ^e in expression (16). The maximal value of the supercurrent I (16) (with Φ replaced by Φ^e) as a function of Φ^e, $I_{\max}(\Phi^e)$, is shown in Fig. 9. This curve determines the boundary of the steady-state domain in the (I,Φ^e) plane. The function $I_{\max}(\Phi^e)$ is 2π periodic, but due to the terms proportional to $p-q$ in Eq. (16), it is not invariant under the transformation $\Phi^e\to\Phi^e$. The symmetry is restored if we simultaneously change Φ^e to $-\Phi^e$ and I to $-I$. Note that in the conventional case $(p=q)$ the boundary of the steady-state domain $I_{\max}(\Phi^e)$ is symmetric with respect to the axes (I,Φ^e) (dashed line in Fig. 9). Thus the critical current I_c in the transport current circuit, for a given direction of the current, depends on the sign of the magnetic flux in the ring. For finite values of the self-inductance $\mathcal{L}$, equations (16) and (17) must be treated self-consistently. The critical current I_c as function of $\mathcal{L}$ is shown in Fig. 10 for two values of the external flux, $\Phi^e=0$ and $\Phi^e=\pi$.

Outside the steady-state domain, the stationary solutions for (θ,Φ) are absent and the system goes to the nonstationary resistive regime. The simple generalization of Eqs. (16), (17) in the framework of the heavily damped resistively shunted junction (RSJ) model[3] leads to equations (see Ref. 7):

$$\frac{d\theta}{dt}=I-\sin\theta-\left[(p+q)\sin\frac{\theta}{2}\cos\frac{\Phi}{2}\times(p-q)\cos\frac{\theta}{2}\sin\frac{\Phi}{2}\right]\cos\chi. \tag{19}$$

$$\frac{d\Phi}{dt}=\frac{\Phi^e-\Phi}{\mathcal{L}}-\sin\Phi-\frac{1}{\kappa}\left[(p+q)\sin\frac{\Phi}{2}\cos\frac{\theta}{2}+(p-q)\cos\frac{\Phi}{2}\sin\frac{\theta}{2}\right]\cos\chi, \tag{20}$$

$$\frac{d\chi}{dt}=-\sin\chi\left[(p+q)\cos\frac{\Phi}{2}\cos\frac{\theta}{2}-(p-q)\sin\frac{\Phi}{2}\sin\frac{\theta}{2}\right]. \tag{21}$$

They can also be presented in the form

$$\dot\theta=-\frac{\partial U}{\partial\theta},\quad \dot\Phi=-\frac{\partial U}{\partial\Phi},\quad \dot\chi=-\frac{1}{2}\frac{\partial U}{\partial\chi}, \tag{22}$$

where the potential U is defined in Eq. (18). The voltages between different terminals are related to the time derivatives of the phase differences

$$V_{21}=\dot\theta,\quad V_{34}=\dot\Phi,\quad \frac{1}{2}(V_{13}+V_{24})=\dot\chi. \tag{23}$$

The time and the voltage are measured in units of e/I_0 and $\hbar I_0/2e^2$, respectively. Note that, in spite of the equilibrium state, the dynamical variable χ relates to an observable quantity. Its time derivative determines the voltage between the ring and the transport circuit. The features of the dynamical behavior of the mesoscopic 4-terminal SQUID are again affected by the terms proportional to $(p-q)$, i.e., by nonlocal coupling. The current–voltage characteristics in the transport channel, $V(I)$ [the time-averaged voltage V_{21} (23)], can be obtained by numerical solution of the coupled system of non-

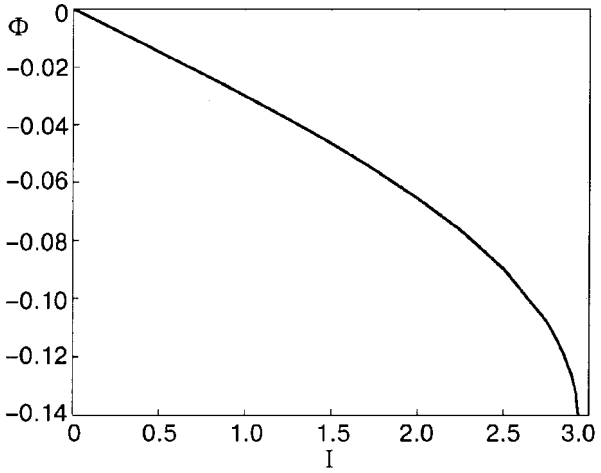

FIG. 11. The flux induced inside the ring as a function of the transport current I. $\mathcal{L}=1$, $\Phi^e=0$.

linear differential equations (20)–(22). As well as the critical current I_c, the voltage $V(I)$ in an applied magnetic flux Φ^e depends on the sign of Φ^e, i.e., on the direction of the external magnetic field. A full dynamical description of the mesoscopic four-terminal SQUID requires a more rigorous approach than the RSJ model and will be the subject of a separate investigation.

In accordance with the stationary (16), (17) or dynamical equations (19)–(21) for θ and Φ, the opposite effect for the influence of transport current circuit on the flux states in the ring takes place. In particular, a current I produces a flux Φ in the ring even in stationary case and in the absence of external flux Φ^e. This effect is proportional to $(p-q)$ and is absent in the conventional case. In Fig. 11 we plot the magnetic flux Φ induced in the ring as a function of the transport current I in the case $\Phi^e=0$.

A special interest is the existence of bistable states in the system described by the potential (18). We emphasize that, in contrast to the usual SQUID, bistable states occur for any inductance $\mathcal{L}$, even for $\mathcal{L}<1$.[5] We will analyze the dependence of these states on the control parameters I and Φ^e in Article II, when the design of the four-terminal qubit will be studied.

5. CONCLUSIONS

We have demonstrated that in ballistic four-terminal Josephson junctions the coherent anisotropic superposition of the macroscopic wave functions of the superconductors in the normal region produces the formation of phase-slip lines (2D analogs of phase-slip centers) and time-reversal symmetry breaking 2D vortex states in it, as well as such effects as phase dragging and magnetic flux transfer. We have calculated the phase-dependent tunneling density of Andreev states in this region as well.

The degree to which the nonlocality of the mesoscopic transport is manifested depends on the characteristics of the system and is most pronounced in the ballistic case.[20] The ballistic four-terminal junctions considered here demonstrate several specific effects absent in the diffusive limit:[4–6] phase dragging, time-reversal symmetry breaking $[(I(\theta)\neq I(-\theta))$, Eq. (14)], and the vortex formation. The latter can mimic the behavior of S–N–S junctions with unconventional superconductors.[21] It has indeed the same origin in the direction-dependent phase of the superconducting order parameter induced in the normal part of the system, though not due to the intrinsic phase difference between different directions in a superconductor. This actually allows us more freedom in controlling the behavior of the junction, which will be exploited in the qubit design based on such a junction in the following paper. The time-reversal symmetry breaking can be also used for direction-sensitive detection of weak magnetic fluxes.

It will be instructive to investigate the role played by finite elastic scattering in the system and look for the analogs of zero bound states, found at surfaces/interfaces of unconventional superconductors (for a review see Ref. 22). This, as well as the vortex dynamics in the system, will be the subject of our further research.

We thank R. de. Bruyn Ouboter for his stimulating interest in this work. One of the authors, A. N. O., would like to acknowledge D-Wave Systems Inc. (Vancouver) for hospitality and support of this research.

APPENDIX

Junction with arbitrary γ's

The Josephson energy of the mesoscopic four-terminal junction, normalized to

$$(\hbar/2e)\pi\Delta_0^2(T)/4eT_c,$$

is expressed by

$$E_J=-\gamma_{12}\cos\theta-\gamma_{34}\cos\phi+E_{\mathrm{coupl}}, \tag{A1}$$

with the coupling energy E_{coupl} given by

$$\begin{aligned}E_{\mathrm{coupl}}=&-\gamma_{13}\cos\left(\frac{-\theta-\phi}{2}+\chi\right)-\gamma_{14}\cos\left(\frac{-\theta+\phi}{2}+\chi\right)\\&-\gamma_{23}\cos\left(\frac{\theta-\phi}{2}+\chi\right)-\gamma_{24}\cos\left(\frac{\theta+\phi}{2}+\chi\right)\\=&-(A\cos\chi+B\sin\chi),\end{aligned} \tag{A2}$$

where

$$A=(\gamma_{13}+\gamma_{24})\cos\left(\frac{\theta+\phi}{2}\right)+(\gamma_{14}+\gamma_{23})\cos\left(\frac{\theta-\phi}{2}\right), \tag{A3}$$

$$B=(\gamma_{13}-\gamma_{24})\sin\left(\frac{\theta+\phi}{2}\right)+(\gamma_{14}-\gamma_{23})\sin\left(\frac{\theta-\phi}{2}\right).$$

Minimizing with respect to χ, we find the minimum to be

$$E_{\mathrm{coupl}}=-\sqrt{A^2+B^2},\quad \chi=\cos^{-1}\left(\frac{A}{\sqrt{A^2+B^2}}\right). \tag{A4}$$

After some manipulations we find

$$\begin{aligned}E_{\mathrm{coupl}}=&-[\gamma_{13}^2+\gamma_{23}^2+\gamma_{14}^2+\gamma_{24}^2+2(\gamma_{13}\gamma_{14}+\gamma_{23}\gamma_{24})\\&\times\cos\phi+2(\gamma_{13}\gamma_{23}+\gamma_{14}\gamma_{24})\cos\theta+2(\gamma_{13}\gamma_{24}\\&+\gamma_{14}\gamma_{23})\cos\theta\cos\phi-2(\gamma_{13}\gamma_{24}\end{aligned}$$

$$-\gamma_{14}\gamma_{23})\sin\theta\sin\phi]^{1/2}. \tag{A5}$$

The last term in the bracket in (A5) vanishes when $\det(\hat{\gamma}_{\text{coupl}})=0$. In that case the current $I(\theta,\phi)$ will be zero at $\theta=0$. On the other hand, if $\det(\hat{\gamma}_{\text{coupl}})\neq 0$, then $I(\theta,\phi)\neq 0$ when $\theta=0$. This is a signature of the phase dragging effect.

In a four-terminal junction with microbridges near T_c one has $\gamma_{ij}\sim 1/R_iR_j$. In that case the last term in (A5) will vanish and E_{coupl} factorizes:

$$E_{\text{coupl}}\sim -\left[\left(\frac{1}{R_1}-\frac{1}{R_2}\right)^2+\frac{4\cos^2(\theta/2)}{R_1R_2}\right]^{1/2} \times\left[\left(\frac{1}{R_3}-\frac{1}{R_4}\right)^2+\frac{4\cos^2(\phi/2)}{R_3R_4}\right]^{1/2}. \tag{A6}$$

In particular, when $R_1=R_2$ and $R_3=R_4$ we find

$$E_{\text{coupl}}\sim -\frac{4}{R_1R_3}\left|\cos\frac{\theta}{2}\right|\left|\cos\frac{\phi}{2}\right|, \tag{A7}$$

which is what one obtains from a Ginzburg-Landau calculation.

In a mesoscopic four-terminal junction with parallel implementation, on the other hand, we have $\gamma_{13}=\gamma_{24}$ and $\gamma_{14}=\gamma_{23}$. This leads to $B=0$ and therefore

$$E_{\text{coupl}}=-|A|,\quad \cos\chi=\text{sign}(A), \tag{A8}$$

which gives $\chi=0$ or π. Notice that in the general case of (A4), χ can take values other than 0 and π.

*E-mail: omelyanchouk@ilt.kharkov.ua

[1] K. K. Likharev, Rev. Mod. Phys. **51**, 101 (1979).
[2] I. O. Kulik, A. N. Omelyanchouk, and E. A. Kel'man, Fiz. Nizk. Temp. **3**, 1107 (1977) [Sov. J. Low Temp. Phys. **3**, 537 (1977)].
[3] A. Barone and G. Paterno, *Physics and Applications of the Josephson Effect*, Wiley, New York (1982).
[4] E. D. Vol and A. N. Omelyanchouk, Fiz. Nizk. Temp. **20**, 107, (1994) [Low Temp. Phys. **20**, 87 (1994)].
[5] R. de Bruyn Ouboter, A. N. Omelyanchouk, and E. D. Vol, Physica B **205**, 153 (1995); **239**, 203 (1997).
[6] L. G. Aslamazov and A. I. Larkin, JETP Lett. **9**, 87 (1969).
[7] R. de Bruyn Ouboter and A. N. Omelyanchouk, Superlattices Microstruct. **23**, 1005 (1999).
[8] B. J. Vleeming, *Ph.D. Thesis*, Leiden University (1998).
[9] I. O. Kulik, Zh. Éksp. Teor. Fiz. **57**, 1745 (1970) [Sov. Phys. JETP **30**, 944 (1970)].
[10] I. O. Kulik and A. N. Omelyanchouk, Fiz. Nizk. Temp. **4**, 296 (1978) [Sov. J. Low Temp. Phys. **4**, 142 (1978)]; C. W. J. Beenakker and H. van Houten, Phys. Rev. Lett. **66**, 3056 (1991).
[11] Y. Imry, *Introduction to Mesoscopic Physics*, Oxford, New York (1997).
[12] A. F. Andreev, Zh. Éksp. Teor. Fiz. **46**, 1823 (1964) [Sov. Phys. JETP **19**, 1228 (1964)].
[13] J. P. Heida, B. J. van Wees, T. M. Klapwijk, and G. Borghs, Phys. Rev. B **57**, R5618 (1998).
[14] V. Barzykin and A. M. Zagoskin, Superlattices Microstruct. **25**, 797 (1999).
[15] U. Ledermann, A. L. Fauchére, and G. Blatter, Phys. Rev. B **59**, R9027 (1999).
[16] Malek Zareyan and A. N. Omelyanchouk, Fiz. Nizk. Temp. **25**, 240 (1999) [Low Temp. Phys. **25**, 175 (1999)].
[17] A. N. Omelyanchouk and Malek Zareyan, Physica B **291**, 81 (2000).
[18] M. Buttiker, Phys. Rev. Lett. **37**, 1761 (1986).
[19] G. Eilenberger, Z. Phys. **214**, 195 (1968).
[20] I. O. Kulik, A. N. Omel'yanchuk, and R. I. Shekhter, Fiz. Nizk. Temp. **3**, 1543 (1977) [Sov. J. Low Temp. Phys. **3**, 740 (1977)].
[21] A. Huck, A. van Otterlo, and M. Sigrist, Phys. Rev. B **56**, 14163 (1997); A. M. Zagoskin, J. Phys.: Condens. Matter **9**, L419 (1997); cond-mat/9903170 (1999).
[22] S. Kashiwaya and Y. Tanaka, Rep. Prog. Phys. **63**, 1641 (2000).

This article was published in English in the original Russian journal. Reproduced here with stylistic changes by AIP.

On the two-dimensional character of the superconducting transition in underdoped high-temperature superconductors

G. G. Sergeeva*

Kharkov Physico-Technical Institute National Research Center, ul. Akademicheskaya 1, 61108 Kharkov, Ukraine

(Submitted March 16, 2001; revised April 12, 2001)
Fiz. Nizk. Temp. **27**, 845–849 (August 2001)

The 3D→2D dimensional crossover in the superconducting state of quasi-two-dimensional high-T_c superconductors is investigated. The consistent pattern of the superconducting state of 2D and 3D systems is used to find a universal temperature dependence of the ratio of the squares of the penetration depths of a magnetic field directed along the $\hat{\mathbf{c}}$ axis, i.e., $\lambda^2(0)/\lambda^2(T/T_c)$, from which one can obtain a relation between the superconducting transition temperature T_c and $\lambda^{-2}(0)$. This yields the temperature $T_{\rm cr}$ of the dimensional crossover as the boundary of the region of ''two-dimensionality'' of the superconducting state, where for $T>T_{\rm cr}$ the results of measurements of the penetration depth begin to deviate from the universal dependence found. It is shown that the size of the region of three-dimensional superconducting fluctuations can be determined from measurements of $\lambda(T/T_c)$ and the resistance along the $\hat{\mathbf{c}}$ axis and turns out to be finite, attesting to the 2D character of the superconducting transition in quasi-2D HTSCs. © *2001 American Institute of Physics.* [DOI: 10.1063/1.1399199]

1. INTRODUCTION

Quasi-2D high-T_c superconductors (HTSCs), i.e., underdoped compounds, have such distinctive properties as a semiconductor trend of the resistance along the $\hat{\mathbf{c}}$ axis, $\rho_c(T)$, a large interval of 2D superconducting fluctuations, $\Delta_{2D}\sim T_c$, and the appearance of a pseudogap state at $T\leqslant T^*$. This has led to the conjecture that the superconducting transition in these compounds is due to a Berezinskiĭ–Kosterlitz–Thouless (BKT) transition at a temperature $T_{\rm BKT}<T_{c0}$, where T_{c0} is the temperature of the superconducting transition in the CuO_2 planes in mean field theory (see the review[1] and the references cited therein). Even though a two-dimensional character of the superconducting fluctuations and the hallmarks of the BKT transition have been observed in the majority of quasi-2D HTSCs,[2,3] it is as yet unclear whether such a transition can be observed in bulk superconductors when the finite value of the interaction along the $\hat{\mathbf{c}}$ axis is taken into account.[4,5] The most convincing evidence comes from measurements of the resistance for ultrathin YBCO films,[5] from which one can determine the temperature of the BKT transition: as the number of layers increases, $T_{\rm BKT}$ increases from 30 K (for a film one monolayer thick) to 80 K for a 10-layer film. Because of this difference between T_c, $T_{c0}\leqslant T^*$, and $T_{\rm BKT}$ and also because of doubts about whether a BKT transition can in principle be realized in a bulk sample, the character of the superconducting transition in quasi-2D HTSCs remains an open question.[4,5]

Taking the finite interactions along the $\hat{\mathbf{c}}$ axis into account can lead to a dimensional crossover both for $T>T_c$ and in the superconducting state at temperatures close to T_c (see, e.g., Refs. 4–6). There is a well-known theoretical model of such a superconducting transition in layered structures:[7–9] at a sufficiently low probability for charge hops between layers the system behaves as two-dimensional with a finite region Δ_{3D} of three-dimensional superconducting fluctuations. The question of the large difference between the temperatures T_c, T_{c0}, and $T_{\rm BKT}$ will, of course, be answered once the mechanism of high-temperature superconductivity is understood. For example, the spin-fluctuation model of pairing, for which $T_c\sim J_c$ and $T_{c0}\sim J_{ab}$, the anisotropy of the exchange interactions of the quasi-2D HTSCs in the copper–oxygen plane, J_{ab}, and along the $\hat{\mathbf{c}}$ axis, $J_c\ll J_{ab}$, leads to $T_c\ll T_{c0}$ and to a large value of the interval Δ_{2D}. In Refs. 10 and 11 it was shown that the two-dimensionality of the superconducting fluctuations in the normal state is also responsible for such properties of quasi-2D HTSCs as the temperature dependence of the probability $t_c(T)$ for the tunneling of charge along the $\hat{\mathbf{c}}$ axis and the semiconductor trend of the resistivity $\rho_c(T)$. As the temperature is lowered, $t_c(T)$ decreases rapidly, and at $T\sim T_c^0$ the dimensional crossover 2D→3D occurs before the BKT transition. The temperature T_c^0 at which the resistivity $\rho_c(T)$ stops growing is of the same order as the temperature of the superconducting transition in a bulk sample (in mean field theory). This attests to the 3D character of the superconducting transition with a finite region of three-dimensionality of the superconducting fluctuations; in a layered system this transition occurs according to the Kats scenario[7]

$$T_c^0/\varepsilon_F > t_c(T_c^0), \tag{1}$$

at sufficiently small values of $t_c(T_c^0)$ (ε_F is the Fermi energy). Measurements of the temperature dependence of the resistivity $\rho_c(T)$ make it possible to determine the region of 3D superconducting fluctuations in the normal state, Δ_{3D}^N:

$$\Delta_{3D}^N \simeq T_c^0 - T_c \ll \Delta_{2D}^N. \tag{2}$$

It is known[6,12] that as the temperature is lowered in the superconducting state, the reverse crossover 3D→2D occurs at a temperature $T_{\rm cr}$ whose value depends on the correlation length $\xi_c(T)$ along the $\hat{\mathbf{c}}$ axis. The goal of this paper is to

investigate the superconducting state of quasi-2D HTSCs and to determine the region of 3D superconducting fluctuations, $\Delta_{3D}^{S} \simeq (T_c - T_{cr})$, for $T < T_c$. A universal temperature dependence is found for the ratio of the squares of the penetration depths for a magnetic field directed along the $\hat{\mathbf{c}}$ axis, $\lambda^2(0)/\lambda^2(T/T_c)$. The temperature T_{cr} of the dimensional crossover is determined as the boundary of the region of ''two-dimensionality'' of the superconducting state, where for $T > T_{cr}$ the results of measurements of the magnetic-field penetration depth begin to deviate from the universal dependence (6) found above.

2. ON THE UNIVERSAL DEPENDENCE OF T_c ON $\lambda^{-2}(0)$

The magnetic-field penetration depth $\lambda(T)$ is given by the London formula $\lambda(T) \sim n_{s,3}^{-1/2}(T)$, where $n_{s,3}(T)$ is the three-dimensional superfluid density, which is related in an obvious way to the 2D density $n_s(T)$: $n_{s,3}(T) = n_s(T)\nu/l$, where ν is the number of layers and l is the lattice period. It was shown by Pokrovskiĭ[13] that in quasi-2D HTSCs the magnetic-field penetration depth $\lambda(T)$ and the density $n_s(T)$ of the 2D superfluid component are related by

$$\lambda^2(0)/\lambda^2(T) = n_{s,3}(T)/n_{s,3}(0) = n_s(T)/n_s(0). \tag{3}$$

It can be shown that for quasi-2D HTSCs with less than optimal doping concentration this relation leads to a universal dependence $T_c(\lambda^{-2}(0))$ (Uemura plot), which was found in measurements of the muon relaxation rate.[14]

For a 2D degenerate system equation (3) can be expressed in terms of the ratio of the values of the dimensionless stiffness $\rho_s(T/T_c)/\rho_s(0) = n_s(T/T_c)/n_s(0)$, where $\rho_s(T/T_c)$ satisfies the universal relation[15]

$$\rho_s(T/T_c) = \exp\left[-\frac{Te^{-1}}{T_c \rho_s(T/T_c)} \right]. \tag{4}$$

The solution of this equation gives $\rho_s(0) = 1$, and for $T = T_c$

$$\rho_s(T/T_c)|_{T=T_c} = e^{-1}, \tag{5}$$

which was obtained in Ref. 15 and is plotted in Fig. 1. Equations (3) and (4) imply a universal character of the temperature dependence of the ratio of the squares of the penetration depths of the magnetic field:

$$\lambda^2(0)/\lambda^2 T/T_c) = \rho_s(T/T_c)/\rho_s(0) = \exp\left[-\frac{Te^{-1}\lambda^2(T/T_c)}{T_c \lambda^2(0)} \right], \tag{6}$$

and also a simple relation between the values of $\lambda^2(T)$ and $n_s(T)$ at $T = T_c$ and $T = 0$:

$$\lambda^2(0)/\lambda^2(T_c) = n_s(T_c)/n_s(0) = \mathrm{e}^{-1}. \tag{7}$$

Using (7) and the well-known Kosterlitz–Thouless–Nelson formula,[16] which relates the density of the 2D superfluid component $n_s(T_c)$ with the transition temperature T_c,

$$k_B T_c = \frac{h^2}{32\pi m} n_s(T_c), \tag{8}$$

we obtain a universal relation between the density $n_s(0)$ at $T = 0$ and the transition temperature T_c:

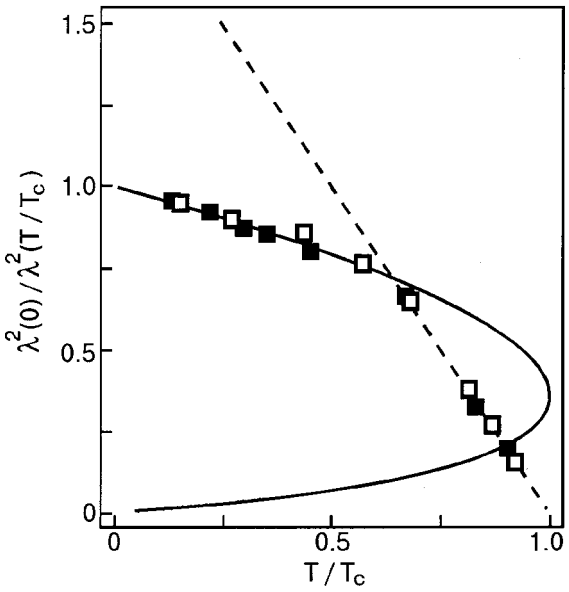

FIG. 1. Temperature dependence of $\lambda(0)^2/\lambda^2(T/T_c)$. The dashed line is the BCS dependence, and the solid curve is the universal dependence (6). The results of measurements for $La_{1.85}Sr_{0.15}CuO_4$ (Ref. 19) (□) and $YBa_2Cu_3O_{6.66}$ (Ref. 14) (■).

$$T_c = \frac{h^2 \mathrm{e}^{-1}}{32 k_B \pi m} n_s(0), \tag{9}$$

where k_B is Boltzmann's constant. An analogous relation was obtained in a different form in Refs. 17 and 18. In a 2D superconductor the role of the effective penetration depth is played by the magnetic screening length

$$L_s(T) = \frac{mc^2}{2\pi n_s(T) e^2}, \tag{10}$$

which is related to the London penetration depth as

$$L_s = 2\lambda^2/d. \tag{11}$$

Here d is the thickness of the CuO_2 plane, and e is the charge of the electron.

It is seen from expressions (7)–(11) that the superconducting transition temperature is proportional to $\lambda^{-2}(0)$,

$$T_c = k\lambda^{-2}(0), \tag{12}$$

where the coefficient of proportionality

$$k = \frac{c^2 h^2 \mathrm{e}^{-1} d}{64 k_B \pi^2 e^2} \tag{13}$$

depends only on universal constants and the thickness of the CuO_2 plane, which is the same for all cuprate HTSCs.

Thus relation (12), which was found in measurements of the muon relaxation rate[14] for quasi-2D HTSCs, is in fact universal and is a consequence of the general relations (4) and (8) for the superconducting state of 2D systems. Relation (12) should hold for superconductors in which the superconducting state is two-dimensional at $T < T_{cr}$, i.e., for superconductors with a 2D character of the transition. Unfortunately, to compare expression (12) with the relation obtained in Ref. 14 it is necessary to know the coefficient relating the muon relaxation rate with the quantity $\lambda^{-2}(0)$.

3. DETERMINATION OF THE DIMENSIONAL CROSSOVER TEMPERATURE T_{cr}

It is known[12] that as the temperature is lowered in the superconducting state, the coherence length along the $\hat{\mathbf{c}}$ axis, $\xi_c(T/T_c)$, decreases, and on reaching the temperature T_{cr}, where $\xi_c(T_{cr}/T_c)$ becomes less than the interlayer distance s, a 3D→2D dimensional crossover occurs:

$$\xi_c(T_{cr}/T_c)=\frac{1}{\sqrt{2}}\left(1-\frac{T_{cr}}{T_c}\right)^{-1/2}\xi_c(0)<s. \tag{14}$$

As we see from this equation, the dimensional crossover temperature T_{cr} depends on the ratio $\xi_c(0)/s$ and on the number of copper–oxygen layers in the cell. It is clear that crossover to the 2D superconducting state can occur in that region of temperatures where the 3D density of the superfluid component becomes comparable to the 2D density $n_s(T)$ multiplied by the ratio of the number of layers to the lattice period.[13] The temperature T_{cr} can be determined as the boundary of the region of ''two-dimensionality'' of the superconducting state, where the results of measurements of the magnetic-field penetration depth begin to deviate from the universal dependence (6).

Near the superconducting transition temperature, for $T_c>T>T_{cr}$, where the temperature dependence of $\lambda_c(T)$ is determined by the 3D superconducting fluctuations, the BCS microscopic theory gives

$$\lambda^2(0)/\lambda^2(T/T_c)=2(1-T/T_c). \tag{15}$$

A plot of $\lambda^2(0)/\lambda^2(T/T_c)$ is shown in Fig. 1 [the solid line corresponds to the universal dependence (6) and the dashed line to expression (15)], along with the results of measurements of the penetration depth of a magnetic field directed along the $\hat{\mathbf{c}}$ axis for $La_{1.85}Sr_{0.15}CuO_4$ with $T_c=37\,K$[19] and $YBa_2Cu_3O_{6.66}$ with $T_c\simeq 53\,K$.[14] We see that the 3D density of the superfluid component becomes comparable to $n_s(T)$ at $T\sim 0.7T_c$. In processing the results of the measurements, the quantity $\lambda^2(0)$ was determined from expression (15) as the average for the experimental points of $\lambda(T/T_c)$ for $T/T_c>0.7$. The measured values of $\lambda(T)$ for $La_{1.85}Sr_{0.15}CuO_4$ and $T>25\,K$ are well described by relation (15), while for $T\leqslant 20\,K$ they agree within the measurement error with the universal dependence (6). This simple calculation allows us to estimate a value $T_{cr}\sim 26\,K$ for the compound $La_{1.85}Sr_{0.15}CuO_4$ and to determine the temperature interval in which the superconducting state is three-dimensional:

$$\Delta_{3D}^S\simeq T_c-T_{cr}\simeq 11\,K.$$

4. DISCUSSION OF THE RESULTS AND CONCLUSIONS

It was shown in Secs. 2 and 3 that for $T<T_{cr}$ the ratio $\lambda^2(0)/\lambda^2(T/T_c)$ in quasi-2D HTSCs has a universal character, is given by relation (6), and attests to the two-dimensionality of the superconducting state. This leads to two important conclusions which are general for this class of superconductors:

1) In the universal relation (12) between T_c and $\lambda^{-2}(0)$ (Ref. 14) the coefficient of proportionality depends only on universal constants. Although this relation has been attracting great interest for 13 years now, the known versions of the function $T_c(\lambda^{-2}(0))$ either contain an adjustable parameter for fitting or some quantity that characterizes the superconductor (e.g., the correlation length[20]);

2) of the superconducting transition taking place according to the Kats scenario[7] with a finite region of 3D superconducting fluctuations,

$$\Delta_{3D}=\Delta_{3D}^N+\Delta_{3D}^S=T_c^0-T_{cr}, \tag{16}$$

is of a 2D character. The value of Δ_{3D} is independent of the accuracy with which T_c is determined and can be found from measurements of $\rho_c(T)$ and $\lambda(T)$. From measurements of the resistivity along the $\hat{\mathbf{c}}$ axis one can determine the temperature T_c^0 of the 2D→3D dimensional crossover in the normal state,[11] and measurements of $\lambda_c(T)$, as was shown above, can be used to find the temperature T_{cr} of the reverse crossover in the superconducting state. For example, for $La_{1.85}Sr_{0.15}CuO_4$ single crystals resistive measurements[21] give $T_c^0\sim 41.5\,K$, and measurements[19] of $\lambda(T)$ give $T_{cr}\sim 26\,K$ and, with allowance for Eq. (16), $\Delta_{3D}\sim 15.5\,K$.

The fact that $T_{BKT}<T_c$ and lies in the 3D superconducting fluctuation region[11] Δ_{3D}^S gives the superconducting properties of quasi-2D HTSCs a specific feature that is apparently one of the reasons for the continuing discussion as to the character of the superconducting transition in these compounds. In the normal state the superconducting fluctuations are two-dimensional in a large temperature interval $\Delta_{2D}\sim T_c$, and there the temperature dependence of the correlation length in the copper–oxygen plane and also that of $t_c(T)$ and $\rho_c(T)$ are determined by the superconducting transition temperature in the plane, T_{BKT}. In this case the probability of charge tunneling along the $\hat{\mathbf{c}}$ axis decreases as the temperature is lowered, until the 2D→3D dimensional crossover occurs at T_c^0. In the superconducting state the reverse dimensional crossover 3D→2D at $T_{cr}\sim 0.7T_c$ leads to the situation that for $T<T_{cr}$ the superconductor is a 2D system with a transition temperature T_c and a universal dependence of $\lambda^2(0)/\lambda^2(T/T_c)$ (Eq. (6)).

The author is extremely grateful to V. Yu. Gonchar and V. V. Kabanov for a discussion of this paper and some very important comments.

*E-mail: gsergeeva@kipt.kharkov.ua

[1] S. L. Cooper and K. E. Gray, in *Physical Properties of High Temperature Superconductors IV*, edited by D. M. Ginsberg, World Scientific, Singapore (1994), pp. 61–188.
[2] S. Martin, A. T. Fiory, R. M. Fleming, G. P. Espinoza, and A. S. Cooper, Phys. Rev. Lett. **62**, 677 (1989).
[3] D. H. Kim, A. M. Goldman, J. H. Kang, and R. T. Kampwirth, Phys. Rev. B **40**, 8834 (1989).
[4] Y. Matsuda, S. Komiyama, T. Onogi, T. Terashima, K. Shimura, and Y. Bando, Phys. Rev. B **48**, 10498 (1993).
[5] Y. Matsuda, S. Komiyama, T. Terashima, K. Shimura, and Y. Bando, Phys. Rev. Lett. **69**, 3228 (1992).
[6] Z. Tešanović, L. Xing, L. Bulaevskii, Q. Li, and M. Suenaga, Phys. Rev. Lett. **69**, 3563 (1992).
[7] E. I. Kats, Zh. Éksp. Teor. Fiz. **56**, 1675 (1969) [Sov. Phys. JETP **29**, 897 (1969)].
[8] Vik. S. Dotsenko and M. V. Feigel'man, Zh. Éksp. Teor. Fiz. **83**, 345 (1982) [Sov. Phys. JETP **56**, 189 (1982)].
[9] L. N. Bulaevskiĭ, Usp. Fiz. Nauk **116**, 449 (1975) [Sov. Phys. Usp. **18**, 514 (1975)].
[10] G. Sergeeva, Physica C **341–348**, 181 (2000).

[11] G. G. Sergeeva, V. Yu. Gonchar, and A. V. Voitsenya, Fiz. Nizk. Temp. **27**, 634 (2001) [Low Temp. Phys. **27**, 468 (2001)]; G. G. Sergeeva, cond-mat/0009212.
[12] T. Schneider and H. Keler, Phys. Rev. B **47**, 5915 (1993).
[13] V. L. Pokrovskiĭ, JETP Lett. **47**, 629 (1988).
[14] Y. J. Uemura, V. J. Emery, A. R. Moodenbaugh *et al.*, Phys. Rev. B **38**, 909 (1988); Phys. Rev. Lett. **64**, 2082 (1990).
[15] A. Z. Patashinskiĭ and V. L. Pokrovskiĭ, *Fluctuation Theory of Phase Transitions* [Pergamon Press, Oxford (1979); Nauka, Moscow (1982)].
[16] B. I. Halperin and D. R. Nelson, J. Low Temp. Phys. **36**, 599 (1979).
[17] V. B. Gusynin, V. M. Loktev, and S. G. Sharapov, Zh. Éksp. Teor. Fiz. **115**, 1243 (1999) [JETP **88**, 685 (1999)].
[18] V. M. Loktev, R. M. Quick, and S. G. Sharapov, Fiz. Nizk. Temp. **26**, 567 (2000) [Low Temp. Phys. **26**, 414 (2000)].
[19] G. Aeppli, R. J. Cava, E. J. Ansaldo, J. H. Brewer, S. R. Kreitzman, G. M. Luke, D. R. Noakes, and R. F. Kiefl, Phys. Rev. B **35**, 7129 (1987).
[20] T. Schneider, Physica C **195**, 82 (1992).
[21] T. Ito, H. Takagi, S. Ishibashi *et al.*, Nature (London) **350**, 596 (1991).

Translated by Steve Torstveit

Resonance phenomena in phase-slip centers

A. B. Agafonov and I. V. Zolochevskiĭ

B. Verkin Institute for Low Temperature Physics and Engineering, National Academy of Sciences of Ukraine, pr. Lenina 47, 61103 Kharkov, Ukraine

V. M. Dmitriev[a)]

B. Verkin Institute for Low Temperature Physics and Engineering, National Academy of Sciences of Ukraine, pr. Lenina 47, 61103 Kharkov, Ukraine; International Laboratory of High Magnetic Fields and Low Temperatures, 95 Gajowicka St., 53-421 Wroclaw, Poland

(Submitted January 12, 2001)
Fiz. Nizk. Temp. **27**, 850–859 (August 2001)

The resonance properties of nonequilibrium regions of phase-slip centers arising in tin films of different thicknesses under the influence of a dc transport current are investigated experimentally for films which are uniform over their width. It is confirmed that an important role in the mechanism of excitation of the non-Josephson oscillation (NJO) is played by the inelastic electron–phonon relaxation time τ_ε of the charge imbalance. It is shown that two intercoupled resonance systems exist in samples containing phase-slip centers in the NJO regime. The change in shape of the amplitude–frequency characteristics of the NJO signal as the sample thickness is changed is explained by the influence of the transport electric current on the rate of relative tuning of the NJO frequency ω_0 and the relaxation frequency ω_r of the nonequilibrium region of the phase-slip center.
[DOI: 10.1063/1.1399200]

Dedicated to the memory of G. E. Churilov

INTRODUCTION

In long quasi-one-dimensional superconductors with transverse dimensions smaller than the coherence length $\xi(T)$ in the supercritical current regime, when the transport current density j through the sample is greater than the critical current density j_c, a dynamic resistive state arises, with the formation of phase-slip centers (PSCs).[1,2] Under certain conditions the electric potential becomes nonstationary—so-called non-Josephson oscillations (NJOs) appear. In Ref. 3 the nonequilibrium spatial structure of a PSC was analyzed in detail, and the basic properties of its individual regions in direct current (dc) and the effect of various relaxation processes on them were investigated. The present study is devoted to investigation of the resonance properties of nonequilibrium regions of the PSCs with allowance for various mechanisms of quasiparticle relaxation in the presence of the field of the NJO.

It has been shown previously that a NJO arises in a quasinormal region of size $2d_N(T)=2[\xi(T)l_E(T)]^{1/2}$(where $\lambda_E(T)$ is the penetration depth of a weak longitudinal electric field into the superconductor) in a PSC, and its frequency is much less than the frequency of oscillation of the energy gap $\Delta(T)$ in the core of the PSC.[4,5] This is evidence of the special nonequilibrium-quasiparticle relaxation processes in the PSC that lead to excitation of the NJO. According to the model of Refs. 6 and 7, the nonstationarity arises because excess quasiparticles that have acquired an energy $\varepsilon_1>\Delta$ as a result of multiple Andreev reflection inside a quasinormal region of size $2d_N(T)$ in the PSC undergo relaxation to the level of the energy gap Δ, accompanied by the radiation of bremsstrahlung photons. The energy $(\varepsilon_1-\Delta)$ released in this relaxation excites a collective mode of weakly damped plasma oscillations of superconducting electrons at a frequency $\omega_0\approx(\varepsilon_1-\Delta)/\hbar$ (Ref. 8) in a nonequilibrium region of size $2l_E(T)$ in the PSC. Since only a small fraction, proportional to the ratio $(\varepsilon_1-\Delta)/\Delta$, of the quasiparticles injected into the $2l_E(T)$ region take part in the formation of the NJO, the amplitude of the plasma oscillations is small.

According to Ref. 9, the frequencies of the plasma oscillations of superconductors with a small transverse cross section lie in the interval from zero to a certain damping frequency ω_d, which can be several orders of magnitude lower than the plasma frequency ω_p in a normal metal ($\omega_p^2=4\pi ne^2/m$, where m, e, and n are the electron mass, charge, and density). The frequency ω_d decreases with decreasing density n_S of Cooper pairs or with increasing quasiparticle conductivity σ and increasing inelastic impurity scattering time $\tau_{\rm imp}$. It is for this reason that ω_d is comparatively low in the purer samples, for which $\tau_{\rm imp}$ is larger, and also at temperatures close to the critical temperature, where σ is close in size to the conductivity σ of the normal metal. Within the nonequilibrium region this mode propagates like an electromagnetic wave in a long line. Because of its weak damping, it can form a standing wave. In that case a resonance of the plasma oscillations arises in a nonequilibrium superconductor, the characteristics of this resonance depending on the electrophysical properties of the sample.

The nonequilibrium state arising upon the injection of quasiparticles into the superconductor is due to an imbalance of the branches of the excitation spectrum. By analyzing the

TABLE I. Physical parameters of superconducting tin films.

Sample No.	d, nm	w, μm	L, μm	T_c, K	R_{300}, Ω	$R_{4,2}$, Ω	ξ(0), nm	$l_E(0)$, μm	l_{eff}, nm
1	58	1.4	47	3.822	82	7.50	101	4.7	94.4
2	76	1.8	51	3.810	53	4.30	105	5	107.6
3	174	1.5	34	3.779	17.5	0.72	127	7.2	221.4
4	294	1.8	43	3.802	11	0.41	130	7.4	245.4
5	698	1.8	84	3.767	8.9	0.173	146	10.6	479.2

Note: d, w, and L are the thickness, width, and length of the sample; $\xi(0)$ and $l_E(0)$ are the coherence length and the penetration depth of a weak longitudinal electric field into the superconductor at temperature 0 K; l_{eff} is the effective mean free path of the electron.

processes that occur here, one can obtain information about the mechanisms for relaxation of a charge imbalance in the superconductor. Since the conditions for propagation of plasma waves are determined by the characteristics of the sample, such an analysis can yield the interrelationship between the relaxation and nonstationary processes in a nonequilibrium superconductor.

1. EXPERIMENTAL PROCEDURES AND RESULTS

The goal of the present study is to elucidate how the propagation of an electromagnetic field, the frequency ω_0 of the NJO signal generated by a film, and the resonance frequency ω_r of the PSC are influenced by the characteristics of a nonequilibrium superconductor and the relaxation processes occurring in it. We investigated nonequilibrium regions of PSCs arising in uniform (over width) tin films of different thicknesses under the influence of a dc transport current in the presence of the alternating current of a NJO. The details of the experimental layout and techniques for creating PSCs in the superconducting film and measuring their main parameters with the dc and ac circuits decoupled are described in Ref. 10. The resistive state of the samples with a dc current flowing through them was studied by the conventional four-probe method with analog recording of the current–voltage (I–V) characteristics. The results of the measurements were used to determine the electrical characteristics of the samples (see Table I).

The films were deposited in a vacuum of the order of 10^{-8} torr with oil-free pumping and can therefore be assumed to be quite pure. We therefore attribute the change in resistivity of the samples mainly to a change in the mean free path of the electrons on account of the size effect. We measured the I–V characteristics of these uniform superconducting films (channels) at different temperatures. A Tektronix 2710 spectrum analyzer was used to obtain the frequency and amplitude of the ac electric potential (the NJO signal) as functions of the transport current and temperature. The curves obtained were used to construct the amplitude–frequency (A–F) and frequency–current characteristics of the NJO signal. The experimental A–F characteristics for samples of different thicknesses are presented in Fig. 1.

2. DISCUSSION OF THE RESULTS

2.1. Influence of the supercurrent and external fields on the relaxation time for the quasiparticle charge imbalance in uniform superconducting films

The resonance properties of superconducting films of small transverse cross section are governed by their total impedance, comprised of their active resistance R, capacitive reactance X_C, and inductive reactance X_L. The absolute value of these components depends on the state of the sample. In the equilibrium state of the superconductor the resistance R is due solely to completely normal quasiparticles, which absorb energy from the electromagnetic field, and the reactive components X_C and X_L are determined by its capacitance C and inductance L.

The capacitance of a narrow superconducting film under conditions such that the electric current flowing along it is much less than critical and nonlinear effects need not be

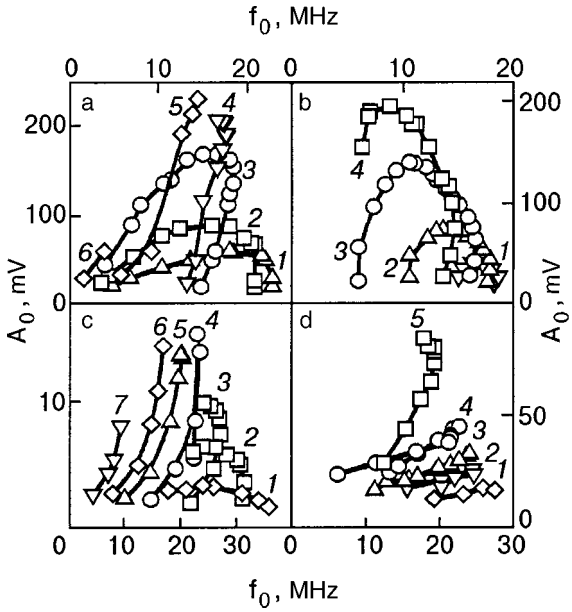

FIG. 1. Amplitude–frequency characteristics of the non-Josephson oscillation signal generated by samples of different thicknesses d: 700 nm (sample No. 5) (a); 300 nm (sample No. 4) (b); 170 nm (sample No. 3) (c); 58 nm (sample No. 1) (d) at various temperatures near T_c. The temperature of the measurements decreases with increasing number of the curve.

taken into account is determined solely by its surface area, i.e., its geometric dimensions. The inductance of a linear conductor such as any of the films investigated here can always be represented as a geometric inductance L_g and a kinetic inductance L_k connected in series. The first of these is determined by the transverse cross section and length of the conductor, and the second characterizes the internal inertial properties of the charge carriers. Ordinarily the condition $L_g \gg L_k$ is satisfied, and it is only in superconductors of small transverse cross section that the situation can change to the reverse and the kinetic inductance become larger than the geometric.

A nonequilibrium situation can arise in a superconductor under the influence of such factors as the passage of a current larger than the critical current, the injection or extraction of quasiparticles, and the action of electromagnetic and magnetic fields. It was shown in Ref. 11 that in the temperature region where $\Delta(T) \ll k_B T_c$, a one-dimensional superconductor found in a nonequilibrium state can be represented by the equivalent circuit of a long line with the following distributed parameters per unit length: normal resistance R, kinetic inductance L_k, conductance G, which determines the damping of the charge imbalance, and nonequilibrium capacitance C, which characterizes the energy stored in the field of the nonequilibrium potential. These quantities are expressed in terms of the physical parameters of the superconductor:

$$R=\frac{mV_F}{ne^2 l_{\text{eff}}^s}=\frac{1}{\sigma s}, \quad \frac{m}{n_S e^2 s}=\frac{\tau_0}{\sigma s},$$
$$G=\frac{3ne^2 s}{mV_F\tau_Q}=\frac{\sigma s}{l_E^2}, \quad C=\frac{3ne^2 s\tau_\varepsilon}{mV_F\tau_Q}=\frac{\sigma s\tau_\varepsilon}{l_E^2}. \tag{1}$$

Here V_F is the velocity of an electron on the Fermi surface, s is the cross-sectional area of the sample, σ is the conductivity of the film in the normal state, τ_0 is the response time of the supercurrent to an external influence, n_S is the density of Cooper pairs, and l_E is the penetration depth of a weak longitudinal electric field into the superconductor at an effective relaxation time of the charge imbalance equal to τ_Q. Sometimes instead of τ_0 it is more convenient to use the Ginzburg–Landau relaxation time $\tau_{GL}=(\pi\hbar/8k_B)(T_c-T)^{-1}$, which differs from τ_0 in the ''dirty'' limit only by a numerical coefficient: $\tau_{GL}=5.79\tau_0$ (Ref. 11).

In expressions (1) the conductance G and the nonequilibrium capacitance C depend primarily on the penetration depth of a weak longitudinal electric field into the superconductor, $l_E=\sqrt{D\tau_Q}$, where $D=l_{\text{eff}}V_F/3$ is the diffusion coefficient of normal quasiparticles with a mean free path l_{eff}. In other words, these parameters depend on the effective relaxation time of the charge imbalance. According to the theory of Ref. 12, which takes into account all the relaxation processes in a nonequilibrium superconductor, the effective relaxation time of the charge imbalance is determined by the time τ_ε for the inelastic scattering of electrons on phonons, the time τ_S for scattering on magnetic impurities with a spin flip, the elastic scattering time in the presence of supercurrent, which depends on the momentum p_S of the Cooper pairs, and the time for elastic scattering on anisotropies of the gap,

$$\tau_Q=\frac{4k_BT}{\pi\Delta}\left(\frac{\tau_\varepsilon}{2\Gamma}\right), \tag{2}$$

where $\Gamma=1/\tau_S+1/2\tau_\varepsilon+D/2\,(p_S^2/\hbar^2-(1/\Delta)\,\partial^2\Delta/\partial\mathbf{r}^2)$, with $\mathbf{r}$ the radius vector. The films under study contained no magnetic impurities. In addition, the contribution of the anisotropy of the gap to the relaxation of the imbalance of quasiparticle excitations can be neglected, since changes in $\Delta(T)$ occur over distances of the order of $\xi(T)$, which is much less than $l_E(T)$. Then the most important electron-scattering mechanisms remaining are inelastic scattering with a relaxation time τ_ε and elastic scattering of quasiparticles under conditions such that a supercurrent close to the critical value is flowing through the sample. The contribution of each of these mechanisms to the scattering of quasiparticles depends on the temperature. The contributions of the two mechanisms are equal, i.e., a sort of crossover occurs, under the condition $\tau_\varepsilon=3\tau_{GL}$ (Ref. 13). In the neighborhood of this ''crossover'' temperature one cannot neglect the contribution of either of the relaxation times, since τ_Q will be determined by both processes. In tin films the crossover occurs at $t_{\text{cross}}=T/T_c=0.992$,[3] and experiments on the study of PSCs are usually done in the temperature interval $0.950<T/T_c<0.999$. Thus in this temperature interval a transition occurs from relaxation governed mainly by an elastic mechanism ($\tau_\varepsilon \gg \tau_{GL}$) to the case of predominantly inelastic relaxation ($\tau_\varepsilon \ll \tau_{GL}$).

In Ref. 3 a study was made of how the resistive properties of superconducting channels are influenced by the various mechanisms for relaxation of a quasiparticle charge imbalance. Let us consider the influence of external perturbations and the relaxation mechanisms on the resonance properties of PSCs. At a temperature $T<T_c$ the parameters of the superconductor can depend on the value of the electric current flowing through the film (or, in other words, on the velocity of the condensate), the magnetic field H, and the power P of the electromagnetic field. If these perturbations are small and have only a weak effect on the density n_S of Cooper pairs, then this regime for the superconductor will be linear. If the density n_S of Cooper pairs in the sample is considerably different in the presence and absence of the perturbing influences, then the sample will be in the nonlinear regime. Let us take into account the influence of the perturbations on n_S. For this we use the following relations: $n_S(\nu_S)/n \propto (\Delta/\Delta_0)^2$ (Ref. 14), $(\Delta/\Delta_0)^2 \propto (1-h^2)$ (Ref. 15), $(\Delta/\Delta_0)^3 \propto (1-p^{0.5})$ (Ref. 16), where Δ_0 is the equilibrium value of the energy gap at some temperature T, ν_S is the velocity of the condensate at a temperature T near T_c, $t=T/T_c$, $h=H/H_c$, and $p=P/P_c$. Then $(n_S(h)/n) \propto (1-h^2)$ and $(n_S(p)/n) \propto (1-p^{0.5})^{2/3}$. We also use the equation of the depairing curve:[17]

$$j=2e\psi_0^2\left(\frac{\hbar}{m\xi(T)}\right)f^2(1-f^2)^{1/2}, \tag{3}$$

where ψ_0 is the unperturbed value of the electron wave function and $f=|\psi|/\psi_0$. Since for $T<T_c$ the density of Cooper pairs $n_S(\nu_S)=|\psi|^2$, $n_{S0}=\psi_0^2$ (n_{S0} is the density of the con-

densate in the absence of current at the given temperature),[18] Eq. (3) can be reduced to the more convenient form

$$\frac{n_S^3(\nu_S)}{n_{S0}^3}-\frac{n_S^2(\nu_S)}{n_{S0}^2}+\frac{4}{27}\frac{j_S^2(\nu_S)}{j_c^2}=0. \tag{4}$$

This equation has three real roots. Choosing the physically meaningful root and taking into account the functional dependence of n_S on the magnetic field[15] and the rf power,[16] we obtain an expression for $n_S(j,h,p)$:

$$\frac{n_S}{n_{S0}}=\frac{n_S(j,h,p)}{n_{S0}}=\frac{1}{3}\left\{1+2\cos\left[\frac{1}{3}\arccos\left(1-2\frac{j_S^2}{j_c^2}\right)\right]\right\}$$
$$\times(1-h^2)(1-p^{0.5})^{2/3}. \tag{5}$$

This equation is conveniently used for analyzing the experimental results in a study of the properties of superconducting films in the nonequilibrium state.

Near T_c, when our expression (5) for the density of Cooper pairs and temperature dependence of the energy gap $\Delta(T)=3.2k_BT_c(1-t)^{1/2}$ obtained in Ref. 17 are taken into account, expression (2) for the effective relaxation time of a charge imbalance in the nonlinear regime can be written as

$$\tau_Q=\tau_Q(j,t,h,p)=\frac{4k_BT}{\pi\Delta}\left(\frac{\tau_\varepsilon}{2\Gamma}\right)$$
$$=\frac{1.25\tau_\varepsilon}{\pi[(1-t)(n_S/n_{S0})]^{1/2}}\left(\frac{3\tau_{GL}}{\tau_\varepsilon+3\tau_{GL}}\right)^{1/2}. \tag{6}$$

Figure 2 shows the relaxation time τ_Q calculated according to formula (6) for one of the samples at a temperature equal to the crossover temperature $t_{\rm cross}=0.992$, plotted as a function of the time-averaged supercurrent density $\overline{j_S}$ (normalized to j_c) in the absence of external fields (curve *2*) and at several values of the electromagnetic power p and magnetic field h (curves *3–6*). We see that taking the elastic scattering into account leads to a decrease in the relaxation time τ_Q in comparison with the values calculated without taking the influence of the supercurrent on the relaxation into account (straight line *1*). The action of the fields on the sample leads to an increase in the relaxation time with increasing electromagnetic and magnetic fields.

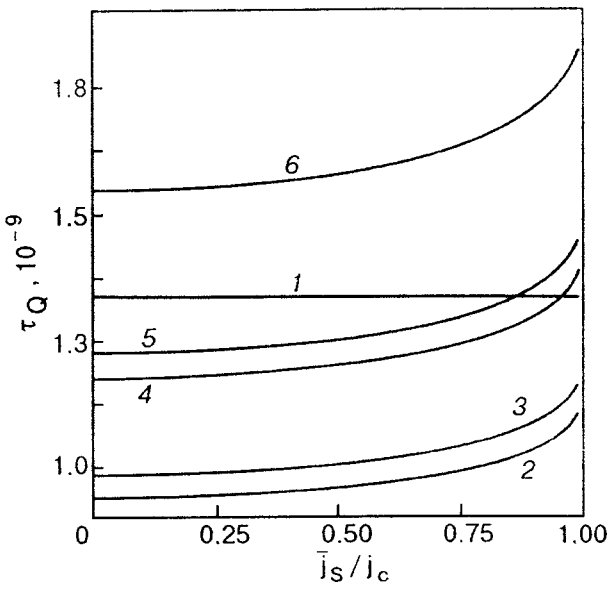

FIG. 2. Dependence of the relaxation time τ_Q on the time-averaged supercurrent density $\overline{j_S}$ normalized to j_c; the curves were calculated according to formula (6) for different values of the electromagnetic power p and magnetic field h: *1*—relaxation time τ_Q calculated without taking the influence of the supercurrent on the relaxation into account; *2*—$p=0$, $h=0$; *3*—$p=0$, $h=0.3$; *4*—$p=0.3$, $h=0$; *5*—$p=0$, $h=0.6$; *6*—$p=0.6$, $h=0$. The temperature $T/T_c=0.992$.

2.2. Influence of the relaxation mechanisms on the frequency of the non-Josephson oscillation

A theoretical model explaining the NJO effect has been proposed in Refs. 4, 6, and 7, according to which the governing mechanism leading to the NJO is relaxation of the nonequilibrium distribution of quasiparticles having an energy $\varepsilon_1>\Delta$ acquired as a result of multiple Andreev reflection within a region $2d_N(T)$. These quasiparticles are efficiently scattered by weak oscillations of the order parameter $|\tilde{\Delta}|\sim\Delta\gamma^{2/3}$ at the boundaries of the $2d_N(T)$ region if $\varepsilon_1-\Delta\sim|\tilde{\Delta}|$. Here $\gamma=\hbar/2\tau_\varepsilon\Delta$ is the depairing factor, and Δ is the energy gap at temperature T and depends on the value of the supercurrent flowing through the sample. Upon relaxation the quasiparticles go from an energy level ε_1 to the level of the energy gap Δ. Relaxation is accompanied by the transfer of momentum from the quasiparticle to the condensate of Cooper pairs by the radiation of a bremsstrahlung photon with energy $\hbar\omega_0=(\varepsilon_1-\Delta)$, since at low values of the energy to be lost the inelastic quasiparticle scattering processes involving phonon emission are unimportant. Quasiparticles with energy $\varepsilon_1-\Delta\gg|\tilde{\Delta}|$ do not transfer momentum to the condensate, and bremsstrahlung emission is impossible for them on account of the energy and momentum conservation laws.

Thus the NJO effect is observed in a PSC under the conditions $\hbar\omega_0=\varepsilon_1-\Delta$ and $\hbar\omega_0\cong\alpha\Delta\gamma^{3/2}$, where α is a factor of the order of unity. In this case the NJO signal generated by the sample can be written

$$\hbar\omega_0=\varepsilon_1\frac{\alpha\gamma^{3/2}}{1+\alpha\gamma^{3/2}}. \tag{7}$$

The energy ε_1 of the quasilevel is determined by the parameters of the superconductor and the size $2d_N$ of the quasinormal region:[4]

$$\varepsilon_1=\frac{\pi\hbar V_F}{2(2d_N)}. \tag{8}$$

The values of ε_1 and γ depend on the value of the electric current, temperature, and the presence of magnetic and electromagnetic fields, i.e., $\varepsilon_1=\varepsilon_1(j,t,h,p)$ and $\gamma_1=\gamma_1(j,t,h,p)$. Taking this into account, we can express the NJO frequency ω_0 in terms of the characteristics of the superconductor as

$$\omega_0=\omega(j,t,h,p)=\pi A\left[\frac{\alpha\gamma^{3/2}}{1+\alpha\gamma^{3/2}}\right]\left[\frac{3\tau_{GL}+\tau_\varepsilon}{3\tau_{GL}}\right]^{1/8}\left(\frac{n_S}{n_{S0}}\right)^{1/8}. \tag{9}$$

Here

$$A=\left(\frac{V_F^{3/2}(1+0.76\xi_0/l_{\rm eff})^{1/2}(1-t)^{3/4}}{4.313(l_{\rm eff}\tau_\varepsilon)^{1/2}\xi_0}\right)^{1/2}$$

is a coefficient that depends on the parameters of the superconductor, and the ratio n_S/n_{S0} is given by Eq. (5).

It is of interest to compare the NJO frequency ω_0 for tin and aluminum films. On tin films of various thicknesses the NJO is observed, as a rule, at frequencies of the order of tens of megahertz in an interval of reduced temperatures $0.970 \leqslant T/T_c \leqslant 0.997$. For them both the inelastic and elastic relaxation mechanisms are operative. For the aluminum samples the NJO signal is observed at frequencies of the order of a few megahertz in approximately the same temperature interval[19] as for the tin films. However, for them the influence of the supercurrent is expected to come into play at $t_{\rm cross}\approx 0.9995$.

Let us consider how the NJO frequency is influenced by each of the quantities appearing in formula (9). The factor A reflects the dependence of the NJO frequency on the geometric dimensions of the sample, since the mean free path $l_{\rm eff}$ is determined by the film thickness d. An estimate of the factor A for tin and aluminum films shows that its value does not depend very strongly on $l_{\rm eff}$. For example, at $t=t_{\rm cross}$ for sample No. 1 ($l_{\rm eff}\cong 94$ nm) the factor $A=6.2\times 10^{10}{\rm s}^{-1}$, while for sample No. 5 ($l_{\rm eff}\cong 479$ nm) $A=3.71\times 10^{10}{\rm s}^{-1}$. For aluminum films the factor A is of the same order of magnitude ($\sim 10^{10}$ s^{-1}). The ratio of these factors for the two metals remains of the order of unity at all temperatures in the existence region of the NJO, even though $l_{\rm eff}$ in the Al and Sn films differs by an order of magnitude. Thus, it turns out that $l_{\rm eff}$ is not the parameter that governs the frequency range of the NJO signal. The ratio of the factors containing the depairing factor γ for the tin and aluminum films turns out to be of the order of several tens. An estimate of the value of the third cofactor in (9), which reflects the relation of the NJO frequency to the relaxation times τ_ε and τ_{GL}, shows that they are also close in magnitude for the two metals: their ratio varies from 0.741 at $T/T_c=0.970$ to 0.83 at $T/T_c=0.997$. This factor contains the temperature dependence of the NJO frequency: the ratio between τ_ε and τ_{GL} is determined by the temperature of the sample. According to calculations using the parameters of the real tin and aluminum samples, the NJO frequencies for the tin films are of the order of tens of megahertz, while for the aluminum films they are of the order of a few megahertz, in complete correspondence with the experimental data. Thus it is established that it is the second term that describes the experimentally observed factor-of-tens difference between the NJO frequencies in tin and aluminum films. We recall that the depairing factor γ that enters into this cofactor is equal to the ratio $\hbar/2\tau_\varepsilon\Delta$. Since the values of the energy gap near T_c are very small in both tin and aluminum, the difference of γ for Al and Sn superconductors is due to the different inelastic relaxation times τ_ε in these materials. These times in tin and aluminum differ by two orders of magnitude. Our analysis shows that the inelastic electron–phonon relaxation of the quasiparticle charge imbalance plays an important role in the NJO effect. The inelastic electron–phonon relaxation time τ_ε determines the value of the nonstationary perturbation of the order parameter, $\tilde{\Delta}\propto\Delta\gamma^{3/2}$, on which the quasiparticles involved in the NJO effect are scattered with a transfer of momentum to the condensate.

One can estimate the NJO frequency in superconducting films with a shorter time τ_ε than in tin, e.g., in films of lead and the high-T_c superconductor YBCO. The NJO frequency for lead films ($T_c=7.2$ K, $V_F=4.3\times 10^7$cm/s, $\xi_0=82.2$ nm, $l_{\rm eff}=700$ nm, $\tau_\varepsilon=0.2\times 10^{-10}$ s) is of the order of a few hundred megahertz. For YBCO films ($T_c=90$ K, $V_F=1.7\times 10^7$ cm/s, $\xi_0=1.8$ nm, $l_{\rm eff}=7$ nm, $\tau_\varepsilon=5.58\times 10^{-14}$ s) we obtain a NJO frequency of the order of a few hundred gigahertz.

Let us consider the influence of the value of the supercurrent flowing through the PSC on the NJO frequency. According to the microscopic theory of the current-induced resistive state,[5] in a quasinormal region of the PSC of size $2d_N(T)$ the supercurrent oscillates at the Josephson frequency ω_J (from zero to j_c). The linear parts of the I–V characteristic, which are multiples of the dynamic resistance of the PSC and are continued to the intercept with the current axis, determine the so-called cutoff current. The value of the cutoff current on the I–V characteristic at zero voltage is, in the zeroth approximation, equal to the time-averaged supercurrent flowing in the nonequilibrium region of the PSC. In real tin samples the time-averaged supercurrent density $\overline{j_S}$ can vary from $0.4j_c$ to $0.8j_c$. Figure 3 shows the curve calculated according to formula (9), which reflects the influence of the supercurrent on the NJO frequency. In the calculation the parameters of sample No. 4 were used, and the value of the coefficient α was taken equal to 0.7. As we see from Fig. 3, the value of the averaged supercurrent flowing through the nonequilibrium region of the PSC does not have a substantial effect on the NJO frequency. The calculated values of the NJO frequency are in good agreement with the experimental data obtained for this sample. As the temperature of the sample is lowered, the calculated values of the NJO frequency decrease (see the inset in Fig. 3). Analogous behavior is also characteristic for the real amplitude–frequency characteristics of the NJO signal: as the temperature is lowered, the $A_0(f)$ curves for all the samples gradually shift to ever lower frequencies (see Fig. 1).

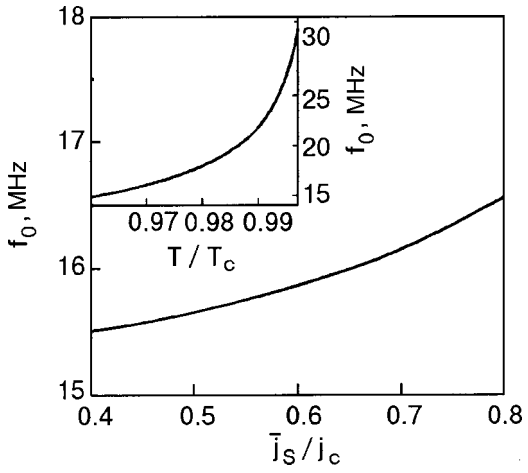

FIG. 3. Dependence of the NJO frequency $f_0=\omega_0/2\pi$ on the time-averaged supercurrent density $\overline{j_S}$ normalized to j_c. The temperature $T/T_c=0.970$. The inset shows the dependence of the NJO frequency f_0 on the reduced temperature T/T_c.

Thus it has been shown that the NJO frequency in superconducting films depends strongly on the inelastic electron–phonon relaxation time τ_ε of the quasiparticle charge imbalance. A change in the fraction of the time-averaged supercurrent $\overline{j_S}$ flowing through the PSC will lead to a change in the NJO frequency of only a few percent.

2.3. Influence of the relaxation mechanisms on the resonance frequency of a PSC

As we said in the Introduction, the NJO is governed by processes occurring in a quasinormal region of size $2d_N(T)$, while the resonance of the plasma oscillations is governed by the processes and characteristics of a region of size $2l_E(T)$.[8] One can regard a part of the PSC of size $2d_N(T)$ as a sort of self-excited oscillator, generating oscillations of the electromagnetic field with frequency ω_0, and the remaining part of the PSC as an external circuit with a resonance frequency ω_r.[8] When the values of ω_0 and ω_r are close enough, the action of this electromagnetic field in a region $2l_E(T)$ excites low-frequency oscillations (with frequency ω_0) of the density of Cooper pairs.

In Ref. 8 the conditions for resonance of the low-frequency plasma oscillations of the condensate were determined from an analysis of an equivalent electrical circuit for the PSC:

$$\omega_{r1}^2=\frac{1}{L_kC},\quad \omega_{r2}^2=\frac{2}{L_kC}\left(1-\frac{(1+RG)^2C}{2L_kG^2}\right). \tag{10}$$

After using the relations $C=G\tau_\varepsilon$ and $L_k=R\tau_0$ from Ref. 11, we obtained the resonance frequency of the PSC in the form

$$\omega_{r1}^2=\frac{1}{4\tau_\varepsilon\tau_0},\quad \omega_{r2}^2=\frac{1}{2\tau_\varepsilon\tau_0}\left(1-\frac{25\tau_\varepsilon}{8\tau_0}\right). \tag{11}$$

At fixed values of the current and temperature, ω_r will differ from the value calculated according to Eq. (11) only for film that are short compared to $l_E(T)$. If the length L of the film is less than $2l_E(T)$, then a part of the nonequilibrium region penetrates from the narrow channel into its ''banks.''

Thus, according to Eq. (11), the resonance frequency of a PSC is determined by the inelastic relaxation time τ_ε and the response time τ_0 of the supercurrent to an external perturbation. The time τ_0 in the dirty limit was determined in Ref. 11:

$$\tau_0(T)=\frac{2k_BT_c\hbar}{\pi\Delta^2(T)}. \tag{12}$$

In formulas (11) only τ_0 depends on the temperature and current. Therefore, its variation upon changes in these parameters will also determine the behavior of the resonance frequency of the PSC. When this dependence is taken into account, the expression for τ_0 becomes

$$\tau_0\cong\frac{0.2\hbar}{\pi k_BT_c(1-T/T_c)(n_S/n_{S0})}\approx\frac{5\times10^{-13}}{(T_c-T)(n_S/n_{S0})}\frac{[S]\cdot[K]}{[K]}. \tag{13}$$

At temperatures near the crossover point ($T/T_c=0.992$) the time τ_0 comes out to be of the order of 10^{-11} s. However, even for $T/T_c=0.999$ the time τ_0 becomes of the order of 10^{-10} s (we note that at this temperature the NJO is observed experimentally for tin and aluminum samples). This value of τ_0, taken together with the standard value of τ_ε in (11), gives a value of the order of 10^7–10^8 Hz for the resonance frequency of the nonequilibrium region. This agrees with the experimentally observed values of the NJO signal frequency.

Thus at certain temperatures of the sample the values of the frequency ω_0 of the NJO field and the resonance frequency ω_r of the PSC turn out to be quite close. As a result, the electromagnetic field of the NJO excites low-frequency plasma oscillations of the density of Cooper pairs at the NJO frequency ω_0 in a nonequilibrium region of size $2l_E(T)$ in the PSC.

2.4. Influence of the sample thickness on the amplitude–frequency characteristics of the NJO signal

We see from expression (11) that the resonance frequency ω_r is independent of the value of the transverse cross section s of the film. To a first approximation this is due to the fact that the nonequilibrium capacitance C, according to (1), is directly proportional to the transverse cross section of the sample, while the kinetic inductance L_k is inversely proportional to it. Therefore, decreasing s leads to a simultaneous decrease of the capacitance and increase of the inductance, leaving the resonance frequency $\omega_r=(1/(LC)^{1/2})$, unchanged. This can explain why the resonance is always observed in approximately the same frequency range for tin samples of different cross sections. It follows from the A–F characteristic shown in Fig. 1 that the resonance frequency of the nonequilibrium region is $\omega_r\approx10^7$ Hz for all the samples, and only the shape of the A–F characteristic changes with the thickness of the film: the thicker the sample, the closer the form of the A–F characteristic to the resonance curve of a low-Q oscillator circuit.

As we have said, in samples containing PSCs in the NJO regime there exist two coupled resonance systems: a quasinormal layer of size $2d_N(T)$ with the electromagnetic field of the NJO at frequency ω_0, and a region of size $2l_E(T)$ with a resonance frequency ω_r and plasma oscillations at the frequency ω_0. The frequencies ω_0 and ω_r depend on temperature and on the value of the transport current. The rate and direction of the relative tuning of ω_0 and ω_r upon changes in these parameters determine the shape of the amplitude–frequency characteristic of the experimentally observed NJO signal. It is convenient to represent these processes with the aid of an analogy with the passage of a signal from a sweep generator (with a signal frequency varying periodically in time) through a parametric oscillatory circuit. The response signal of the circuit will depend on the sweep rate and on the range of variation of the resonance frequency of the circuit under study. For example, at a fixed resonance frequency of the circuit and complete overlap of the passband of the circuit and sweep range, the A–F characteristic of the circuit will have the standard bell-shaped form. If the sweep does not overlap the entire passband of the circuit or if the resonance frequency of the circuit changes simultaneously with the sweep and at close to the sweep rate, then one will observe only fragments of the resonance curve of the circuit or an A–F characteristic of complex shape.

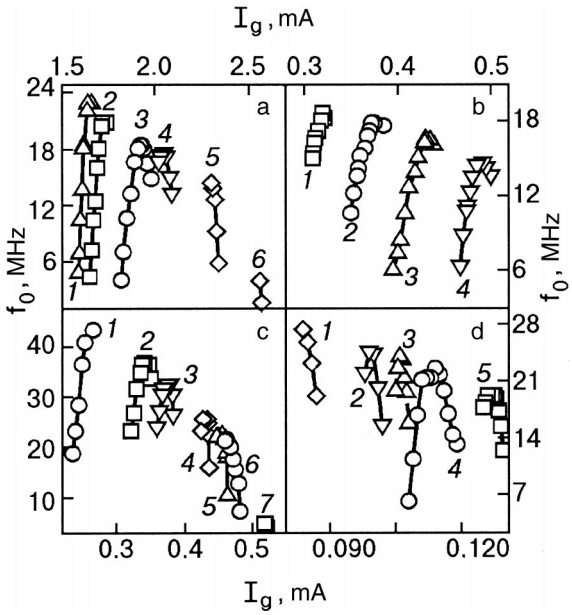

FIG. 4. Dependence of the NJO frequency f_0 on the generation current I_g for samples of different thicknesses d: 700 nm (sample No. 5) (a); 300 nm (sample No. 4) (b); 170 nm (sample No. 3) (c); 58 nm (sample No. 1) (d) at various temperatures near T_c. The temperature of the measurements decreases with increasing number of the curve.

Our experiments have shown that in thick samples, in which the mean free path l_{eff} is comparatively large, the resonance frequency ω_r of the circuit remains practically unchanged under variation of the current, and only the NJO frequency ω_0 undergoes tuning. Therefore the family of amplitude–frequency characteristics measured at various temperatures on samples about 1 μm thick (Fig. 1a) has an arrangement such that the maxima of the curves are found at approximately the same frequency. Curves *1*, *2*, and *3* are taken at temperatures for which the frequency range of the NJO completely overlaps the passband of the nonequilibrium region $2l_E(T)$. Plasma oscillations of the condensate are excited under the influence of the NJO field in the entire range, and therefore the shape of the amplitude–frequency curves is close to conventional. The remaining curves (*4,5,6*) are only fragments of the resonance curve of the nonequilibrium region $2l_E(T)$. Similar A–F characteristics are also shown in Fig. 1b. As the thickness of the samples decreases, the resonance frequency ω_r and the NJO frequency ω_0 become stronger functions of current. This confirms the frequency–current characteristics of the NJO signal for samples of different thicknesses (Fig. 4). We see that in the thinner samples, with a smaller electron mean free path, the maximum change in frequency occurs in a smaller interval of currents than in the case of samples with larger l_{eff}. As a result, A–F characteristics of complex shape are formed, including some loop-shaped (Fig. 1c, 1d). If the rate of retuning of the NJO frequency ω_0 with changing current is higher than that of the resonance frequency ω_r, then the A–F characteristics will have a shape closer to that of an ordinary resonance circuit, and as the rate of tuning of the frequency ω_0 increases, the A–F characteristic becomes a loop-shaped curve. In the limiting case when the two rates are the same, the curve goes over to a straight line. This accounts for the experimentally observed transition from A–F characteristics having the shape of ordinary resonance curves for a low-Q circuit for samples around 1 μm thick to a shape corresponding to a resonance circuit with inductance and capacitance that depend on the electric current for samples several hundred microns thick.

Thus studies of the rf characteristics of superconducting films containing phase-slip centers in the non-Josephson oscillation regime have shown that they are mainly determined by their dynamic properties that depend on the relaxation time in the nonequilibrium region, on the density of Cooper pairs, and on the electron mean free path.

CONCLUSION

In this study we have established experimentally that elastic and inelastic scattering processes leading to a decrease in the effective relaxation time of a charge imbalance to the equilibrium state play an important role in phase-slip centers. We have confirmed that an important role in the mechanism of excitation of non-Josephson oscillations is played by inelastic electron–phonon relaxation of the charge imbalance. The inelastic electron–phonon relaxation time τ_ε determines the frequency range in which the NJO effect exists. The time-averaged supercurrent flowing in the nonequilibrium regions of the PSCs has a small effect on the frequency of the NJO signal. It is shown that in samples containing PSCs found in the NJO regime there exist two intercoupled resonance systems. The first, of size $2d_N(T)$, governs the mechanism of excitation of the NJO. The second, which is a nonequilibrium region of size $2l_E(T)$ in the PSC, acts as a load circuit for the first system and is the region of excitation and existence of a low-frequency collective plasma mode. The resonance frequency calculated on the basis of a nonequilibrium superconductor model of this region coincides with the frequency of the NJO signal observed in experiment.

The dependence of the shape of the amplitude–frequency characteristics on the thickness of the samples is explained by the different influence of the transport electric current on the relative tuning rate of the frequency ω_0 of the NJO field and the resonance frequency ω_r of the nonequilibrium region $2l_E(T)$ of the PSC.

[a)]E-mail: dmitriev@ilt.kharkov.ua

[1] W. J. Skocpol, M. R. Beasley, and M. Tinkham, J. Low Temp. Phys. **16**, 145 (1974).
[2] V. P. Galaĭko, V. M. Dmitriev, and G. E. Churilov, Fiz. Nizk. Temp. **3**, 1010 (1977) [Sov. J. Low Temp. Phys. **3**, 491 (1977)].
[3] G. E. Churilov, A. B. Agafonov, D. A. Dikin, and V. M. Dmitriev, Fiz. Nizk. Temp. **24**, 737 (1998) [Low Temp. Phys. **24**, 555 (1998)].
[4] G. A. Gogadze, Fiz. Nizk. Temp. **12**, 1102 (1986) [Sov. J. Low Temp. Phys. **12**, 622 (1986)].
[5] B. I. Ivlev and N. B. Kopnin, Usp. Fiz. Nauk **142**, 435 (1984) [Sov. Phys. Usp. **27**, 206 (1984)].
[6] G. A. Gogadze, V. M. Dmitriev, V. N. Svetlov, and G. E. Churilov, *Abstracts of the Twenty-Fourth All-Union Conference on Low Temperature Physics* [in Russian], Tbilisi (1986), Part 1, p. 196.
[7] G. A. Gogadze, Fiz. Nizk. Temp. **14**, 196 (1988) [Sov. J. Low Temp. Phys. **14**, 108 (1988)].
[8] G. E. Churilov, D. A. Dikin, A. B. Agafonov, V. M. Dmitriev, U. Zimmermann, and K. Keck, Fiz. Nizk. Temp. **20**, 879 (1994) [Low Temp. Phys. **20**, 689 (1994)].
[9] J. Mooij and G. Schon, Phys. Rev. Lett. **55**, 114 (1985).

[10] G. E. Churilov, V. M. Dmitriev, A. P. Beskorsyĭ, and V. N. Svetlov, Radiotekh. Elektron. (Moscow) **55**, 1759 (1975).
[11] A. M. Kadin, L. N. Smith, and W. J. Skocpol, J. Low Temp. Phys. **38**, 497 (1980).
[12] A. Schmid, in *Proceedings NATO Advanced Study Institute on Nonequilibrium Superconductivity, Phonons and Kapitza Boundaries*, edited by K. E. Gray, Plenum Press, New York (1981).
[13] M. Stuivinga, J. E. Mooij, and T. M. Klapwijk, J. Low Temp. Phys. **46**, 555 (1982).
[14] J. Bardeen, Rev. Mod. Phys. **34**, 667 (1962).
[15] D. H. Douglas, Jr., IBM J. Res. Dev. **6**, 44 (1962).
[16] G. E. Churilov, D. A. Dikin, and V. M. Dmitriev, Fiz. Nizk. Temp. **19**, 1191 (1993) [Low Temp. Phys. **19**, 846 (1993)].
[17] P. G. de Gennes, *Superconductivity of Metals and Alloys*, Benjamin, New York (1966); Mir, Moscow (1968).
[18] V. L. Ginzburg and L. D. Landau, Zh. Éksp. Teor. Fiz. **20**, 1064 (1950).
[19] D. A. Dikin, G. E. Churilov, V. N. Svetlov, and V. M. Dmitriev, Fiz. Nizk. Temp. **14**, 204 (1988) [Sov. J. Low Temp. Phys. **14**, 113 (1988)].

Translated by Steve Torstveit

LOW-TEMPERATURE MAGNETISM

Phase states and spectra of coupled magnetoelastic waves in a ferromagnet with inclined anisotropy

L. Ya. Arifov, Yu. A. Fridman, V. I. Butrim, and O. A. Kosmachev

*V. I. Vernadskiĭ Tavricheskiĭ National University, ul. Yaltinskaya 4, 95007 Simferopol, Ukraine**

(Submitted January 3, 2001; revised April 24, 2001)
Fiz. Nizk. Temp. **27**, 860–864 (August 2001)

The spectra of coupled magnetoelastic waves in a ferromagnet with an inclined easy axis are determined. Analysis of the spectra obtained shows that such a system can have one more phase in addition to the ferromagnetic and canted phases. This phase can be interpreted as inhomogeneous. The region of fields and magnetoelastic coupling parameters in which this phase can be realized is determined. © *2001 American Institute of Physics.*
[DOI: 10.1063/1.1399201]

1. INTRODUCTION

It is well known that in the microscopic description of magnetically ordered insulators the spin Hamiltonian contains terms of the form $S_n^i \beta_{ij} S_n^j$ corresponding to the one-ion anisotropy (OA) due to the spin–orbit interaction (S_n^i is the ith component of the spin operator at site n).[1] Analogous terms for the magnetic dipole energy can be singled out, but in real crystals their contribution is always much smaller than that of the OA.

It is interesting to consider the case when the only nonzero components are $\beta_{zz}=\beta_1$ and $\beta_{xz}=\beta_{zx}=\beta_2$. Such a model describes the inclined anisotropy in the $X0Z$ plane containing the axis of easy magnetization (the ''easy axis''), which is oriented at an angle φ_0 to the $0Z$ axis. This model is of interest because it gives a completely adequate description of the anisotropy energy of disoriented films of iron garnets. For example, it was shown in Ref. 2 that in the framework of the two-parameter model[3] an inclined orientation of the easy axis is realized in (111) disoriented films. Here the easy axis lies in the same plane as the angle of disorientation. In Ref. 2 this plane was $(\bar{1}10)$. The magnetization reversal of (112) films [a particular case of a disoriented (111) film] was studied in Ref. 4. It was shown in that paper that if the external magnetic field is applied in the plane $(\bar{1}10)$, then the magnetization vector will also lie in that plane. Thus, if coordinates X and Z are introduced in the $(\bar{1}10)$ plane, it can be shown that the anisotropy energy (see Ref. 4) will be described by two constants: β_1 and β_2.

Theoretical studies of magnetically ordered systems with inclined anisotropy have up till now been limited to a phenomenological description of homogeneous phases and their existence conditions. It is therefore of interest to study the spectra of elementary excitations in such systems and of possible phase transitions in them. In addition to the magnetic subsystem we shall also take into account the elastic subsystem, i.e., the magnetoelastic (ME) interaction. This is primarily for the reason that taking the ME coupling into account gives rise to hybridized elementary excitations—coupled ME waves—in the system and also has a substantial influence on the dynamics of the system in the neighborhood of phase transitions.[5]

2. DISPERSION RELATION AND POLARIZATION STATES OF THE SYSTEM

The Hamiltonian of the system can be written as

$$\mathcal{H}=-\frac{1}{2}\sum_{n,n'} J(n-n')\mathbf{S}_n\cdot\mathbf{S}_{n'}-\beta_1\sum_n (S_n^z)^2 + 2\beta_2\sum_n (S_n^z S_n^x+S_n^x S_n^z)-H\sum_n S_n^z + \nu\sum_{n,i,j} S_n^i S_n^j u_{ij}(n)+\int dr\left\{\frac{\lambda+\eta}{2}\sum_i u_{ii}^2+\eta\sum_{i\neq j} u_{ij}^2 + \lambda\sum_{i\neq j} u_{ii}u_{jj}\right\}. \quad (1)$$

Here $J(n-n')>0$ is the exchange integral, $\beta_1<0$, $\beta_2>0$ are the OA constants, H is the external magnetic field expressed in energy units, ν is the ME coupling constant, $u_{ij}(n)=1/2[(\partial u_i/\partial x_j)+(\partial u_j/\partial x_i)]$ is the symmetric part of the components of the strain tensor, and λ and η are elastic moduli.

The first three terms in Hamiltonian (1) describe the magnetic subsystem. The OA energy operator is chosen such that for $H=0$ the equilibrium magnetization direction lies out of the ''easy plane'' at a small angle $\varphi_0 \ll 1$ determined by the relation $\tan 2\varphi_0=-4\beta_2/\beta_1$. Here it is assumed that $|\beta_1|>\beta_2$ and $\beta_i \ll J_0$, where J_0 is the zeroth Fourier component of the exchange interaction. A phenomenological analysis shows that in this case the equilibrium magnetic moment lies in the $Z0X$ plane. Because of this behavior of the equilibrium magnetic moment, this system can be called a ferromagnet with an inclined easy axis.

Let us investigate the spectra of coupled ME waves of the system described by Hamiltonian (1). For this we must take into account the influence of the OA and ME interac-

tion. This can be done most accurately by using the Hubbard operator technique.[6] The Hubbard operators are constructed on the basis of eigenfunctions of the one-site Hamiltonian of the system and describe the transition of a magnetic ion from a state with magnetic quantum number M to a state with magnetic quantum number M'. The Hubbard operator technique is applicable for systems with $S \geqslant 1$, and to simplify the calculations we shall henceforth assume that $S=1$. We shall also assume that the magnetic field is high enough that the magnetization vector is directed along the field.

Separating out the mean field in the exchange part of (1), we obtain the one-site Hamiltonian of the system:

$$\mathcal{H}_0(n) = -\overline{H}S^z - \beta_1(S^2)^2 + 2\beta_2(S^zS^x + S^xS^z) + vS^iS^ju_{ij}, \tag{2}$$

where $\overline{H} = H + J_0\langle S^z\rangle$.

Solving the one-ion problem with Hamiltonian (2), we determine the energy levels of the magnetic ion:

$$E_1 = -\beta_1 - \chi + \frac{v}{2}(u_{xx}^{(0)} + u_{yy}^{(0)} + 2u_{zz}^{(0)}) - 2\left(\beta_2 + \frac{v}{2}u_{xz}^{(0)}\right)^2 \times \frac{\chi + (v/2)(u_{xx}^{(0)} - u_{yy}^{(0)})}{\chi[\chi + \beta_1 + (v/2)(u_{xx}^{(0)} + u_{yy}^{(0)} - 2u_{zz}^{(0)})]},$$

$$E_0 = v(u_{xx}^{(0)} + u_{yy}^{(0)}) + 4\left(\beta_2 + \frac{v}{2}u_{xz}^{(0)}\right)^2 \times \frac{\beta_1 + v(u_{yy}^{(0)} - u_{zz}^{(0)})}{[\beta_1 + v(u_{yy}^{(0)} - u_{zz}^{(0)})][\beta_1 + v(u_{xx}^{(0)} - u_{zz}^{(0)})] - \overline{H}^2}, \tag{3}$$

$$E_{-1} = -\beta_1 + \chi + \frac{v}{2}(u_{xx}^{(0)} + u_{yy}^{(0)} + 2u_{zz}^{(0)}) + 2\left(\beta_2 + \frac{v}{2}u_{xz}^{(0)}\right)^2 \times \frac{\chi - (v/2)(u_{xx}^{(0)} - u_{yy}^{(0)})}{\chi[\chi - \beta_1 - (v/2)(u_{xx}^{(0)} + u_{yy}^{(0)} - 2u_{zz}^{(0)})]}$$

and the eigenfunctions of the operator (2):

$$\Psi(1) = (1-\zeta^2p^2)|1\rangle + \sqrt{2}\zeta p|0\rangle - \zeta^2f^2|-1\rangle,$$

$$\Psi(0) = \sqrt{2}\zeta p|1\rangle + [1-\zeta^2(p^2+\tilde{p}^2)]|0\rangle + \sqrt{2}\zeta\tilde{p}|-1\rangle,$$

$$\Psi(-1) = -\zeta^2\tilde{f}|1\rangle + \sqrt{2}\zeta\tilde{p}|0\rangle + (1-\zeta^2\tilde{p}^2)|-1\rangle. \tag{4}$$

In expressions (3) and (4) we have introduced the following notation: $\chi^2 = \overline{H}^2 + (\nu/4)(u_{xx}^{(0)} - u_{yy}^{(0)})^2$; $u_{ij}^{(0)}$ are the spontaneous strains;

$$\zeta^2 = \frac{\beta_2^2}{\overline{H}(\overline{H}^2 - \beta_1^2)}; \quad p^2 = \frac{\overline{H}(\overline{H}-\beta_1)}{\overline{H}+\beta_1};$$

$$\tilde{p}^2 = \frac{\overline{H}(\overline{H}+\beta_1)}{\overline{H}-\beta_1}; \quad f^2 = \overline{H}-\beta_1; \tilde{f}^2 = \overline{H}+\beta_1;$$

$|M\rangle$ are the eigenvectors of the operator S^z.

The spontaneous strains $u_{ij}^{(0)}$ are determined from the minimum free energy density and in the low-temperature case under consideration here ($T \ll T_c$) have the form

$$u_{xx}^{(0)} = u_{yy}^{(0)} = \frac{u_{zz}^{(0)}}{2} = -\frac{v}{2\eta}, \quad u_{zx}^{(0)} = \frac{v\beta_2}{\eta(\overline{H}+\beta_1)}, u_{yz}^{(0)} = u_{xy}^{(0)} = 0. \tag{5}$$

The eigenfunctions (4) of the one-site Hamiltonian (2) are used for constructing the Hubbard operators $X^{M'M} = |\Psi(M')\rangle\langle\Psi(M)|$, which are related to the spin operators by the expressions

$$S^+ = 2\zeta[pH^1 + (p+\tilde{p})(H^0 + X^{1-1}) + \tilde{p}H^{-1}] + \sqrt{2}\zeta^2[(2p^2-f^2)X^{01} + (2\tilde{p}^2 - \tilde{f}^2)X^{-10}] + \sqrt{2}[1-\zeta^2(p-\tilde{p})^2])(X^{10} + X^{0-1}),$$

$$S^- = (S^+)^+,$$

$$S^z = H^1 - H^{-1} - 2\zeta^2[p^2H^1 - (p^2-\tilde{p}^2)H^0 - \tilde{p}^2H^{-1}] + \zeta^2(f^2-\tilde{f}^2)(X^{1-1} + X^{-11}) + \sqrt{2}\zeta p(X^{10} + X^{01}) - \sqrt{2}\zeta\tilde{p}(X^{-10} + X^{0-1}). \tag{6}$$

In relations (6) $H^M \equiv X^{MM}$ are the diagonal Hubbard operators.

Let us write the components of the strain tensor in the form $u_{ij} = u_{ij}^{(0)} + u_{ij}^{(1)}$, where $u_{ij}^{(1)}$ is the dynamic part of the strain tensor, describing the vibrations of the magnetic ion about its equilibrium position. Quantizing the dynamic part $u_{ij}^{(1)}$ in the standard way,[7] we obtain the Hamiltonian of transformation of magnons into phonons and vice versa:

$$\mathcal{H}_{\rm tr} = \sum_n \left\{ \sum_M \mathcal{P}_M H_n^M + \sum_\alpha \mathcal{P}_\alpha X_n^\alpha \right\}.$$

Here $\mathcal{P}_{M(\alpha)} = 1/\sqrt{N}\,\Sigma_{k,\lambda}(b_{k,\lambda} + b_{-k,\lambda}^+)T_n^{M(\alpha)}(k,\lambda)$, where $b_{k,\lambda}^+$ ($b_{k,\lambda}$) are the creation (annihilation) operators of λ-polarized phonons, $T^{M(\alpha)}(k,\lambda)$ are the amplitudes of transformation of magnons into phonons and vice versa, N is the number of sites of the crystal lattice, and α are the root vectors determined by the Hubbard operator algebra.

The dispersion relation for coupled ME waves is constructed from an equation of the Larkin type for the total Green's function of the system.[8] This equation can be written in the form

$$\det|\delta_{ij} + x_{ij}| = 0, \tag{7}$$

where

$$x_{ij} = G_0^\alpha(\omega)b(\alpha)c_{ij}(\alpha) + B_0(k,\lambda,\lambda')G_0^\alpha(\omega)b(\alpha) \times T^{-\alpha}(k,\lambda)G_0^\beta(\omega)b(\beta)T^\beta(-k,\lambda')c_{ij}(\alpha,\beta);$$

$$B^0(k,\lambda,\lambda') = \frac{D_\lambda(k,\omega_n)}{1 - Q_{\lambda\lambda'}D_\lambda(k,\omega_n)};$$

$$Q_{\lambda\lambda'} = T^\alpha(-k,\lambda)G_0^\alpha(\omega_n)T^{-\alpha}(k,\lambda');$$

$$\mathbf{b}(\alpha) = \langle\alpha\cdot\mathbf{H}\rangle_0; \quad D_\lambda(k,\omega_n) = \frac{2\omega_\lambda(k)}{\omega_n^2 - \omega_\lambda^2(k)}$$

is the Green's function of a free λ-polarized phonon, $G_0^{\alpha}(\omega)=\{\omega+(\boldsymbol{\alpha}\cdot\mathbf{E})\}^{-1}$ is the zeroth Green's function, and $c_{ij}(\alpha,\beta)$ are interaction matrix elements whose explicit form is given in Ref. 9. Equation (7) is valid for arbitrary temperatures and arbitrary relationships among the values of the material constants.

Let us investigate the spectra of coupled ME waves of this system. We shall assume that the wave vector **k** is parallel to the $0Z$ axis. In this case the nonzero components of the polarization unit vector are e_{τ}^{x}, e_{t}^{y}, and e_{l}^{z}, and the nonzero transformation amplitudes can be written in the form

$$T^{10}(k,\tau)=T^{01}(k,\tau)=i\frac{v}{2\sqrt{2}}T^{0}(k,\tau)e_{\tau}^{x}k;$$

$$T^{10}(k,t)=-T^{01}(k,t)=\frac{v}{2\sqrt{2}}T^{0}(k,t)e_{t}^{y}k;$$

$$T^{0}(k,\lambda)=\frac{e^{i\mathbf{k}\cdot\mathbf{n}}}{\sqrt{2m\omega_{\lambda}(k)}}.$$

It follows from Eq. (7) that the magnetic subsystem actively interacts with t- and τ-polarized quasiphonons but does not interact with longitudinally polarized acoustic excitations. The spectrum of the t- and τ-polarized quasiphonons, respectively, have the forms

$$\omega_1^2(k)=\omega_{\tau}^2(k)\frac{E_{1-1}[E_{10}+J(k)+a_0]+2J(k)\zeta^2[E_{10}(p+\tilde{p})^2+E_{1-1}(2p^2-\tilde{p}^2+2p\tilde{p}-f^2)]}{E_{1-1}[E_{10}+J(k)]+2J(k)\zeta^2[E_{10}(p+\tilde{p})^2+E_{1-1}(2p^2-\tilde{p}^2+2p\tilde{p}-f^2)]},$$
$$\omega_2^2(k)=\omega_{t}^2(k)\frac{E_{1-1}[E_{10}+J(k)+a_0]+2J(k)\zeta^2[E_{10}(p+\tilde{p})^2-E_{1-1}(4p^2+\tilde{p}^2-2p\tilde{p}-f^2)]}{E_{1-1}[E_{10}+J(k)]+2J(k)\zeta^2[E_{10}(p+\tilde{p})^2-E_{1-1}(4p^2+\tilde{p}^2-2p\tilde{p}-f^2)]}, \tag{8}$$

and the spectrum of quasimagnons can be written

$$\varepsilon^2(k)=(E_{10}+J(k))\times\left(E_{10}+J(k)+4J(k)\zeta^2\frac{4J(k)-E_{-10}(p-\tilde{p})^2}{E_{-10}+J(k)}\right). \tag{9}$$

In formulas (8) and (9) we have introduced the following notation: $E_{ij}=E_i-E_j$, and $a_0=\nu^2/2\eta$ is the magnetoelastic coupling parameter.

From Eq. (8) we obtain the spectra of quasiphonon excitations as a function of the external field and material constants of the system:

$$\omega_1^2(k)=\omega_{\tau}^2(k)\frac{2J_0\alpha k^2+H-H_{c1}}{2J_0\alpha k^2+H-H_{c1}+2J_0a_0}. \tag{10}$$

$$\omega_2^2(k)=\omega_{t}^2(k)\frac{2J_0\alpha k^2+H-H_{c2}}{2J_0\alpha k^2+H-H_{c2}+2J_0a_0}. \tag{11}$$

In expressions (10) and (11) we have $\alpha=J_0R_0^2$, R_0 is the interaction radius, and the fields H_{c1} and H_{c2} have the form

$$H_{c1}=|\beta_1|+\frac{6\beta_2^2}{J_0},\quad H_{c2}=|\beta_1|-\frac{2\beta_2^2}{J_0}.$$

These fields can be interpreted as the fields of reorientational phase transitions, since the state of the system becomes unstable, and the spectra of t- and τ-polarized quasiphonons (in the long-wavelength limit $\alpha k^2\ll a_0$) "soften" at $H=H_{c1}$ and $H=H_{c2}$, respectively, and have the form

$$\omega_1^2(k)=\omega_{\tau}^2(k)\frac{\alpha k^2}{a_0},\quad \omega_2^2(k)=\omega_{t}^2(k)\frac{\alpha k^2}{a_0}.$$

In addition, at these fields ME gaps appear in the quasimagnon spectrum:

$$\varepsilon_1^2(0)=\left[a_0+2\frac{4\beta_2^2(J_0+|\beta_1|)^2+\beta_2^2|\beta_1|J_0}{J_0(J_0+|\beta_1|)(J_0+2|\beta_1|)}\right]\times\left[a_0+2\frac{\beta_2^2(7J_0+8|\beta_1|)|\beta_1|}{J_0(J_0+|\beta_1|)(J_0+2|\beta_1|)}\right], \tag{12}$$

$$\varepsilon_2^2(0)=\left[a_0-2\frac{4\beta_2^2(J_0+|\beta_1|)^2+\beta_2^2|\beta_1|J_0}{J_0(J_0+|\beta_1|)(J_0+2|\beta_1|)}\right]\times\left[a_0-2\frac{\beta_2^2(7J_0+8|\beta_1|)|\beta_1|}{J_0(J_0+|\beta_1|)(J_0+2|\beta_1|)}\right]. \tag{13}$$

CONCLUSION

Analysis of the spectra of coupled magnetoelastic waves leads to the following conclusions about the phase states and dynamic properties of a ferromagnet with inclined anisotropy. At fields $H>H_{c1}$ the system is found in the ferromagnetic phase. When the field is decreased to H_{c1} the system undergoes a phase transition, as follows from the "softening" of the τ-polarized quasiphonon mode. Further decrease of the magnetic field to the value H_{c2} again leads to a phase transition, this time occurring via the t-polarized quasiphonon mode. At fields $H<H_{c2}$ the system undergoes a transition to an elastic phase with a continuous variation of the magnetization direction from zero to $\tan 2\varphi_0=4\beta_2/|\beta_1|$ (at $H=0$). Thus analysis of the spectra of coupled magnetoelastic waves attests to the realization of three phases in the system: a ferromagnetic phase (for $H>H_{c1}$), an elastic phase (for $H<H_{c2}$), and an additional phase in the field interval $H_{c2}\leqslant H\leqslant H_{c1}$. Unfortunately, the mathematical formalism used in the present study does not permit description of the state of the system in that phase. However, a comparison of our data with the experimental results[2,10,11] suggests that it supports the existence of (for example) a domain structure, the existence region of which is determined by the relation

$\Delta H = H_{c1} - H_{c2} = 8(\beta_2^2/J_0)$. It follows from this relation that for $\beta_2 = 0$ the inhomogeneous phase vanishes, and the usual situation is realized in the system: two phases (ferromagnetic and canted) exist in the ferromagnet, and the phase transition occurs via the τ-polarized quasiphonon branch at $H_c = |\beta_1|$ (see, e.g., Ref. 8).

In addition, it follows from expression (13) that for certain relationships among the ME coupling parameters, OA constant, and ME interaction constant

$$\left(2\frac{\beta_2^2|\beta_1|(7J_0+8|\beta_1|)}{J_0(J_0+|\beta_1|)(J_0+2|\beta_1|)} < a_0 < 2\frac{(4\beta_2^2(J_0+|\beta_1|)^2+\beta_2^2|\beta_1|J_0}{J_0(J_0+|\beta_1|)(J_0+2|\beta_1|)} \right)$$

the ME gap in the quasimagnon spectrum (at $H = H_{c2}$) becomes negative. In that case, as for $\beta_2 = 0$, the inhomogeneous phase will not be realized in the system. Thus in the region of system parameters determined above, the magnetoelastic interaction compensates the influence of the inclined one-ion anisotropy. This fact is completely understandable, since the ME interaction plays the role of an ''effective'' anisotropy.

*E-mail: MAN@expl.cris.crimea.ua

[1] A. I. Akhiezer, V. G. Bar'yakhtar, and S. V. Peletminskii, *Spin Waves* [North-Holland, Amsterdam (1968); Nauka, Moscow (1967)].
[2] Yu. A. Burym, S. V. Dubinko, Yu. N. Mitsai, L. N. Borovitskaya, and A. R. Prokopov, Ukr. Fiz. Zh. (Russ. Ed.) **37**, 777 (1992).
[3] E. M. Gyorgy, A. Rosencwaig, E. J. Blount, W. J. Tabor, and M. E. Lanes, Appl. Phys. Lett. **18**, 479 (1971).
[4] Yu. A. Burym, S. V. Dubinko, and Yu. N. Mitsai, Preprint IMF 48.89 [in Russian], Institute of Metal Physics, Academy of Sciences of the Ukr. SSR, Kiev (1989).
[5] E. A. Turov and V. G. Shavrov, Usp. Fiz. Nauk **140**, 429 (1983) [Sov. Phys. Usp. **26**, 593 (1983)].
[6] R. O. Zaĭtsev, Zh. Éksp. Teor. Fiz. **68**, 207 (1975) [Sov. Phys. JETP **41**, 100 (1975)].
[7] L. D. Landau and E. M. Lifshitz, *Statistical Physics*, 3rd ed., Part I [Pergamon Press, Oxford (1980); Nauka, Moscow (1976)].
[8] Yu. N. Mitsai and Yu. A. Fridman, Teor. Mat. Fiz. **81**, 263 (1989).
[9] Yu. N. Mitsai, Yu. A. Fridman, O. V. Kozhemyako, and O. A. Kosmachev, Fiz. Nizk. Temp. **25**, 690 (1999) [Low Temp. Phys. **25**, 513 (1999)].
[10] A. R. Prokopov, S. V. Dubinko, A. O. Khrebtov, and M. I. Eremina, Fiz. Tverd. Tela (St. Petersburg) **39**, 1415 (1997) [Phys. Solid State **39**, 1255 (1997)].
[11] M. B. Sagdatkireeva and A. R. Mukhutdinova, *Seventeenth International School–Seminar "New Magnetic Materials of Microelectronics"* [in Russian], Moscow (2000)

Translated by Steve Torstveit

Impurity states in triangular two-dimensional Heisenberg antiferromagnets

M. N. Abdullaev

*G. M. Abdullaev Physics Institute, Academy of Sciences of the Azerbaijan Republic, pr. G. Dzhavida 33, 370143 Baku, Azerbaijan**

(Submitted February 28, 2001)
Fiz. Nizk. Temp. **27**, 865–871 (August 2001)

A theoretical study is made of the spin excitations in two-dimensional three-sublattice Heisenberg antiferromagnets containing an impurity atom in one of the sublattices. It is assumed that the coupling parameter between the impurity and matrix is positive, so that the impurity atom and the atom of the sublattice containing the impurity have the same spin directions in the ground state. In the Green's function method those functions are chosen that consist of combinations of sums and differences of the spin deviation operators. From the poles of these functions expressions are obtained for the states A_1, B_1, E_1, and E_2 of the group D_{6h}, and these expressions are used to determine their energies. © *2001 American Institute of Physics.* [DOI: 10.1063/1.1399202]

Research on the magnetic properties of low-dimensional magnetic systems has been attracting a lot of attention recently.[1–4] In particular, this is true of studies of the role of magnetic and nonmagnetic impurities in magnetic systems of this kind and also the role of magnetic impurities in nonmagnetic crystals in various temperature ranges. This is because the influence of impurity atoms on the various properties (magnetic, thermodynamic, superconducting, etc.) of the host crystal in the low-dimensional case is considerably different from that in the three-dimensional case.

The impurity problem in three-dimensional magnetic systems has been studied on the basis of the spin-wave approximation, in which the coupling between the impurity and host matrix is assumed weak. It is well known that the introduction of an impurity atom in a crystal lattice gives rise to discrete energy levels. A characteristic property of these levels is their location in the continuum of band excitations (virtual states) or outside the continuum (local states).

This problem has been studied by many authors[5,6] for both nonmagnetic and magnetic crystals. The main objects chosen for investigation in the magnetic studies have been one- and two-sublattice cubic crystals.

In the case of weak coupling between the atomic layers, ferromagnetic and antiferromagnetic crystals can be treated as two-dimensional systems. The impurity problem in a two-dimensional antiferromagnet has been studied on the basis of the spin-wave approximation[7] for $T=0$ and on the basis of a consistent spin-wave theory[8] for $T\neq 0$.

There is another low-dimensional magnetic structure for which the introduction of an impurity atom will lead, for example, to a shift of the point of transition between different ordered states.[9] Good examples of such compounds are the three-sublattice antiferromagnets VX_2 (X=Cl, Br, I). In them the spins of the individual sublattices in the Néel state lie in the ac plane at angles of 120°. The change in the spectrum of these crystals under the influence of spin–nuclear[10] and spin–phonon interactions has been studied in an ideal case.[11] In the course of such studies one must address the role of impurity atoms in the process of elementary excitation in these compounds.

In structures of the $LiCrO_2$ and $AgCrO_2$ type the spins of the sublattices lie in the $c-(xy)$ plane at angles of 120°. The situating of the spins of the sublattices in some plane or other is related to the anisotropy field relative to the c axis.

In this study we consider a one-impurity perturbation in a two-dimensional three-sublattice hexagonal antiferromagnet. The spin of the impurity atom is in the direction of the spin of the atom for which the impurity has been substituted in one of the sublattices. We also investigate the appearance of discrete levels and determine their energy.

HAMILTONIAN OF THE SYSTEM AND THE EQUATIONS OF MOTION

A triangular Heisenberg antiferromagnet containing an impurity is described by the Hamiltonian

$$\begin{aligned} H_{\rm ex}=&2I\sum_{l,\Delta_1} S_l\cdot S_{l+\Delta_1}-2I\sum_{\Delta_1} S_1\cdot S_{1+\Delta_1}\\ &+2I'\sum_{\Delta_1} S_1'\cdot S_{1+\Delta_1}+2I\sum_{l,\Delta_2} S_l\cdot S_{l+\Delta_2}\\ &-2I\sum_{\Delta_2} S_1\cdot S_{1+\Delta_2}+2I'\sum_{\Delta_2} S_1\cdot S_{1+\Delta_2}\\ &+2I\sum_{l+\Delta_1,l+\Delta_2} S_{l+\Delta_1}\cdot S_{l+\Delta_2},\\ H_{\rm ani}=&-D\left[\sum_l (S_l^z)^2+\sum_{l+\Delta_1}(S_{l+\Delta_1}^z)^2+\sum_{l+\Delta_2}(S_{l+\Delta_2}^z)^2\right]\\ &+D(S_1^z)^2-D'(S_1'^z)^2, \end{aligned} \tag{1}$$

where I, I' and D, D' are the parameters of the exchange and anisotropy fields, respectively, for the host and impurity atoms. The symmetry of the system under study is D_{6h}.

In order to express the Hamiltonian (1) in terms of the spin deviation operators, it is necessary to transform from the

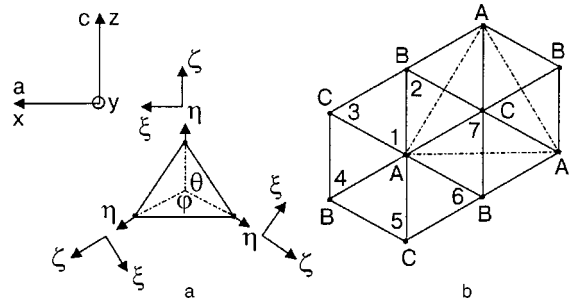

FIG. 1. a) 120° Néel structure on a three-sublattice structure ABC; shown are the local coordinate system $(\xi\eta\zeta)$ for each site and the global coordinate system (xyz); θ and φ are the angles of deviation of the global coordinate system from the site system at B and C, respectively. b) The chemical and magnetic unit cells are represented by equilateral triangles with sides a and $d=a\sqrt{3}$, respectively. In the chemical (ABC) cell the corners are occupied by atoms of different sublattices, and in the magnetic (AAA) cell by atoms of the same sublattice. The six nearest neighbors of the impurity atom 1 are denoted by 2, 3, ..., 7.

global coordinate system to a site system. According to Fig. 1, which shows the arrangement of the atomic spins, the relations between them are as follows:

$$S^x_{l+\Delta_1}=S^\xi_{l+\Delta_1}\cos\theta-S^\zeta_{l+\Delta_1}\sin\theta;$$

$$S^x_{l+\Delta_2}=S^\xi_{l+\Delta_2}\cos\varphi-S^\zeta_{l+\Delta_2}\sin\varphi;$$

$$S^z_{l+\Delta_1}=S^\zeta_{l+\Delta_1}\cos\theta+S^\xi_{l+\Delta_1}\sin\theta;$$

$$S^z_{l+\Delta_2}=S^\zeta_{l+\Delta_2}\cos\varphi+S^\xi_{l+\Delta_2}\sin\varphi, \tag{2}$$

where the angles θ and φ are the deviation of the magnetization of the first sublattice from the second and third sublattices, respectively.

The direction of the coordinate axis $0y$ is chosen perpendicular to the plane of the figure. Also shown in Fig. 1 are the chemical and magnetic cells.

Using the Holstein–Primakoff transformation, we can express the spin operators in terms of the Bose operators for each site:

$$S^\xi_l=S-a^+_l a_l;\quad S^\xi_{l+\Delta_1}=S-b^+_{l+\Delta_1}b_{l+\Delta_1};$$

$$S^\xi_{l+\Delta_2}=S-c^+_{l+\Delta_2}c_{l+\Delta_2},$$

$$S^\zeta_l=\sqrt{s/2}(a_l+a^+_l);\quad S^\zeta_{l+\Delta_1}=\sqrt{s/2}(b_{l+\Delta_1}+b^+_{l+\Delta_1});$$

$$S^\zeta_{l+\Delta_2}=\sqrt{s/2}(c_{l+\Delta_2}+c^+_{l+\Delta_2}),$$

$$S^\eta_l=-i\sqrt{s/2}(a_l-a^+_l);$$

$$S^\eta_{l+\Delta_1}=-i\sqrt{s/2}(b_{l+\Delta_1}-b^+_{l+\Delta_1});$$

$$S^\eta_{l+\Delta_2}=-i\sqrt{s/2}(c_{l+\Delta_2}-c^+_{l+\Delta_2}), \tag{3}$$

With the aid of transformations (2) and (3) we can express Hamiltonian (1) in terms of the spin deviations.

We introduce the Green's functions in matrix form:

$$\begin{pmatrix} \langle\langle x^-_l(t);x^+_{l'}(t')\rangle\rangle & \langle\langle x^-_l(t);y^+_{l'}(t')\rangle\rangle & \langle\langle x^-_l(t);z^+_{l'}(t')\rangle\rangle \\ \langle\langle y^-_l(t);x^+_{l'}(t')\rangle\rangle & \langle\langle y^-_l(t);y^+_{l'}(t')\rangle\rangle & \langle\langle y^-_l(t);z^+_{l'}(t')\rangle\rangle \\ \langle\langle z^-_l(t);x^+_{l'}(t')\rangle\rangle & \langle\langle z^-_l(t);y^+_{l'}(t')\rangle\rangle & \langle\langle z^-_l(t);z^+_{l'}(t')\rangle\rangle \end{pmatrix}$$

$$=\begin{pmatrix} G^{11}_{l;l'} & G^{12}_{l;l'} & G^{13}_{l;l'} \\ G^{21}_{l;l'} & G^{22}_{l;l'} & G^{23}_{l;l'} \\ G^{31}_{l;l'} & G^{32}_{l;l'} & G^{33}_{l;l'} \end{pmatrix}=\hat{G},$$

$$\begin{pmatrix} \langle\langle x^+_l(t);x^+_{l'}(t')\rangle\rangle & \langle\langle x^+_l(t);y^+_{l'}(t')\rangle\rangle & \langle\langle x^+_l(t);z^+_{l'}(t')\rangle\rangle \\ \langle\langle y^+_l(t);x^+_{l'}(t')\rangle\rangle & \langle\langle y^+_l(t);y^+_{l'}(t')\rangle\rangle & \langle\langle y^+_l(t);z^+_{l'}(t')\rangle\rangle \\ \langle\langle z^+_l(t);x^+_{l'}(t')\rangle\rangle & \langle\langle z^+_l(t);y^+_{l'}(t')\rangle\rangle & \langle\langle z^+_l(t);z^+_{l'}(t')\rangle\rangle \end{pmatrix}$$

$$=\begin{pmatrix} H^{11}_{l;l'} & H^{12}_{l;l'} & H^{13}_{l;l'} \\ H^{21}_{l;l'} & H^{22}_{l;l'} & H^{23}_{l;l'} \\ H^{31}_{l;l'} & H^{32}_{l;l'} & H^{33}_{l;l'} \end{pmatrix}=\hat{H}, \tag{4}$$

where $x^\pm_l=a_l\pm a^+_l$, $y^\pm_l=b_l\pm b^+_l$, $z^\pm_l=c_l\pm c^+_l$.

We note that the indices in the subscripts of $x^\pm_l$, $y^\pm_l$, and $z^\pm_l$ run over the first, second, and third sublattices, respectively, in the first coordination sphere. Each Green's function matrix in (4) has dimensions of 7×7. Each column of the first and second matrices form pairwise closed systems of equations of motion, from the solutions of which one can determine them.

The Green's functions in (4) and the functions conjugate to them satisfy equations in matrix form and comprise a separate system:

$$\begin{pmatrix} E & 0 & 0 \\ 0 & E & 0 \\ 0 & 0 & E \end{pmatrix}\begin{pmatrix} G^{11} & G^{12} & G^{13} \\ G^{21} & G^{22} & G^{23} \\ G^{31} & G^{32} & G^{33} \end{pmatrix}$$

$$-(\hat{V}^0_1+\hat{V}_1)\begin{pmatrix} H^{11} & H^{12} & H^{13} \\ H^{21} & H^{22} & H^{23} \\ H^{31} & H^{32} & H^{33} \end{pmatrix}=\frac{1}{\pi}\begin{pmatrix} 1 & 0 & 0 \\ 0 & 1 & 0 \\ 0 & 0 & 1 \end{pmatrix},$$

$$\begin{pmatrix} E & 0 & 0 \\ 0 & E & 0 \\ 0 & 0 & E \end{pmatrix}\begin{pmatrix} H^{11} & H^{12} & H^{13} \\ H^{21} & H^{22} & H^{23} \\ H^{31} & H^{32} & H^{33} \end{pmatrix}$$

$$-(\hat{V}^0_2+\hat{V}_2)\begin{pmatrix} G^{11} & G^{12} & G^{13} \\ G^{21} & G^{22} & G^{23} \\ G^{31} & G^{32} & G^{33} \end{pmatrix}=0; \tag{5}$$

$$\begin{pmatrix} E & 0 & 0 \\ 0 & E & 0 \\ 0 & 0 & E \end{pmatrix}\begin{pmatrix} H^{+11} & H^{+12} & H^{+13} \\ H^{+21} & H^{+22} & H^{+23} \\ H^{+31} & H^{+32} & H^{+33} \end{pmatrix}$$

$$-(\hat{V}^0_1+\hat{V}_1)\begin{pmatrix} G^{+11} & G^{+12} & G^{+13} \\ G^{+21} & G^{+22} & G^{+23} \\ G^{+31} & G^{+32} & G^{+33} \end{pmatrix}=0,$$

$$\begin{pmatrix} E & 0 & 0 \\ 0 & E & 0 \\ 0 & 0 & E \end{pmatrix} \begin{pmatrix} G^{+11} & G^{+12} & G^{+13} \\ G^{+21} & G^{+22} & G^{+23} \\ G^{+31} & G^{+32} & G^{+33} \end{pmatrix} - (\hat{V}_2^0 + \hat{V}_2) \begin{pmatrix} H^{+11} & H^{+12} & H^{+13} \\ H^{+21} & H^{+22} & H^{+23} \\ H^{+31} & H^{+32} & H^{+33} \end{pmatrix} = -\frac{1}{\pi} \begin{pmatrix} 1 & 0 & 0 \\ 0 & 1 & 0 \\ 0 & 0 & 1 \end{pmatrix}. \quad (6)$$

The Green's functions G^+ and H^+ contained in (6) are also determined by expressions (4) in which the plus and minus signs are interchanged.

Combining the two systems into one equation, we can write them in symbolic form as

$$\left[\begin{pmatrix} \hat{E} & -\hat{V}_1^0 \\ -\hat{V}_2^0 & \hat{E} \end{pmatrix} - \begin{pmatrix} 0 & -\hat{V}_1 \\ \hat{V}_2 & 0 \end{pmatrix} \right] \begin{pmatrix} \hat{G} & -\hat{H}^+ \\ \hat{H} & -\hat{G}^+ \end{pmatrix} = \frac{E}{\pi} \begin{pmatrix} \hat{1} & 0 \\ 0 & \hat{1} \end{pmatrix}, \quad (7)$$

where

$$\hat{V}_1 = 2IS \begin{pmatrix} \varepsilon & \lambda_\theta & \lambda_\varphi & \lambda_\theta & \lambda_\varphi & \lambda_\theta & \lambda_\varphi \\ \lambda_\theta & -\rho_\theta & 0 & 0 & 0 & 0 & 0 \\ \lambda_\varphi & 0 & -\rho_\varphi & 0 & 0 & 0 & 0 \\ \lambda_\theta & 0 & 0 & -\rho_\theta & 0 & 0 & 0 \\ \lambda_\varphi & 0 & 0 & 0 & -\rho_\varphi & 0 & 0 \\ \lambda_\theta & 0 & 0 & 0 & 0 & -\rho_\theta & 0 \\ \lambda_\varphi & 0 & 0 & 0 & 0 & 0 & -\rho_\varphi \end{pmatrix},$$

$$\hat{V}_2 = 2IS \begin{pmatrix} \varepsilon & \lambda_0 & \lambda_0 & \lambda_0 & \lambda_0 & \lambda_0 & \lambda_0 \\ \lambda_0 & -\rho_\theta & 0 & 0 & 0 & 0 & 0 \\ \lambda_0 & 0 & -\rho_\varphi & 0 & 0 & 0 & 0 \\ \lambda_0 & 0 & 0 & -\rho_\theta & 0 & 0 & 0 \\ \lambda_0 & 0 & 0 & 0 & -\rho_\varphi & 0 & 0 \\ \lambda_0 & 0 & 0 & 0 & 0 & -\rho_\theta & 0 \\ \lambda_0 & 0 & 0 & 0 & 0 & 0 & -\rho_\varphi \end{pmatrix}.$$

In the case of a one-impurity substituent atom differing from the host atom both in the exchange coupling with the nearest neighbors and in spin, the matrices of the perturbation will be of seventh order (in the case under consideration). Their general form is presented in Eq. (7), and their elements are given by the following relations:

$$\varepsilon = -\left(\frac{I'}{I} - 1\right)(Z_1 \cos\theta + Z_2 \cos\varphi) + \frac{D}{U}\left(\frac{D'S'}{DS} - 1\right),$$

$$\lambda_0 = \left(\frac{S'}{S}\right)^{1/2} \frac{I'}{I} - 1, \quad \lambda_\theta = \left[\left(\frac{S'}{S}\right)^{1/2} \frac{I'}{I} - 1\right] \cos\theta,$$

$$\lambda_\varphi = \left[\left(\frac{S'}{S}\right)^{1/2} \frac{I'}{I} - 1\right] \cos\varphi, \quad Z_1 = Z_2 = 3,$$

$$\rho_\theta = \left[\left(\frac{S'}{S}\right)^{1/2} \frac{I'}{I} - 1\right] \cos\varphi,$$

$$\rho_\varphi = \left[\left(\frac{S'}{S}\right)^{1/2} \frac{I'}{I} - 1\right] \cos\varphi,$$

where Z_1 and Z_2 are the numbers of nearest neighbors.

The angle indices of the matrix elements arise because of the horizontal components S'^x, S'^z, and the index zero because of the perpendicular component S'^y of the spin vector of the impurity atom relative to the ac plane.

SPECTRUM OF IMPURITY LEVELS

The spectrum of elementary excitations in a two-dimensional three-sublattice antiferromagnet is determined by the poles of the Green's function in (7), i.e.,

$$\det \left| \hat{1} - \begin{pmatrix} \hat{G}^0 & -\hat{H}^{0+} \\ \hat{H}^0 & -\hat{G}^{0+} \end{pmatrix} \cdot \begin{pmatrix} 0 & \hat{V}_1 \\ \hat{V}_2 & 0 \end{pmatrix} \right| = 0. \quad (8)$$

To simplify the calculations of this determinant, let us reduce it to quasidiagonal form. This procedure is performed with the aid of a unitary matrix constructed on the principles of group theory. Using symmetrized combinations of atomic wave functions, one can construct the corresponding unitary matrix:[12]

$$U = \begin{pmatrix} 1 & 0 & 0 & 0 & 0 & 0 & 0 \\ 0 & \frac{1}{\sqrt{6}} & \frac{1}{\sqrt{6}} & \frac{1}{\sqrt{3}} & 0 & 0 & -\frac{1}{\sqrt{3}} \\ 0 & \frac{1}{\sqrt{6}} & -\frac{1}{\sqrt{6}} & \frac{1}{2\sqrt{3}} & \frac{1}{2} & \frac{1}{2} & \frac{1}{2\sqrt{3}} \\ 0 & \frac{1}{\sqrt{6}} & \frac{1}{\sqrt{6}} & -\frac{1}{2\sqrt{3}} & \frac{1}{2} & -\frac{1}{2} & \frac{1}{2\sqrt{3}} \\ 0 & \frac{1}{\sqrt{6}} & -\frac{1}{\sqrt{6}} & -\frac{1}{\sqrt{3}} & 0 & 0 & -\frac{1}{\sqrt{3}} \\ 0 & \frac{1}{\sqrt{6}} & \frac{1}{\sqrt{6}} & -\frac{1}{2\sqrt{3}} & -\frac{1}{2} & \frac{1}{2} & \frac{1}{2\sqrt{3}} \\ 0 & \underbrace{\frac{1}{\sqrt{6}}}_{A_1} & \underbrace{-\frac{1}{\sqrt{6}}}_{B_1} & \underbrace{\frac{1}{2\sqrt{3}}}_{E_1} & \underbrace{-\frac{1}{2}}_{E_2} & -\frac{1}{2} & \frac{1}{2\sqrt{3}} \end{pmatrix}. \quad (9)$$

In obtaining this matrix we chose the plane in which the impurity atom and its neighbors are located to be perpendicular to the sixfold axis.

Using the unitary matrix (9), one can separate the determinant (8) into a product of factors having the following form:

$$D_{A_1}(E)=\det\Bigg(\begin{vmatrix}1 & 0\\ 0 & 1\end{vmatrix}-2IS\begin{vmatrix}H_{11}^{0+} & \sqrt{6}H_{12}^{0+}\\ \sqrt{6}H_{21}^{0+} & \sum_i H_{2i}^{0+}\end{vmatrix}$$
$$\cdot\begin{vmatrix}\varepsilon & \sqrt{6}\lambda_0\\ \sqrt{6}\lambda_0 & -\rho_\theta\end{vmatrix}+2IS\begin{vmatrix}H_{11}^{0} & \sqrt{6}H_{12}^{0}\\ \sqrt{6}H_{21}^{0} & \sum_i H_{2i}^{0+}\end{vmatrix}$$
$$\times\begin{vmatrix}\varepsilon & \frac{\sqrt{6}}{2}(\lambda_\theta+\lambda_\varphi)\\ \frac{\sqrt{6}}{2}(\lambda_\theta+\lambda_\varphi) & -\rho_\theta\end{vmatrix}$$
$$-\frac{(2IS)^2}{E}\begin{vmatrix}G_{11}^{0} & \sqrt{6}G_{12}^{0}\\ \sqrt{6}G_{21}^{0} & \sum_i G_{2i}^{0+}\end{vmatrix}$$
$$\cdot\begin{vmatrix}\varepsilon & \frac{\sqrt{6}}{2}(\lambda_\theta+\lambda_\varphi)\\ \frac{\sqrt{6}}{2}(\lambda_\theta+\lambda_\varphi) & -\rho_\theta\end{vmatrix}\cdot\begin{vmatrix}\varepsilon & \sqrt{6}\lambda_0\\ \sqrt{6}\lambda_0 & -\rho_\theta\end{vmatrix}\Bigg), \tag{10}$$

$$D_{B_1}(E)=1-2IS\Big(H_{22}^{0}-H_{25}^{0}+2H_{24}^{0}-2H_{23}^{0}-H_{22}^{0+}$$
$$+H_{25}^{0+}-2H_{24}^{0+}+2H_{23}^{0+}\Big(\rho_\theta-\frac{(2IS)^2}{E}(G_{22}^{0}$$
$$+G_{24}^{0}-G_{25}^{0}-G_{23}^{0})\rho_\theta^2, \tag{11}$$

$$D_{E_1}(E)=a_{11}\times a_{22}=\Big[1-2IS(H_{22}^{0}-H_{24}^{0}+H_{23}^{0}-H_{25}^{0}$$
$$-H_{22}^{0+}+H_{24}^{0+}-H_{23}^{0+}+H_{25}^{0+})\rho_\theta$$
$$-\frac{(2IS)^2}{E}(G_{22}^{0}+G_{23}^{0}-G_{24}^{0}-G_{25}^{0})\rho_\theta^2\Big]\times a_{22}, \tag{12}$$

$$D_{E_2}(E)=b_{11}\times b_{22}=\Big[1-2IS(H_{22}^{0}-H_{24}^{0}+H_{23}^{0}-H_{25}^{0}$$
$$-H_{22}^{0+}+H_{24}^{0+}+H_{23}^{0+}-H_{25}^{0+})\rho_\theta$$
$$-\frac{(2IS)^2}{E}(G_{22}^{0}-G_{23}^{0}-G_{24}^{0}+G_{25}^{0})\rho_\theta^2\Big]\times b_{22}. \tag{13}$$

To obtain the second diagonal element in the determinants D_{E_1} and D_{E_2} it is necessary to replace ρ_θ by ρ_φ in (12) and (13).

When the Green's function matrix in (8) is set into the unit cell, coincident elements appear. Because of this, the number of elements contracts, and the elements that remain are those which are contained in (10)–(13). Since the upper and lower indices of these coincide, we shall keep only one of them.

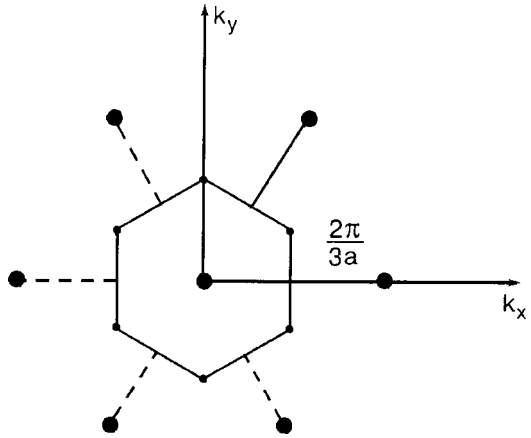

FIG. 2. Brillouin zone constructed with respect to the direct magnetic unit cell, which is represented by equilateral triangles (AAA) with side $a\sqrt{3}$.

We see from Eqs. (10)–(13) that states of the A_1 type depend on four parameters (ε, λ_0, λ_φ, ρ_θ); E_1 and E_2 depend on two (ρ_θ, ρ_φ), and B_1 on one (ρ_φ). Therefore, we begin by solving the equation for an irreducible representation of the B_1 type. To demonstrate the clarity of the graphic solution of this equation, we consider the simple case

$$\theta=\varphi=2\pi/3; \quad \mathbf{k}=(k_x;0;0).$$

Numbering the atoms of the first coordination sphere as in Fig. 1, we obtain the following equation:

$$1-\frac{\rho}{\pi}N^{-1/3}\sum_{k_x}\Big(1+2\cos\frac{\sqrt{3}}{2}ak_x\Big)\frac{M_{22}-L_{22}+M_{23}-L_{23}}{(E/2IS)^2-A_{22}+A_{23}}$$
$$+\frac{\rho^2}{\pi}N^{-1/3}\sum_{k_x}\frac{1+2\cos\frac{\sqrt{3}}{2}ak_x}{(E/2IS)^2-A_{22}+A_{23}}=0, \tag{14}$$

where

$$M_{22}-L_{22}+M_{23}-L_{23}=\frac{3}{4}\Big(\frac{D}{I}+6\gamma_{k_x}\Big),$$
$$A_{22}-A_{23}=Z^2\Big(1-\gamma_{k_x}+\frac{D}{4IS}\Big)\Big(1+\frac{1}{2}\gamma_{k_x}-\frac{D}{Iz}\Big),$$
$$\gamma_{k_x}=\frac{1}{z}(1+2\cos ak_x).$$

In these expressions the wave vector k_x takes on all values from the first Brillouin zone, which is constructed for an equilateral triangle of the direct unit cell (see Fig. 2). As we see from Fig. 1, this primitive cell has a side of length $d=a\sqrt{3}$. It can be shown by a straightforward calculation[13] that the Brillouin zone for a two-dimensional three-sublattice antiferromagnet has the shape of a plane hexagon. Here a is the lattice constant.

The graphical solution of the quadratic equation with respect to $1/\rho$ in (14) for the irreducible representation B_1 is shown in Fig. 3. Plotted on the vertical axis is the quantity $1/\rho$, which lies in the domain $(-\infty,-2)$ or $0,\infty)$. The latter is determined from expression (7) for ρ_φ at $\varphi=4\pi/3$. It is seen in Fig. 3 that Eq. (14) can have solutions only for positive values of $1/\rho$. Among the latter are certain values for which solutions of equation (14) do not exist, since the wave vector

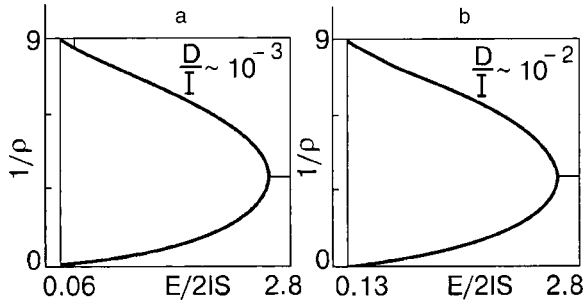

FIG. 3. Roots of the quadratic equation with respect to $1/\rho$ in (14) as functions of the dimensionless quantity $E/2IS$.

corresponding to them ''falls out'' of the first Brillouin zone. In particular, for $k_x \to 4\pi/3\sqrt{3}$ the solution of the equation goes to zero, i.e., $1/\rho \to 0$. Therefore, the summation in (14) is done within the limits $0 \leqslant k_x \leqslant 4\pi/3\sqrt{3}$. The density of the B_1 state is determined by the crossing of the $1/\rho$ line with the curves shown in Fig. 3.

Let us now consider the A_1 states. The energy of the A_1 state is determined analogously, by equating the real part of expression (10) to zero. Since this equation is of the fourth degree with respect to the various combinations of the four perturbation parameters contained in it (ε, λ_0, λ_θ, ρ_θ), its solution in graphical form involves a lot of work, and its analytical solution is an awkward expression. Therefore, it is necessary to find an approximate approach for solving this equation. For $S' \neq S$, $I' = I$ the number of parameters of the perturbation decreases to three (ε, λ_θ, ρ_θ), and for $S' = S$, $I' \neq I$ to two (ε, ρ_θ), but the equation remains one of fourth degree with respect to their combinations. For $S' = S$, $I' = I$ the equation reduces to a quadratic equation for a single perturbation parameter $D/I\,(D'/D - 1) = \varepsilon'$:

$$\frac{1}{\varepsilon'^2} - \frac{1}{\varepsilon'}\frac{2}{\pi}N^{-1/3} \times \sum_{k_x} \frac{L_{11}\left[\left(\frac{E}{2IS}\right)^2 - A_{22} - A_{23}\right] - L_{12}A_{21}}{\left[\left(\frac{E}{2IS}\right)^2 - A_{11}\right]\left[\left(\frac{E}{2IS}\right)^2 - A_{22} - A_{23}\right] - 2A_{12}A_{21}} - \frac{1}{\pi}N^{-1/3} \times \sum_{k_x} \frac{\left(\frac{E}{2IS}\right)^2 - A_{22} - A_{23}}{\left[\left(\frac{E}{2IS}\right)^2 - A_{11}\right]\left[\left(\frac{E}{2IS}\right)^2 - A_{22} - A_{23}\right] - 2A_{12}A_{21}} = 0,$$

where

$$A_{22} + A_{23} = \left(z - \frac{D}{2I}\right)\left(z + \frac{D}{4I}\right) + \frac{1}{2}\left(z - \frac{5D}{4I}\right)z\gamma_k + \frac{3}{2}(z\gamma_k)^2, \quad L_{11} = -\left(z - \frac{D}{I}\right),$$

$$2A_{12}A_{21} = \frac{1}{2}\left[z\left(z - \frac{9}{4}\right)\gamma_{k_x} - (z\gamma_{k_x})^2\right] \times \left[\left(z + \frac{D}{I}\right)z\lambda_{k_x} - (z\gamma_{k_x})^2\right], \quad L_{12} = -\frac{1}{2}z\gamma_{k_x},$$

$$A_{11} = \left(z - \frac{D}{2I}\right)^2 - (z\gamma_{k_x})^2, A_{21} = \frac{1}{2}z\gamma_{k_x}\left(z + \frac{D}{I} - z\gamma_{k_x}\right). \tag{15}$$

Only in one particular case, for $k_x \geqslant 0$, $D' \gg D$, $I \sim D$, can the approximation solution of this equation be obtained in analytical form: $E_{A_1} \approx IS\sqrt{37 - 3(\varepsilon'/2 - 1)^{-1}}$, from which it follows that the level E_{A_1} falls into a spectral band of width $E \approx 2IS\sqrt{10}$.

*E-mail: physic@lan.ab.az

[1] Y. Fukumoto and A. Oguchi, J. Phys. Soc. Jpn. **68**, 3665 (1999).
[2] Yu. A. Fridman and D. V. Spirin, Fiz. Nizk. Temp. **26**, 374 (2000) [Low Temp. Phys. **26**, 273 (2000)].
[3] J. Stolze and M. Vogel, Phys. Rev. B **61**, 4026 (2000).
[4] J. A. Simpson, R. A. Cowley *et al.*, J. Phys.: Condens. Matter **9**, 8693 (1997).
[5] A. A. Maradudin, E. W. Montroll, and G. H. Weiss, in *Solid State Physics*, Suppl. 3, Academic Press, New York (1963) [Russian translation: *Dynamic Theory of the Crystal Lattice in the Harmonic Approximation*, Mir, Moscow (1965)].
[6] Yu. A. Izyumov and M. V. Medvedev, *Theory of Magnetically Ordered Crystals Containing Impurities* [in Russian], Nauka, Moscow (1970).
[7] N. Bulut, D. Hone, and D. I. Scalapina, Phys. Rev. Lett. **62**, 2192 (1989).
[8] V. Yu. Irkhin, A. A. Katanin, and M. I. Katsnelson, Phys. Rev. B **60**, 14779 (1999).
[9] M. W. Moore, P. Day, C. Wilkinson, and K. R. A. Ziebeck, Solid State Commun. **53**, 1009 (1985).
[10] T. Suzuki and Y. Natsume, J. Phys. Soc. Jpn. **56**, 1577 (1987).
[11] M. N. Abdullayev, Fizika **3**, 19 (1997).
[12] V. Heine, *Group Theory in Quantum Mechanics* [Pergamon Press, London (1960); IL, Moscow (1963)].
[13] V. V. Eremenko, *Introduction to Optical Spectroscopy of Magnets* [in Russian], Naukova Dumka, Kiev (1975).

Translated by Steve Torstveit

Magnetostriction during field transformation of the domain structure of an easy-plane antiferromagnet in the case of a magnetoelastic mechanism for the multidomain state

V. M. Kalita and A. F. Lozenko*

Institute of Physics of the National Academy of Sciences of Ukraine, pr. Nauki 46, 03650 Kiev, Ukraine
(Submitted March 5, 2001)
Fiz. Nizk. Temp. **27**, 872–878 (August 2001)

The features of the transformation of the multidomain state of an easy-plane antiferromagnet in an external magnetic field are investigated in the case of a magnetoelastic origin of the multidomain state. Experimental data are presented on the field dependence of the induced magnetostriction of the easy-plane two-sublattice antiferromagnet $CoCl_2$ at different temperatures. In the discussion of the experiments and in the theoretical description we use the approximation of a continuous distribution of domains in the easy plane. It is shown that the orientational distribution of the domains upon the introduction of a magnetic field depends only on the magnitude and direction of the field and is independent of temperature. These features of the distribution of domains can be explained by a matching of their equilibrium magnetostriction with the elasticity of defects wherein the elasticity of the domains compensates the elasticity of the defects.
[DOI: 10.1063/1.1399203]

The antiferromagnetic phase of many antiferromagnets (AFMs) is realized in the form of a multidomain state that satisfies the given symmetry of the crystal.[1] The question of the thermodynamic favorability or equilibrium nature of the domain structure is of a fundamental character, unlike the case of ferromagnets,[2] in an AFM there are no magnetostatic fields.

An equilibrium multidomain state in an AFM can occur because of the higher entropy in the multidomain situation. The entropy mechanism is temperature-dependent and operates in a finite temperature interval near the Néel temperature T_N (Ref. 1). At the same time, in many AFMs a multidomain state is observed at $T \to 0$, when the entropy mechanism loses its effectiveness.

The formation of a multidomain state in an AFM can result from ''metallurgical'' defects of the crystal lattice, which, by creating local anisotropy fields, orient the antiferromagnetic vector **L**. Even in perfect crystals there are always intrinsic defects. However, the effect of defects in a perfect crystal will be different. For example, linear defects give rise to inhomogeneity of the antiferromagnetic state.[3] In the case of a screw dislocation, in going around it one finds that the spin of one sublattice will be transformed into the spin of the other sublattice. If the anisotropy[4,5] is taken into account, the influence of a dislocation will lead to the formation of domains with uniform **L**.

An important role in the formation of the domain structure in an AFM is played by the magnetoelastic forces, which, like the magnetic anisotropy forces, tend to hold the spins in certain directions.[6] Magnetoelasticity is particularly important in an AFM[7,8] with very large values of the anisotropic magnetostriction. The value of the anisotropic magnetostriction depends on the direction of **L**. For different directions of **L** in the domains their magnetostriction will also have different directions, which can lead to mechanical stresses between domains. The mechanism giving rise to a multidomain state based on the matching of the magnetostriction of the domains is called magnetoelastic.[8]

An example of matching of the magnetostriction of domains is considered in Ref. 9. In the case of two domains one can achieve a between them. In the case of a hexagonal AFM, around the point at which three domains lying in the easy plane come together, with a 120° rotation of **L**, there will be a region of dilatation or compression, giving rise to local stresses.[9] These stresses can be compensated by placing in that region a defect which compresses or expands the lattice.

An external magnetic field can cause an AFM to go from a multidomain to a homogeneous (single-domain) state. Restoration of the homogeneous state of the crystal in a magnetic field is accompanied by straining of the crystal. By measuring the magnetostriction of the crystal as a function of **H**, one can study the process of transformation of the multidomain structure.[6,8]

In this paper we analyze the results of magnetostriction measurements at different temperatures during the restructuring of the multidomain state brought on in the two-sublattice easy-plane AFM $CoCl_2$ by the introduction of a field **H**.[10,11] The value of the induced magnetostriction in $CoCl_2$ is $\sim 10^{-3}$, and the multidomain state is of a magnetoelastic nature.[8] Restructuring of the domains and the tilting of the spins toward **H** in the homogeneous state in $CoCl_2$ occur at experimentally accessible fields. The field H_{ff} at which the spins of the sublattices collapse (the spin-flip field) is equal to 32 kOe at $T = 4.2$ K. The restructuring of the multidomain state and the tilting of the spins after a homogeneous state is established are separated with respect to field. The transition to the homogeneous state at different temperatures occurs in fields $\sim 0.3 H_{ff}(T)$.[12]

The formation of domains in $CoCl_2$ is confirmed by

neutron-diffraction studies.[13] According to Refs. 1, 6, and 13–15, the existence of the multidomain state in $CoCl_2$ should be attributed to the presence of two sets of three twofold axes in the easy plane of the crystal. Directions along one of these sets of axes can turn out to be energetically favorable, which would bring about a symmetry-related realization of the multidomain state,[1,2] and the transition in a magnetic field from a multidomain state to the homogeneous state with allowance for this crystallographic anisotropy occurs by reorientation of the spins.[13] In a study of antiferromagnetic resonance it was noted that the in-plane anisotropy in $CoCl_2$ is extremely small, and in a description of the field dependence of the low-frequency branch of the antiferromagnetic resonance it does not need to be taken into account.[7] The in-plane anisotropy in $CoCl_2$ has not been observed experimentally because of its small size; this makes it difficult to analyze the restructuring of the multidomain state taking place through the spin-reorientation process.

In Refs. 15 and 16 a mechanism was proposed to explain the influence of the surface on the formation of thermodynamically favorable equilibrium antiferromagnetic domains through allowance for their magnetoelasticity. In Ref. 16 it was asserted that the stresses on the surface due to the homogeneous magnetostriction of an AFM act like the appearance of surface charges, as in ferromagnets. The elastic energy of these charges counteracts the uniform strain of the AFM and thereby leads to the formation of a multidomain state. The multidomain state described theoretically in Refs. 15 and 16 was obtained through the elastic matching of the magnetostriction of the whole crystal and the elasticity of its surface. In Ref. 16 the magnetic-field dependence of the magnetostriction of the crystal during the transition from a multidomain to a homogeneous state was obtained theoretically. The applicability of that surface mechanism[15,16] of creation of the multidomain state to the case of $CoCl_2$ can be judged from the similarity of the theoretical dependence of the magnetostriction and the experimentally observed magnetostriction.

THE EXPERIMENT AND ITS STATISTICAL ANALYSIS

On the basis of data obtained by a dilatometric method[17] for the induced magnetostriction of $CoCl_2$ single crystals it was shown in Ref. 8 that for $T=4.2$ K the dependence of the relative elongation $\varepsilon=\Delta l/l$ of the crystal is directly proportional to the square of H. Figure 1 shows the field dependence of the longitudinal elongation of $CoCl_2$ at different temperatures as a function of the square of **H** at the beginning of the restructuring of the domain structure. This dependence can be written in the form

$$\varepsilon(T,H)=k(T)H^2, \tag{1}$$

where $k(T)$ is a temperature-dependent coefficient. Relation (1) holds in a large interval of ε from 0 to $0.25\varepsilon_s$, where ε_s is the spontaneous anisotropy of the magnetostriction of the homogeneous state at $H=0$,[12] which is determined by extrapolating $\varepsilon(H^2)$ for the homogeneous state to $H\to 0$.

The slope of the lines in Fig. 1 depends on the temperature. Figure 2 shows the temperature dependence of the coefficient of proportionality in Eq. (1), normalized to its value at $T=4.2$ K, $\tilde{k}(T)=k(T)/[k(T=4.2\,\mathrm{K})]$. For comparison in

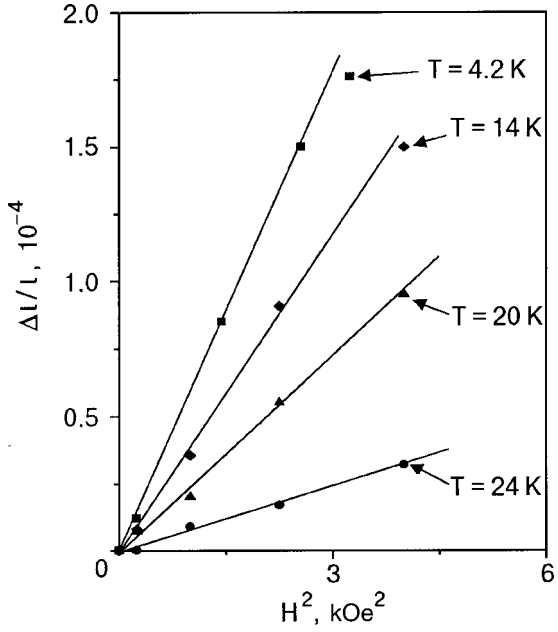

FIG. 1. Relative longitudinal elongation of the $CoCl_2$ crystal versus the square of the magnetic field for different temperatures.

Fig. 2 we also show the dependence on T of the normalized spontaneous magnetostriction $\tilde{\varepsilon}_s(T)=\varepsilon_s(T)/[\varepsilon_s(T=4.2\,\mathrm{K})]$.[12]

Taking into account the similarity of the temperature dependence of $\tilde{k}$ and $\tilde{\varepsilon}_s$, we can write the relative elongation of the $CoCl_2$ crystal in the multidomain state upon introduction of a magnetic field as

$$\varepsilon(T,H)=\varepsilon_s(T)\frac{H^2}{H_d^2}, \tag{2}$$

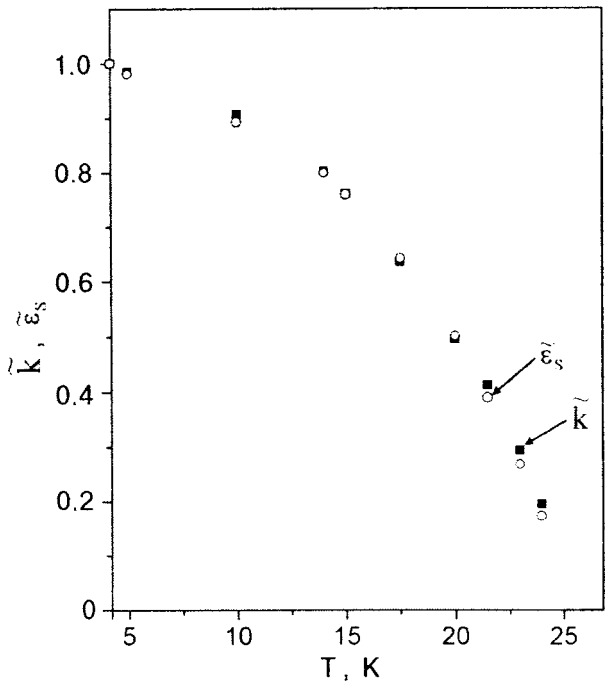

FIG. 2. Temperature dependence of the spontaneous magnetostriction $\tilde{\varepsilon}_s$ normalized to the value at $T=4.2$ K and of the coefficient of proportionality $\tilde{k}$.

where H_d^2 is a temperature-independent (to within the error of this experiment) parameter having a value $\approx 9.5\,\mathrm{kOe}^2$.

The mechanism of formation of the multidomain state involving the elasticity of the surface should lead to a temperature dependence of the parameter H_d^2 in (2) similar to the temperature dependence of the fourth power of the sublattice magnetization. If such a temperature dependence had held over the temperature interval shown in Fig. 1, then at $T \approx 24\,\mathrm{K}$ the parameter H_d^2 would have decreased by more than an order of magnitude relative to its value at 4.2 K. Thus, on the basis of the temperature–field curves of the magnetostriction in the multidomain region, we can conclude that the multidomain state in $CoCl_2$ is of a different nature than that proposed in Refs. 15 and 16.

Using the experimental results reported here, let us discuss the features of the domain distribution in $CoCl_2$. In analyzing the experimental data from the study of the magnetostriction in $CoCl_2$ we shall proceed from the degeneracy of the directions of the spins of the sublattices in the easy plane. We shall also assume that the domains with different orientations of **L** in the easy plane are equivalent and that the distribution of domains as a function of the direction of **L** is continuous.

It was shown in Ref. 13 that the elongation of $CoCl_2$ along the field **H** in the single-domain region, when the multidomain state is destroyed by a magnetic field and the vector **L** is perpendicular to the magnetic field (**L**$\perp$**H**) everywhere in the crystal, is described by the function

$$\varepsilon(T,H)=\varepsilon_s(T)\left(1-\xi\frac{H^2}{H_{ff}^2(T)}\right), \tag{3}$$

where ξ is a field- and temperature-independent parameter determined experimentally in Ref. 13. The relative longitudinal elongation ε of a domain with **L** not perpendicular to **H** in the multidomain state is

$$\varepsilon=\varepsilon_s(T)\left(1-\xi\frac{H^2\cos^2\varphi}{H_{ff}^2}\right)(\cos^2\varphi-\sin^2\varphi), \tag{4}$$

where φ is the angle between the vector **H** and the perpendicular to the direction specified by the vector **L**. By averaging (4) over all orientations of the domains, we obtain the magnetostriction of the multidomain crystal as

$$\overline{\varepsilon}=\frac{1}{\pi}\int_0^{\pi}\varepsilon_s(T)\left(1-\xi\frac{H^2\cos^2\varphi}{H_{ff}^2}\right)\times(\cos^2\varphi-\sin^2\varphi)p(\varphi)d\varphi, \tag{5}$$

where $p(\varphi)$ is the probability density of the distribution of domains as a function of φ for the specified direction of **H**.

At $H=0$ all of the directions of orientation of the domains are equiprobable, and the probability density is equal to a φ-independent constant. The introduction of a field **H** destroys the equiprobability of the distribution. Since the distribution is symmetric with respect to φ for small variations of the probability density, it can be written in the form

$$p(\varphi)=1+\alpha(\cos^2\varphi-1/2), \tag{6}$$

where α is a small parameter. Substituting (6) into (5), calculating the value of $\overline{\varepsilon}$, and equating (5) with (2), we find that in order for relations (4)–(6) to agree with experiment it is necessary that $p(\varphi)$ have the form

$$p(\varphi)=1+4\frac{H^2}{H_d^2}\left(\cos^2\varphi-\frac{1}{2}\right). \tag{7}$$

Thus for satisfactory agreement with experiment it is necessary that the distribution of the orientations of the domains in **H** be independent of temperature.

DISCUSSION

Distribution (7) was introduced phenomenologically and meets the requirements of symmetry and conformity to the experimental dependence of $\varepsilon(H)$ in the region of restructuring of the multidomain state. Let us determine the theoretically expected form of this distribution in the case of the entropy mechanism[1,6,18] and the magnetoelastic mechanism.[8,9]

We shall analyze the restructuring of the multidomain state under the influence of a magnetic field in accordance with the principle of minimum free energy of the crystal, elaborated in Ref. 2, which states that the equilibrium distribution of domains should correspond to the minimum free energy of the crystal. We determine the expression for the free energy with allowance for the continuous distribution of domain orientations.

The energy of an isotropic AFM in a magnetic field **H** can be determined using the Hamiltonian

$$\hat{H}=\frac{1}{2}\sum_{\alpha\beta ij}I_{\alpha\beta}\,\mathbf{s}_{\alpha i}\cdot\mathbf{s}_{\beta j}-\mathbf{H}\cdot\sum_{\alpha i}\mathbf{s}_{\alpha i}, \tag{8}$$

where the indices $\alpha,\beta=1,2$ indicate the sublattice and i,j enumerate the positions of the ion in them. The energy per unit cell of the AFM as a function of **H** when **L**$\perp$**H** is given by

$$e=-zI_{12}s^2-\frac{H^2}{2zI_{12}}, \tag{9}$$

where z is the number of nearest neighbors, s is the average spin of an ion, and I_{12} is the intersublattice exchange parameter. The term in (9) that is independent of **H** will not be considered further.

If the in-plane anisotropy is small, we shall assume that the domains can be oriented arbitrarily in the plane. In the field **H** the domains with **L**$\perp$**H** will be energetically favorable. In terms of the angle φ between **H** and the perpendicular to **L** the exchange energy in a domain in which $\varphi\neq 0$, when the spins in it are tilted toward **H**, the energy per unit cell becomes

$$e=-\frac{H^2\cos^2\varphi}{2zI_{12}}. \tag{10}$$

The exchange energy of the AFM in the multidomain state is equal to the sum

$$E=-\frac{V}{V_0}\sum_i p_i\frac{H^2\cos^2\varphi_i}{2zI_{12}}, \tag{11}$$

where V and V_0 are the volumes of the crystal and of the unit cell, φ_i is the angle of orientation of the domains with probability P_i, and $P_i=V_i/V$, where V_i is the volume of such domains. The sum (11) for the exchange energy of the multidomain AFM can be written in the form of an integral over φ:

$$E=-\frac{1}{\pi}\frac{V}{V_0}\int_0^{\pi}p(\varphi)\frac{H^2\cos^2\varphi}{2zI_{12}}d\varphi. \tag{12}$$

In the free energy of the multidomain state upon the formation of identical domains it is necessary to take into account their permutations, which leads to an additional contribution to the free energy:

$$\Delta F=T\sum_i \ln N_i(\varphi_i,V_i)!, \tag{13}$$

where $N_i(\varphi_i,V_i)$ is the number of identical domains of volume V_i and orientation angle φ_i. If the domains with different φ_i have the same shape and volume, then $V_i/V=N_i/N$, where $N=V/V_d$ is the total number of domains, and V_d is the volume of an individual domain at $H=0$. In this approximation the entropy contribution to the free energy can be written in the form of an integral:

$$\Delta F=\frac{T}{\pi}\frac{V}{V_d}\int_0^{\pi}p(\varphi)\ln p(\varphi)d\varphi. \tag{14}$$

When the contributions to the free energy of the crystal from the exchange energy (12) and from the entropy correction (14) are both taken into account, the equilibrium state when a field **H** is introduced is determined from the minimum of the free energy, which we write in the form

$$F_1=E+\Delta F=\frac{1}{\pi}\int_0^{\pi}\left[-\frac{V}{V_0}p(\varphi)\frac{H^2\cos^2\varphi}{2zI_{12}}+T\frac{V}{V_d}p(\varphi)\ln p(\varphi)\right]d\varphi. \tag{15}$$

Minimizing F_1 in the case of small **H**, we find an expression for $p(\varphi)$ in the form

$$p(\varphi)=1+\frac{1}{2}\frac{V_d}{V_0}\frac{1}{T}\frac{H^2}{I_{12}z}\left(\cos^2\varphi-\frac{1}{2}\right). \tag{16}$$

Comparing (16) and (7), we find that the parameter H_d^2 is directly proportional to T:

$$H_d^2=8\frac{V_0}{V_d}I_{12}zT. \tag{17}$$

The value of H_d in (17) decreases with increasing domain volume V_d and increases with increasing antiferromagnetic exchange I_{12}. The temperature independence of H_d^2 for $CoCl_2$ could be explained by assuming that the domain volume V_d is directly proportional to T. However, such an assumption is incorrect, since it implies that the domain volume goes to zero as $T\to 0$. Thus we can state that the multidomain state in $CoCl_2$ is not of an entropic nature.

Let us determine the distribution of domains in the case of a magnetoelastic mechanism.[8] According to Ref. 9, at the places where three domains lying in the easy plane and having different directions of **L** come together there arise local compressive or dilatative stresses, while the rest of the domains are nearly unstressed. These local stresses can be compensated by defects that locally expand or compress the lattice. It was shown in Ref. 9 that when the strains at places where domains with different orientations of **L** come together are compensated by the strains of a defect, the elastic strains of the defect will be localized. The lattice deformations created by a defect become ''screened'' by equilibrium deformations of domains. Here it is necessary to distinguish the interaction of a defect with the domains surrounding it and the interaction between defects[19] with allowance for the domains surrounding them. The interaction of a defect and the domains surrounding it is energetically favorable, but it is temperature dependent.[9] The temperature dependence of the corresponding energy benefit is determined by the dependence of the antiferromagnetic vector L on T.

When the elasticity of the defects is localized by domains, there will be no interactions between defects. In the homogeneous state the energy of interaction between defects will be almost the same as in the paramagnetic phase. Since the interaction between defects in the paramagnetic phase increases the energy of the crystal, while no interaction between defects occurs in the multidomain state because of the screening of the elasticity of the defects by domains, we find that the multidomain state will be favored by an amount equal to the energy of interaction between defects in the paramagnetic state. The temperature dependence of this energy benefit is not due to the dependence of $L(T)$. Assuming that this energy benefit is decisive in the formation of the multidomain state and is independent of T, the restructuring of the multidomain state in a magnetic field **H** will be described by minimizing the function

$$F_2=\frac{1}{\pi}\int_0^{\pi}\left\{-p(\varphi)\frac{H^2\cos^2\varphi}{2zI_{12}}+f(p(\varphi))\right\}d\varphi, \tag{18}$$

where f specifies the contribution to the free energy due to the operation of the mechanism whereby the multidomain state arises due to localization of the elasticity of defects by domains surrounding them. In small fields, considering the second term in (6) as a small deviation in the distribution, which we denote by $\Delta p(\varphi)$, we write the functional (18) in the form

$$F_2=\frac{1}{\pi}\int_0^{\pi}\left\{-\Delta p(\varphi)\frac{H^2\cos^2\varphi}{2zI_{12}}+\frac{1}{2}\eta(\Delta p(\varphi))^2\right\}d\varphi, \tag{19}$$

where η is a positive, temperature-independent parameter equal to the second derivative $\eta=d^2f/dp^2$ determined at $p=1$. By minimizing F_2 we obtain an expression for the density of the distribution in the form

$$p(\varphi)=1+\frac{H^2}{2\eta I_{12}z}\left(\cos^2\varphi-\frac{1}{2}\right). \tag{20}$$

From (20) and (7) we find that, as is required by experiment, the parameter H_d^2 is independent of T and is given by

$$H_d^2 = 8\,\eta I_{12}\, z. \tag{21}$$

The behavior of the magnetostriction in $CoCl_2$ during the restructuring of the multidomain state in a magnetic field **H** can be explained by the action of a temperature-independent source of its multidomain character, which requires matching of the elasticity between the domains and between the domains and defects.

CONCLUSION

When a magnetic field **H** is turned on, the magnetostriction in $CoCl_2$ at the start of the process of destruction of the multidomain state is proportional to the square of **H** at all temperatures, and the temperature dependence of the coefficient of proportionality is similar to that for the temperature dependence of the spontaneous magnetostriction of the homogeneous state. An analysis of the magnetostriction reveals that the distribution of the domains is determined by their orientation in the magnetic field **H** and depends on the field but not on the temperature.

From the theoretically determined dependence of the magnetostriction on **H** it is found that the formation of the multidomain state in $CoCl_2$ is brought about by a magnetoelastic mechanism. The temperature independence of this mechanism is due to compensation of the elasticity of the defects by elasticity of the domains surrounding them. The matching of the stresses between domains leaves the domains in an equilibrium state and leads to screening of the interaction between defects.

The authors thank Prof. S. M. Ryabchenko for comments made in a discussion of this study.

*E-mail: lozenko@iop.kiev.ua

[1] M. M. Farztdinov, Usp. Fiz. Nauk **84**, 611 (1964) [Sov. Phys. Usp. **7**, 855 (1965)].
[2] V. G. Bar'yakhtar, A. N. Bogdanov, and D. A. Yablonskiĭ, Usp. Fiz. Nauk **156**, 47 (1988) [Sov. Phys. Usp. **31**, 810 (1988)].
[3] B. A. Ivanov, V. E. Kireev, and V. P. Voronov, Fiz. Nizk. Temp. **23**, 845 (1997) [Low Temp. Phys. **23**, 635 (1997)].
[4] A. S. Kovalev and A. M. Kosevich, Fiz. Nizk. Temp. **3**, 259 (1977) [Sov. J. Low Temp. Phys. **3**, 125 (1977)].
[5] I. E. Dzyaloshinskiĭ, JETP Lett. **25**, 414 (1977).
[6] M. M. Farztdinov, *Physics of Magnetic Domains in Antiferromagnets and Ferrites* [in Russian], Nauka, Moscow (1981).
[7] A. F. Lozenko, P. E. Parkhomchuk, S. M. Ryabchenko, and P. A. Trotsenko, Fiz. Nizk. Temp. **14**, 941 (1988) [Sov. J. Low Temp. Phys. **14**, 517 (1988)].
[8] V. M. Kalita, A. F. Lozenko, S. M. Ryabchenko, and P. A. Trotsenko, Ukr. Fiz. Zh. **43**, 1469 (1998).
[9] V. M. Kalita and A. F. Lozenko, Fiz. Nizk. Temp. **27**, 489 (2001) [Low Temp. Phys. **27**, 358 (2001)].
[10] J. W. Leech and A. J. Manuel, Proc. Phys. Soc. London, Sect. B **59**, 210 (1956).
[11] M. E. Lines, Phys. Rev. **131**, 546 (1963).
[12] V. M. Kalita, A. F. Lozenko, and S. M. Ryabchenko, Fiz. Nizk. Temp. **26**, 671 (2000) [Low Temp. Phys. **26**, 489 (2000)].
[13] M. K. Wilkinson, J. W. Cable, E. O. Wollan, and W. C. Koehler, Phys. Rev. **113**, 497 (1959).
[14] A. N. Bogdanov and I. E. Dragunov, Fiz. Nizk. Temp. **24**, 1136 (1998) [Low Temp. Phys. **24**, 852 (1998)].
[15] E. V. Gomonaj and V. M. Loktev, Fiz. Nizk. Temp. **25**, 699 (1999) [Low Temp. Phys. **25**, 520 (1999)].
[16] E. V. Gomonaj and V. M. Loktev, cond-mat/0010258 (2000).
[17] Z. A. Kazeĭ, M. V. Levanidov, and V. I. Sokolov, Prib. Tekh. Éksp. **2**, 196 (1981).
[18] Y. Y. Li, Phys. Rev. **101**, 1450 (1956).
[19] A. M. Kosevich, *Theory of the Crystal Lattice* [in Russian], Vishcha Skhola, Kharkov (1988).

Translated by Steve Torstveit

Interlayer coupling in Tb/Fe bilayers and Tb/Au/Fe trilayers with sharp or rough interface

E. V. Shypil,* A. M. Pogorily, D. I. Podyalovski, and Y. A. Pogoryelov

Institute of Magnetism, National Academy of Sciences of Ukraine, 36-b Vernadsky Ave., Kiev 03142, Ukraine

(Submitted March 5, 2001; revised April 24, 2001)
Fiz. Nizk. Temp. **27**, 879–885 (August 2001)

Bilayer films Fe/Tb (Tb on Fe) having a sharp interface and Tb/Fe (Fe on Tb) having a rough interface are prepared by molecular beam epitaxy to study the interlayer magnetic coupling. The magnetic properties of these bilayers are characterized *ex situ* using ferromagnetic resonance (FMR). The polar magnetooptical Kerr effect, and a SQUID magnetometer. The resulting perpendicular magnetic anisotropy (PMA) is discussed as an effect of the interlayer magnetic coupling. PMA is observed at rough as well as at sharp interfaces, and the anisotropy energies are estimated. When a monolayer of Au is interposed at either kind of interface, the PMA is observed to disappear and the overall magnetic moment increases. It is also shown that in ultrathin films the demagnetizing factor depends on the substrate roughness and should be taken into account in the FMR data.
[DOI: 10.1063/1.1399204]

INTRODUCTION

Coupling between ferromagnetic metal layers separated by nonmagnetic metal interlayers (first reported by Grünberg *et al.*[1] in Fe/Cr multilayers) has been observed in many systems: Fe/Al,[2] Fe/Ag,[3] Fe/Au,[2,4–7] Fe/Pd,[8] Fe/Cu.[8,9] Indirect exchange coupling between a ferromagnetic (Fe) layer and a rare-earth metal (Tb) separated by nonmagnetic metal interlayers (Cu, Au, Pt, Ta) has also been found.[10] The authors concluded that perpendicular magnetic anisotropy (PMA) in Fe/Tb multilayers is due to a short-range interaction between the nearest neighbors (Fe-Tb) at the interface. Besides this interaction, a long-range indirect exchange via a nonmagnetic metal interlayer was also observed. Although this first and the only work on Fe/M/Tb structures,[10] where M is a nonmagnetic metal, showed interesting results, it also raised many questions. It became clear that the coupling modes need further investigation.

It is important to note that magnetic properties of amorphous rare-earth–transition-metal alloy films and multilayers have been studied extensively in the past.[11–24] Among them the Tb–Fe system, which shows significant PMA and is already finding application as magnetooptic data storage media, has been investigated more. Tb/Fe multilayers show better promise for this purpose than do alloy films, and their magnetic properties have been also well investigated.[16–24] Antiferromagnetic coupling of Tb and Fe magnetic moments at the interface has been established,[15,25] similar to antiferromagnetic interactions in amorphous alloys. It was also noticed that when the thickness of the individual layers is small, a few monolayers (MLs), then the roughness of the interface and its effect on the interfacial magnetic interactions cannot be neglected.

As a consequence of the different atomic radii R and surface energies of Tb and Fe, different structures can be expected for Tb grown on Fe (Fe/Tb, sharper interface) or Fe grown on Tb (Tb/Fe, rougher interface).[26] This is shown schematically in Fig. 1. The magnetic properties of both kinds of interfaces have been studied on regard to PMA, and it was shown that the rough interface is a stronger source of PMA at room temperature than the sharp one.[19–21]

However, so far most of the studies reported on Tb/Fe, even those regarding rough and sharp interfaces,[19–24] have been done on multilayers, which are usually characterized as follows: (i) both kinds of interface, sharp and rough, are present together and it is impossible to have a clear picture as to each kind of interface; (ii) some thickness spread of the same layers is always present; (iii) conclusions are drawn with allowance for the integral picture of interactions in the multilayer, though it is clear that the coupling there is a sum of couplings at two kinds of interfaces plus a collective interaction of all the layers in the structure. All these aspects make the overall picture unclear and can affect the results.

Therefore to clarify the obscure points concerning magnetic interactions it is necessary to investigate *single* Tb/Fe and Fe/Tb interfaces. If the real thickness of the films participating in the coupling is taken into account, the problem can be formulated as follows: to use modern technology for the preparation of ultrathin films of high quality and to measure them with the corresponding accuracy.

The present work is undertaken to systematically study the interlayer interactions in single Tb/Fe bilayers by carefully preparing samples under the cleanest conditions with either a sharp or a rough interface. Also the effect of an Au monolayer introduced at the interface is investigated.

EXPERIMENTAL DETAILS

Two sets of samples, Fe/Tb bilayers and Fe/Au/Tb trilayers on quartz substrate were prepared by electron-beam evaporation in an MBE system with a background pressure of $(1-5)\times 10^{-10}$ Torr and a pressure of $(1-3)\times 10^{-9}$ Torr maintained during the film growth. To minimize interdiffusion of layers the substrate temperature during

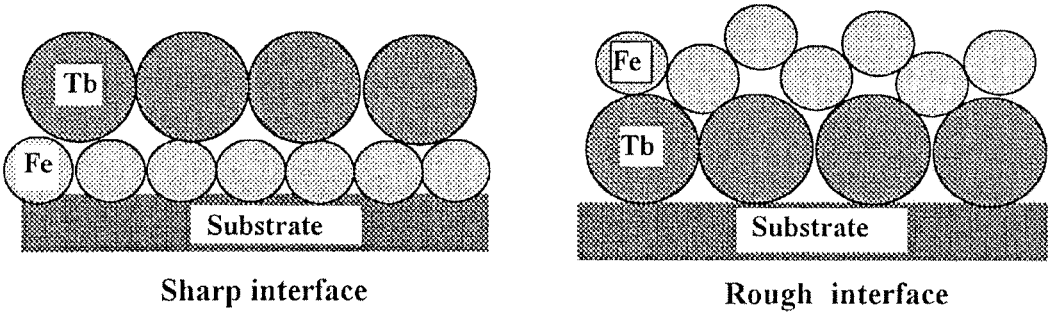

FIG. 1. Schematic picture of sharp and rough structural interfaces in Tb/Fe bilayers.

evaporation was kept no higher than 0 °C. The rates of evaporation did not exceed 0.4Å/s and were independently controlled with quartz crystal monitors. All the samples were protected with a 100 Å thick layer of Al_2O_3.

The very small amounts of magnetic material in the present ultrathin films make for difficult measurements. We used a SQUID magnetometer, ferromagnetic resonance (FMR), and the polar magnetooptical Kerr effect (PMOKE) for characterizing the films magnetically.

SQUID (Quantum Design MPMS-5S) measurements of the films were done with the magnetic field applied either perpendicular or parallel to the sample plane and at temperatures 77 to 300 K. The FMR was measured at room temperature by means of conventional modulation rf spectrometer at 9.41 GHz, with an applied magnetic field (up to 0.7 T) in the film plane. The PMOKE was measured at room temperature using a 630 nm laser in an applied field up to 1.8 T perpendicular to the film plane. These measurements allowed us to infer the effect of substrate roughness and film surface on shape anisotropy.

The thicknesses of the individual layers, d_{Fe} and d_{Tb}, were chosen on the basis of our previous experiments[27–29] and published data,[10] where ferrimagnetic ordering of Fe/Tb multilayers has been shown. This is caused by the interface properties, where the contact of ferromagnetic Fe and paramagnetic Tb causes a magnetic moment to be induced in the Tb layer. The coupling is not restricted to the first Tb ML. It was described by a ''magnetic interface'' of finite volume, spread into both layers close to the interface, where Fe and Tb atoms are antiparallel-coupled, showing PMA. The ratio of MLs, N_{Tb}/N_{Fe}, participating in the completed ''magnetic interface'' is usually in the range of 1 to 2, where N_{Tb} and N_{Fe} are the numbers of corresponding MLs involved in the coupling. In this range, the anisotropy energy is constant and has an approximate value $k_{\perp} \cong 5 \times 10^6$ erg/cm^3 (Ref. 29). It was also shown that the radius of pair interaction in this system is 7–15 Å.[27,29] Hence it follows that magnetic interactions at Tb/Fe interfaces begin when each of the layers, d_{Fe} and d_{Tb}, reaches 3 MLs.

Taking into account that the atomic radii are $R_{Fe} = 1.27$ Å and $R_{Tb} = 1.78$ Å, we chose $d_{Fe} = 8$ Å and $d_{Tb} = 12$ Å to obtain 3 MLs of Fe and 3 MLs of Tb. Samples with $d_{Tb} = 40$ Å were also prepared to study interfaces with an excess of Tb.

RESULTS AND DISCUSSION

Control films

Individual magnetic layers were initially studied. The hysteresis loop for an 8 Å Fe film at 295 and 77 K shows good saturation as well as low coercivity with in-plane magnetization (Fig. 2a). For 200 Å Tb and 12 Å Tb films the temperature dependence of the magnetization, measured with an applied field of 250 mT, are shown in Fig. 2b. To avoid distortion of the curves, substrate correction was not done. The thicker film shows the typical behavior for metallic Tb over the temperature range from 4 to 300 K—ferromagnetic below 218 K and paramagnetic above 230 K,[30] whereas the 12 Å Tb film shows paramagnetic behavior in the entire temperature range. The ferromagnetic resonance field was measured to be 49 mT for a 200 Å Fe film, in good agreement with published data of 50 mT (for the same frequency),[31,32] whereas the 8 Å Fe film showed a magnetic resonance line at

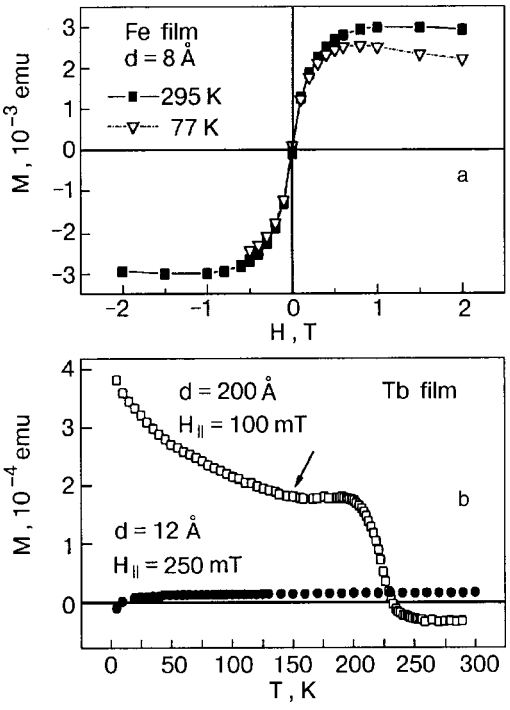

FIG. 2. Magnetization data for control films. *M* versus *H* for 8 Å Fe (a) and M versus T for 12 Å Tb (b) control films, measured with $H_{\|} = 250$ mT by SQUID. In (b) a Tb film 200 Å thick is also shown.

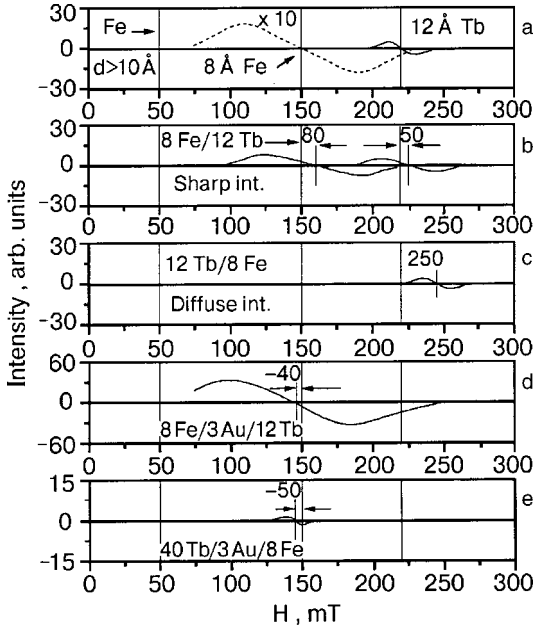

FIG. 3. FMR data for bilayers and trilayers. Positions of $H_{\|}$ are shown for three control films: thick Fe, thin Fe, and thin Tb films (a); bilayer with sharp interface (b); bilayer with rough interface (c); trilayer with Au introduced into sharp (d) and rough (e) interfaces.

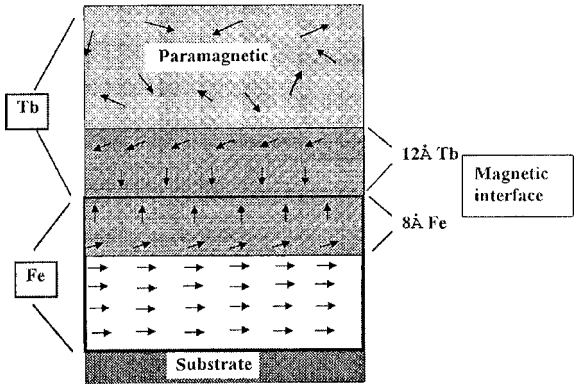

FIG. 4. Model of interlayer interaction at an Fe/Tb interface.

150 mT. In the case of a 12 Å Tb film the electron paramagnetic resonance occurred at 220 mT. These are shown in Fig. 3a.

It is well known that FMR for an in-plane magnetized film is described by the equation

$$(\omega/\gamma)^2 = H_{\|}[H_{\|} + N_{\text{eff}} M_s - 2k_{\perp}/M_s], \tag{1}$$

where $\omega = 2\pi f$; f is the microwave frequency; γ is the gyromagnetic ratio; $H_{\|}$ is the external magnetic field; M_s is the saturation magnetization; $N_{\text{eff}} = (N_{\perp} - N_{\|})$, where $N_{\|}$ and $N_{\perp}$ are the demagnetizing factors in-plane and perpendicular to film and $k_{\perp}$ is the PMA energy. An additional condition for the demagnetizing factors is $(N_{\perp} + 2N_{\|}) = 4\pi$. The influence of internal stresses caused by the difference in thermal expansion of the film and substrate are taken into account in the value of N_{eff}.

It is also known that for the thick Fe film $N_{\perp} = 4\pi$ and therefore $N_{\|} = 0$. However for the ultrathin film, when the film thickness is comparable to the substrate roughness and the film becomes wavy, $N_{\perp} \neq 4\pi$. Hence, for the thinner Fe film the shape anisotropy changes compared to a perfectly flat film.[33] It has been shown that in the limit of few atomic layers the average demagnetizing factor $N_{\perp}$ for a film containing n atomic layers is reduced to $N_{\perp} = 4\pi(1 - A/n)$ (where A is a constant, having definite values for layers with different structure),[34] while the magnetization changes much more slowly.[33] It has also been shown by Reiger[35] that ultrathin epitaxial Fe films show the full bulk atomic magnetic moment even for the first Fe ML.

The roughness of the quartz substrate used in the current work was measured by an AFM and was estimated as 5–10 Å, which is comparable to the thickness of the 8 Å Fe. The FMR line for the 8 Å Fe film was shifted to higher H compared to the thick Fe film. This shift can be attributed to the change of demagnetizing factors; $N_{\perp}$ and $N_{\|}$ were calculated using $M_s = 1760$ G and $H_{\|} = 150$ mT: $N_{\perp} = 6.56$ and $N_{\|} = 3.0$.

Coming back to the magnetic properties of the control films, our above data show that the 8 Å Fe film is ferromagnetic at room temperature whereas the 12 Å Tb film is paramagnetic even down to 5 K.

Bilayers—the interlayer interaction at the Fe/Tb interface

It has been shown that when thin Fe and Tb films are layered on one another, a small magnetic moment is induced in the thin Tb film by the Ruderman–Kittel–Kasuda–Yosida (RKKY) interaction.[10,26] Moreover, antiferromagnetic coupling of Tb and Fe magnetic moments at the interface has also been established,[15,25] similar to the antiferromagnetic interactions in amorphous alloys. Hence, three kinds of interactions are to be discussed at Fe/Tb interfaces: (i) between Fe–Tb atoms with antiparallel orientation, which gives the main contribution to the PMA. The RKKY interaction is evaluated for this case as $D_{\text{Fe–Tb}} = -2.152 \times 10^{-14}$ erg/$r^3_{\text{Fe–Tb}}$, where D is an interaction constant and $r_{\text{Fe–Tb}} = 3.03$ Å;[36] (ii) the ferromagnetic interaction between Fe – Fe atoms, which is one order of magnitude smaller, $D_{\text{Fe–Fe}} = -4.805 \times 10^{-15}$ erg/$r^3_{\text{Fe–Fe}}$, where $r_{\text{Fe–Fe}} = 2.5$ Å; (iii) the interaction between Tb atoms which are magnetized at the interface. It is also ferromagnetic, with $D_{\text{Tb–Tb}} = 3.47 \times 10^{-16}$ erg/$r^3_{\text{Tb–Tb}}$, where $r_{\text{Tb–Tb}} = 3.5$ Å. The interaction between Fe atoms gives a magnetization component in the plane of the film, while the Fe–Tb interaction results in a perpendicular magnetization component (Fig. 4). In bare outlines this model was first discussed by Yamauchi *et al.*,[25] where they described four regions in the magnetic structure of artificially layered Tb–Fe films: ferrimagnetically coupled Tb–Fe, ferromagnetic Fe, ferromagnetic Tb, and magnetically compensated Tb regions. Later this magnetic structure was improved by Shan and Sellmyer,[15] who emphasized that nanoscale layer thicknesses should be used to show large PMA. Hoffmann and Scherschlicht[10] confirmed this simple model of the multilayer system: ferromagnetic Fe (in-plane anisotropy)/ferrimagnetic Fe/Tb (perpendicular anisotropy)/ paramagnetic Tb/ferrimagnetic Fe/Tb (perpendicular anisotropy)/... . In Fig. 4 we show the detailed magnetic

TABLE I. Polar magnetooptical Kerr effect data.

Sample	Θ_K, min	H_s, mT	Θ_{Ks}, min
8 Fe	11.0		
12 Tb	5.9		
8 Fe/12 Tb	12.1	30	0.75
8 Fe/40 Tb	11.8	240	0.80
12 Tb/8 Fe	9.4	150	0.12
40 Tb/8 Fe	11.3	15	1.0
8 Fe/3 Au/12 Tb	13.6	550	7.3
8 Fe/3 Au/40 Tb	11.8	520	5.5
12 Tb/3 Au/8 Fe	11.8	590	5.5
40 Tb/3 Au/8 Fe	11.7	590	5.3

Θ_K is the PMOKE angle at $H=1.7$ T (high-field component);
H_s is the saturation magnetic field (lower-field component);
Θ_{Ks} is the PMOKE angle of saturation (lower field component).

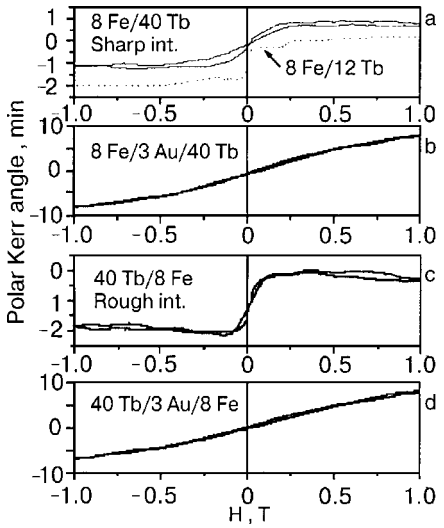

FIG. 5. PMOKE loops for bilayers (a and c) and trilayers (b and d). Only the low-field component is shown here.

structure of one interface. One can see that if d_{Fe} and d_{Tb} are chosen equal to the ''magnetic interface,'' the in-plane component will tend to a minimum.

Magnetic resonance signals for two samples, one for each of two pairs of bilayers which were prepared, (i) 8 Fe/12 Tb and 8 Fe/40 Tb (with sharp interface) and (ii) 12 Tb/8 Fe and 40 Tb/8 Fe (with rough interface), are shown in Fig. 3b, 3c. (Henceforth the number proceeding the chemical symbol refers to the layer thickness in Å.) Data for 8 Fe/12 Tb show two resonance lines close to that for the control films 8 Fe and 12 Tb. The magnetic resonance signal for the rough 12 Tb/8 Fe interface is significantly different from those of 8 Fe/12 Tb. The Fe signal is absent, and the Tb line is shifted 5 times as much as in Fig. 3b.

Table I shows PMOKE data for: 1) control films, 2) bilayers without Au, and 3) trilayers with Au. The in-plane magnetization component, which is always present in the natural state and characterizes the Fe–Fe interactions, is usually observed at high fields (>1 T) and was well seen for all the samples. The PMOKE signals were not saturated in our experiment up to the maximal field. That is why the PMOKE angles at $H=1.7$ T are given for all the samples for comparison.

Besides the high-field component, other important features could be seen in the PMOKE data for the bilayers and trilayers as well. For the bilayers we could see two directions of magnetization. The perpendicular magnetization component was always observed at low fields, usually up to 100 mT. This follows from the perpendicular geometry that is used in the PMOKE method. We present the saturation magnetic fields and saturated PMOKE angles for bilayers.

The shift of $H_{\parallel}$ for both lines to higher fields compared with the control films in the FMR experiment indicates the appearance of PMA in the bilayers due to the Fe–Tb interaction. The magnetization now is out of the plane. The PMOKE data (Fig. 5a and 5c) support this conclusion. In other words, the PMA energy is a measure of the Fe–Tb interaction at the interface. Calculation of the anisotropy energy based on Eq. (1) for the sharp 8 Fe/12 Tb interface gives the value $k_{\perp}=0.7\times10^5$ erg/cm^3. The PMOKE data show a rotation angle of 0.75 min caused by this perpendicular magnetic component.

Having an excess of Tb, the 8 Fe/40 Tb sample produces almost the same rotation (0.8 min) which besides occurs in almost one order wider field range (240 mT as against 30 mT). This can be interpreted as due to Tb layers with in-plane magnetization in addition to the ''magnetic interface'' (Fig. 4). For the case of 12 Tb/8 Fe (rough interface) the PMOKE angle is only 0.12 min. This is connected with a great variety of angles between Fe and Tb magnetic moments, due to interface roughness, also resulting in the extension of the field range, where this interaction occurs (150 mT as compared to 30 mT for 8 Fe/12 Tb). There is a significant decrease of the Fe signal, and no FMR signal was observed (Fig. 3c). For the bilayers with rough interfaces the ultrathin Fe film can be in the superparamagnetic state, leading to disappearance of the FMR signal. With more Tb atoms, for the 40 Tb/8 Fe bilayer, the perpendicular rotation increases significantly (to 1.0 min from 0.12 min for 12 Tb/8 Fe) and also the range of Fe–Tb interaction becomes narrower (15 mT against 150 mT for 12 Tb/8 Fe; see Table I). This means that the sharp and rough interfaces, having a different distribution of atoms, need different ratios of Fe and Tb monolayers participating in the completed ''magnetic interface.'' In other words, the sharp and rough interfaces with the same respective layer thicknesses have different effective interface compositions, making direct correlation to the PMA less straightforward.

Interaction in Fe/Au/Tb trilayers

To further understand the extent of coupling in the Fe-Tb system, we introduced one ML of Au at the interface. FMR signals for the trilayers are shown in Fig. 3d and 3e, only one FMR signal was observed. It is easily seen that the introduction of Au at the interface causes a significant decrease in the resonance field as compared to the field for the 8 Fe/12 Tb bilayer. Now $H_{\parallel}$ is even smaller than that for the 8 Fe film. This means that only one Au ML interposed between Fe and Tb layers was enough to shield the short-range magnetic interactions which resulted in PMA. This is further illustrated in the PMOKE data (Fig. 5). It is natural to suppose that all the magnetic moments in such trilayers are already in the film plane. Though the same PMOKE data for the trilayers,

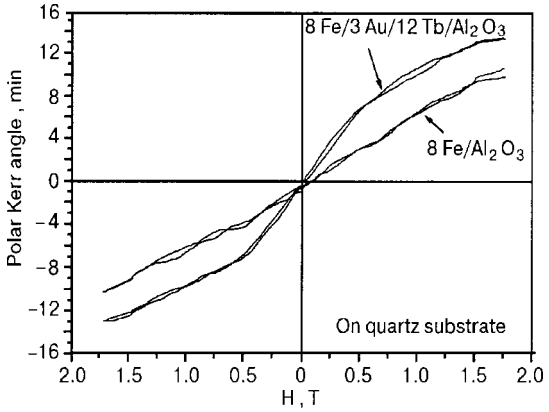

FIG. 6. PMOKE loop for a trilayer 8 Å Fe/3 Å Au/12 Å Tb compared with an 8 Å Fe control film.

as compared with the control Fe film (Fig. 6), show that some small loop of magnetization with a jog at higher fields (500–600 mT) is still present. This means that the angle between Fe and Tb magnetic moments is nonzero. The Fe and Tb layers still interact via the monolayer of Au. The PMOKE angles and fields for the jogs are shown in Table I for the different trilayers with Au.

The other characteristic feature is the increase of the total magnetic moment in the trilayers (Fig. 6). The same changes of the PMOKE loop shape are observed for both kinds of interface. The small values of the Kerr rotation angles and the weak FMR signals for the case of the rough interface again indicate that Fe magnetic moments are highly disordered there.

Thus one ML of Au at the Fe–Tb interface dramatically affects the magnetic interactions, entirely eliminating the short-range exchange between Fe and Tb atoms. Instead, a long-range indirect exchange interaction via the nonmagnetic Au interlayer is observed, leading to an increase in the total magnetic moment. Pan *et al.*[37] have proposed that a magnetic moment is induced in the Au by the Fe to describe the enhancement of the Fe magnetic moment in an FeAu alloy film prepared by alternate monatomic deposition. Hoffman also observed that the net magnetic moment for Fe/Au/Tb/Au multilayers is larger than that of pure Fe layers.[10] Magnetic moment induced in Tb still exists. Its orientation with respect to the Fe moment is a point of future study.

CONCLUSIONS

In summary, using FMR and PMOKE methods we investigated the magnetic interactions in the Fe/Tb bilayer system with sharp as well as rough interfaces. The exchange interaction at the Fe–Tb interface induces a magnetic moment in the thin Tb film that results in two FMR signals, which are shifted from that of free Fe and Tb films. This shift has been interpreted as an indication of attributed Tb–Fe interaction resulting in a perpendicular anisotropy.

The different distribution of atoms in sharp and rough interfaces with the same respective layer thicknesses leads to different environments for the Tb–Fe interactions and hence to different effective compositions.

One monolayer of Au interposed into single Tb-Fe interfaces of both kinds destroys the ''magnetic interface,'' breaking the short-range interaction. Instead a long-range indirect exchange via the nonmagnetic Au interlayer appears.

We thank Jagadeesh S. Moodera, Francis Bitter Magnet Lab, MIT, Cambridge, Massachusetts, USA, for stimulating this work and giving help with preparation of the samples and to Greetha P. Berera for the SQUID measurements. This work was supported by CRDF UP2-2117 and NSF International Collaborative Grant No. 9940368.

*E-mail: elena@im.imag.kiev.ua

[1] P. Grunberg, R. Schreiber, Y. Pang, M. B. Brodski, and H. Sowers, Phys. Rev. Lett. **57**, 2442 (1986).
[2] A. Fuss, S. Demokritov, P. Grünberg, and W. Zinn, J. Magn. Magn. Mater. **103**, L221 (1992).
[3] J. Unguris, R. J. Celotta, and D. T. Pierce, J. Magn. Magn. Mater. **127**, 205 (1993).
[4] J. Unguris, R. J. Celotta, and D. T. Pierce, J. Appl. Phys. **75**, 6437 (1994).
[5] J. Unguris, R. J. Celotta, and D. T. Pierce, Phys. Rev. Lett. **79**, 2734 (1997).
[6] S. N. Okuno and K. Inomata, Phys. Rev. B **51**, 6139 (1995).
[7] U. Rücker, S. Demokritov, E. Tsymbal, P. Grünberg, and W. Zinn, J. Appl. Phys. **78**, 387 (1995).
[8] Z. Celinski and B. Heinrich, J. Magn. Magn. Mater. **99**, L25 (1991)91).
[9] F. Pan, K. Tao, T. Yang, and B. X. Liu, Phys. Status Solidi A **135**, 573 (1993).
[10] H. Hoffmann and R. Scherschlicht, Fesfkörperprobleme (Helbig, Vieweg, Braunschweig/Wiesbaden (1998), p. 275.
[11] P. Chaudhari, J. J. Cuomo, and R. J. Gambino, Appl. Phys. Lett. **22**, 337 (1973).
[12] Y. Mimura and N. Imamura, Appl. Phys. Lett. **28**, 746 (1976).
[13] N. Sato, Y. Aoki, and S. Miyaoka, IEEE Trans. Magn. **MAG-20**, 1022 (1984).
[14] N. Sato, J. Appl. Phys. **59**, 2514 (1986).
[15] Z. S. Shan and D. J. Sellmyer, Phys. Rev. B **42**, 10433 (1990).
[16] B. Scholz, R. A. Brand, and W. Keune, Hyperfine Interact. **68**, 409 (1991)91).
[17] A. Fnidiki, J. Juraszek, J. Teillet, F. Richomme, and J. P. Lebertois, J. Magn. Magn. Mater. **165**, 405 (1997).
[18] A. E. Freitag and A. R. Chowdhury, J. Appl. Phys. **82**, 5039 (1997).
[19] J. Juraszek, A. Fnidiki, and J. Teillet, J. Appl. Phys. **84**, 379 (1998).
[20] W. S. Kirn, W. Andra, and W. Kleeman, Phys. Rev. B **58**, 6346 (1998).
[21] W. S. Kirn, W. Kleeman, J. Tappert, and W. Keune, J. Appl. Phys. **84**, 4384 (1998).
[22] B. Lanchava and H. Hoffman, J. Magn. Magn. Mater. **192**, 403 (1999).
[23] A. E. Freitag and A. R. Chowdhury, J. Appl. Phys. **85**, 4696 (1999).
[24] A. E. Freitag and A. R. Chowdhury, J. Appl. Phys. **85**, 5756 (1999).
[25] K. Yamauchi, K. Habu, and N. Sato, J. Appl. Phys. **64**, 5748 (1988).
[26] B. Scholz, R. A. Brand, and W. Keune, Phys. Rev. B **50**, 2537 (1994).
[27] O. M. Kuz'mak, E. V. Shipil, V. I. Shevchenko, and S. Ya. Kharitonski, Ukr. Fiz. Zh. **36**, 765 (1991).
[28] O. Kuz'mak, A. Pogorily, and V. Shevchenko, J. Magn. Magn. Mater. **148**, 36 (1995).
[29] E. Shipil and A. Pogorily, J. Magn. Magn. Mater. **157/158**, 293 (1996).
[30] W. C. Thobum, S. Legvold, and F. H. Spedding, Phys. Rev. **112**, 56 (1958).
[31] R. F. Soohoo, *Magnetic Thin Films*, Harper and Row, New York (1965).
[32] J. R. Fermin, Antonio Azevedo, F. M. de Aguiar, Biao Li, and S. M. Rezende, J. Appl. Phys. **85**, 7316 (1999).
[33] M. Farle, Rep. Prog. Phys. **61**, 755 (1998).
[34] B. Heinrich, *Ultrathin Magnetic Structures*, Vols. I and II Berlin, Springer (1994).
[35] E. Reiger, E. Reinwald, G. Garreeu, M. Ernst, M. Zolfl, F. Bensch, S. Bauer, H. Preis, and G. Bayreuther [to be published in J. Appl. Phys. (MMM'99, paper DQ 02)].
[36] Y. J. Wang, H. Cai, Q. Tang, K. M. Yang, J. Y. Li, and J. L. Wang, J. Magn. Magn. Mater. **68**, 84 (1987).
[37] F. Pan, K. Tao, and B. X. Liu, J. Appl. Phys. **74**, 1929 (1993).

This article was published in English in the original Russian journal. Reproduced here with stylistic changes by AIP.

Magnetooptical studies of the $H-T$ phase diagram of an Fe/Si multilayered film

A. B. Chizhik,* D. N. Merenkov, and S. L. Gnatchenko

B. Verkin Institute for Low Temperature Physics and Engineering, National Academy of Sciences of Ukraine, pr. Lenina 47, 61103 Kharkov, Ukraine

K. Fronc and R. Zuberek

Institute of Physics, Polish Academy of Sciences, Al. Lotnikow 32/46, 02-668 Warsaw, Poland
(Submitted March 21, 2001; revised April 11, 2001)
Fiz. Nizk. Temp. **27**, 886–895 (August 2001)

The magnetization reversal of a multilayered Fe/Si film having cubic magnetocrystalline anisotropy is investigated in the temperature interval 25–300 K by magnetooptical methods. It is found that the growth of the biquadratic exchange interaction as the temperature is lowered causes a spontaneous second-order phase transition from a collinear antiferromagnetic state to a noncollinear state. The presence of cubic anisotropy in the film gives rise to spontaneous and magnetic-field-induced first-order phase transitions between noncollinear states. Magnetooptical studies permit constructing the $H-T$ magnetic phase diagram of the multilayered Fe/Si film for an orientation of the external field along the hard magnetization axis [110]. A calculation of the $H-T$ phase diagram in the framework of a model taking into account the bilinear exchange and cubic anisotropy, with constants I_1 and K that are assumed to be independent of temperature, and also the biquadratic exchange with a linearly temperature-dependent constant I_2. Satisfactory agreement is obtained between the experimental and calculated phase diagrams. [DOI: 10.1063/1.1399205]

INTRODUCTION

The magnetic properties of Fe/Si layered structures have been investigated quite intensively in recent years.[1–6] Particular interest has been devoted to the spin configurations that are stable in this structure and to the study of their behavior as a function of temperature and external magnetic field, from which one can judge the character of the exchange interaction between iron layers. As the temperature is changed one observes a transformation of the magnetization curves of Fe/Si films,[1,3,6] a phenomenon that finds explanation in the framework of a theory which takes into account the competition of the bilinear and biquadratic exchange between layers of a ferromagnetic metal.[7,8] It has been established[3,6] that the changing relationship between the energies of the bilinear and biquadratic exchange interactions with changing temperature leads to a change in the equilibrium spin configuration of the ground state of the system and affects the spin configurations that are stable in the magnetic field. Up till now, however, the $H-T$ phase diagram of an Fe/Si layered structure has not been constructed. The goal of the present study was to investigate the magnetization reversal process in a multilayered Fe/Si film over a wide range of temperatures, to analyze the experimental results in the framework of a model that takes into account the different temperature dependence of the bilinear and biquadratic exchange interaction constants, and to construct the $H-T$ magnetic phase diagram.

EXPERIMENT

We present the results of a study of the magnetization reversal process in an $(\mathrm{Fe}30\,\text{Å}/\mathrm{Si}15\,\text{Å})\times 11$ multilayered film prepared by dc magnetron sputtering. A single-crystal GaAs wafer was used as the substrate. The investigation was done using the meridional Kerr effect. The sample was placed in an optical helium cryostat, permitting measurements to be made in the temperature interval 25–300 K. The magnetic field was imposed parallel to the plane of the film. The experimental apparatus is described in greater detail in Ref. 9, and the preparation of the sample, in Ref. 5.

Magnetic resonance studies showed that the Fe/Si multilayered film has cubic anisotropy and an easy axis oriented in the plane of the film along the [100] and [010] directions.[5] Magnetooptical studies at room temperature lead to the conclusion that collinear and noncollinear stable spin structures exist in an Fe/Si multilayered film, and these structure can be found in a stable or in a metastable state.[5] In the present study the magnetization reversal process was investigated in the temperature interval 25–300 K. From the experimental results the $H-T$ magnetic phase diagram of the Fe/Si multilayered structure is constructed in the case when the magnetic field is directed along the hard axis [110].

Figure 1 shows typical curves of the field dependence of the angle of rotation Φ of the plane of polarization measured for three temperatures in various magnetic field intervals. The experimental curves are normalized to Φ_s, the value of the angle of rotation of the plane of polarization in the saturated state. The characteristic features on the $\Phi(H)$ curves due to various phase transitions are demonstrated in Fig. 1a–e.

The curves shown in Fig. 1a, 1b, 1c were obtained at a temperature of 300 K. As we see in Fig. 1a, the magnetization process begins from a state in which the Kerr rotation is zero. In a certain interval of fields the magnetization reversal

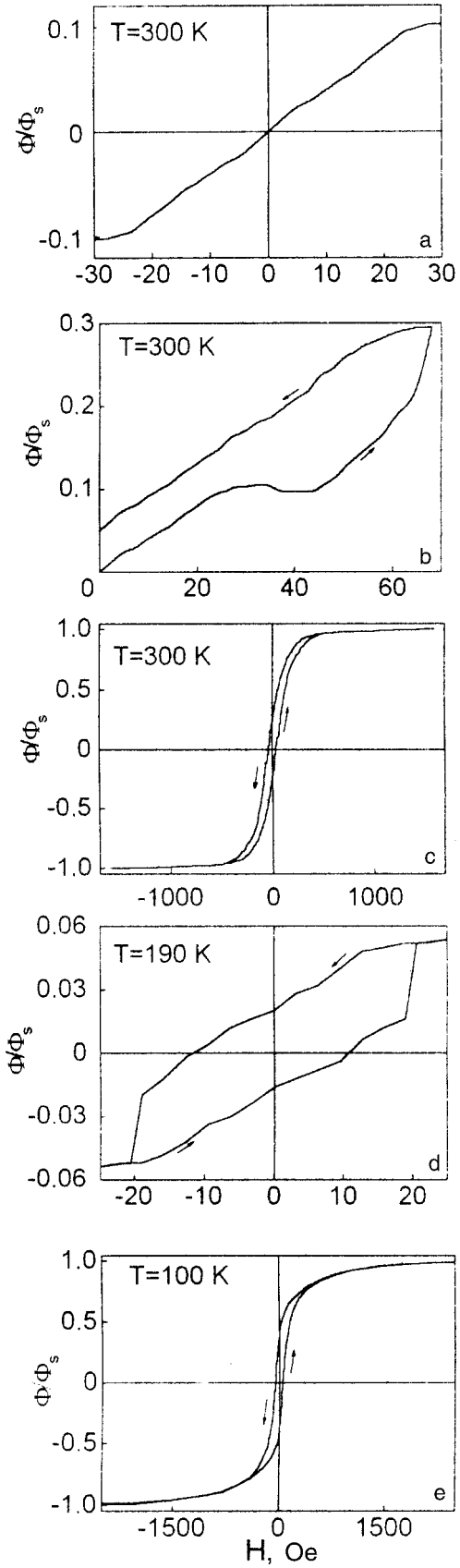

FIG. 1. Field dependence of the angle of rotation of the plane of polarized of reflected light, measured in an (Fe30 Å/Si15Å)×11 multilayered film at different temperatures.

has a reversible nonhysteretic character. In a field of around 70 Oe (Fig. 1b) a relatively sharp increase in the Kerr rotation angle is observed, after which, as the field is decreased, the system returns to a state with a nonzero value of Φ at $H=0$. As the field is increased further (Fig. 1c) a smooth growth of the rotation angle is observed, going to saturation at $H\approx 1500$ Oe. Decreasing the magnetic field to zero after the film has been in the saturated state returns the system to a state with a nonzero value of Φ.

As the temperature is lowered one observes the following changes in the field dependence of the Kerr effect:

—In the temperature interval 195–300 K near $H=0$ (Fig. 1a) a monotonic nonhysteretic variation of the rotation angle occurs. At temperatures of 170–195 K the $\Phi(H)$ curve in low fields exhibit a jump, and magnetization reversal in the neighborhood of $H=0$ is accompanied by hysteresis. The $\Phi(H)$ curve measured at $T=190$ K in low fields is shown in Fig. 1d.

—The feature near the field $H\approx 70$ Oe on the room-temperature $\Phi(H)$ curves (Fig. 1b) persists in the temperature interval 170–300 K. The value of the magnetic field that must be reached before the system returns to a state with nonzero Φ at $H=0$ decreases with decreasing temperature.

—At temperatures below 170 K the shape of the magnetization-reversal curve changes. Figure 1e shows the field dependence of the Kerr effect measured at $T=100$ K. This curve has none of the features observed in low fields at $T>170$ K. The magnetization reversal is accompanied by hysteresis for $H<500$ Oe. In higher fields one observes a monotonic nonhysteretic growth of the Kerr rotation with increasing field, just as at high temperatures.

—With decreasing temperature the value of the field at which saturation is observed on the $\Phi(H)$ curve increases.

In addition to the field curves $\Phi(H)$ we also measured the temperature dependence of the Kerr effect in the absence of magnetic field (Fig. 2). At $T=300$ K a state with zero Kerr rotation at $H=0$ was created in the Fe/Si film under study by means of magnetization reversal in low fields. Then the temperature was lowered and the $\Phi(T)$ curve was measured. In the temperature interval 195–300 K the value of Φ equals zero. At $T<195$ K a smooth increase in the rotation angle with decreasing temperature is observed, and at a tempera-

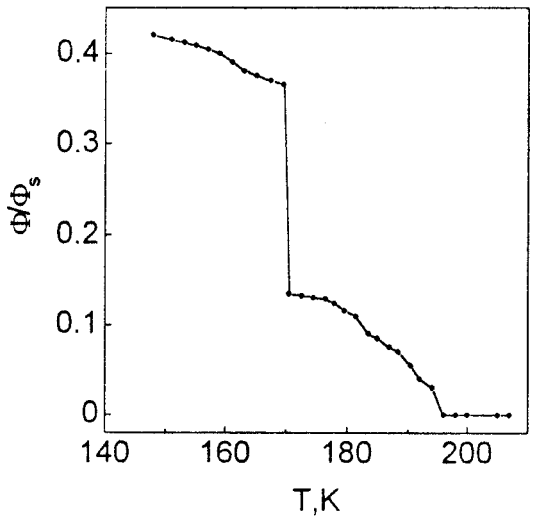

FIG. 2. Temperature dependence of the angle of rotation of the plane of polarization of reflected light, measured in zero magnetic field.

ture of around 170 K the $\Phi(T)$ curve has a jump. As the temperature is lowered further, the Kerr rotation angle again increases smoothly.

CALCULATION OF THE PHASE DIAGRAM

The phase diagram was calculated in the framework of a theoretical model taking into account the bilinear and biquadratic exchange interaction between two magnetic layers of iron separated by nonmagnetic spacer layers and the cubic anisotropy in the iron layers.[7,8] It was assumed that the magnetic moments inside the iron layer are ordered ferromagnetically and that the magnetization in the first and second iron layers lies at angles of θ_1 and θ_2 to the easy axis (the [100] direction).

The expression for the energy of this system has the form

$$E = I_1 \cos(\theta_1 - \theta_2) + I_2 \cos 2(\theta_1 - \theta_2) + Kd(\cos^2\theta_1 \sin^2\theta_1 + \cos^2\theta_2 \sin^2\theta_2) - HMd \times [\cos(\theta_1 - \varphi) + \cos(\theta_2 - \varphi)], \quad (1)$$

where I_1 and I_2 are the bilinear and biquadratic exchange interaction constants, respectively, K is the cubic anisotropy constant, H is the external magnetic field, M is the saturation magnetization, d is the thickness of the Fe layer, and φ is the angle between the [100] direction and the direction of the magnetic field.

To determine the stable spin configurations, which in the magnetic system under study can exist as stable or metastable, we did a numerical analysis of Eq. (1) under the condition $H=0$. As was shown in Refs. 1 and 6, the bilinear exchange constant and cubic anisotropy constant in a multilayered Fe/Si system depend on temperature to a considerably smaller degree than does the biquadratic exchange constant. In view of this, we took only the temperature dependence of the biquadratic exchange into account in the investigated model. Thus the change in spin configuration of the system upon a change in temperature is determined by the constant I_2. We had previously obtained the values of the constants $I_1 = 0.6\ \text{erg/cm}^2$ and $K = 2.4\times 10^5\ \text{erg/cm}^2$ at room temperature.[6] From the results of the numerical calculations we constructed three-dimensional plots of $E(\theta_1, \theta_2)$, from which we established the values of the pairs of angles θ_1 and θ_2 for the stable spin configurations. The calculated functions $\theta_1(I_2)$ and $\theta_2(I_2)$ are presented in Fig. 3. In Fig. 3a these functions are shown for spin configurations corresponding to the absolute minimum of the energy, i.e., for stable states. Figure 3b shows the functions $\theta_1(I_2)$ and $\theta_2(I_2)$ for spin configurations that correspond to local minima on the energy surface $E(\theta_1, \theta_2)$ and can exist as metastable states.

These calculations showed that the following spin configurations, corresponding to different values of the biquadratic exchange constant I_2, can exist in the system under study in the absence of an external magnetic field (the form of the spin configurations is shown in Fig. 4):

1) for $I_2 < 0.37\ \text{erg/cm}^2$ the collinear antiferromagnetic configuration A is stable, and the noncollinear configurations B can exist in a metastable state;

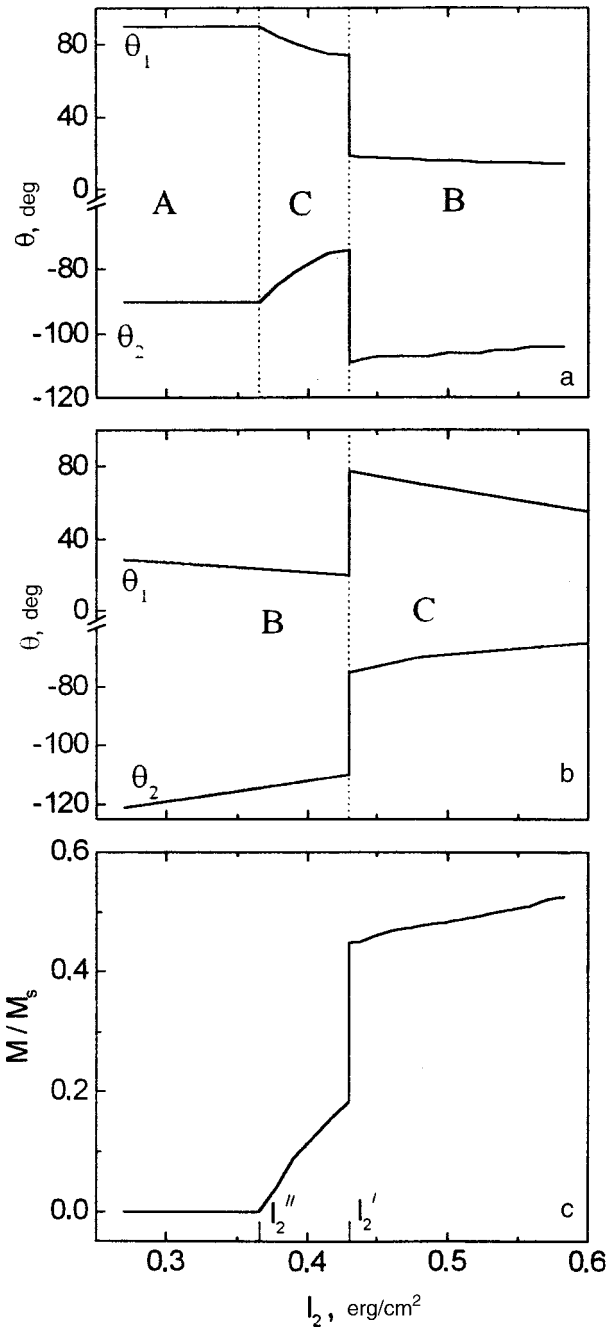

FIG. 3. Calculated curves of the angles θ_1 and θ_2 for stable (a) and metastable (b) configurations and of the projection of the total magnetization M/M_s on the [110] direction (c) as functions of the biquadratic exchange interaction parameter I_2. A, B, and C are the existence regions of the spin configurations shown in Fig. 4.

2) for $0.37\ \text{erg/cm}^2 < I_2 < 0.43\ \text{erg/cm}^2$ the noncollinear configurations C are stable, and the noncollinear configurations B can exist as metastable;

3) for $I_2 > 0.43\ \text{erg/cm}^2$ the noncollinear configurations B are stable, and the noncollinear configurations C can exist in a metastable state.

For comparison with the experimental results we calculated the projection of the total magnetization on the [110] direction as a function of the constant I_2. Figure 3c shows the $M(I_2)$ curve normalized to the saturation magnetization M_s. The choice of the [110] direction is motivated by the fact that the value of the Kerr rotation angle in the experi-

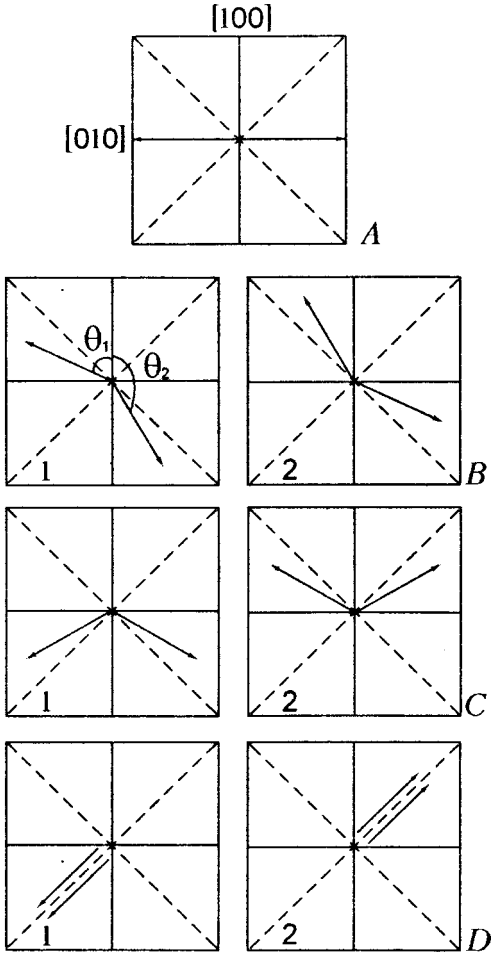

FIG. 4. Stable spin configurations: *A*—the collinear configuration; *B*,*C*—noncollinear configurations; *D*—the collinear configuration in a magnetic field.

ments was proportional to the projection of the magnetization on this axis.

We also did a calculation of the field dependence of the magnetization of the system. The values of the angles θ_1 and θ_2 in the stable configurations were calculated for different values of H at fixed I_2. Then, knowing θ_1 and θ_2, we determined the projection of the magnetization on the [110] direction, along which the external field was oriented. Figure 5 shows the three characteristic $M(H)$ curves in different magnetic-field scales; the curves were calculated for three different initial spin configurations that are stable in zero field (these curves are also normalized to the saturation magnetization M_s):

1. $I_2 = 0.27\ \mathrm{erg/cm^2}$ (Fig. 5a). In the absence of field the initial antiferromagnetic collinear spin configuration *A* is realized. In a magnetic field the spin structure becomes noncollinear (state *C*), and the magnetization is nonzero. We note that in the *C* configuration in a magnetic field $\mathbf{H} \| [110]$ the relation $\theta_2 = 90° + \theta_1$ ceases to hold, i.e., the magnetic configuration *C* becomes asymmetric with respect to the direction of the external field. Increasing the field leads to a smooth increase in the magnetization on account of a change in the angle between the magnetic moments of the iron layers in the state *C* and then to a first-order phase transition to the state *B*, which is accompanied by a jump on the $M(H)$ curve. On further increase in field one observes a smooth growth of the magnetization on account of a change in the degree of noncollinearity of the state *B*, and then the system undergoes a second-order phase transition to the saturated collinear state *D*.

2. $I_2 = 0.38\ \mathrm{erg/cm^2}$ (Fig. 5b). In the absence of field the noncollinear spin configuration *C* is stable. Magnetization reversal is accompanied by a jump in magnetization, corresponding to a first-order phase transition between two noncollinear states *C*. Increasing the field initially leads, as in the first case, to a smooth increase in the magnetization in the state *C*, and then there is a first-order phase transition from this state to state *B* and a subsequent smooth increase in the magnetization in this state, and finally a second-order phase transition to the saturated collinear state *D*.

3. $I_2 = 0.47\ \mathrm{erg/cm^2}$ (Fig. 5c). In the absence of field the noncollinear spin configuration *B* is stable. Magnetization reversal is accompanied by a jump in the magnetization corresponding to a first-order phase transition between two noncollinear states *B*. An increase in magnetic field is accompanied by a smooth increase in the magnetization, corresponding to a decrease in the angle between the magnetic moments of the iron layers in the noncollinear spin configuration *B* with a subsequent second-order transition to the saturated collinear state *D*.

From the results of these calculations we constructed the phase diagram in the coordinates $H-I_2$ (Fig. 6). The solid lines represent lines of first-order phase transitions between the noncollinear states *B* and *C* and also between noncollinear states of the same type (type *B* or *C*). The line of first-order phase transitions between states of the same type corresponds to $H=0$ on the phase diagram. On this line there exist two singular points. Point I_2' corresponds to a first-order phase transition between the noncollinear states *B* and *C*. The point I_2'' corresponds to a second-order phase transition between collinear antiferromagnetic state *A* and the noncollinear state *C*. We note that this point is simultaneously a critical point terminating a line of phase transitions between states of type *C*.

Lines of second-order phase transitions from the noncollinear state B to a collinear saturated state *D* are shown by a dotted line on the phase diagram (Fig. 6).

DISCUSSION

Let us compare our experimental data with the results of a calculation. We first compare the temperature dependence of the Kerr rotation angle (Fig. 2) with the calculated dependence of the magnetization $M(I_2)$ shown in Fig. 3c. Since the biquadratic exchange interaction increases with decreasing temperature, one can conclude that these curves are in good qualitative agreement. After analyzing the experimental dependence $\Phi(T)$ and comparing it to the calculated dependence $M(I_2)$, we may conclude that at $T \approx 195\ \mathrm{K}$ the Fe/Si multilayered film undergoes a spontaneous second-order phase transition between the collinear antiferromagnetic state *A* and the noncollinear state *C*, and at $T \approx 170\ \mathrm{K}$ there is a spontaneous first-order phase transition between the noncollinear configurations *B* and *C*, which is accompanied by a jump on the $\Phi(T)$ curve.

Lowering the temperature leads to a decrease in the angle between the magnetic moments of the iron layers in

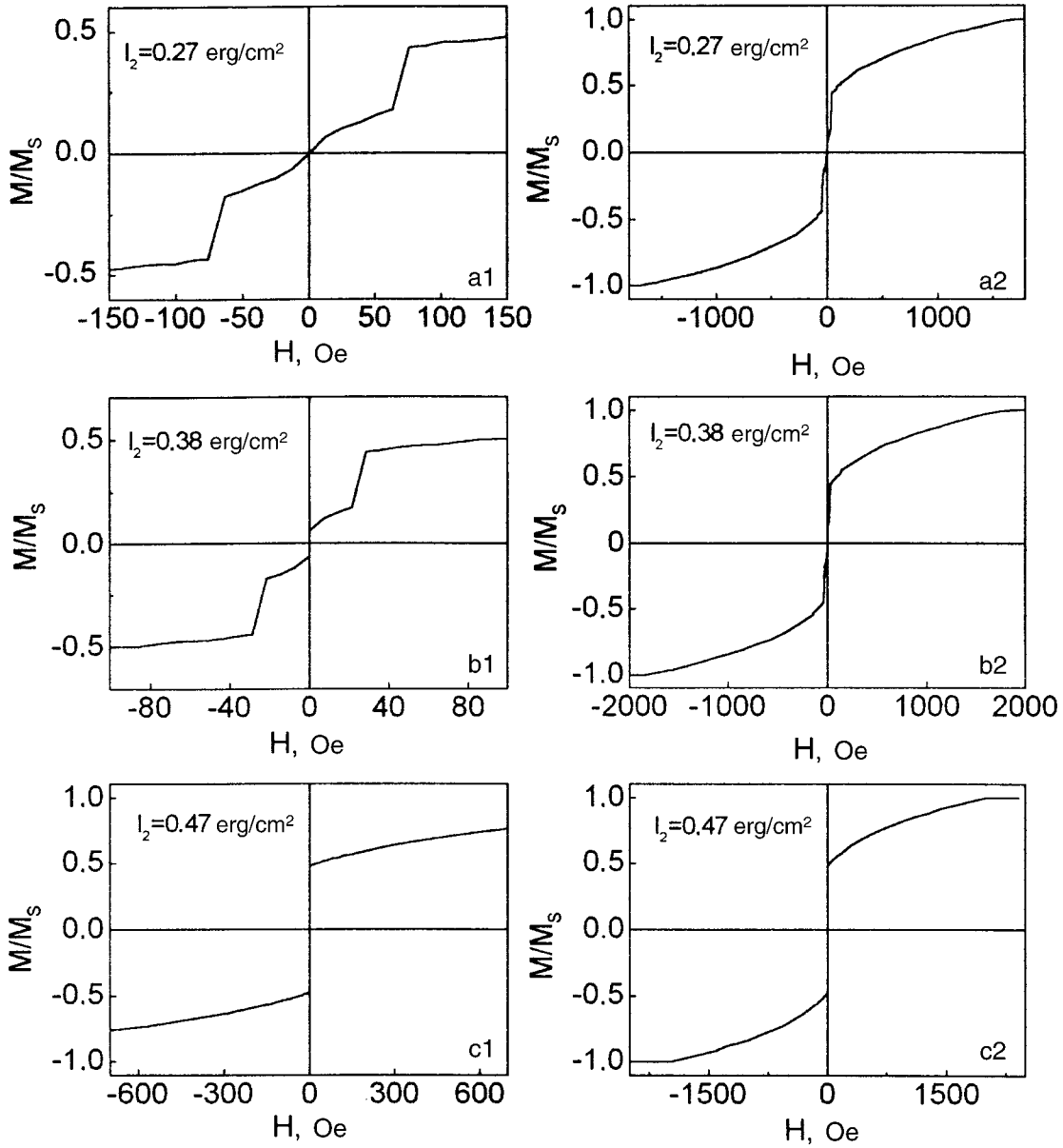

FIG. 5. Calculated field dependence of the projection of the total magnetization on the [110] direction for different values of I_2.

the noncollinear configurations B and C and, accordingly, to growth of the spontaneous magnetization and the Kerr rotation angle (Fig. 2). Thus in the absence of magnetic field the possible stable structures are A, B, and C, which succeed one another as the temperature is lowered.

Let us now compare the field dependence of the Kerr rotation (Fig. 1) with the calculated dependence of the magnetization (Fig. 5). The monotonic nonhysteretic variation of the Kerr rotation in small fields (Fig. 1a), which is observed in the temperature interval 195–300 K, is due to the formation of the noncollinear spin configuration C in the magnetic field and to the change in its degree of noncollinearity as the field increases. The reversibility of this process accounts for the absence of hysteresis.

In this same temperature interval the experimental curves of $\Phi(H)$ have a feature as the magnetic field increases: the Kerr rotation angle increases slowly at first and then more sharply (Fig. 1b), and after reaching the field at which the sharp increase in the Kerr rotation angle is observed the $\Phi(H)$ curve becomes irreversible. As is clearly seen in Fig. 1b, the $\Phi(H)$ curve has appreciable hysteresis, and the value of Φ does not return to zero when the magnetic field is removed. This feature on the $\Phi(H)$ curve (Fig. 1b) can be juxtaposed with the jump accompanying the first-order phase transition between states B and C on the $M(H)$ curve (Fig. 5a1). Then the behavior of $\Phi(H)$ can be explained as follows. Upon reaching the field of the transition from state C to state B, the curve of the Kerr rotation angle increases sharply. The absence of a clear jump on the experimental curve of $\Phi(H)$ may be due to inhomogeneity of the sample. As the magnetic field is removed, the reverse transition from the state B to the state C does not occur, and state B exists in the film as metastable even at $H=0$. The possibility of existence of a metastable configuration B in the absence of field is confirmed by the calculation.

Further increase in the field leads to an increase in the angle between the magnetic moments of the iron layers in the noncollinear configuration B; this is accompanied by an

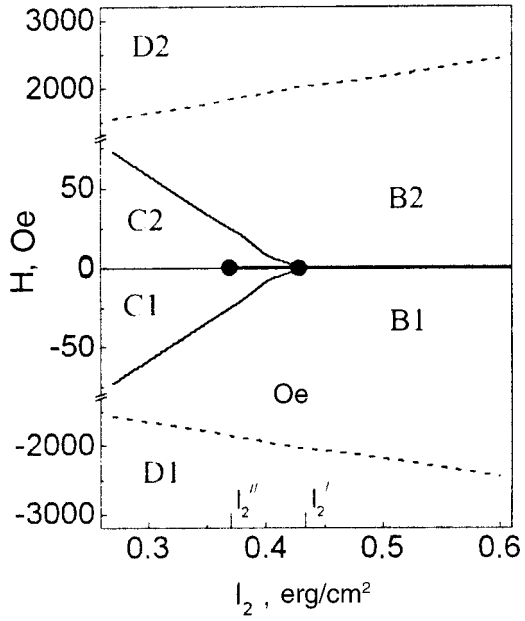

FIG. 6. Calculated $H-I_2$ phase diagram. The existence regions of different magnetic phases (see Fig. 4) are indicated. At $H=0$ and $I_2<I_2''$ the antiferromagnetic state A is realized. The solid lines on the diagram represent lines of first-order phase transitions, and the dashed lines are lines of second-order phase transitions.

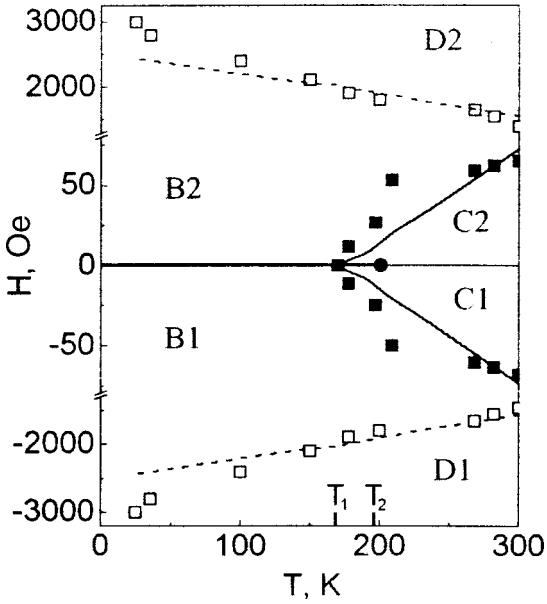

FIG. 7. The $H-T$ phase diagram of an (Fe30 Å/Si15Å)×11 multilayered film with cubic anisotropy in the case when the external field is oriented along the hard magnetization axis [110]. The points represent experimental results, and the lines show the results of the calculation. T_1 and T_2 are the temperatures of spontaneous phase transitions.

increase in the total magnetic moment (Fig. 5a2) and, accordingly, in the Kerr rotation angle (Fig. 1c) and by a subsequent transition to the saturated collinear state D.

In the temperature interval 170–195 K, where in zero field the noncollinear configuration C is stable, the $\Phi(H)$ curves lack the nonhysteretic segment observed in low fields at higher temperatures. Magnetization reversal of the sample in low fields occurs by means of a first-order phase transition between state of the same type ($C_1 \leftrightarrow C_2$). The transition is accompanied by appreciable hysteresis (Fig. 1d). This transition corresponds to the jump on the calculated $M(H)$ curve at $H=0$ (Fig. 5b). The behavior of the Fe/Si multilayered film in high fields in this temperature interval is similar to its behavior for $195\,\mathrm{K}<T<300\,\mathrm{K}$. On further increase in the field one observes a first-order transition to the noncollinear state B and then a second-order transition to the saturated collinear state D.

At $T<170\,\mathrm{K}$ in the absence of field the thermodynamic equilibrium state[4] is the noncollinear configuration B. In a magnetic field the Fe/Si multilayered film undergoes magnetization reversal accompanied by hysteresis (Fig. 1e), which corresponds to a first-order phase transition between two states of type B ($B_1 \leftrightarrow B_2$). This transition corresponds to the jump on the calculated $M(H)$ curve at $H=0$ (Fig. 5c). As the field is increased, the film undergoes a second-order transition to the saturated collinear state D, as at higher temperatures.

Our experimental investigations and calculations enable us to construct the $H-T$ magnetic phase diagram of a (Fe30 Å/Si15Å)×11 multilayered film in the case when the magnetic field is oriented along the hard magnetization direction [110]. The resulting diagram is presented in Fig. 7. The points represent the results of the experimental investigations, and the lines are the results of the calculation.

In order to construct the calculated phase diagram in the $H-T$ plane it is necessary to determine the temperature dependence of the biquadratic exchange constant I_2. First we established a relation between I_2 and T for several temperatures. In this step we chose four temperatures, viz., the maximum and minimum temperatures of the investigated range (25 and 300 K) and the two singular points $T=170\,\mathrm{K}$ and $T=195\,\mathrm{K}$ at which we observed spontaneous phase transitions between spin configurations. For the temperatures 170 and 195 K, corresponding to singular points on the phase diagram, the relation between I_2 and T is easily established.

To determine the relation between I_2 and T for the temperatures 25 and 300 K we compared the experimental values of Φ/Φ_s with the calculated value of M/M_s (Fig. 3) in zero magnetic field. In determining I_2 at the temperature 25 K it was assumed that after the magnetic field is removed, the film does not break up into domains but remains homogeneous. The magnetization reversal process, i.e., the formation of domains with the opposite orientation of the magnetic moment, begins when the field is turned on in the opposite direction (Fig. 1e). Then on the basis of the experimentally determined value of Φ/Φ_s we could establish the values of the angles θ_1 and θ_2. At $T=25\,\mathrm{K}$ and $H=0$ we have $\Phi/\Phi_s=0.52$, and the angles are found to be $\theta_1=14°$ and $\theta_2=104°$. Using the calculated functions $\theta_1(I_2)$ and $\theta_2(I_2)$ shown in Fig. 3a, we find that at $T=25\,\mathrm{K}$ the value of I_2 is $0.58\,\mathrm{erg/cm^2}$. The value of I_2 at $T=300\,\mathrm{K}$ was found in an analogous way. In that case the constant I_2 was determined using the experimental value of Φ/Φ_s measured not in the thermodynamic equilibrium configuration A, where $\Phi/\Phi_s=0$ at $H=0$, but in the metastable configuration B that is realized in the film after the magnetic field is removed. At $T=300\,\mathrm{K}$ and $H=0$ we measured $\Phi/\Phi_s=0.2$ in the metastable state B. This corresponds to the angles $\theta_1=33°$ and $\theta_2=123°$ for the magnetic layers of iron. Using the functions

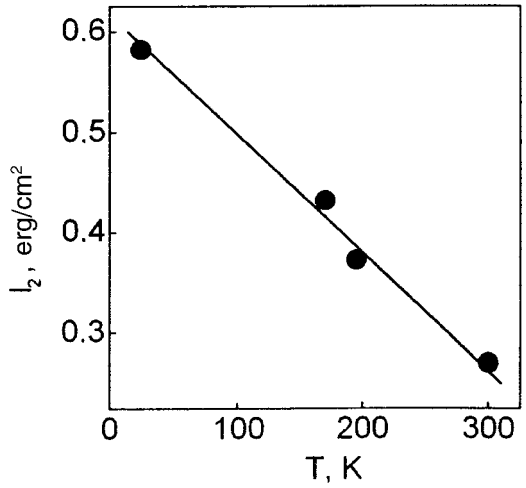

FIG. 8. Temperature dependence of the biquadratic exchange interaction.

$\theta_1(I_2)$ and $\theta_2(I_2)$ given in Fig. 3b, we find $I_2 = 0.27$ erg/cm^2 at $T = 300$ K.

It follows from Ref. 3 that the temperature dependence of the biquadratic exchange constant in an Fe/Si multilayered film can be approximated by a linear function. The values found for I_2 for the four temperatures ($T = 25$, 170, 195, and 300 K) are also described well by a linear dependence (Fig. 8). The linear dependence $I_2(T)$ was used to go from the phase diagram calculated in the coordinates $H-I_2$ (Fig. 6) to the calculated $H-T$ phase diagram (Fig. 7).

As we see from Fig. 7, the experimental and calculated phase diagrams are in completely satisfactory agreement. This demonstrates that all of the possible spin configurations formed in an Fe/Si multilayered film can be adequately described over a wide range of temperatures and magnetic fields in the framework of a theoretical model that takes into account the bilinear and biquadratic exchange and the cubic anisotropy. We note that this good agreement of the calculated and experimental phase diagrams is achieved in a simplified treatment in which only the temperature dependence of the biquadratic exchange interaction is taken into account, while the bilinear exchange interaction and the magnetocrystalline anisotropy are assumed constant. Therefore, we can conclude that it is the change of the biquadratic exchange with temperature that is responsible for the change of the spin configuration of an Fe/Si multilayered film and the transformation of the magnetization-reversal curves as the temperature is changed.

CONCLUSION

The bilinear exchange is known to stimulate collinear ordering of the spins, and the biquadratic exchange, 90° ordering. The fact that the biquadratic exchange interaction and cubic anisotropy are comparable to the bilinear exchange interaction in Fe/Si multilayered films leads to the formation of different collinear and noncollinear magnetic configurations and to phase transitions between these states. At room temperature, when the bilinear exchange dominates the biquadratic exchange, the collinear configuration, with antiferromagnetic ordering of the magnetic moments of the iron layers, is the thermodynamic equilibrium state. The growth of the biquadratic exchange with decreasing temperature causes a transformation of the spin configuration to a noncollinear state. An important role is also played by the cubic anisotropy, the presence of which leads to the formation of two types of noncollinear configurations in an Fe/Si multilayered film, and spontaneous and magnetic-field-induced first-order phase transitions between the noncollinear states arise in the system.

*E-mail: chizhik@ilt.kharkov.ua

[1] E. E. Fullerton and S. D. Bader, Phys. Rev. B **53**, 5112 (1996).
[2] Y. Saito, K. Inomata, and K. Yusu, Jpn. J. Appl. Phys. **35**, L100 (1996).
[3] J. Kohlhepp, F. J. A. den Broeder, M. Valker, and A. van der Graaf, J. Magn. Magn. Mater. **165**, 431 (1997).
[4] R. Zuberek, K. Fronc, R. Szymczak, M. Baran, E. Mosiniewicz-Szablewska, S. L. Gnatchenko, A. B. Chizhik, F. Stobiecki, and H. Szymczak, J. Magn. Magn. Mater. **196–197**, 83 (1999).
[5] A. B. Chizhik, K. Fronc, S. L. Gnatchenko, D. N. Merenkov, and R. Zuberek, J. Magn. Magn. Mater. **213**, 19 (2000).
[6] G. J. Strijkers, J. T. Kohlhepp, H. J. M. Swagten, and W. J. M. de Jonge, Phys. Rev. Lett. **84**, 1812 (2000).
[7] M. Rührig, R. Schäfer, A. Hubert, J. A. Wold, S. Demokritov, and P. Grünberg, Phys. Status Solidi A **125**, 635 (1991).
[8] V. V. Kostyuchenko and A. K. Zvezdin, J. Magn. Magn. Mater. **176**, 155 (1997).
[9] S. L. Gnatchenko, A. B. Chizhik, D. N. Merenkov, V. V. Eremenko, H. Szymczak, R. Szymczak, K. Fronc, and R. Zuberek, J. Magn. Magn. Mater. **186**, 139 (1998).

Translated by Steve Torstveit

ELECTRONIC PROPERTIES OF METALS AND ALLOYS

Concentration dependence of the density of states in the Pauli paramagnets $YNi_{5-x}Cu_x$

A. M. Gurevich, V. N. Eropkin, N. N. Prentslau, and A. V. Terekhov

B. Verkin Institute for Low Temperature Physics and Engineering, National Academy of Sciences of Ukraine, pr. Lenina 47, 61103 Kharkov, Ukraine

V. M. Dmitriev*

B. Verkin Institute for Low Temperature Physics and Engineering, National Academy of Sciences of Ukraine, pr. Lenina 47, 61103 Kharkov, Ukraine; International Laboratory of High Magnetic Fields and Low Temperatures, 95 Gajowicka St., 53-421 Wroclaw, Poland

A. S. Ermolenko and A. G. Kuchin

Institute of Metal Physics, ul. Sof'i Kovalevskoĭ 18, 620219 Ekaterinburg, Russia
(Submitted April 12, 2001)
Fiz. Nizk. Temp. **27**, 896–900 (August 2001)

The temperature dependence and concentration dependence of the heat capacity C and surface resistance R_s are measured in the compounds $YNi_{5-x}Cu_x$ ($x=0$, 0.1, 0.2, 0.25, 0.6, and 1.25). The measured values of $C(x)$ and $R_s(x)$ are used to determine the concentration dependence of the density of states $N(E,x)$. A maximum is observed on $N(E,x)$ at $x=0.2$. The results constitute direct experimental confirmation of the nonmonotonic dependence of $N(E,x)$ that has previously been predicted theoretically. It is found that at certain values of x the low-temperature heat capacity of the compounds $YNi_{5-x}Cu_x$ increases with decreasing temperature, and the temperature dependence of the electrical resistance has a minimum at $T=10$ K. Below 10 K the temperature dependence of the resistance obeys a logarithmic law. © *2001 American Institute of Physics.* [DOI: 10.1063/1.1399206]

INTRODUCTION

It has been shown theoretically[1,2] that in the pseudobinary alloy $YNi_{5-x}Cu_x$, which is a typical Pauli paramagnet, the density of states $N(E)$ at the Fermi level varies nonmonotonically with increasing copper concentration x and reaches a maximum at $x=0.2$.

The experimental study of $N(E)$ is often done with the aid of measurements of the electronic heat capacity C_e, magnetic susceptibility χ, and surface electrical resistance R_s.

The experimental dependence of $\chi(x)$ obtained in Ref. 3 corresponds qualitatively to the calculated averages of the magnetic moment $M(x)$ determined from Refs. 1 and 2.

With the goal of obtaining more-reliable data on the dependence of the density of states $N(E)$ on the copper content in the compounds $YNi_{5-x}Cu_x$, in the present study we have investigated experimentally the electronic heat capacity $C_e(x)$ and the surface resistance $R_s(x)$ for a series of $YNi_{5-x}Cu_x$ samples with different values of x.

SAMPLES AND MEASUREMENT PROCEDURES

The samples were polycrystalline $YNi_{5-x}Cu_x$, with x taking the values 0, 0.1, 0.2, 0.25, 0.6, and 1.25.

The temperature dependence of the heat capacity C was measured by absolute calorimetry in the temperature interval 1.5–20 K. A sample of mass 2–3 g was placed in a sealable copper container equipped with a germanium resistance thermometer and a heater. The heating was carried out by a stepped method. The error of measurement did not exceed 1%.

The samples had a complex surface geometry with a nonidentical transverse cross-sectional area, and this was true of samples with different concentrations x. This made it difficult to determine precisely the absolute value of their resistivity $\rho(x,T)$ from the resistance R measured in dc current. Therefore, for determining the concentration dependence of $N(E)$ from the Ohmic losses, R_s was investigated at a frequency of 2 MHz, where the classical skin effect was fully operative. In the temperature interval 4.2–300 K the resistance R_s was measured by a resonator method, with a copper sample as the standard.[4] For these measurements we built an oscillatory circuit without using tin solder, since the transition of tin to the superconducting state at $T=5-6$ K would decrease the accuracy of the R_s measurements and would also make it hard to determine the influence of the magnetic field on the Ohmic losses of the compound at helium temperatures. We took into account that $R_s^n \propto \rho$ ($n \cong 2$) for both diamagnets and for magnetic materials.[5]

EXPERIMENTAL RESULTS

Figure 1 shows the experimental dependence of the heat capacity in the temperature interval 1.5–10 K in the coordinates C/T versus T^2. It has been established experimentally that at temperatures above 4 K the temperature dependence

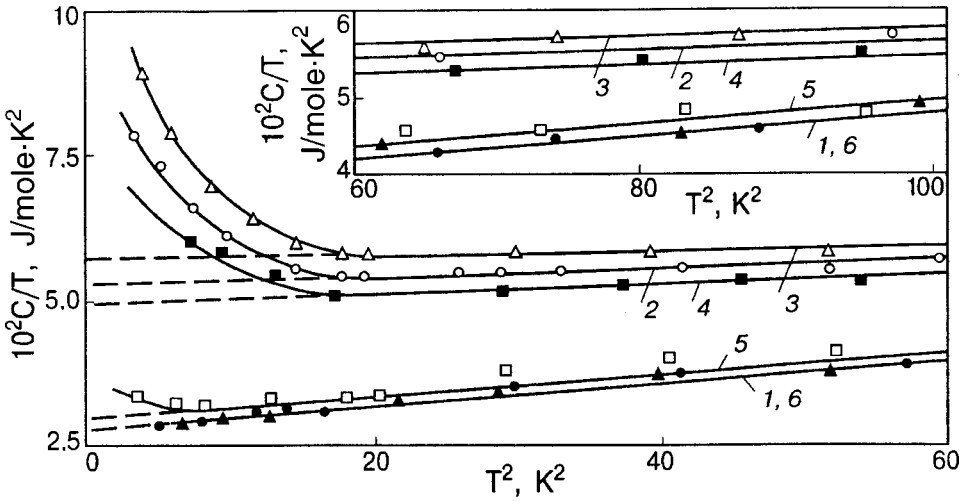

FIG. 1. C/T versus T^2 for $YNi_{5-x}Cu_x$ compounds with different values of x: 0 (*1*), 0.1 (*2*), 0.3 (*3*), 0.25 (*4*), 0.6 (*5*), and 1.25 (*6*). The inset shows the same dependences for $T^2 \approx 60-100\ \mathrm{K}^2$.

of the heat capacity of the compounds under study is well described by the expression

$$C(T) = \gamma T + \beta T^3. \tag{1}$$

The first term on the right-hand side of this expression represents the electronic heat capacity C_e, and the second term the lattice heat capacity. It is seen in the figure that for $T < 4$ K, for all of the samples except the compounds with $x = 0$ and $x = 1.25$, the heat capacity increases differently with decreasing temperature for samples with different x. Therefore, to determine γ in Eq. (1) by extrapolation of the ratio C/T as a function of T^2 to $T = 0$ we used the values of the heat capacity in the range 4–10 K.

Figure 2a shows the temperature dependence of R_s for the compound YNi_5 measured at a frequency of 2 MHz in the temperature interval 4.2–300 K. The $R_s(T)$ curves of the alloys $YNi_{5-x}Cu_x$ are similar to that shown in Fig. 2a and are therefore not shown in the figure. As we see from Fig. 2a, in the temperature interval 50–300 K the $R_s(T)$ curve is close to linear, and for $T < 50$ the surface resistance depends weakly on temperature.

It should be pointed out that the $R_s(T)$ curves for all the samples studied have an anomaly at $T \approx (270 \pm 5)$ K in the form a slight deviation from the straight trend. In the $YNi_{5-x}Cu_x$ samples with $x = 0$ and $x = 0.2$ there is also a slight minimum of R_s in the temperature interval 35–45 K (not shown in the figure).

It is observed in the experiments that a slight ($\sim 0.5-1\%$) negative magnetoresistance exists in the temperature interval 4.2–300 K for the $YNi_{5-x}Cu_x$ samples with $x = 0$ and $x = 1.25$. In the compounds with $x = 0.1$, 0.25, and 0.6 the influence of a static magnetic field on the Ohmic losses is extremely weak ($< 0.5\%$) and appears only at $T < 100$ K, and in the systems with $x = 0.2$ it is absent altogether.

It is found that for all of the samples studied, with their different values of x, the temperature dependence of R_s has a minimum at $T = 10$ K (see Fig. 2b, 2c). The dashed curve in Fig. 2b, 2c shows the calculated temperature dependence $R_s \propto (\ln T^{-1})^{0.5}$, which confirms the logarithmic growth of the measured resistivity ρ, according to the law $\rho(T) \propto R_s^2(T)$, as the temperature is lowered below 10 K.

From the $C(T)$ data we determined the coefficients γ and β in Eq. (1) for all the samples studied. It is seen in Fig. 1 that the coefficient β (the slope of the straight lines) differs

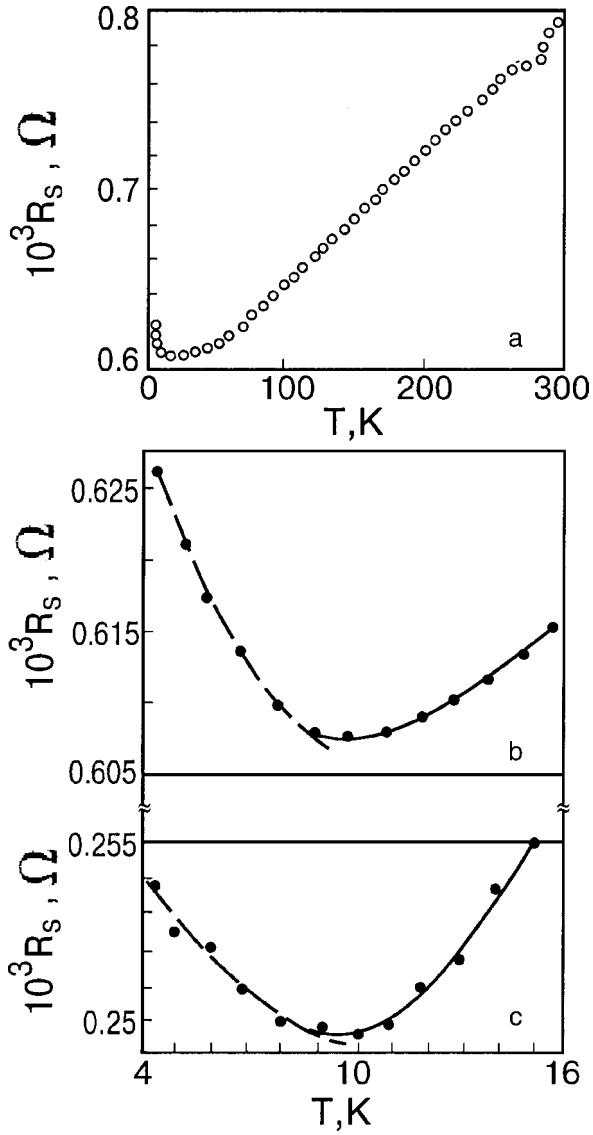

FIG. 2. Temperature dependence of R_s for YNi_5 at a frequency of 2 MHz (a). The $R_s(T)$ curve in the temperature interval 4.2–16 K for YNi_5 (b) and $YNi_{4.8}Cu_{0.2}$ (c). The dashed curve is $R_s^2 \propto (\ln 1/T)$.

little for samples with different copper concentrations, and so the Debye temperature, which is 389 K for the sample with $x=0$, varies only slightly (5%) with increasing x. At the same time, the coefficient γ varies substantially and nonmonotonically. Figure 3a shows the measured concentration dependence of γ (points), from which we see that γ is maximum for $x=0.2$.

Also shown in Fig. 3a is the relative concentration dependence of the difference in heat capacities measured at $T=2$ K and the regular dependence C_r (i.e., the extrapolation from the high-temperature region; it is shown by the dashed lines in Fig. 1).

In Fig. 3b, curve *1* shows $R_s(x)$ at 10 K. It is seen that for $x=0.2$ the surface resistance has a minimum value. Also shown in this figure is the concentration dependence of the difference of the surface resistances measured at temperatures of 4.2 and 10 K, relative to the value $R_s(10)$ (curve *2*).

It follows from Fig. 3a, 3b that the curves of $\gamma(x)$ and $[(C-C_r)/C_r](x)$ practically coincide, and a correlationj is observed between the curves of $[(R_s(4.2)-R_s(10))/R_s(10)](x)$ and $R_s(x)$.

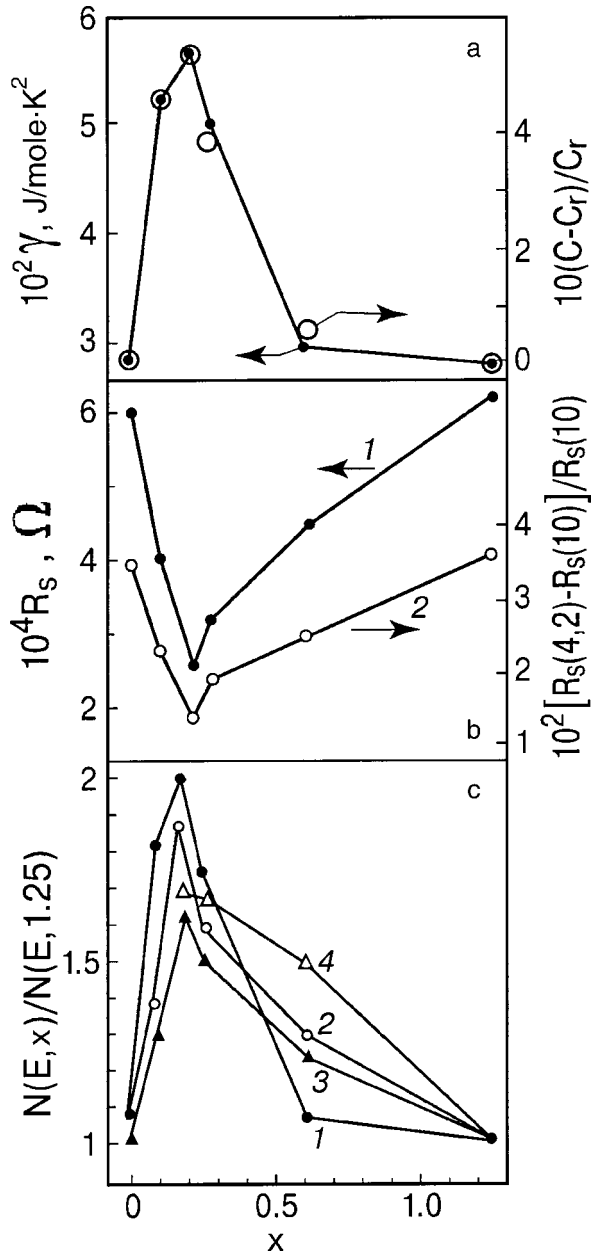

FIG. 3. Concentration dependence of γ (points), $(C-C_r)/C_r$ (circles) (a); $R_s(10)$ (*1*), $(R_s(4.2)-R_s(10))/R_s(10)$ (*2*) (b); $N(E,x)/N(E,1.25)$ determined from the heat capacity (*1*), Ohmic losses (*2*), magnetic susceptibility (*3*), and theoretically from Refs. 1 and 2 (*4*) (c).

DISCUSSION OF THE RESULTS

The high values of the Debye temperature of all the $YNi_{5-x}Cu_x$ compounds studied cause the linear part of C/T versus T^2 to continue for a long way (to 10 K), and this permits a reliable determination of $\gamma(T)$. For YNi_5 we obtained a value $\gamma=28\,\mathrm{mJ\cdot K^{-2}\,mole^{-1}}$. The calculated value $\gamma=20\,\mathrm{mJ\cdot K^{-2}\,mole^{-1}}$ was determined in Ref. 2. In Ref. 6 the value $\gamma=37\,\mathrm{mJ\cdot K^{-2}\,mole^{-1}}$ was obtained experimentally, although the value of the lattice contribution to the heat capacity agrees with the value obtained in the present study. The fact that the experimental values of γ are larger than the calculated value indicates that there is a substantial contribution from the exchange and electron–phonon interactions and also from spin fluctuations.[7,8] They determine the enhancement factor that must be taken into account when calculating $N(E)$ from the experimental data for γ, χ, or ρ.[7,8] Since we are interested in the concentration dependence of $N(E)$ and not the absolute values of $N(E)$, in Fig. 3c we give the concentration dependence of the relative density of states $N(E,x)/N(E,1.25)$ calculated with allowance for the experimental values of γ (curve *1*) and the resistivity $\rho\propto R_s^2$ (curve *2*) by the standard formula given in Refs. 9 and 10. Here we also give the concentration dependence obtained from measurements of the magnetic susceptibility[3] (curve *3*) and the dependence calculated theoretically from Refs. 1 and 2 (curve *4*).

We see from Fig. 3c that $N(E,x)/N(E,1.25)$ is nonmonotonic, and at $x=0.2$ a maximum of $N(E)$ is observed regardless of which of the measured parameters is used to calculate the density of states—the heat capacity, the resistivity, or the magnetic susceptibility. This circumstance, together with the similarity of curves *1–4* in Fig. 3c, supports the assertion that the theoretical results presented in Refs. 1 and 2 are in agreement with the experimental results.

The curves in Fig. 3c were constructed on the assumption that the enhancement factors given above are independent of x. If such a dependence actually does exist it would more likely affect the sharpness of the maximum rather than its position on the x axis.

The nonmonotonic concentration dependence of $N(E)$ may be explained as follows: for the binary alloy YNi_5 the theoretical $N(E)$ curve has a small local maximum somewhat above the Fermi level.[2] As Ni is replaced by Cu a filling of the $3d$ band occurs, since copper has more $3d$ electrons than nickel does. As a result, the Fermi level in the $YNi_{5-x}Cu_x$ system shifts to higher energies and passes through a maximum, and this is what causes the nonmonotonic character of the change in $N(E)$ with changing copper concentration.

Our results for $YNi_{5-x}Cu_x$ compounds essentially agree with the results of Ref. 7 for the systems $Lu(Co_{1-x}Ga_x)_2$ and $Lu(Co_{1-x}Sn_x)_2$. For $x=0$ no anomalies of the heat capacity are observed, and a value $\gamma=24.6\,\mathrm{mJ\cdot K^{-2}\,mole^{-1}}$ is ob-

tained for $LuCo_2$; this value is close to our value for γ in YNi_5. However, even small admixtures of Cu, Ga, or Sn have an appreciable effect on the parameters of the system. In particular, the value of γ increases, and at temperatures below 4 K one observes appreciable growth of the ratio C/T. At the same time, large amounts of the dopant have practically no effect on the properties of the compound. At certain values of x both in $YNi_{5-x}Cu_x$ and $Lu(Co_{1-x}Sn_x)_2$ the values of γ and χ pass through maxima, and the ratios $\gamma(x)_{\max}/\gamma(0)$ and $\chi(x)_{\max}/\chi(0)$ are not equal.

Our results and our analysis of the results presented in Refs. 1–3 and 7 indicate that the nonmonotonic concentration dependence of γ, χ, and ρ in a number of paramagnetic pseudobinary alloys is due to features of the electronic structure of these alloys. Two factors are important here: the influence of doping on the width of the d band, and the relative displacement of the Fermi level and the local density of states of the substituted and substituent elements. A comparison of $\gamma(x)$ and $R(x)$ indicates that it is the actual density of states at the Fermi level that is decisive. Thus we assume that the increase in γ on doping is due to an increase in $N(E_F)$ against the background of strong spin fluctuations of the electron–phonon and other interactions.

It is interesting to note that the growth of the ratio C/T for different x at $T<4$ K coincides with the concentration dependence of $\gamma(x)$, as is seen in Fig. 3a. This means that those interactions in the system which cause the nonmonotonic character of the concentration dependence of $\gamma(x)$ are also responsible for the low-temperature anomalies of the heat capacity. However, at low temperatures the resistance of the samples increases with decreasing T. Thus, while the growth of γ upon doping is accompanied by a decrease in the resistance (see curve *1* in Fig. 3b), the increase in the ratio C/T with decreasing temperature occurs against the background of a growing resistance (Figs. 1 and 2b, 2c). Such behavior of the system may be due to the charge carriers becoming heavier.

The minimum observed on the temperature dependence of the resistance (Figs. 2b, 2c) is also interesting. The depth of the resistance minimum depends on the copper concentration and reaches an extremal value for $x=0.2$. At the same time, the temperature at which the resistance minimum is observed is independent of x. When the temperature is lowered below that at which the minimum of the Ohmic losses is observed, the resistance increases by a logarithmic law, which is characteristic of the Kondo effect.[11]

CONCLUSION

From the experimentally measured concentration dependence of the heat capacity and surface resistance of the compound $YNi_{5-x}Cu_x$ we have established that its density of states varies nonmonotonically with increasing copper concentration and passes through a maximum at $x=0.2$. This is direct experimental confirmation of previous theoretical predictions about the concentration dependence of $N(E,x)$ for $YNi_{5-x}Cu_x$ compounds.

We have observed and investigated the low-temperature anomalies of the heat capacity (its increase with decreasing temperature).

We have observed a feature on the temperature dependence of the surface resistance in the form of a minimum at $T=10$ K. As the copper content in the compound is varied, the temperature at which the minimum is observed remains unchanged, while the depth of the minimum is lowest at $x=0.2$.

This study was supported by the Ministry of Education and Science of Ukraine, Contract No. 2M/75-2000, and also by the Russian Foundation for Basic Research, project P2001 — Ural No. 01-02-96420.

*E-mail: dmitriev@ilt.kharkov.ua

[1] M. Simizu, J. Inoue, and S. Nagasava, J. Phys. F: Met. Phys. **14**, 2673 (1984).
[2] M. Simizu, M. Miyaraki, and J. Inoue, J. Magn. Magn. Mater. **74**, 309 (1988).
[3] A. G. Kuchin, A. S. Ermolenko, V. J. Khrabrov, G. M. Makarova, and E. J. Belozerov, J. Magn. Magn. Mater. **159**, L309 (1996).
[4] V. M. Dmitriev, M. N. Ofitserov, and N. N. Prentslau, in *Intercollegiate Scientific–Technical Collection on Radio Engineering* [in Russian], Vol. 97 (1993), p. 91.
[5] V. L. Gurevich, Zh. Tekh. Fiz. **28**, 2352 (1958) [*sic*].
[6] F. Kayzel, *Magnetic and Thermodynamic Properties of* RNi_5 *Compounds*, Thesis, Amsterdam (1997).
[7] K. Murata, K. Fukamichi, T. Sakakibara, T. Goto, and K. Suzuki, J. Phys.: Condens. Matter **5**, 1525 (1993).
[8] L. Nordström, M. S. S. Brooks, and B. Johansson, Phys. Rev. B **46**, 3459 (1992).
[9] P. G. de Gennes, *Superconductivity of Metals and Alloys*, Benjamin, New York (1966); Mir, Moscow (1968).
[10] V. G. Livshits, *Physical Properties of Metals and Alloys* [in Russian], Gos. Nauch.-Tekhn. Izd. Mashinostr. Lit., Moscow (1959).
[11] A. A. Abrikosov, *Fundamentals of the Theory of Metals*, [North-Holland, Amsterdam (1988); Nauka, Moscow (1987)].

Translated by Steve Torstveit

PHYSICAL PROPERTIES OF CRYOCRYSTALS

Dimers of phenol in argon and neon matrices

A. M. Plokhotnichenko,* E. D. Radchenko,† Yu. P. Blagoĭ, and V. A. Karachevtsev

B. Verkin Institute for Low Temperature Physics and Engineering, National Academy of Sciences of Ukraine, pr. Lenina 47, 61103 Kharkov, Ukraine
(Submitted May 21, 2001)
Fiz. Nizk. Temp. **27**, 901–914 (August 2001)

The IR absorption spectra of phenol molecules in solid rare gas matrices of argon (10–12 K) and neon (4.5–5 K) are investigated at molar ratios of phenol:matrix of 1:1000 to 1:30 in the frequency range 400–4000 cm^{-1}. Bands of dimers and larger complexes of phenol molecules are observed in the absorption spectrum of both matrices as the matrix ratio decreases. The first additional bands to appear in the spectral region of the stretching vibrations of the O–H group as the phenol concentration increases are two bands attributed to dimers with one and two hydrogen bonds. The absorption coefficients are determined for the bands of stretching vibrations of the O–H and C–O groups, O–H planar bending vibrations of monomers, and the stretching vibrations of the hydrogen-bonded O–H groups of the phenol molecules. The features of the formation of H-bonded complexes in low-temperature matrices are discussed. A model is proposed which permits calculation of the number of monomers, dimers, and larger complexes in argon and neon matrices for molecules which are close in size to the phenol molecule. [DOI: 10.1063/1.1399207]

INTRODUCTION

The study of weakly bound molecular complexes has remained an active field of research for many years.[1–3] The intermolecular interaction plays a key role in such extremely important topics in biophysics as molecular recognition (the ability of many biomolecules to form strictly specified molecular complexes) or the formation of the structure of biopolymers. Furthermore, a large number of chemical reactions begin with the formation of weakly bound complexes. Another related question concerns the working mechanisms of catalysts, including enzymes.

In studying molecular complexes, in which two or more molecules are bound by relatively weak intermolecular forces, one often uses the method of low-temperature matrix isolation in combination with infrared (IR) absorption spectroscopy. The samples are obtained by the joint deposition of a matrix gas and the substance to be investigated on a cold substrate. In addition to the isolated molecules, molecular complexes of various sizes and composition can form in the matrix. The presence of molecular complexes in a matrix sample can be judged from the appearance of additional spectral bands, not present in the spectrum of the isolated molecules, as the concentration is increased; these are obtained at sufficiently large matrix ratios M—the number of atoms of the matrix per molecule of the substance under investigation. Since the bands of monomers in the matrix IR spectra are ordinarily quite narrow (their half-widths usually lie in the range from 0.001 cm^{-1} to several cm^{-1}; Refs. 4–6), the absorption bands of the molecular complexes can easily be observed even if they are only 1–2 cm^{-1} away from the monomer bands. Determination of the number of such complexes in this type of study is a complicated problem. At the same time, knowledge of the quantitative parameters of the complexes is important in the study of complexes containing hydrogen bonds, since the change of the intensity of the hydrogen-bond band in comparison with the monomer bands can be used, together with the value of the spectral shift, to determine the binding energy of the molecules in the complex.

For certain molecules a low-temperature matrix can stabilize less stable forms of complexes in much larger quantities than in systems in thermodynamic equilibrium, and in some cases this can make them easier to observe.

Phenol molecules have repeatedly[7–13] attracted interest as objects in which to study H-bonded complexes (i.e., complexes in which the molecules are bound by a hydrogen bond) in view of the rather simple molecular structure (a benzene ring and one O–H group). Phenol dimers have been studied in the gas phase[10] and in cooled beams[11,12] by the methods of rotational coherent spectroscopy and Raman scattering. In those studies a type of dimer with the phenol molecules in almost perpendicular planes has been observed.

The goal of the present study was to investigate the IR absorption spectrum of phenol molecules in matrices of argon and neon, to determine the possible structures of the dimers of phenol molecules, and to estimate their number at different matrix ratios.

EXPERIMENT

The phenol samples in an argon matrix were prepared in a helium immersion cryostat by the joint cooling of gaseous flows of argon and phenol on a CsI substrate cooled to 15–16 K.[14] To achieve the lower temperatures needed for preparing samples of phenol in a neon matrix, the cryostat

was equipped with an additional cooling valve to permit the admission of liquid helium into the heat exchanger of the sample holder. This refinement made it possible to maintain a stable sample temperature in the range 3–5 K with an open cold valve and 7–30 K with it closed. As the substrates for the neon samples we used copper mirrors. The samples were annealed for 30 min at 30 K for the argon matrices and at 7–8 K for the neon. To prevent evaporation of the matrix gas from the surface of the sample during annealing, the samples were coated beforehand with a heavier rare gas—krypton for the argon matrix and argon for the neon matrix. The thickness of the protective film was around 10 μm. The rate of cooling the substance to be studied was regulated by the temperature of its evaporation from the Knudsen cell (in the range 30–45 °C) and for the different samples was chosen within the range $(0.5–1.5)\times10^{-8}$ mole/(cm^{2}min). The required rate of deposition of the matrix gas was set by a needle valve within the range $(0.5–5)\times10^{-6}$ mole/(cm^{2}min). The sample preparation time varied from 50 to 120 min for obtaining a value of the product of the phenol concentration times the thickness of the sample in the range 0.6–1.2 μmole/cm^2. The thickness of the matrix varied from 10 to 150 μm. To reduce the possible influence on the structure of the sample due to the heat released in the condensation of the matrix gas, the matrix gas was cooled to liquid nitrogen temperature at the entrance to the vacuum chamber. The rates of deposition of the matrix gas and phenol were measured by quartz microbalances which were at the same temperature as the sample holder. This made it possible to prepare samples with specified matrix ratios with an accuracy of 10% or better. The absolute quantities of the substances in the sample were determined from the rate of deposition and the sample preparation time to the same accuracy.

Before the phenol was loaded into the Knudsen cell it was purified by recrystallization from the gas phase. In addition, immediately before the sample was prepared from the substance found in the Knudsen cell the volatile impurities were driven off in a process monitored by quartz microbalances.

The IR spectra were recorded with a resolution of 1 cm^{-1} in the range 1700–400 cm^{-1} and with a resolution of 3 cm^{-1} in the range 3800–2800 cm^{-1} on a Specord IR-75 double-beam grating spectrometer connected to a personal computer. In the recording of the spectra the temperature of the samples was maintained at a level of 10–12 K for the argon matrix and 4.5–5 K for the neon.

RESULTS AND DISCUSSION

IR absorption spectra of phenol in an argon matrix

Figure 1 shows the absorption spectrum of phenol in an argon matrix at $T=11$ K in the region of the stretching vibrations of the protons at different matrix ratios. The band at $\nu=3635$ cm^{-1} corresponds to stretching vibrations of the O–H groups of the isolated molecules (monomers).[7,15] As the concentration of the phenol molecules increases, bands of stretching vibrations of the O–H groups—proton donors in the H-bonded complexes—appear. At low concentrations these complexes are represented mainly by a comparatively

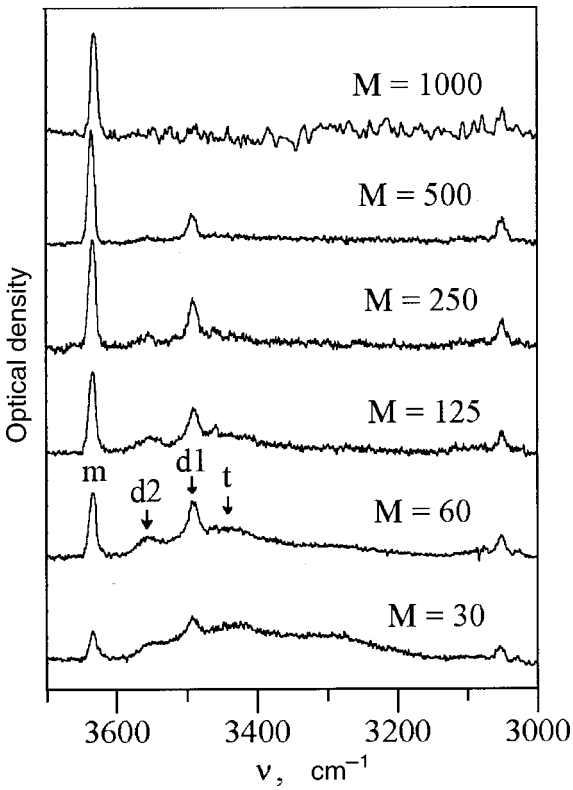

FIG. 1. IR absorption spectra of phenol in the region of the proton stretching vibrations in the argon matrix for different matrix ratios at $T=11$ K (before annealing): *m* indicates monomers ($\nu=3635$ cm^{-1}), *d*1 and *d*2 dimers ($\nu=3490$ and 3555 cm^{-1}), and *t* trimers ($\nu=3430$ cm^{-1}) of phenol.

narrow band at $\nu=3490$ cm^{-1} (*d*1 dimers) and also by a very weak band at $\nu=3555$ cm^{-1} (*d*2 dimers). As the concentration is increased, another two additional wide bands appear: first a band in the frequency region 3500–3350 cm^{-1}, with a maximum near $\nu=3430$ cm^{-1} (trimers) and then a band of larger complexes in the frequency range 3380–3180 cm^{-1} with a maximum at around $\nu=3300$ cm^{-1}. We note that the intensity of the band of vibrations of the free O–H group ($\nu=3635$ cm^{-1}) decreases with increasing phenol concentration, while the bands of C–H stretching vibrations ($\nu=3048$ cm^{-1}) remains practically unchanged.

Figure 2 shows the results of an annealing of the matrix at a temperature of 30 K for a matrix ratio $M=250$. Upon annealing of the sample the intensities of the bands at $\nu=3490$, 3430, and 3300 cm^{-1} increase, while that of the $\nu=3555$ cm^{-1} band decreases. The intensity of the band of vibrations of the free O–H group also decreases slightly.

Since the bands at $\nu=3490$ and 3555 cm^{-1} appear first as the phenol concentration increases, they should be attributed to H-bonded dimers of phenol. Possible types of these dimers with one and two hydrogen bonds are shown in Fig. 3. In addition to these two, another type of dimer with the so-called T-shaped structure has been discussed in the literature.[7–9] In that structure the role of the acceptor of the hydrogen bond is played by the π-electron system of the benzene ring. However, recent *ab initio* calculations of the energy and vibrational spectra of the surface structures of phenol dimers,[7] the results of which are in good agreement with experimental data,[10–12] have shown that the spectral shift of the band of O–H stretching vibrations in the donor

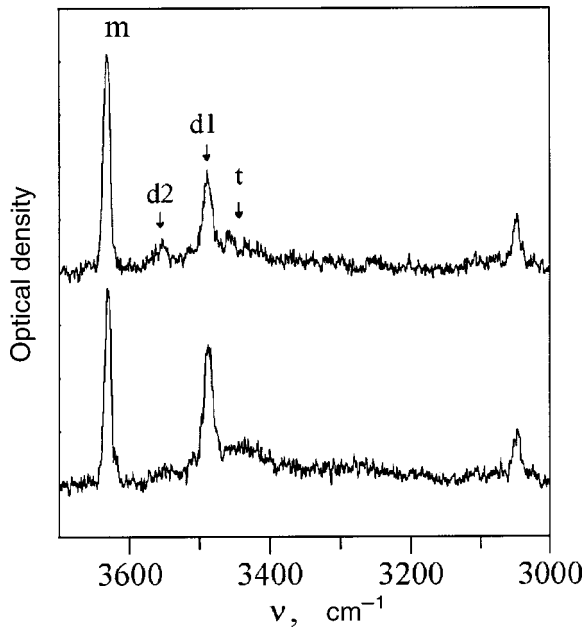

FIG. 2. IR absorption spectra of phenol in the region of the proton stretching vibrations in an argon matrix at a matrix ratio $M=250$ and $T=11$ K: before annealing (upper curve) and after annealing for 30 min at 30 K (lower curve). The notation is the same as in Fig. 1.

molecule of the hydrogen bond of the T-shaped dimer is around 10 cm^{-1}, which is much smaller than the shift observed in the experimental spectra. For this reason we will not consider the T-shaped dimer structure further. In Ref. 10 the rotational constants of the phenol dimers were determined by the method of rotational coherent spectroscopy; from these constants the structure of the H-bonded complexes in the gas phase was reconstructed. The energetically most favorable structure was attributed to the type Dim. 1 (see Fig. 3) with the molecules lying in nearly perpendicular planes. In the matrix this geometry may break down. It is known[2,3,16] that the energy of a hydrogen bond and the shift of the O–H stretching vibrations depend strongly on the O–O distance and the O–H$\cdots$O angle in the chain of atoms forming the hydrogen bond. The largest binding energy and the largest shift of the band to low frequencies are observed when the atoms are arranged in a straight line. Therefore, of the two spectral bands of dimers the band at $\nu=3490$ cm^{-1}, for which the shift is larger, should be attributed to the Dim. 1 structure. This band may correspond to dimers with different angles of rotation around the hydrogen bond, which are indistinguishable in the IR spectra. The spectral shift of the band at $\nu=3490$ cm^{-1} relative to the monomer band, which is 145 cm^{-1}, is close to the value 126 cm^{-1} which is observed in the Raman scattering spectra for phenol

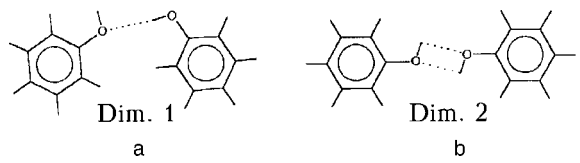

FIG. 3. Possible types of H-bonded dimers of phenol: a—dimer with one hydrogen bond (several structures can exist, differing by rotation of one of the molecules around the hydrogen bond); b—planar dimer with two hydrogen bonds.

dimers in experiments with cooling in supersonic beams;[11,12] this confirms the attribution of this band to the dimers Dim. 1.

The band at $\nu=3555$ cm^{-1} may correspond either to dimers of the Dim. 2 type, which are shown in Fig. 3 (these dimers are discussed, e.g., in Ref. 13) or of the Dim. 1 type, with a highly distorted hydrogen bond. The dimers Dim. 2 were not observed in Refs. 10 and 11, but they can arise in a low-temperature matrix, since the matrix cell can preserve them in a metastable state. Then the annealing of the matrix can convert Dim. 2 into dimers with one hydrogen bond, and this would lead to a decrease in the intensity of this band, as occurs in experiment. In a dimer of the Dim. 2 type the O–H $\cdots$O chains are strongly bent, and that should be accompanied by a decrease in the spectral shift. In addition, in such a dimer both phenol molecules should lie in the same plane, and that decreases the probability of their formation in comparison with dimers of the Dim. 1 type and, as a result, should lead to a lower intensity of the band in the spectrum. We note that the $\nu=3555$ cm^{-1} band in the absorption spectra has a lower intensity than the $\nu=3490$ cm^{-1} band. However, such effects can arise in dimers of the Dim. 1 type in which the hydrogen bond is strongly distorted by the matrix. To elucidate the question of whether the $\nu=3555$ cm^{-1} band should be attributed to Dim. 2 or to distorted dimers of the Dim. 1 type, we employed the usual tool in such cases—a change of matrix. For this purpose we used a neon matrix, since neon atoms are considerably smaller than argon atoms and therefore the packing of the dimers in the neon and argon matrices should be very different. If dimers of the Dim. 1 type with an appreciably distorted geometry are present in the sample, then packing in different matrices will most likely stabilize the structures with a different degree of distortion. This should lead to different values of the shifts of the absorption bands of the distorted dimers, relative to the monomer bands, in different matrices. We shall return to this question in more detail in discussing the spectra of phenol in a neon matrix.

The band with the maximum near $\nu=3430$ cm^{-1}, which appears in the spectrum on decreasing matrix ratio immediately after the $\nu=3490$ and 3555 cm^{-1} bands, is most likely due to phenol trimers. The broad band with a maximum at around $\nu=3300$ cm^{-1}, which is observed in the spectra of the most concentrated samples, is apparently due to the appearance of larger hydrogen-bonded complexes (as compared to dimers and trimers). These band are much wider than the dimer bands, indicating the presence of large complexes in the sample which are distorted to different degrees by the matrix.

The bands of the free and bound O–H groups are well separated from one another in the spectrum and one can easily determine their integrated intensities, which are given in Table I as the values reduced to the same 10^{-5} moles of phenol per square centimeter of area of the sample. Since the number of O–H groups does not change upon the formation of hydrogen bonds, the following relations should hold at all concentrations:

$$\frac{I_m}{K_m}+\frac{I_h}{K_h}=N$$

TABLE I. Integrated intensities of the monomer components of the bands of C–O stretching (str. C–O) and O–H planar bending (bend. O–H) vibrations and the bands of the stretching vibrations of the O–H groups of the phenols in the free (str. O–H (m)) and H-bonded [O–H···O ($d1$)—dimers of type Dim. 1, O–H···O ($d2$) — Dim. 2, and O–H···O – all complexes] in Ar and Ne matrices, given as the values reduced to 10^{-5} moles per square centimeter of area of the sample, for different values of the matrix ratio M. For the argon matrix two values—before and after annealing—are given.

M	Integrated intensity, cm^{-1}											
	str. C–O		bend. O–H		str. O–H (m)		O–H···O ($d1$)		O–H···O ($d2$)		O–H···O	
	Ar	Ne	Ar	Ne	Ar	Ne	Ar	Ne	Ar	Ne	Ar	Ne
	1260		1176		3635	3650	3490	3507	3555	3563	3600–3150	
1000	26/26	22	30/29	24	48/47	40	12/15	21	0/0	11	12/15	20–40
500	25/23	13	29/26	21	43/45	33	11/20	20	2/0	9	12/23	68–80
250	23/19	6	28/22	10	45/39	15	20/32	16	3/1	5	43/63	150–200
125	15/12	0	19/14	0	35/29	0	19/31	0	5/2	0	65/98	250–300
60	11/5	–	14/6	–	26/17	–	19/21	–	7/3	–	120/200	–
30	3/ < 2	–	4/ < 1	–	12/ < 10	–	12/12	–	6/2	–	250/260	–

or

$$I_m + \frac{I_h}{C} = NK_m = I_0, \tag{1}$$

where I_m and I_h are the integrated intensities of the bands of free and bound O–H groups, K_m and K_h are the corresponding molar integral absorption coefficients, N is the number of moles of the substance per unit cross-sectional area of the light beam, $C = K_h/K_m$ is the coefficient of the enhancement of the intensity of the band upon the formation of a hydrogen bond, and I_0 is the intensity of the band of free O–H groups in the absence of complexes in the sample, i.e., in the limit of low concentrations.

From relations (1) for any two concentrations one can find K_m and K_h. Their averaged values, which satisfy (1) to experimental accuracy at all concentrations, are $C = 5$, $K_m = (52 \pm 5) \times 10^5$ cm/mole and $K_h = (260 \pm 30) \times 10^5$ cm/mole. As the size of the complex increases, the maximum of the band of the hydrogen bond shifts to lower frequencies, and it is expected that K_h will also increase. Therefore, the value of K_h given above should be regarded as averaged over the different complexes (dimers, trimers, etc.). However, since this averaged value satisfies relation (1) at all concentrations, the dependence of K_h on the size of the complex is not strong, and the range of variation of this quantity most likely lies within the stated error limits. Knowledge of K_h enables us to use the intensity of the $\nu = 3490$ cm^{-1} band to determine the number of H-bonded dimers of phenol. Since only one of the molecules in dimer Dim. 1 is a proton donor, the fraction N_d of molecules that are part of a dimer is

$$N_d = 2I_d \frac{2I_d}{(K_h N)}, \tag{2}$$

where I_d is the integrated intensity of the $\nu = 3490$ cm^{-1} dimer band.

The results of calculations of $N_d(M)$ are presented in Table II. The $\nu = 3355$ cm^{-1} band was not taken into account in these calculations, since in the majority of spectra its intensity is less than the error to which the intensities of the other bands are determined.

The intensity of the $\nu = 3635$ cm^{-1} band is determined not only by free O–H groups but also by O–H groups which are acceptors of the hydrogen bond in the phenol complexes. As was shown in Refs. 11 and 12, the frequencies of these vibrations differ by only 2 cm^{-1}, and in our spectra they merge into a single band. For this reason the intensity of the

TABLE II. Fractions (%) of the phenol in the form of monomers (N_m), dimers (N_d), and other (larger) complexes of phenol in Ar and Ne matrices and the monomer fraction for hydroquinone (Hq) in an Ar matrix, at different matrix ratios M. For phenol in an Ar matrix two values—before and after annealing—are given, and also the monomer and dimer fractions calculated for a random distribution of molecules in the sample.

M	Monomers N_m		Dimers N_d		Other complexes		Monomers of Hq (Ref.18)	Monomers (calculation)		Dimers (calculation)	
	Ar	Ne	Ar	Ne	Ar	Ne	Ar	Ar	Ne	Ar	Ne
1000	95/90	75	5/10	20	0/0	5	90	94	91	6	8
500	90/81	56	10/16	18	0/3	26	–	89	83	10	14
250	80/69	26	16/24	14	4/7	60	66	80	70	16	20
125	53/40	0	15/23	0	32/37	100	40	63	49	22	22
60	40/18	–	15/17	–	45/65	–	18	39	–	22	–
30	12/ < 5	–	10/5–10	–	80/ > 85	–	–	17	–	11	–

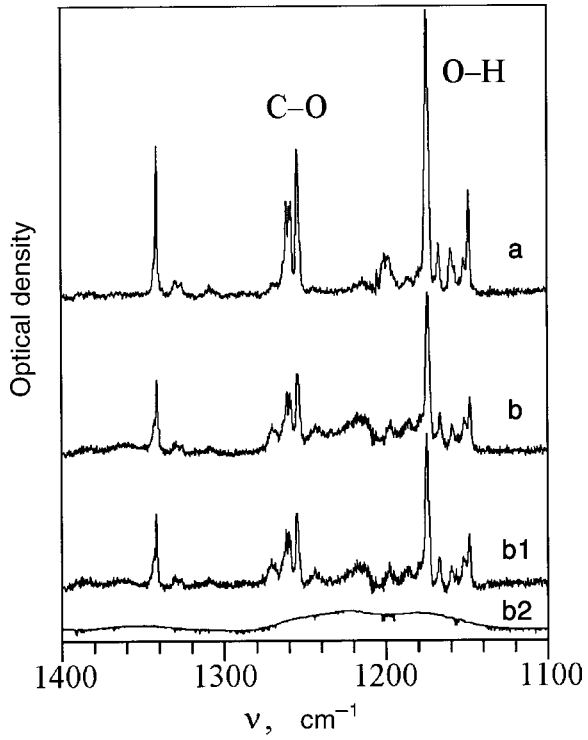

FIG. 4. IR absorption spectra of phenol in the region of the C–O stretching vibrations and the O–H planar bending vibrations in an argon matrix at matrix ratios $M=1000$ (a) and 125 (b). Curves b1 and b2 are the result of a separation of curve b into components with narrow and wide bands, respectively.

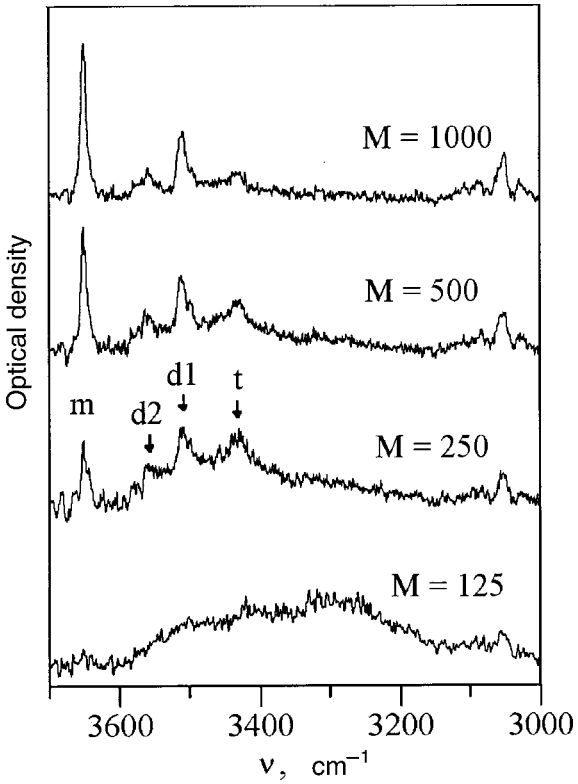

FIG. 5. IR absorption spectra of phenol in the region of the proton stretching vibrations in a neon matrix for different matrix ratios at $T=5$ K: m indicates monomers ($\nu=3650$ cm^{-1}), $d1$ and $d2$ dimers ($\nu=3507$ and 3563 cm^{-1}), and t trimers ($\nu=3430$ cm^{-1}) of phenol.

$\nu=3635$ cm^{-1} band cannot directly serve as a measure of the number of monomers. More-reliable data on the number of monomers can be obtained from the concentration dependence of the intensity of the bands of C–O stretching vibrations ($\nu=1260$ cm^{-1}) and the O–H planar bending vibration ($\nu=1176$ cm^{-1}),[15] since the formation of the hydrogen bond perturbs these vibrations both in the proton-donor and proton-acceptor molecules. Figure 4 shows a portion of the spectrum containing these bands for two concentrations, $M=1000$ and 125. For $M=1000$ the spectrum essentially contains only narrow monomer bands. As M decreases, much the wider bands of complexes appear, overlapping with the monomer bands, and at $M=125$, as can be seen in the figure, the spectrum is a superposition of narrow and wide bands. For a more precise determination of the integrated intensities of the narrow (corresponding to monomers) spectral band we used a special program to separate the spectrum into two components, having narrow (Fig. 4b1) and wide (Fig. 4b2) bands. The integrated intensities of the monomer bands at $\nu=1260$ and 1176 cm^{-1} are given in Table I for the different phenol concentrations. Calculations of the number of dimers from the intensities of the O–H stretching bands at low concentrations show that at $M=1000$ the unannealed sample contains about 5% dimers of phenol. Taking this into account and using the values of the integrated intensities of the $\nu=1260$ and 1176 cm^{-1} bands, we determine the absorption coefficients for the vibrations: $K_{1260}=(28\pm3)\times10^5$ cm/mole and $K_{1176}=(32\pm3)\times10^5$ cm/mole.

Table II gives the monomer fractions N_m found as the averages of the values of $I_{1260}(M)/NK_{1260}$ and $I_{1176}(M)/NK_{1176}$ for these two bands.

IR absorption spectra of phenol in a neon matrix

Figure 5 shows the spectra of phenol in a neon matrix in the region of the proton stretching vibrations for the different concentrations, and Fig. 6 shows the spectrum in the region

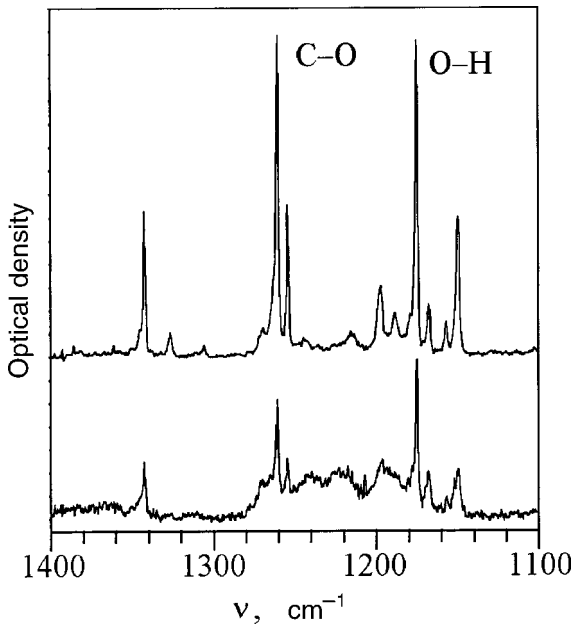

FIG. 6. IR absorption spectra of phenol in the region of the C–O stretching vibrations and O–H planar bending vibrations in a neon matrix at matrix ratios $M=1000$ (upper curve) and 250 (lower curve).

of the C–O stretching and O–H bending vibrations. Annealing of the samples at 7–8 K did not cause any substantial changes in the spectra.

As in the case of the argon matrix, the absorption spectra of phenol in a neon matrix in the region of the proton stretching vibrations have five bands of stretching vibrations of the O–H group which are shifted somewhat to higher frequencies: a monomer band at $\nu=3650$ cm^{-1}, dimer bands at $\nu=3563$ and 3507 cm^{-1} (the spectral shifts relative to the monomer bands are 87 and 143 cm^{-1}, respectively), a trimer band at $\nu=3430$ cm^{-1}, and a band of larger complexes at $\nu=3300$ cm^{-1}. The bands were assigned to the various complexes on the basis of their order of appearance in the absorption spectrum with increasing phenol concentration.

Starting from the spectral shift of 143 cm^{-1} and working by analogy with the argon matrix, the band at $\nu=3507$ cm^{-1} should be attributed to the hydrogen-bonded dimers Dim. 1. The band at $\nu=3563$ cm^{-1} corresponds to the $\nu=3555$ cm^{-1} band in the argon matrix and belongs either to the dimers Dim. 2 or to dimers with a single, but highly distorted, hydrogen bond. As we have said, the value of the spectral shift of the band of the hydrogen bond is very sensitive to the relative position of the molecules in the dimer.[2,3,7,16] Therefore, even small variations of the dimer structures due to the inhomogeneity of the matrix environment will lead to appreciable broadening of the O–H stretching bands of the dimers in comparison with the monomer bands. In liquids, where the inhomogeneity of the environment and, hence, the variations of the structure of the complexes are large, the width of the absorption band due to the hydrogen bond is usually comparable to the value of its spectral shift.[2] In our spectra the width of the absorption band of dimers with a hydrogen bond is approximately the same for both matrices and for both types of dimers and does not exceed 20 cm^{-1} (at half maximum). This is evidence of the small dispersion of such geometric parameters of the complexes as the O–O distance and the O–H$\cdots$O angle in the chain of atoms forming the hydrogen bond in the dimers of each of the two types. The difference of the spectral shifts of the O–H stretching bands of the dimers in the argon (80 cm^{-1}) and neon (87 cm^{-1}) matrices is several times smaller than the width of these bands. This means that the difference of the structures of the dimers of each type in the different matrices is less than the variation of these structures within a given matrix, and we can state that the $\nu=3563$ cm^{-1} band in the neon matrix and the $\nu=3555$ cm^{-1} band in the argon matrix correspond to practically the same structure.

The size of a phenol dimer is of the same order of magnitude as that of an atom of the matrix. It can therefore not be ruled out that there is only a small number (say, ten) of types of cavities with substantially different geometries which can accommodate phenol dimers with a single hydrogen bond. These phenol dimer+matrix complexes can differ spectrally and each give a band in the IR spectrum. Such a phenomenon, which is called matrix splitting, is very often observed.[4,5] In rare-gas matrices the value of this splitting for isolated molecules is usually not more than 10 cm^{-1} (Ref. 5), but for the O–H stretching vibrations in hydrogen-bonded complexes much larger values of the splitting cannot be ruled out. In different matrices either the number of components into which the spectral band is split or the value of the splitting will differ strongly, making it possible to distinguish matrix splitting from other effects. The van der Waals diameters of the argon and neon atoms (0.376 and 0.316 nm, respectively)[17] are quite different, and so the hypothesis that there exist only two types of spectrally distinguishable matrix cells in which the phenol dimers can be fixed in the two matrices, with identical degrees of distortion of the hydrogen bond, is improbable, and most likely the $\nu=3563$ cm^{-1} band ($\nu=3555$ cm^{-1} in the argon matrix) should be attributed to the dimers Dim. 2.

Table I gives the integrated intensities of the absorption bands of the phenol molecules in the neon matrix: monomers ($\nu=1260$ and 1176 cm^{-1}) and stretching vibrations of the free O–H group ($\nu=3650$ cm^{-1}), dimers with stretching vibrations of the O–H group ($\nu=3563$ and 3507 cm^{-1}), and other complexes ($\nu=3600$–3150 cm^{-1}). The number of monomers, dimers, and larger complexes of phenol, calculated on the basis of these data, are presented in Table II. In determining the fractions comprised of monomers and complexes it was assumed that the integral absorption coefficients in the neon and argon matrices are the same. Since in Dim. 2 both O–H groups form hydrogen bonds, the total number of dimers should be given by the formula

$$N_d=(I_{d2}+2I_{d1})/(K_hN), \tag{3}$$

where I_{d1} and I_{d2} are the integrated intensities of the $\nu=3507$ and 3563 cm^{-1} bands, respectively.

As expected, the molecular complexes in the neon matrix turn out to be much larger than in the argon matrix at the same matrix ratios. The molar volume of solid neon is approximately 1.7 times smaller than that of argon, and therefore to obtain the same volume concentration of the molecules to be investigated the matrix ratio for the neon sample must be the same number of times larger. However, as we see from Table II, the number of monomers in the neon matrix becomes the same as in the argon matrix only at a matrix ratio that is approximately three times larger.

COMPUTER SIMULATION OF THE FORMATION OF MOLECULAR COMPLEXES IN A MATRIX

Physical justification of the model

In the joint deposition of molecular streams of the substance to be studied and a matrix gas on a cold substrate, the matrix sample forms as a polycrystalline film. The sizes of the crystallites in a thin argon film lie in the range 0.1–1 μm for samples grown at a temperature of 15–17 K.[17] At such grain sizes one can neglect the volume of the grain boundaries and assume that the sample is a single crystal of the matrix substance with a random distribution of impurity molecules over its volume.

The ratio of the molar volumes of phenol and argon in the solid phase is equal to 3.9, and we shall therefore assume that the phenol molecule occupies four sites of the argon lattice. The distance between close-packed planes in the argon crystal is 0.307 nm,[17] which is somewhat smaller than the size of the phenol molecule in the direction perpendicular to the plane of the benzene ring. We shall assume that in the argon crystal the impurity molecule substitutes for four atoms of the matrix, as is shown in Fig. 7a, and does not cause

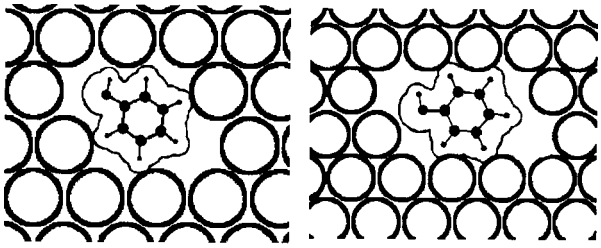

FIG. 7. Proposed arrangement of the phenol molecule in the argon (a) and neon (b) matrices.

substantial distortions to the crystal structure. The ratio of the molar volumes of phenol and neon is 6.6, and we shall assume that the impurity molecule substitutes for six neon atoms, as is shown in Fig. 7b. The distance between close-packed planes in the neon crystal is approximately 20% smaller than in the argon crystal, and therefore the phenol molecule most likely cannot be incorporated into the neon lattice without distorting it, but the lattice distortions were not taken into account in the model.

Based on these considerations we constructed a model on the assumptions that:

1) the sample is a single crystal of the matrix substance with a face-centered cubic (fcc) structure in which the impurity molecules substitute for some atoms of the matrix and do not introduce distortions to the overall structure of the lattice;

2) the impurity molecule lies in one of the close-packed planes of the matrix;

3) the impurity molecule is assumed to be part of a complex if even one of the nearest-neighbor lattice sites is occupied by another molecule.

Computational method

The numbers of monomers and complexes are sometimes estimated with the use of probability theory[5] by calculating the number of molecules having one or more neighbors in the matrix. However, such calculations are very difficult for nonspherical molecules and for models taking into account the discrete structure of the matrix. We therefore chose a method of direct numerical simulation of the process of formation of the matrix sample.

The cubic part of the fcc crystal of the matrix substance was modeled by a three-dimensional numerical array. One of the axes of the cube was oriented perpendicular to one of the close-packed planes, and another axis of the cube was oriented along one of the directions of the smallest interatomic distances in this plane. Each element of the array was placed in correspondence with one lattice site, the coordinates of which were determined by the indices of the element. An impurity molecule occupied four sites of the argon or six sites of the neon matrix in the configuration described above. The array was filled by a procedure in which all of the elements were successively ''scanned'' and at each vacant site of the lattice the first site occupied by an impurity molecule is picked at random with a probability $1/(M+V)$, where V is the number of lattice sites occupied by an impurity molecule). Then another procedure is used to align the ''molecule'' by placing the second site at random in one of the twelve possible directions, and then the third site in one of the three close-packed planes, etc., taking into account the dependence of the indices of the array on the position of the sites for the fcc lattice. To eliminate the effect of the boundaries of the ''sample,'' periodic boundary conditions were introduced, i.e., for a molecule found at the face of the cube a molecule located on the opposite face was regarded as neighboring. The size of the cube was varied from 120 to 48 sites on a side for low and high impurity concentrations, respectively.

After the array was completely filled the number of monomers and complexes consisting of two, three, etc. molecules was counted up. Since the process of ''sample preparation'' in this model is determined by random processes and the samples are of small size, the results of the calculation can have significant fluctuations. Therefore, depending on the number of molecules in the ''sample'' the calculation was repeated many times for each concentration until the standard deviation of the number of monomers and dimers became less than 2%.

Comparison of the results of the calculation and experiment

The results of the calculations are presented in Table II. The experimental values of the numbers of monomers and complexes of phenol in the argon matrix are given in pairs, for before and after annealing of the matrix. The influence of annealing at temperatures of 25–30 K on the number of hydrogen-bonded complexes of phenol and diphenols was investigated in Ref. 18. It was shown that annealing affects the number of H-bonded complexes differently for different phenols. The intensity of the spectral bands of some derivatives of phenol (hydroquinone and resorcin) are hardly changed by annealing, while for others (pyrocatechol) there is a small (by 20–30%) increase in the intensity of the band of the hydrogen bond. The greatest effect of annealing is observed for phenol, for which the intensity of the band of the stretching vibration of the H-bonded proton increases by a factor of 1.5–2. The different role of annealing for the different derivatives of phenol is due to the different position of the O–H groups in their molecules. As was shown in Ref. 18, phenol molecules at temperatures above 30 K cannot move along the sample but can randomly vary their orientation on account of thermal vibrations and the diffusive motion of matrix atoms. This process has been called ''orientational diffusion.'' For the first group of derivatives mentioned the probability of formation of a hydrogen-bonded complex is very high even during growth of the sample because of the presence of two O–H groups quite far separated along the benzene ring. Therefore the role of ''orientational diffusion'' for these molecules is small. For phenol with one O–H group the probability of formation of a hydrogen-bonded dimer during growth of the film is small, and the ''orientational diffusion'' during annealing markedly increases the number of complexes with such bonds.

During annealing the number of complexes does not change on account of ''orientational diffusion''—only the number of hydrogen bonds increases. This conclusion is confirmed in the present study by the fact that the number of monomers of hydroquinone determined in Ref. 18 (Table II)

is in good agreement with the number of monomers of phenol in the annealed samples. Therefore, in comparing the results of the calculation and experiment for the argon matrix one should use the experimental values for the annealed samples.

Annealing of the neon matrix, as we have said, does not lead to changes in the IR spectra. This is probably because the mobility of the phenol molecules in the surface layer of the growing sample is higher in the neon matrix than in the argon, and the neon matrix is completely annealed right during growth. Therefore, for the neon matrix only one value of the integrated intensity and for the fraction of monomers and complexes is given for each concentration in Tables I and II.

A comparison of the calculated fractions of monomers and dimers with the values determined from the experimental results indicates that a larger number of phenol complexes is found in the real matrix. This is particularly true for the neon matrix.

A process that can alter the distribution of the phenol molecules is their motion along the sample, i.e., translational diffusion. At low enough temperatures the diffusion of impurity molecules in the prepared samples can be neglected. During growth of the sample, however, a ''warm'' zone may arise in a surface layer, and for a certain time the necessary conditions for the diffusion of impurity molecules might exist in it. This process will give rise to an additional number of complexes (in comparison with the random distribution of molecules) if the substance under study is insoluble in the solid phase of the matrix. The degree of influence of this limited-time diffusion depends on such factors as the substrate temperature, the size of the molecules under study, the rate of deposition of the sample, and the matrix substance. It is known[5] that in the case of small (di- or triatomic) molecules at temperatures above $0.3T_m$ (T_m is the melting temperature of the matrix substance), diffusion in a surface layer of a growing sample is so significant that it is almost impossible to obtain isolated molecules. Even for comparatively large molecules, however, diffusion in the surface layer of the growing sample can have an appreciable influence on the formation of molecular complexes.

Incorporating translational diffusion effects

It is clear from general arguments that the average length over which impurity molecules can move after striking the cooled matrix cannot be large for molecules roughly the size of the phenol molecule. We shall assume that this is not more than 5–10 times the minimum interatomic distance in the crystal of the matrix gas, since otherwise practically no isolated molecules would be observed in the matrix at concentrations of 1:100–1:1000. Under our conditions of sample preparation (substrate temperature 15 K for the argon and 5 K for the neon matrix, maximum rate of deposition 5×10^{-6} mole/(cm^{2}min) of a matrix gas cooled to 77 K), even at the maximum sample thickness (0.15 mm) the temperature difference between the surface of the sample and the substrate due to release of the heat of condensation is not more than 0.01 K. Therefore, diffusion is possible only in a limited region near the place where each successive ''hot'' molecule strikes the surface, and only for a short time. Diffusive motion under the conditions for the existence of a ''hot'' region around an impurity object (molecule or complex) depends substantially on the size of that object, since the strength of the barrier will depend to a significant degree on the number of atoms of the matrix that are moved during the displacement of the impurity by an amount equal to the minimum interatomic distance in the crystal,[19] i.e., as the size of the complex increases, the strength of the barrier increases and the rate of its diffusion decreases. Since in our model the rate of diffusion of the monomers of phenol was assumed to be small from the start, we shall assume that it is negligible for all complexes. Based on these assumptions, the model can be amended with the following items:

1) translational diffusion can lead to a random displacement of impurity molecules by a distance not greater than 10 intersite distances in the matrix crystal;

2) translational diffusion is possible only for monomers; once formed, the molecular complexes remain immobile.

In our numerical simulation of the diffusion of monomers it was assumed that an elementary event (step) is the random displacement of a molecule by a distance ranging from zero to the maximum dimension of the molecule, and its acquisition of a new random orientation. After the random filling of the ''sample'' and the first counting of the number of monomers and complexes, a special procedure is carried out in which all the elements of the array are successively ''scanned,'' and when the first site marked as belonging to a monomer is found, this monomer is completely removed and the site is marked as the first found. Then one of the twelve sites nearest to the marked site is picked at random, and, starting at that site, a new molecule is constructed. If this brings the molecule to the face of the cube, then it enters the sample from the opposite side. In such a procedure the center of the molecule can be displaced from zero to the ''length'' of the molecule. The average displacement of the center of the molecule in one step will be approximately equal to one interatomic distance in the argon crystal and 1.5 interatomic distances in the neon. After this has been done for all of the isolated molecules in the first diffusion step, the numbers of monomers, dimers, etc. are again counted up. The maximum number of diffusion steps in the calculations was equal to six for the argon matrix and eight for the neon.

Figure 8a shows the fraction of impurity molecules that are isolated in the argon matrix as calculated for different numbers of diffusion steps, and also the number of phenol monomers found experimentally. Analogous results are shown in Fig. 8b for dimers. We see that the results of the experiment and calculation are in good agreement if it is assumed that the phenol molecule makes 1–2 diffusion steps. Table III gives the results of a calculation of the number of monomers and small complexes in an argon matrix at the different concentrations for the first three diffusion steps. The results of similar calculations and experiments for phenol in a neon matrix are shown in Fig. 9. Despite the large error of the experimental data, one nevertheless can discern a discrepancy between the experimental and calculated data, especially for the dimers. If one proceeds from an analysis of the data for monomers (Fig. 9a) then it can be assumed that the phenol molecule in the neon matrix makes 4–6 diffusion steps. In that case, however, the calculation predicts a much larger number of dimers than is observed in the experiment.

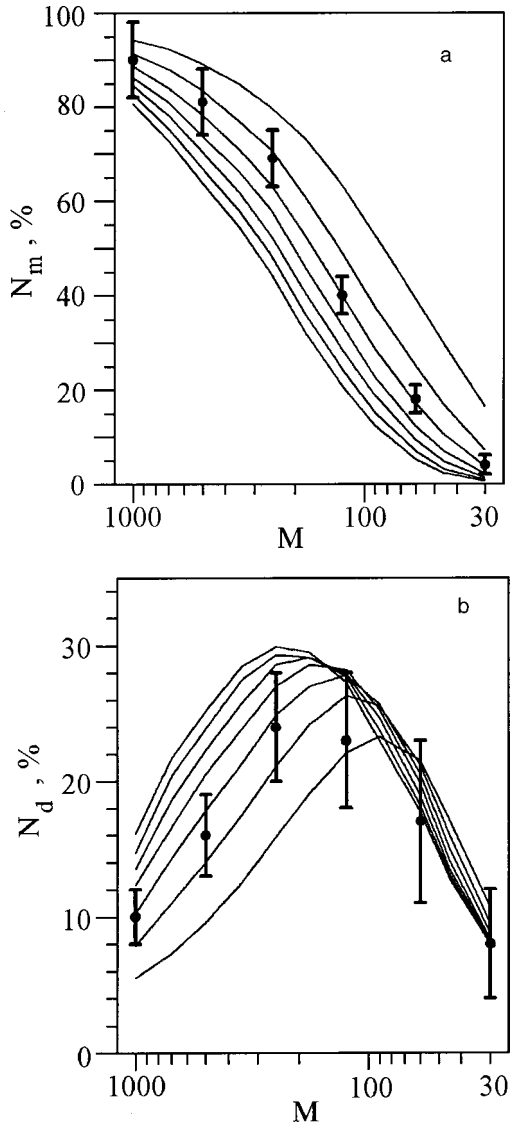

FIG. 8. Monomer fraction N_m (a) and dimer fraction N_d (b) for phenol molecules in an argon matrix as a function of the matrix ratio for different numbers of diffusion steps S (solid curves): $S=0$, 1, 2, 3, 4, 5, 6 (in part a from top to bottom; in part b from bottom to top). The curves with the vertical bars are the experimental values (after annealing) from Table II.

In the calculations we assumed that all the complexes, including dimers, remain immobile. This assumption tends to overestimate the number of dimers in the calculation, since at almost all concentrations the formation of dimers from two monomers occurs faster than the loss of dimers to the formation of trimers from a dimer and a monomer. Therefore the discrepancy between the calculation and experiment can be regarded as evidence of a deviation specifically from this assumption. As we have said, the phenol molecule should create strong distortions of the neon lattice around it. These distortions and defects may be one of the factors increasing the mobility of the molecules and complexes in the neon matrix.

CONCLUSIONS

Two types of hydrogen-bonded dimers are formed in frozen argon and neon matrices as the concentration of the phenol molecules is increased. The dimers having a spectral shift of 145 cm^{-1} in the argon and 143 cm^{-1} in the neon matrix relative to the monomer absorption bands of the stretching vibration of the O–H group are formed by two phenol molecules with a single hydrogen bond. Their structure is practically the same in both matrices and is probably close to the undistorted structure in the gas phase, in which the corresponding spectral shift is 126 cm^{-1}.

The other group of dimers, having a spectral shift of 80 cm^{-1} in the argon and 87 cm^{-1} in the neon matrix relative to the monomer absorption bands are most likely formed with two hydrogen bonds. The structure of the dimers of phenol with a single hydrogen bond corresponds to more intense absorption bands in the spectrum as compared to the bands of the dimers with two hydrogen bonds. This indicates that the first type of dimer structure is preferable in solid rare-gas matrices. We note that in the argon matrix the dimers with two hydrogen bonds are less stable than in the neon matrix. The influence of annealing on the intensity of the absorption bands of dimers and monomers of phenol in the argon matrix is due to the orientational diffusion of the phenol molecules which arises when the temperature is raised to 30 K.

On the basis of the integrated intensities of the absorption bands and the information about the absolute concentra-

TABLE III. Calculated fractions of molecules in complexes consisting of N molecules in an argon matrix for different numbers of diffusion steps S and different matrix ratios M.

	Fraction of the molecules, %			
M	$S=0$	$S=1$	$S=2$	$S=3$
		$N=1$		
1000	94.2	91.3	88.7	86.2
500	89.1	83.4	78.2	73.8
250	79.5	70.5	62.9	57.6
125	63.2	49.0	40.0	33.6
60	39.2	25.1	17.1	12.2
30	16.5	7.2	3.7	2.1
		$N=2$		
1000	5.5	7.9	10.2	12.3
500	9.6	14.0	17.8	20.5
250	15.9	21.1	24.9	27.0
125	22.1	26.3	27.8	28.2
60	21.5	21.2	20.5	19.8
30	10.7	9.5	8.8	8.3
		$N=3$		
1000	0.3	0.8	1.0	1.4
500	1.1	2.2	3.3	4.6
250	3.5	5.9	8.4	10.3
125	8.6	13.2	16.0	18.0
60	12.6	15.6	16.1	17.4
30	7.7	7.7	7.9	8.1
		$N=4$		
1000	0.0	0.0	0.1	0.1
500	0.2	0.4	0.7	0.9
250	0.8	1.9	2.5	3.3
125	3.5	6.2	8.4	9.9
60	7.6	10.0	11.4	12.1
30	5.9	6.3	6.2	6.3
		$N>4$		
1000	0.0	0.0	0.0	0.0
500	0.0	0.0	0.0	0.2
250	0.3	0.6	1.3	1.8
125	2.6	5.3	7.8	10.3
60	19.1	28.1	34.9	38.5
30	59.2	69.3	73.4	75.2

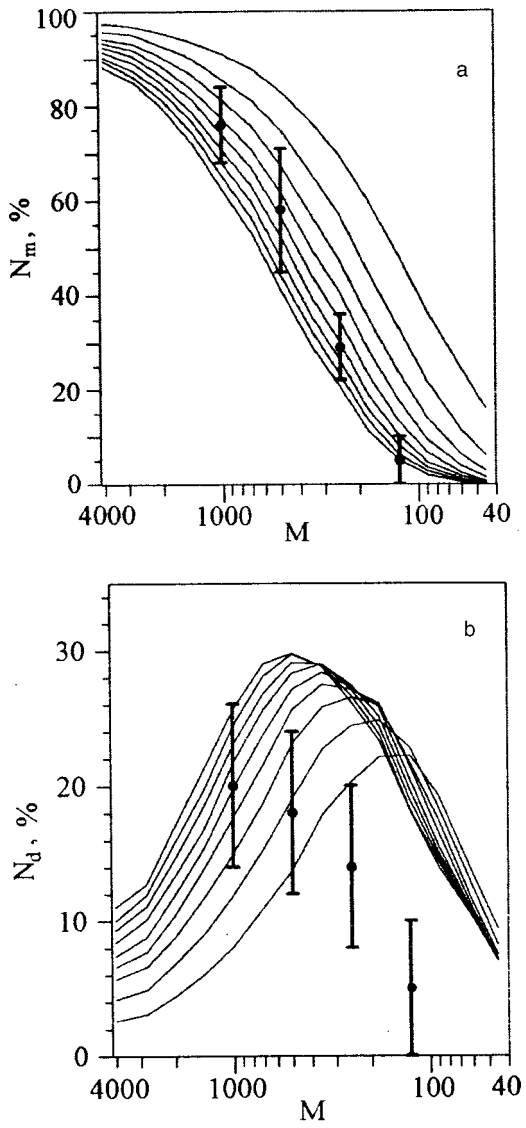

FIG. 9. Monomer fraction N_m (a) and dimer fraction N_d (b) for phenol molecules in a neon matrix as a function of the matrix ratio for different numbers of diffusion steps S (solid curves): $S=0$, 1, 2, 3, 4, 5, 6, 7, 8 (in part a from top to bottom; in part b from bottom to top). The curves with the vertical bars are the experimental values from Table II.

tion of the substance under study in the matrix, the absorption coefficients in the various spectral bands were determined, and the numbers of monomers and dimers of phenol were estimated for the different matrices and different matrix ratios.

A computational model was proposed for determining the numbers of monomers, dimers, and larger complexes of molecules such as phenol in a matrix. A comparison of the calculated monomer and dimer fraction with the results derived from experiments indicates that the real matrices contain larger numbers of phenol complexes. This may be due to translational diffusion of phenol molecules during growth of the sample. Limited diffusion in a surface layer of the growing sample can be taken into account through the motion of only the monomers. Such diffusion leads to a nearly twofold increase in the number of dimers in comparison with the random distribution of phenol molecules over the sample in the range of matrix ratios $M=500-200$.

In the neon matrix the mobility of the phenol molecule during growth of the sample is higher, and therefore the calculation (in the framework of the proposed model) would require taking into account the motion of the simplest complexes in addition to that of the monomers. Such a mobility of the complexes in the neon matrix would lead to a much lower number of isolated phenol dimers than in the argon matrix for the same number of monomers.

*E-mail: plokhotnichenko@ilt.kharkov.ua
†Deceased

[1] G. C. Pimentel and A. L. McClellan, *The Hydrogen Bond* [Freeman, San Francisco (1960); Mir, Moscow (1964)].
[2] N. D. Sokolov (Ed.), *The Hydrogen Bond* [in Russian], Nauka, Moscow (1985).
[3] A. Weber (Ed.), *Structure and Dynamics of Weakly Bound Complexes*, Reidel, Dordrecht (1987).
[4] A. J. Downs and S. C. Peake, *Molecular Spectroscopy, Specialist Periodical Reports of the Chemical Society*, Vol. 1, London (1973), p. 523.
[5] S. Cradock and A. Hinchcliffe, *Matrix Isolation* (Cambridge University Press, Cambridge, 1975).
[6] L. H. Jones, S. A. Ekberg, and B. Swanson, J. Chem. Phys. **85**, 3203 (1986).
[7] T. K. Ghosh and E. Miyoshi, Theor. Chim. Acta **105**, 31 (2000).
[8] K. Sagarik and P. Asawakun, Chem. Phys. **219**, 173 (1997).
[9] S. Sun and E. R. Bernstein, J. Phys. Chem. **100**, 13366 (1996).
[10] L. L. Connell, S. M. Ohline, P. W. Joireman, T. C. Corcoran, and P. M. Felker, J. Chem. Phys. **96**, 2585 (1992).
[11] G. V. Hartland, B. F. Henson, V. A. Venturo, and P. M. Felker, J. Phys. Chem. **96**, 1164 (1992).
[12] T. Ebata, T. Watanabe, and N. Mikami, J. Phys. Chem. **99**, 5761 (1995).
[13] M. C. Moreau Descoings, G. Goethals, and J. P. Seguin, Bull. Soc. Chim. Belg. **97**, 127 (1988).
[14] E. D. Radchenko, G. G. Sheina, N. A. Smorygo, and Yu. P. Blagoi, J. Mol. Struct. **116**, 386 (1984).
[15] H. Lampert, W. Mikenda, and A. Karpfen, J. Phys. Chem. A **101**, 2254 (1997).
[16] V. M. Bilobrov, *The Hydrogen Bond. Intramolecular Interaction* [in Russian], Naukova Dumka, Kiev (1991).
[17] B. I. Verkin and A. F. Prikhot'ko (Eds.), *Cryocrystals* [in Russian], Naukova Dumka, Kiev (1983).
[18] A. M. Plokhotnichenko, A. Yu. Ivanov, E. D. Radchenko, G. G. Sheina, and Yu. P. Blagoi, Fiz. Nizk. Temp. **19**, 1029 (1993) [Low Temp. Phys. **19**, 732 (1993)].
[19] I. Ya. Fugol', A. M. Ratner, and A. G. Belov, "Exciton-stimulated processes in matrices of inert elements," in *Chemistry of Low Temperatures and Cryochemical Technology, Issue 2* [in Russian], Izd. MGU, Moscow (1990).

Translated by Steve Torstveit

LATTICE DYNAMICS

Thermal expansion of single crystals of the layered compounds $TlGaSe_2$ and $TlInS_2$

N. A. Abdullaev, T. G. Mamedov, and R. A. Suleĭmanov

*Institute of Physics of the Academy of Sciences of the Azerbaijan Republic, pr. Dzhavida 33, 370143 Baku, Azerbaijan**

(Submitted December 26, 2000; revised April 14, 2001)
Fiz. Nizk. Temp. **27**, 915–920 (August 2001)

Experimental data are reported from studies of the thermal expansion of single crystals of the layered compounds $TlGaSe_2$ and $TlInS_2$ in the plane of the layers and in the direction perpendicular to the layers in the temperature region 20–300 K. Observed features of the thermal expansion are discussed in the light of the available data on the elastic properties of $TlGaSe_2$ and $TlInS_2$. It is found that the differences in the temperature behavior of the thermal expansion coefficients in the plane of the layers $\alpha_{\parallel}(T)$ in the $TlGaSe_2$ and $TlInS_2$ crystals are due to the different degree of anisotropy of these crystals and to the different value of the ''interlayer'' elastic constant C_{13}. © *2001 American Institute of Physics.*
[DOI: 10.1063/1.1399208]

Single crystals of the layered compounds $TlGaSe_2$ and $TlInS_2$ are of interest in connection with the observation of structural phase transitions in them. A large body of experimental data on the dielectric,[1–3] optical,[3,4] and thermal[5–7] properties of $TlGaSe_2$ and $TlInS_2$ shows evidence of the presence of anomalies in the temperature behavior of a number of physical parameters at temperatures in the phase transition region. In Ref. 2 it was proposed that in $TlGaSe_2$ the phase transition to the ferroelectric phase at $T=107$ K is preceded by a transition to a state with spatial modulation of the structure at $T=120$ K, and this was confirmed by neutron diffraction methods.[8] The data from neutron diffraction measurements in $TlInS_2$ have revealed[9] that in the temperature region 216–200 K there exists an incommensurate phase with a modulation wave vector $\mathbf{q}_{\text{inc}}=(\delta,\delta,0.25)$.

The authors of the present paper made the first observation[6,7] of the features in the temperature dependence of the coefficient of linear thermal expansion (CLTE) of $TlGaSe_2$ and $TlInS_2$ single crystals in the plane of the layers, $\alpha_{\parallel}(T)$, and perpendicular to the layers, $\alpha_{\perp}(T)$, in the temperature range 20–300 K. Later papers[11–13] would report the results of x-ray diffraction studies of the temperature dependence of the lattice parameters of $TlGaSe_2$ and $TlInS_2$ in the phase transition regions. According to the data of Ref. 12, in $TlGaSe_2$ the sharp jump on the $\alpha_{\perp}(T)$ curve is accompanied by an abrupt decrease of smaller size in $\alpha_{\parallel}(T)$ in the temperature interval 100–120 K. In Ref. 13 it was reported that $\alpha_{\perp}(T)$ in $TlGaSe_2$ has two peaks, at temperatures of 107 and 114 K, but the values of $\alpha_{\perp}(T)$ at room temperature did not agree with the data of Refs. 6, 11, and 12. Two peaks on $\alpha_{\perp}(T)$ were also observed for $TlInS_2$ crystals,[13] at 196 and 214 K. The results reported in Ref. 11 on the temperature dependence of $\alpha(T)$ in polycrystalline samples of $TlGaSe_2$ did not reveal any anomalies. It is well known that a general shortcoming of the x-ray method for studying the CLTE is its low sensitivity to relative elongations $\Delta L/L$ (in the best case $\Delta L/L$ reaches values of $\sim 10^{-4}$). This circumstance requires the use of a large temperature step (more than 10 K) in experiments, and that undoubtedly distorts the character of the temperature dependence of $\alpha(T)$ in phase transition regions.

The presence of discrepant and at times even contradictory information about the temperature behavior of the CLTE in single crystals of the layered compounds $TlGaSe_2$ and $TlInS_2$, on the one hand, and the need for models that give a consistent explanation for the features of the thermal expansion of the layered crystals $TlGaSe_2$ and $TlInS_2$ in the light of the results of studies of their elastic properties,[14,15] on the other, prompted the writing of this paper.

EXPERIMENTAL RESULTS AND DISCUSSION

Dilatometric studies were done on an interference dilatometer in the temperature interval 20–300 K. The temperature in the thermostatic chamber was automatically maintained to within 0.05 K or better. The accuracy of the measurements of the CLTE reached 2×10^{-7} K^{-1}.

Samples with a dimension of about 5 mm along the direction of measurement were prepared from single crystals grown by the Bridgman method. The crystal lattice of the $TlGaSe_2$ and $TlInS_2$ crystals has axial symmetry (the axis of symmetry is almost perpendicular to the plane of the layers) and is classified as belonging to space group C_{2h}^6.

Figure 1 shows our data on the temperature dependence of the CLTE of single crystals of $TlGaSe_2$ in the plane of the layers ($\alpha_{\parallel}$) and perpendicular to them ($\alpha_{\perp}$). It is seen that large positive values of $\alpha_{\perp}(T)$ are observed, as is characteristic for practically all layered crystals in the direction of weak coupling.[16] The $\alpha_{\perp}(T)$ curve shows pronounced anomalies in the form of three peaks at temperatures $T=102$, 110, and 120 K. The $\alpha_{\parallel}(T)$ curve is much different. The values of $\alpha_{\parallel}(T)$ are negative below 135 K, and only above that temperature does it take on positive values, going

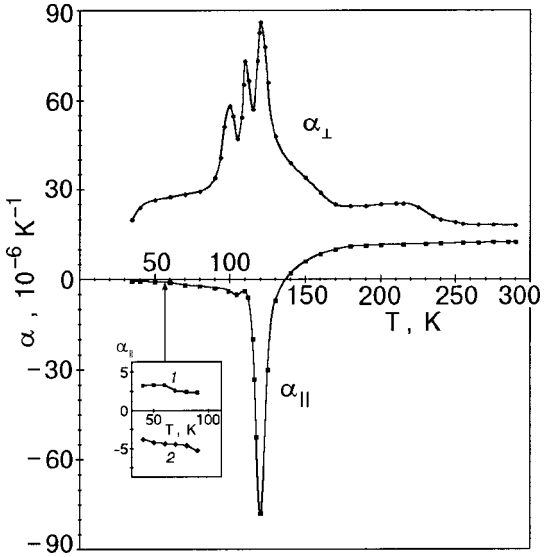

FIG. 1. Temperature dependence of the coefficient of thermal expansion of $TlGaSe_2$ single crystals in the plane of the layers ($\alpha_\parallel$) and perpendicular to the layers ($\alpha_\perp$). The inset shows the contribution to $\alpha_\parallel(T)$ of the first (*1*) and second (*2*) terms of relation (1).

out to a plateau with a value $\alpha_\parallel \approx 12\times10^{-6}\,\mathrm{K}^{-1}$ at $T > 200$ K. At the temperatures $T = 102$ and 120 K the $\alpha_\parallel(T)$ curve has anomalies in the form of pronounced dips.

Figure 2 shows data on the temperature dependence of the thermal expansion of $TlInS_2$ single crystals. It is seen that for the weak coupling direction the values of $\alpha_\perp(T)$ are characteristically large, and at $T \sim 200$ K an anomaly in the form of a pronounced peak is observed, with a maximum value $\sim 150\times10^{-6}\,\mathrm{K}^{-1}$. The $\alpha_\parallel(T)$ curve is featureless, having the standard temperature dependence for the CLTE.

Thus, summarizing the experimental data, we note that a common property of the single crystals of the layered compounds $TlGaSe_2$ and $TlInS_2$ is the presence of large values of $\alpha_\perp(T)$ in the weak coupling direction and sharp peaks in the

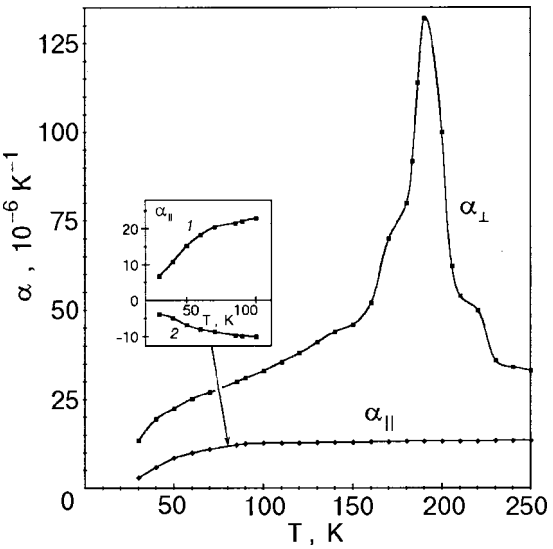

FIG. 2. Temperature dependence of the coefficient of thermal expansion of $TlInS_2$ single crystals in the plane of the layers ($\alpha_\parallel$) and perpendicular to the layers ($\alpha_\perp$). The inset shows the contributions to $\alpha_\parallel(T)$ of the first (*1*) and second (*2*) terms of relation (1).

regions of the phase transition temperatures. A substantial difference is observed in the temperature dependence of $\alpha_\parallel(T)$ at low temperatures (in the region of the phase transition and below):

1) the CLTE in the plane of the layers, $\alpha_\parallel(T)$ is positive in $TlInS_2$ but is negative in $TlGaSe_2$ below 135 K;

2) in $TlGaSe_2$ single crystals the temperature dependence of the CLTE exhibits features in the region of the phase transitions in both directions, while in $TlInS_2$ single crystals there are no features on $\alpha_\parallel(T)$.

To explain the substantial differences in the behavior of $\alpha_\parallel(T)$ in these crystals, let us turn to the known relation for the CLTE in crystals with axial symmetry,[17] which is valid far from the phase transitions:

$$\alpha_\parallel = \frac{C_V}{V}\times\left[\frac{C_{33}}{(C_{11}+C_{12})C_{33}-2C_{13}^2}\,\gamma_\parallel - \frac{C_{13}}{(C_{11}+C_{12})C_{33}-2C_{13}^2}\,\gamma_\perp\right], \tag{1}$$

where C_V is the heat capacity at constant volume, V is the molecular volume, C_{ik} are the elastic constants (C_{11} and C_{12} characterize the intralayer interactions, and C_{33} and C_{13} reflect the weak interlayer coupling), and $\gamma_\parallel$ and $\gamma_\perp$ are the weighted-average Grüneisen parameters:

$$\gamma_\parallel = \sum \gamma_{\parallel,i}C_i / \sum C_i\,,\quad \gamma_\perp = \sum \gamma_{\perp,i}C_i / \sum C_i\,.$$

Here C_i is the contribution of the ith mode to the heat capacity, $\gamma_{\parallel,i} = -\partial \ln \omega_i / \partial \ln a$ is the mode Grüneisen parameter, which characterizes the change in the vibrational frequency upon deformation of the crystal in the plane of the layer (a is the lattice parameter of the crystal in the plane of the layer), $\gamma_{\perp,i} = -\partial \ln \omega_i / \partial \ln c$ is the "interlayer" mode Grüneisen parameter (c is the lattice parameter of the crystal in the direction perpendicular to the layers).

As we see from relation (1), $\alpha_\parallel$ can take negative values in two cases:

1) when the first term is negative because of a negative Grüneisen parameter $\gamma_\parallel$;

2) at positive values of $\gamma_\parallel$ when the second term, which contains the so-called Poisson compression, is dominant. In this case the strong expansion in the direction perpendicular to the layers is accompanied by a lateral compression in the plane of the layers which exceeds the intrinsic expansion in the plane of the layers.

Let us discuss the possibility of realizing the two cases.

At first glance an estimate of the contributions of the two terms to $\alpha_\parallel$ does not seem to present any difficulty. Indeed, if all of the elastic constants of the crystal and also $\alpha_\parallel(T)$ and $\alpha_\perp(T)$ are known, an estimate of the contributions mentioned can be made using relation (1) and the analogous relation for $\alpha_\perp$. The difficulty, however, lies in the absence of knowledge about the constant C_{13}. As we stressed previously in Ref. 14, in which the elastic constants of $TlGaSe_2$ and $TlInS_2$ were determined by ultrasonic methods, the difficulty of determining C_{13} in a layered crystal is due to the complicated nature of preparing samples with a high-quality cleavage surface at an angle to the layers, and for this reason data on the values of C_{13} are lacking altogether or have very

different values in different studies. This is true for all layered crystals without exception. An incorrect determination of C_{13} can also lead to incorrect conclusions as to the mechanism of the negative $\alpha_{\parallel}$ in layered crystals. In view of the importance of this factor, let us discuss it in more detail and consider an example of a ''classic'' layered crystal—graphite. To this day there is a common misconception in the scientific literature as to the nature of the negative $\alpha_{\parallel}$ in graphite,[18,19] based on an incorrect value of C_{13}.

It is well known that graphite is the most typical and fully studied representative of the layered crystals. It was observed experimentally relatively long ago[18] that graphite has a wide temperature region (up to 600 K) in which $\alpha_{\parallel}(T)$ has negative values. The presence of negative values of $\alpha_{\parallel}(T)$ in graphite was explained by the long-standing hypothesis[18] that it is due to Poisson compression. This hypothesis prevailed until quite recently and continues to be accepted in many papers to this day. The reason is that many authors use too high values of the elastic constant, $C_{13}\approx 6\times 10^{11}$ dyn/cm^2. Recent measurements of C_{13} in graphite[20] have shown that the value of C_{13} in Ref. 18 and in many other papers is several times larger than the value measured in Ref. 20, viz., $C_{13}=1.5\times 10^{11}$ dyn/cm^2.

The present authors previously[16] demonstrated for the first time that in view of the smallness of C_{13} in graphite, it is the first term in relation (1) that is responsible for the negative values of $\alpha_{\parallel}(T)$, i.e., the negativity of $\alpha_{\parallel}(T)$ is due to the negative values of $\gamma_{\parallel}$. Back in 1952 it was shown by Lifshitz[10] that a feature of the phonon spectrum of layered crystals is the presence of so-called ''bending waves''—transverse waves propagating in the plane of the layers and polarized perpendicular to them. Because of the ''membrane effect'' inherent to bending waves, viz., the growth of their frequencies under tension in the plane of the layers, the corresponding mode Grüneisen parameters turn out to be negative, and this can lead to negative $\alpha_{\parallel}$ in the case when the bending waves give the dominant contribution to the thermal properties of layered crystals. The latter is possible only in the presence of strong anisotropy of the elastic properties or, more precisely, under the condition $C_{33},C_{13}\ll C_{11},C_{12}$, which, by the way, is by no means valid for all layered crystals.

It was shown in Ref. 16 that the Lifshitz theory can explain completely the temperature dependence of $\alpha_{\parallel}$ and $\alpha_{\perp}$ in layered crystals of C and BN and helps in understanding the behavior of $\alpha_{\parallel}$ and $\alpha_{\perp}$ in the layered crystals GaS, GaSe, and InSe. In particular, it was demonstrated that the negative values of $\alpha_{\parallel}$ in graphite and boron nitride are due mainly to the contribution of bending waves. The weak anisotropy of the elastic properties of GaS, GaSe, and InSe in comparison with that of C leads to the situation that the use of the theory of Ref. 10 for describing the behavior of $\alpha(T)$ in those crystals becomes incorrect. Nevertheless, it can be assumed that acoustic waves (which, strictly speaking, can no longer be called bending waves in the case of weak anisotropy) corresponding to oscillations directed perpendicular to the layers have negative $\gamma_{\parallel}$ and bring about negative values of $\alpha_{\parallel}$ only in a narrow temperature interval: 30–50 K in GaSe, as compared to 0–600 K in graphite. These conclusions are also consistent with the conclusions of Ref. 21, in which a detailed microscopic analysis is given for the low-temperature features of the CLTE in layered crystals.

The main conclusion of the studies described above is that in view of the small values of the elastic constant C_{13} in layered crystals and the presence of low-frequency vibrations with negative Grüneisen parameters $\gamma_{\parallel}$ the negativity of $\alpha_{\parallel}$ turns out to be due predominantly to the contribution of the first term in (1).

We have attempted to apply the analysis carried out above for C, Bn, GaS, GaSe, and InSe to the layered crystals $TlGaSe_2$ and $TlInS_2$. The existing data, both those obtained by us in Refs. 14 and 15 and those given in Refs. 8 and 9, leave no doubt as to the low anisotropy of the elastic properties of the $TlGaSe_2$ and $TlInS_2$ crystals. In addition, whereas in graphite the layers are monatomic planes and in the layered crystals GaS, GaSe, and InSe the layers contain four monatomic planes, the layers in $TlGaSe_2$ and $TlInS_2$ have a more complex, ''seven-stage'' structure. It is clear that in such a case the ''bending waves'' cannot play a substantial role in the thermal properties of the $TlGaSe_2$ and $TlInS_2$ crystals. This is confirmed by direct measurements[8,9] of the dispersion relations of acoustic waves in $TlGaSe_2$ and $TlInS_2$.

Continuing our comparative analysis, we can state further that the $TlGaSe_2$ and $TlInS_2$ crystals are even less anisotropic than GaS, GaSe, and InSe. Therefore, it is reasonable to assume that negative thermal expansion in the plane of the layers in $TlGaSe_2$ and $TlInS_2$ may be absent entirely. In this sense the behavior of the CLTE in $TlInS_2$ is completely understandable, while the negative value of $\alpha_{\parallel}$ over a rather wide temperature region in $TlGaSe_2$ (outside the phase transition region) is in need of a special explanation. Figure 3 shows the temperature dependence of the Grüneisen parameters $\gamma_{\parallel}$ and $\gamma_{\perp}$ for $TlGaSe_2$ and $TlInS_2$, calculated for values of the elastic constant $C_{13}=1.5\times 10^{11}$ dynes/cm^2, which is typical for practically all the layered crystals mentioned

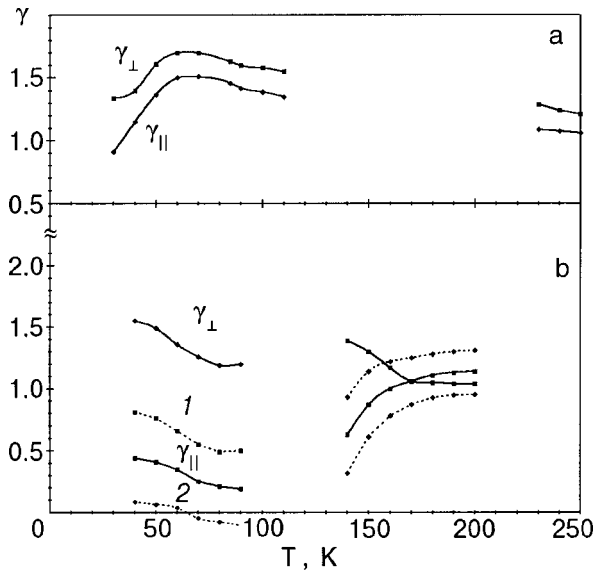

FIG. 3. Temperature dependence of the Grüneisen parameters $\gamma_{\parallel}$ and $\gamma_{\perp}$ for $TlInS_2$ (a) and $TlGaSe_2$ (b), calculated for a value of the elastic constant $C_{13}=1.5\times 10^{11}$ dyn/cm^2. The dotted curves correspond to calculations of $\gamma_{\parallel}(T)$ for $TlGaSe_2$ using $C_{13}=2.5\times 10^{11}$ dyn/cm^2 (*1*) and 0.5×10^{11} dyn/cm^2 (*2*).

above.[16] In addition, the dashed line in Fig. 3 shows the $\gamma_{\parallel}(T)$ curves for $TlGaSe_2$, calculated for two other values of C_{13}. The $\gamma_{\perp}(T)$ curves are hardly sensitive to changes in C_{13}.

In Fig. 3 the difference in the behavior of the Grüneisen parameters of the two crystals outside the region of the phase transitions is obvious. An analysis based on the data of Fig. 3 leads to the following conclusions:

1. The $\gamma_{\parallel}(T)$ and $\gamma_{\perp}(T)$ curves in $TlGaSe_2$ are analogous to the typical behavior for the GaS, GaSe, and InSe crystals and also for other nonlayered anisotropic crystals,[22] in which the behavior of $\gamma_{\parallel}$ has a characteristic decline with decreasing temperature, leading to the situation that at low temperatures $|\gamma_{\parallel}| \ll |\gamma_{\perp}|$. In $TlInS_2$ these features are absent.

2. At values of C_{13} that are typical for the majority of layered crystals the negative CLTE $\alpha_{\parallel}$ in $TlGaSe_2$ turns out to be due to the contribution of Poisson compression (see also the inset in Fig. 1), and its role increases with increasing C_{13}.

3. In view of items 1 and 2, one can understand why $\alpha_{\parallel}$ in $TlGaSe_2$ is negative over a wider range of temperatures as compared to the layered crystals GaS, GaSe, and InSe, in which $\alpha_{\parallel}$ is negative only in a narrow temperature interval. This difference in the behavior of $\alpha_{\parallel}$ can be explained only by taking into consideration that the nature of the negativity of $\alpha_{\parallel}$ in these crystals is different: in GaS, GaSe, and InSe $\alpha_{\parallel}$ is negative mainly because of the negativity of the parameter $\gamma_{\parallel}$ in a narrow temperature interval, while in $TlGaSe_2$ it is because of the predominant role of Poisson compression.

Thus the main reason for the different behavior of $\alpha_{\parallel}$ in $TlGaSe_2$ and $TlInS_2$ may be their different degree of anisotropy. This is also indicated by the values of their elastic constants given in Refs. 14 and 15. We note yet another difference of $TlGaSe_2$ from $TlInS_2$, which was first observed by one of the present authors and co-workers in Ref. 15: as the temperature is lowered from room temperature and the phase transition point is approached, the elastic constant C_{13} remains practically unchanged in $TlInS_2$ but increases very substantially in $TlGaSe_2$. This conclusion was based on measurements of C_{11} and C_{33} (determined from ultrasonic experiments) and $C_{11}-(C_{13}^2/C_{33})$ (experiments on the resonant vibrations of a cantilevered slab made from the layered crystals). We emphasize that in the experiments cited only the relative change in the elastic constant C_{13} was measured to high accuracy. Therefore, unfortunately, we cannot use the absolute values of C_{13}.

Thus C_{13} in $TlGaSe_2$ in the temperature region where $\alpha_{\parallel}$ is negative can be considerably higher than the value of C_{13} that was used above in the calculations of the Grüneisen parameters. In that case the role of Poisson compression in $TlGaSe_2$ increases still more. Incidentally, the relatively large value of C_{13} can also explain the correlation in the behavior of $\alpha_{\parallel}$ and $\alpha_{\perp}$ at the points of the phase transitions in $TlGaSe_2$ and the absence of such a correlation in $TlInS_2$.

CONCLUSION

Experimental studies of the thermal expansion of the layered crystals C, BN, GaS, GaSe, InSe, and the results on $TlGaSe_2$ and $TlInS_2$ in the present study have revealed a peculiarity: $\alpha_{\parallel}$ can take on negative values. The temperature region in which $\alpha_{\parallel}$ is negative varies from 0–600 K in C to 30–50 K in GaS, GaSe, and InSe. In an attempt to establish the mechanism for the negative $\alpha_{\parallel}$ in layered crystals it was found that in each particular case it is necessary to precisely determine the values of two contributions: the actual compression of the layer itself and the Poisson compression of the layer as a result of its strong expansion in the direction perpendicular to the layers. Estimation of the contribution of the second term is made difficult because of the difficulty of determining the constant C_{13}, which can lead to erroneous conclusions as to the nature of the negative $\alpha_{\parallel}$, as happened in the case of graphite.

Analysis shows that in the layered crystals C, BN, GaS, GaSe, and InSe and negative $\alpha_{\parallel}$ is due mainly to the first term, while in the case of $TlGaSe_2$ the negativity of $\alpha_{\parallel}$ may be largely due to the Poisson compression.

The difference of the behavior of the thermal expansion in $TlGaSe_2$ and $TlInS_2$ is explained, on the one hand, by their different degree of anisotropy and, on the other hand, by the large value of the elastic constant C_{13} in $TlGaSe_2$ in comparison with $TlInS_2$.

*E-mail: physic@lan.ab.az

[1] A. A. Volkov, Yu. G. Goncharov, G. V. Kozlov, K. R. Allakhverdiev, and R. M. Sardarly, Fiz. Tverd. Tela (Leningrad) **25**, 3583 (1983) [Sov. Phys. Solid State **25**, 2061 (1983)].
[2] A. A. Volkov, Yu. G. Goncharov, G. V. Kozlov, S. P. Lebedev, A. M. Prokhorov, R. A. Aliev, and K. R. Allakhverdiev, JETP Lett. **37**, 615 (1983).
[3] R. A. Aliev, K. R. Allakhverdiev, A. N. Baranov, N. R. Ivanov, and R. M. Sardarly, Fiz. Tverd. Tela (Leningrad) **26**, 1274 (1984) [Sov. Phys. Solid State **26**, 743 (1984)].
[4] K. R. Allakhverdiev, N. A. Bakhyshov, T. G. Mamedov, and A. I. Nadzhafov, Fiz. Tverd. Tela (Leningrad) **28**, 2243 (1986) [Sov. Phys. Solid State **28**, 1258 (1986)]; K. R. Allakhverdiev, S. S. Guseĭnov, T. G. Mamedov, M. M. Tagiev, and M. M. Shirinov, Izv. Akad. Nauk SSSR, Neorg. Mater. **25**, 1858 (1989).
[5] K. K. Mamedov, A. M. Abdullaev, and E. M. Kerimova, Phys. Status Solidi A **94**, 115 (1986); S. G. Abdullaeva, A. M. Abdullaev, K. K. Mamedov, and N. T. Mamedov, Fiz. Tverd. Tela (Leningrad) **26**, 618 (1984) [Sov. Phys. Solid State **26**, 375 (1984)].
[6] N. A. Abdullaev, K. R. Allakhverdiev, G. L. Belen'kiĭ, T. G. Mamedov, R. A. Suleĭmanov, and Ya. N. Sharifov, Dokl. Akad. Nauk. Azerb. SSR **41**, 21 (1985).
[7] N. A. Abdullaev, K. R. Allakhverdiev, G. L. Belenkii, T. G. Mamedov, R. A. Suleĭmanov, and Ya. N. Sharifov, Solid State Commun. **53**, 601 (1985).
[8] S. B. Vakhrushev, B. E. Kvyatkovskiĭ, N. M. Okuneva, K. R. Allakhverdiev, and R. M. Sardarly, Preprint No. 81 [in Russian], A. F. Ioffe Physicotechnical Institute, Leningrad (1984).
[9] S. B. Vakhrushev, V. V. Zhdanova, B. E. Kvyatkovskiĭ, N. M. Okuneva, K. R. Allakhverdiev, R. A. Aliev, and R. M. Sardarly, JETP Lett. **39**, 291 (1984).
[10] I. M. Lifshitz, Zh. Éksp. Teor. Fiz. **22**, 475 (1952).
[11] B. S. Kul'bushev, S. M. Zaĭtsev, and A. U. Mal'sagov, Izv. Akad. Nauk SSSR, Neorg. Mater. **23**, 511 (1987).
[12] H. D. Hochheimer, E. Gmelin, W. Bauhofer, Ch. von Schnering-Schwarz, G. G. von Schnering, J. Ihringer, and W. Appek, Z. Phys. B **73**, 257 (1988).
[13] O. B. Ploshch and A. U. Sheleg, Kristallografiya **44**, 873 (1999) [Crystallogr. Rep. **44**, 813 (1999)].
[14] Yu. V. Ilisavskiĭ, B. M. Sternin, R. A. Suleĭmanov, F. M. Salaev, and M. Yu. Seidov, Fiz. Tverd. Tela (Leningrad) **33**, 104 (1991) [Sov. Phys. Solid State **33**, 57 (1991)]; K. R. Allakhverdiev, Yu. V. Ilisavskiĭ, T. G. Mamedov, M. K. Neĭmanzade, B. M. Sternin, R. A. Suleĭmanov, and M. Yu. Seidov, Preprint No. 282 [in Russian], Institute of Physics, Academy of Sciences of Azerb. SSR, Baku (1988).
[15] R. A. Suleĭmanov, M. Yu. Seidov, and F. M. Salaev, Fiz. Tverd. Tela (Leningrad) **33**, 1797 (1991) [Sov. Phys. Solid State **33**, 1010 (1991)].

[16] L. G. Belen'kiĭ, R. A. Suleĭmanov, N. A. Abdullaev, and V. Ya. Shteĭnshraĭber, Fiz. Tverd. Tela (Leningrad) **26**, 3560 (1984) [Sov. Phys. Solid State **26**, 2142 (1984)]; R. A. Suleĭmanov and A. Abdullaev, Carbon **31**, 1011 (1993).
[17] T. H. K. Barron, I. C. Collins, and G. K. White, Adv. Phys. **29**, 609 (1980).
[18] I. B. Nelson and D. P. Riley, Proc. Phys. Soc. **57**, 477 (1945).
[19] B. T. Kelly, Philos. Mag. **32**, 859 (1975).
[20] O. L. Blakslee, D. C. Proctor, E. J. Seldin, G. B. Spence, and T. Weng, J. Appl. Phys. **41**, 3373 (1970).
[21] S. B. Feodos'ev, E. S. Syrkin, I. A. Gospodarev, V. P. Popov, A. A. Gurskas, and N. M. Nesterenko, Fiz. Tverd. Tela (Leningrad) **31**, 186 (1989) [Sov. Phys. Solid State **31**, 102 (1989)].
[22] S. I. Novikova, *Thermal Expansion of Solids* [in Russian], Moscow (1974).

Translated by Steve Torstveit

SHORT NOTES

Detection of stacking faults in carbon dioxide clusters

S. I. Kovalenko, D. D. Solnyshkin, É. T. Verkhovtseva,* and V. V. Eremenko

B. Verkin Institute for Low Temperature Physics and Engineering, National Academy of Sciences of Ukraine, pr. Lenina 47, 61103 Kharkov, Ukraine
(Submitted March 19, 2001)
Fiz. Nizk. Temp. **27**, 921–923 (August 2001)

An electron-diffraction study of clusters formed in supersonic jets of carbon dioxide is reported. The mean size of the clusters varies from 4×10^2 to 2×10^4 molecules/cluster. From an analysis of the diffraction patterns obtained it is established that clusters of these sizes have the structure of the bulk crystal. Stacking faults are observed for the first time in clusters with an average size of less than 1.7×10^3 molecules/cluster; the density of these stacking faults increases with decreasing size of the aggregations. It is found that the density of stacking faults in $(CO_2)_N$ clusters is considerably lower than rare-gas clusters. © *2001 American Institute of Physics.* [DOI: 10.1063/1.1399209]

The structure of rare-gas clusters, the interatomic interaction in which is well described by the Lennard-Jones potential, has been studied in sufficient detail (see, e.g., Refs. 1 and 2). In the case of linear molecules there is in addition to the central interaction a substantial contribution of noncentral electrostatic forces, causing the orientational ordering of molecules at low temperatures. The structure of the clusters of such substances as a function of the contribution of the anisotropic component to the total energy of the lattice can differ from the structure of rare-gas clusters. From this standpoint carbon dioxide is of great interest, since the contribution of the anisotropic component to the total lattice energy of CO_2 is more than 50%.[3]

The possible existence of icosahedral clusters of $(CO_2)_N$ was considered in Ref. 4, according to which such a structure becomes stable only in clusters of size $N<13$ molescules/cluster. In electron-diffraction studies[5,6] of carbon dioxide clusters it was established that the crystal structure of the bulk crystal is realized in clusters with mean sizes $\bar{N}$ in the entire interval of values considered (10^2 molecules/cluster $\leqslant\bar{N}<10^5$ molecules/cluster). However, those studies did not investigate stacking faults, the presence of which is important for understanding the mechanism of formation of the crystalline phase in clusters.[7] Thus the goal of the present study was to look for stacking faults in the $(CO_2)_N$ formations.

The investigations were carried out on an apparatus consisting of a standard electron diffractometer, a supersonic cluster-beam generator, and a cooled liquid-hydrogen cryogenic condensation pump for pumping out the gas of the jet. The supersonic gas jet was produced by a conical nozzle (throat diameter 0.34 mm, cone angle 8.6°, and ratio of the cross sections of the entrance and throat 36.7). The diffraction patterns were recorded by electrometric and photometric methods. In the first case a retarding potential can be used to eliminate a significant part of the incoherently scattered electrons and thereby improve the accuracy of determination of the shape of the diffraction peaks. Photographic recording was done for precise determination of the position of the diffraction peaks. The characteristic size $\delta\propto\bar{N}^{1/3}$ of the clusters was determined with the aid of the Selyakov–Scherrer formula from the broadening of the diffraction peaks. The average size of the clusters was varied from 4×10^2 to 2×10^4 molecules/cluster by changing the gas pressure P_0 at the entrance to the nozzle from 0.075 to 0.55 MPa at a constant temperature $T_0=293\pm2$ K. A detailed description

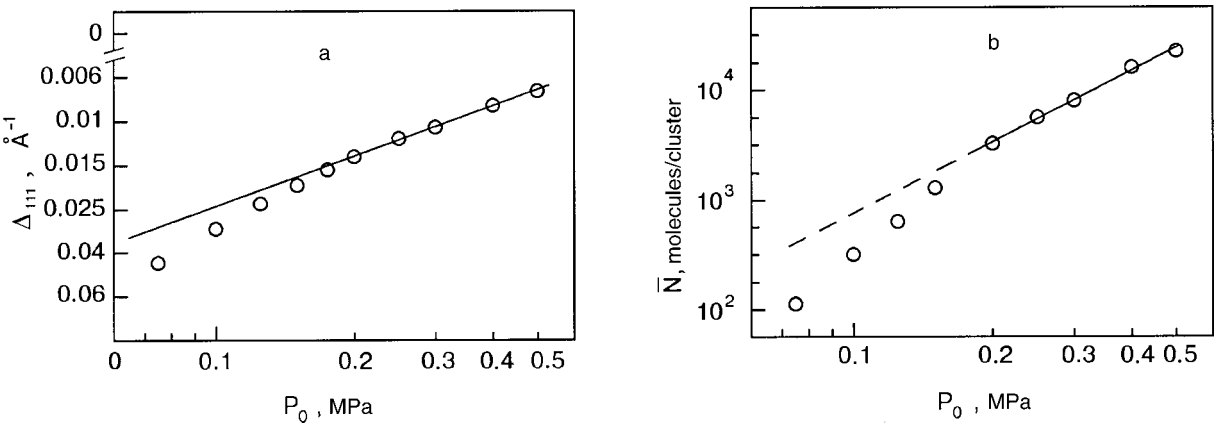

FIG. 1. Broadening Δ_{111} of the (111) diffraction peak as a function of the gas pressure P_0 at the nozzle entrance for a gas temperature $T_0=293$ K (a); the mean size $\bar{N}$ of $(CO_2)_N$ clusters as a function of the pressure P_0 for $T_0=293$ K (b). Both relations are plotted in logarithmic scale.

of the apparatus and the experimental technique is given in Ref. 8.

It was established as a result of these studies that for clusters with $\overline{N} \geqslant 3\times 10^3$ molecules/cluster the positions and relative intensities of the diffraction peaks correspond to the $Pa3$ structure inherent to the bulk crystal. At smaller cluster sizes the relative intensity of the ''superstructural'' peaks due to the orientational ordering of the molecules is found to decrease. This relationship correlates with the results of Ref. 6, where an intensification of the librational motion of the CO_2 molecules in small crystalline clusters was observed. Figure 1a shows the dependence of the broadening Δ_{111} of the (111) diffraction peak as a function of the gas pressure P_0 at the entrance to the nozzle. Here $\Delta_{111}=\sqrt{B^2-b_0^2}/L\lambda$, where B is the half-width of the (111) peak, b_0 is the instrumental width of the diffraction line, L is the distance from the sample to the detector, and λ is the electron wavelength. Figure 1b shows the macroscopic cluster size $\overline{N}$ as a function of the pressure P_0. The presence of this pressure dependence makes it possible to associate the broadening of the diffraction peak with the size of the clusters. As we see from the figure, for $P_0 \geqslant 0.2$ MPa ($\overline{N} \geqslant 3\times 10^3$ molecules/cluster) the experimental points are well described by a straight line, the slope of which, equal to 2.24 ± 0.04 in the coordinates $\log \overline{N}$–$\log P_0$, is in rather good agreement with the value obtained on the basis of mass-spectrometric[9] and electron-diffraction[6] measurements. As is seen in Fig. 1a, in the case of low pressures ($P_0<0.2$ MPa, $\overline{N}<3\times 10^3$ molecules/cluster) one observes a deviation of the experimental points from the indicated straight line toward the side of greater broadening. The deviation increases rather slowly with decreasing P_0 with no sharp change in the character of the function $\Delta_{111}=\varphi(P_0)$, a finding which is evidence that the effect is due to stacking faults[10] and not to the presence of icosahedral formations[11] in the cluster beam. The presence of stacking faults in the small clusters is also confirmed by the shift of the (111) and (200) diffraction peaks toward each other.[10]

The value of the deviation from linearity of the curve of the broadening of the (111) diffraction peak was used to determine the density of the stacking faults. In the calculation we used the well-known relation from structure analysis[10]

$$\frac{1.5\alpha+\beta}{d_{111}} j\cos\varphi=\Delta_{hkl}^{SF}, \qquad (1)$$

where α and β are the density of stacking faults of the ''deformation'' and ''twin'' types, d_{111} is the distance between the close-packed planes, $j\cos\varphi$ is the crystallographic constant for the given family of planes, which in the case of the (111) reflection is equal to 1/4, and Δ_{hkl}^{SF} is the broadening of the lines (hkl) due to the stacking faults.

TABLE I. Experimentally obtained parameters of $(CO_2)_N$ clusters.

Pressure P_0, MPa	δ, Å	$\overline{N}$, molecules/clusters	Δ_{111}^{SF}, Å	$1.5\alpha+>b$	α
0.075	32	380	0.0144	0.185	0.123
0.100	39	711	0.0070	0.090	0.060
0.125	47	1200	0.0038	0.050	0.032
0.150	53	1750	0.0022	0.029	0.019
0.175	58	2300	0.0012	0.015	0.010
0.200	65	3200	0	0	0

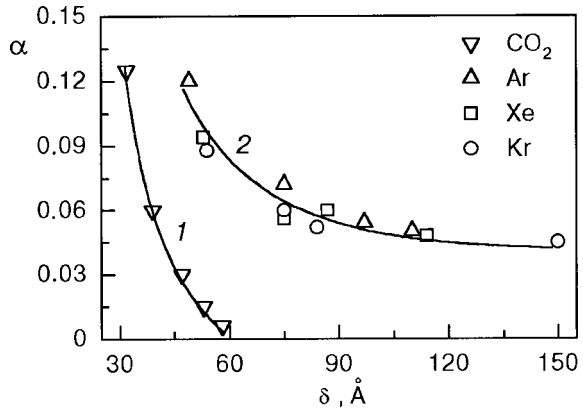

FIG. 2. Density of stacking faults as a function of the characteristic cluster size δ. $(CO_2)_N$ clusters (*1*); rare-gas clusters (*2*).[2]

Substituting all the necessary quantities into Eq. (1) and neglecting β because it is small (this is indicated by the absence of asymmetry of the diffraction peaks), we obtain the values of the density of stacking faults of the ''deformation'' type. All of the quantities determined from the experiment are presented in Table I.

Figure 2 gives the dependence of the density α of stacking faults on the characteristic size of the clusters. Here for comparison we also show the analogous curves for rare-gas clusters. As can be seen in the figure, the density of stacking faults in $(CO_2)_N$ clusters, as in the case of rare gases, increases with decreasing cluster size. However, in the case of carbon dioxide the stacking faults are observed in much smaller clusters and with a lower density than in the rare gases. This finding indicates that the energy of a stacking fault in carbon dioxide crystals is greater, because of the significant contribution of the anisotropic component to the total binding energy of the CO_2 molecule. At the same time our observation of stacking faults in small $(CO_2)_N$ formations gives us reason to assume that the initial stages of formation of the crystalline phase are similar in clusters of carbon dioxide and rare gases.

*E-mail: verkhovtseva@ilt.kharkov.ua

[1] J. Farges, M. F. de Feraudy, B. Raoult, and G. Torchet, Adv. Chem. Phys. **70**, 45 (1988).
[2] S. I. Kovalenko, D. D. Solnyshkin, E. A. Bondarenko, and E. T. Verkhovtseva, Low Temp. Phys. **23**, 190 (1997) [Low Temp. Phys. **23**, 140 (1997)].
[3] V. B. Manzhelii and Yu. A. Freiman (Eds.), *Physics of Cryocrystals*, AIP, New York (1996).
[4] B. W. van de Waal, J. Chem. Phys. **79**, 3948 (1983).
[5] G. D. Stein and J. A. Armstrong, J. Chem. Phys. **58**, 1999 (1973).
[6] G. Torchet, H. Bouchier, J. Farges, M. F. de Feraudy, and B. Raoult, J. Chem. Phys. **81**, 2137 (1984).
[7] B. W. van de Waal, Phys. Rev. Lett. **76**, 1083 (1996).
[8] S. I. Kovalenko, D. D. Solnyshkin, E. T. Verkhovtseva, and V. V. Eremenko, Fiz. Nizk. Temp. **20**, 961 (1994) [Low Temp. Phys. **20**, 758 (1994)].
[9] O. F. Hagena and W. Obert, J. Chem. Phys. **56**, 1793 (1972).
[10] S. S. Gorelik, L. N. Rastorguev, and Yu. A. Skakov, *X-Ray and Electron Diffraction Analysis of Metals* [in Russian], Metallurgizdat, Moscow (1970).
[11] J. W. Lee and G. D. Stein, J. Phys. Chem. **91**, 2450 (1987).

Translated by Steve Torstveit

LETTERS TO THE EDITOR

Influence of twin boundaries on the phase state and vortex dynamics near the melting point in $YBa_2Cu_3O_{7-\delta}$ single crystals

A. V. Bondarenko,* A. A. Prodan, and M. A. Obolenskiĭ

V. N. Karazina Kharkov National University, pl. Svobody 4, 61077 Kharkov, Ukraine

A. G. Sivakov

B. Verkin Institute for Low Temperature Physics and Engineering, National Academy of Sciences of Ukraine, pr. Lenina 47, 61103 Kharkov, Ukraine

(Submitted May 15, 2001)
Fiz. Nizk. Temp. **27**, 924–927 (August 2001)

It is found that at temperatures above the melting point of the vortex lattice T_m and below the temperature T_p corresponding to the onset of pinning on twin boundaries, the current–voltage (I–V) characteristics are linear at low values of the transport current J but are substantially nonlinear at large J. This behavior of the I–V characteristics is interpreted as the coexistence in the temperature region $T_m<T<T_p$ of a pinned vortex lattice which is formed near the planes of the twin boundary at $T<T_p$ and an unpinned vortex liquid far the planes of twin boundaries. © *2001 American Institute of Physics.* [DOI: 10.1063/1.1399210]

The influence of disorder on the phase state and pinning of Abrikosov vortices in high-T_c superconductors is the subject of intensive theoretical and experimental research. It is assumed that in magnetic fields below the second critical field H_{c2} there exists a vortex liquid whose crystallization in the presence of weak disorder comes about in the form of a first-order phase transition at a temperature $T_m(H)$ below the line $H_{c2}(T)$.[1] In the case of strong point disorder[2] or planar defects[3,4] the first-order phase transition is suppressed, and the linear resistivity ρ_l ($\rho_l \equiv dE/dJ$ at $J=0$) becomes less than the resistivity ρ_{ff} of free flux flow at temperatures $T>T_p>T_m$, where the temperature T_p corresponds to the onset of pinning of the vortex liquid. The decrease of ρ_l is explained by the formation of an entangled vortex liquid that has torsional stiffness[3] and, as a consequence, increased viscosity,[5] or by the formation of finite plastic barriers[4] for the entangled liquid, which leads to an exponential decrease of ρ_l (Ref. 6).

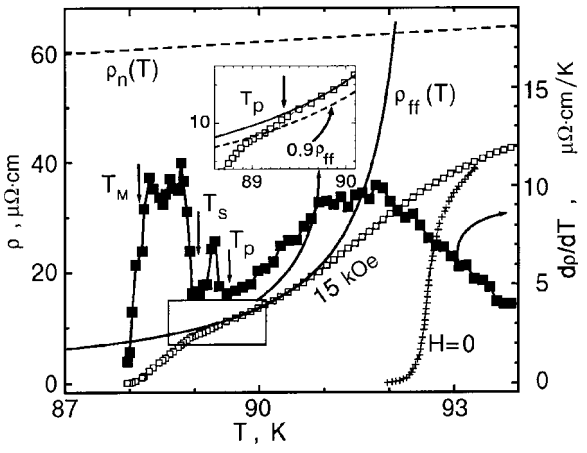

FIG. 1. Temperature dependence of the resistivity ρ at $H=0$ and 15 kOe and the derivative $d\rho/dT$ of the $\rho(T)$ curve measured in a field of 15 kOe. The dashed line shows the extrapolation of the linear part of the temperature dependence of the resistivity in the normal state, $\rho_n(T)$. The solid curve shows the temperature dependence of the resistivity ρ_{ff} of the viscous magnetic flux flow in the Bardeen–Stephen model; T_p corresponds to the start of the pinning of the vortices at twin boundaries.

In this paper we present the results of a study of the dynamics of the magnetic flux near the melting temperature of the vortex lattice in a twinned single crystal of $YBa_2Cu_3O_{7-\delta}$. Previous measurements of this sample at temperatures $T<T_m$ showed[7] that the critical current decreases monotonically with increasing magnetic field. This is evidence that the oxygen content in the sample is close to stoichiometric, $\delta \leqslant 0.03$ (Ref. 8), i.e., the point disorder is very low. The twin boundaries (TBs) in the part of the crystal where the measurements are made have a single direction, and the current vector **J** lies in the ab plane and perpendicular to the TB plane. The measurements were made in a magnetic field $H=15$ kOe in a field orientation $\mathbf{H}\|\mathbf{c}\|$TB. Under these conditions the Lorentz force $\mathbf{F}=\mathbf{J}\times\mathbf{B}$ is parallel to the TB planes.

As we see in Fig. 1, at temperatures $T>89.3$ K the resistivity ρ_l is equal to the resistivity of the viscous flux flow in the Bardeen–Stephen model,[9] $\rho_{ff}(T)=\rho_n(T)B/B_{c2}(T)$, which is obtained following the procedure proposed in Ref. 3 on the assumption that $B_{c2}(T)=(dB_{c2}/dT)(T-T_c)$, where $dB_{c2}/dT=-2.5$ T/K, and the value of $\rho_n(T)$ was determined by extrapolation of the linear part of the temperature dependence of the resistance in the normal state. As we see in Fig. 2a, the I–V characteristics measured at $T>T_p$ are linear, attesting to the unpinned state of the vortex liquid. At temperatures $T \leqslant 87.9$ K the resistance is equal to zero, the I–V curves are nonlinear, and the $E(J)$ curves plotted on a log–log scale have negative curvature. For an exponential

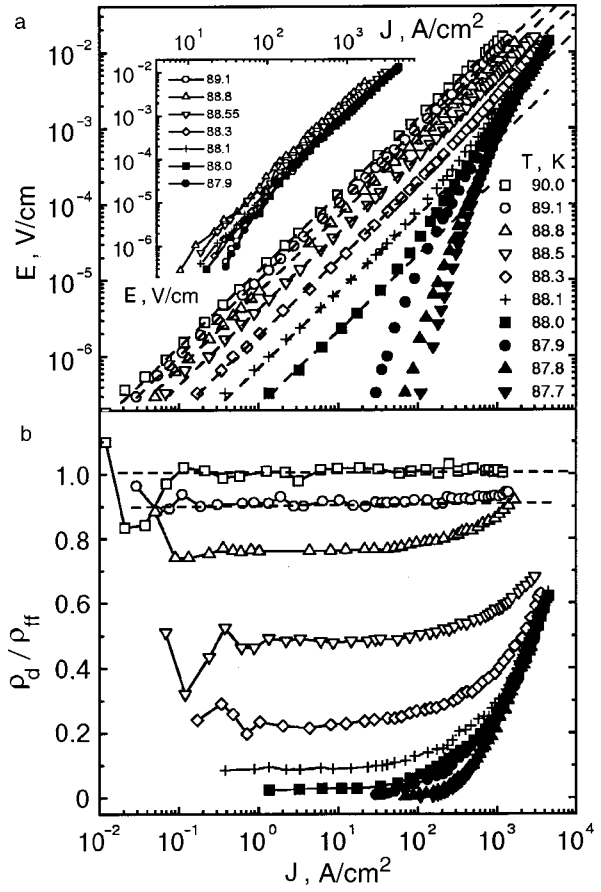

FIG. 2. Current–voltage characteristics in a magnetic field of 15 kOe (a) and the current dependence of the differential resistivity $\rho_d = dE/dJ$, normalized to ρ_{ff} (b) (the $E(J)$ curves are shown in Fig. 2a).

dependence of the form $E(J) \propto \exp[-(J_T/J)^{\mu}]$ a positive curvature indicates positivity of the exponent μ, which is a characteristic trait of vortex lattice creep.[10] In addition, the temperature 87.9 K coincides to within 0.3 K with the melting temperature of the vortex lattice in the untwinned crystals.[1] We therefore associate the temperature $T_m \approx 87.9$ K with the melting point of the vortex lattice.

Thus for $T > T_p$ there exists an unpinned vortex liquid, which is characterized by a linear resistivity $\rho_l = \rho_{ff}$, and for $T < T_m$ there exists a pinned vortex lattice, the creep of which is determined by an exponent $\mu > 0$. In the temperature interval $T_m < T < T_p$, as can be seen in Fig. 2, the I–V characteristics are linear at low values of the transport current but substantially nonlinear at large values. Here the linear resistivity is less than ρ_{ff} (see Fig. 2b). This behavior of the I–V characteristics can be explained by the simultaneous existence of a pinned vortex lattice and an unpinned vortex liquid. Let us discuss this possibility in more detail.

In untwinned crystals the amplitude of the thermal fluctuations u of the vortices is uniform over the volume of the crystal, a circumstance which, in combination with the weak point pinning leads to a first-order phase transition at $T = T_m$ (Ref. 1). In the twinned crystals, however, in the temperature region $T_m < T < T_p$ a fraction of the vortex lines $n_p \approx a_0/d$ (where a_0 is the distance between vortices and d is the distance between twins) is trapped by the TB planes, since the superconducting order is suppressed at the TBs.[11] The amplitude of these vortices is smaller than that of the vortices immersed in the bulk of the crystal on account of their two-dimensional nature.[12] Since the interaction between vortices is effective over a distance equal to the penetration depth λ of the magnetic field, the amplitude u is modulated over a distance $x \approx \lambda$ from the plane of a TB. In the temperature region considered, the penetration depth $\lambda = 30-40$ nm is comparable to the intertwin distance $d \approx 50$ nm in the sample studied, so that one can expect that the amplitude will be modulated at all distances x from the TB planes: the value of u increases continuously with increasing x. If at temperatures $T < T_p$ the rms amplitude $\langle u \rangle$ of the vortices located near a TB plane is larger than $c_L a_0$, where c_L is the Lindemann number, then the unpinned vortex liquid will coexist with the pinned vortices localized at the TB planes. In that case one should observe a linear resistivity $\rho_l \approx (1 - n_p)\rho_{ff}$. In a magnetic field of 15 kOe one has the values $a_0 \approx 38$ nm and $n_p \approx 0.08$, and so the linear resistivity $\rho_l \approx 0.92\rho_{ff}$, which, as can be seen in Figs. 1 and 2b, agrees with the experimental data obtained in the temperature interval $88.9\,\text{K} < T < 89.3\,\text{K}$.

As the temperature is lowered further to the value T_s at which the amplitude $\langle u(T_s) \rangle$ of the vortices located near the TB planes becomes less than $c_L a_0$, the vortex liquid near the TBs will crystallize. Then the linear resistivity should decrease with decreasing temperature in proportion to the decrease in the vortex-liquid volume fraction n_l, which is determined by the ratio $n_l = \rho_l/\rho_{ff}$. Complete crystallization should occur at a temperature T_m close to the melting point of the vortex lattice in the untwinned single crystals, since the amplitude u of the vortices located far from the planes of the TBs differs only slightly from its value in detwinned crystals. This scenario agrees with the experimental data presented in Fig. 1. The resistivity ρ_l decreases almost linearly from a value $0.9\rho_{ff}$ to zero as the temperature is lowered from 88.9 to 87.9 K, which coincides to within 0.3 K with the melting temperature of the vortex lattice in the untwinned crystals.[1] We therefore interpret the temperature $T_s = 88.9$ K as the beginning and $T_m = 87.9$ K as the end of the crystallization of the vortex liquid.

Let us turn to a discussion of the nonlinear components of the I–V characteristics measured in the temperature interval $T_m < T < T_p$. Subtracting the linear components $E_l(J)$, shown by the dashed lines in Fig. 2a, from the measured I–V characteristics, and normalizing the difference to the volume fraction comprised by the pinned vortex lattice, $n_p = (1 - \rho_l/\rho_{ff})$, we obtain the dependence $E_p = (E - E_l)/(1 - \rho_l/\rho_{ff})$ (see the inset in Fig. 2a), which corresponds to motion of the pinned vortex lattice. It is seen that the $E_p(J)$ curves plotted in log–log scale have negative curvature, i.e., the dynamics of the pinned part of the magnetic flux is analogous to the dynamics of the vortex lattice at temperatures $T < T_m$. Furthermore, the $E_p(J)$ curves are shifted to larger transport currents as the temperature is lowered, a trend that correlates with the behavior of the $E(J)$ curves at temperatures $T < T_m$. These relationships are experimental confirmation that the nonlinear components of the I–V characteristics measured in the temperature interval $T_m < T < T_p$ correspond to motion of a pinned vortex lattice.

The experimental data obtained in the present study dif-

fer from previously published results: the resistivity ρ_l decreases almost linearly with temperature in the interval $T_m < T < T_p$, whereas in Ref. 7 for analogous experimental conditions ($\mathbf{H} \| \mathbf{c}$, $\mathbf{J} \| ab$, $\mathbf{J} \perp$ TB) the resistivity ρ_l decreased exponentially. This difference is probably due to the different concentrations of point defects in the single crystals studied. Indeed, in the presence of weak point pinning the resistivity ρ_l decreases sharply from ρ_{ff} to zero near T_m, while at the same time the introduction of point defects leads to pinning of the vortex liquid and to an exponential decrease of the resistivity ρ_l with temperature, $\rho_l \propto \exp(-U_{\rm pl}/T)$, in the interval $T_m < T < T_p$ (Ref. 2). Here the activation energy $U_{\rm pl}$ decreases with increasing magnetic field, $U_{\rm pl} \propto H^{-0.7}$, which is a characteristic trait of plastic motion of an entangled vortex liquid.[6] Thus the entangling of the vortex lines at temperatures $T > T_m$ is realized in the presence of a rather strong random pinning, and this vortex phase is characterized by an exponential decrease of ρ_l. Therefore the exponential decrease of ρ_l observed in Ref. 7 is probably due to a rather high concentration of oxygen vacancies, which are considered to be the main source of point pinning centers in YBCO single crystals. In the sample investigated here the concentration of oxygen vacancies is small, $\delta \leqslant 0.03$. Therefore the formation of an ''entangled'' vortex liquid is improbable, as is confirmed by the linear rather than exponential decrease of $\rho_l(T)$ in our measurements.

We conclude by noting that the experimental results obtained in the present study are evidence of the coexistence of pinned and unpinned vortex phases in the temperature region $T_m < T < T_p$. We have shown that the dynamics of the pinned phase is analogous to that of the vortex lattice at temperatures below T_m. Therefore, we have come to the conclusion that the formation of the vortex-lattice phase starts at temperatures below the temperature at which pinning at the planes of the twin boundaries begins, and this phase comes to fill the entire volume of the crystal as the temperature is lowered to T_m.

*E-mail: Aleksandr.V.Bondarenko@univer.kharkov.ua

[1] H. Safar, P. L. Gammel, D. A. Huse, D. J. Bishop, J. P. Rice, and D. M. Ginzberg, Phys. Rev. Lett. **69**, 824 (1992); W. K. Kwok, S. Flesher, U. Welp, V. M. Vinokur, J. Downey, G. W. Grabtree, and M. M. Miller, Phys. Rev. Lett. **69**, 3370 (1992); M. Charalambous, J. Chaussi, P. Lijay, and V. M. Vinokur, Phys. Rev. Lett. **71**, 436 (1993); W. K. Kwok, J. Fendrich, S. Flesher, U. Welp, J. Downey, and G. W. Grabtree, Phys. Rev. Lett. **72**, 1092 (1994).
[2] J. A. Fendrich, W. K. Kwok, J. Giapintzakis, C. J. van der Beek, V. M. Vinokur, S. Flesher, U. Welp, H. K. Viswanathan, and G. M. Grabtree, Phys. Rev. Lett. **74**, 1210 (1995).
[3] S. Flesher, W. K. Kwok, U. Welp, V. M. Vinokur, M. K. Smith, J. Downey, and G. M. Grabtree, Phys. Rev. B **47**, 14488 (1993).
[4] T. K. Worthington, F. H. Holtzberg, and C. A. Feild, Cryogenics **30**, 417 (1990).
[5] M. C. Marchetti and D. R. Nelson, Phys. Rev. B **42**, 9938 (1990).
[6] V. M. Vinokur, M. V. Feigel'man, V. B. Geshekenbein, and A. I. Larkin, Phys. Rev. Lett. **65**, 259 (1990).
[7] A. V. Bondarenko, A. A. Prodan, M. A. Obolenskiĭ, R. V. Vovk, and T. R. Arouri, Fiz. Nizk. Temp. **27**, 463 (2001) [Low Temp. Phys. **27**, 339 (2001)].
[8] A. A. Zhukov, H. Kupfer, G. Perkins, L. F. Kohen, A. D. Caplin, S. A. Klestov, H. Klaus, V. I. Voronkova, T. Wolf, and H. Wuhl, Phys. Rev. B **51**, 12704 (1995).
[9] J. Bardeen and M. J. Stephen, Phys. Rev. A **140**, 1197 (1965).
[10] D. S. Fisher, M. P. A. Fisher, and D. A. Huse, Phys. Rev. B **43**, 130 (1991); K. H. Fischer and T. Nattermann, Phys. Rev. B **43**, 130 (1991); T. Giamarchi and P. Le Doussal, Phys. Rev. B **55**, 6577 (1997); G. Blatter, M. V. Feigel'man, V. B. Geshkenbein, A. I. Larkin, and V. M. Vinokur, Rev. Mod. Phys. **66**, 1125 (1994).
[11] G. J. Dolan, G. V. Chandrashekhar, T. R. Dinger, C. Feild, and F. Holtzberg, Phys. Rev. Lett. **62**, 827 (1989).
[12] G. Blatter, J. Rhyner, and V. M. Vinokur, Phys. Rev. B **43**, 7826 (1991).

Translated by Steve Torstveit

Observation of enhancement of superconductivity by an external electromagnetic field and of rf phase-slip lines in wide tin films

A. B. Agafonov, I. V. Zolochevkiĭ, and E. V. Khristenko

B. Verkin Institute for Low Temperature Physics and Engineering, National Academy of Sciences of Ukraine, pr. Lenina 47, 61103 Kharkov, Ukraine

V. M. Dmitriev[a)]

B. Verkin Institute for Low Temperature Physics and Engineering, National Academy of Sciences of Ukraine, pr. Lenina 47, 61103 Kharkov, Ukraine; International Laboratory of High Magnetic Fields and Low Temperatures, 95 Gajowicka St., 53-421 Wroclaw, Poland

(Submitted June 6, 2001)
Fiz. Nizk. Temp. **27**, 928–931 (August 2001)

The enhancement of superconductivity by an external electromagnetic field and rf phase-slip lines are observed in wide tin films. The temperature, frequency, and power dependences of the critical current are investigated and demonstrate the phenomena observed. It is shown that this class of nonequilibrium effects is common to both narrow and wide films. © *2001 American Institute of Physics.* [DOI: 10.1063/1.1399211]

A study is made of thin ($d\sim 100$ nm), long ($l\sim 100$ μm), and wide ($w\sim 50$ μm) films of tin deposited on substrates of optically polished crystalline quartz, which provides rather good heat removal from the tin film. The films were obtained by a technology that ensured their serration-free edges. The dc current–voltage (I–V) characteristics were taken by the four-probe method. The frequency of the external irradiation was varied over the range 0–30 GHz; the electric field vector lay in the plane of the film along the direction of the transport current. The samples were shielded by a double shield of annealed Permalloy.

In this communication we present the results obtained for one of many tin samples studied; the results for the others were analogous. The following effects and features on the I–V characteristics were observed.

ENHANCEMENT OF SUPERCONDUCTIVITY

Figure 1 shows families of I–V characteristics for the sample Sn-W4 ($w=42$ μm, $l=92$ μm, $d=120$ nm, $T_c=3.795$ K, resistance $R_n = 0.14$ Ω in the normal state at $T\geqslant T_c$) at various power levels of the irradiation at $f=9.3$ GHz. For the first I–V characteristic the irradiation power P is zero, and the others are numbered in order of increasing power. The initial resistive parts of the first two I–V characteristics are shown in Fig. 1b. It is seen that under irradiation there is an increase in both the critical current for the onset of flux creep, I_c, and in the depairing critical current I_c^{dp}, at which the first phase-slip line due to the direct current (dc PSL) appears.[1]

It has been established that the supercurrent enhancement effect increases with increasing irradiation frequency, and the region of power levels in which $I_c(P)$ is higher than $I_c(0)$ becomes larger as well (see Fig. 2a).

It should also be noted that in wide films the temperature region in which the superconductivity enhancement effect exists increases with increasing irradiation frequency, while the maximum value of the relative increase in the critical current shows a noticeable tendency to decrease (see Fig. 2b).

It is known that microwave irradiation of wide films leads to a lowering of the edge barrier and depinning of the vortex lattice. Therefore the enhancing effect of irradiation at low power levels may be due solely to an increase in the order parameter, as follows from the theory of Ref. 3, which leads to an increase of the edge barrier and of the vortex pinning. Thus in a wide film found in a microwave field there are three competing mechanisms by which the irradiation acts: enhancement of superconductivity, suppression of superconductivity, and the depinning of vortices, the motion of which leads to resistivity. A comparative analysis of the results obtained in the present study for wide films with the analogous results for narrow channels[3] indicates that the phenomenon of enhancement of superconductivity by a microwave field displays the same regularities in the two cases.

PHASE-SLIP LINES DUE TO THE dc CURRENT

It is seen in Fig. 1 that the behavior of the I–V characteristic depends on the irradiation power. I–V characteristics *1–4* exhibit a clear structure of linear segments with dynamic resistances $R_{dn}=nR_{d1}$ (R_{d1} is the dynamic resistance of the first dc PSL), separated by voltage jumps analogous to that which is observed in narrow channels containing phase-slip centers (dc PSCs).[4] As in Ref. 1, we attribute this structure of jumps on the I–V characteristics to the formation of dc PSLs—two-dimensional analogs of the dc PSCs. The dynamic resistance of the first dc PSL, like R_{d1} for dc PSCs, is determined by the penetration depth l_E of a longitudinal electric field into the superconductor and the normal resistance R_n of the film. For the sample Sn-W4 it has a value $R_{d1}=0.023$ Ω and, hence, $l_E=lR_{d1}/2R_n=7.6$ μm. This value of l_E is in good agreement with the value of l_E which we obtained previously for dc PSCs in narrow tin channels[4] prepared by the same technology that was used to make the wide films studied here.

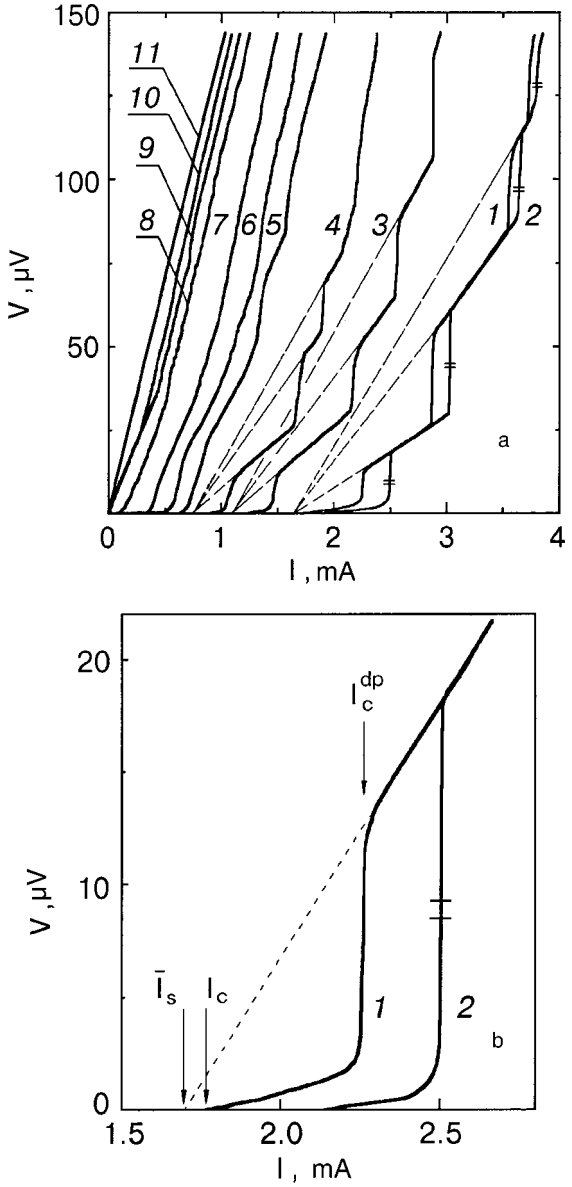

FIG. 1. Family of current–voltage characteristics of the film sample Sn-W4 at different levels of the external irradiation power at $T=3.751$ K and $f=9.3$ GHz (a); fragments of the I–V characteristics *1* and *2* (b). The intercepts of the dashed lines from I–V characteristics *1–4* on the current axis determine the so-called cutoff currents $\bar{I}_s$ (Ref. 4).

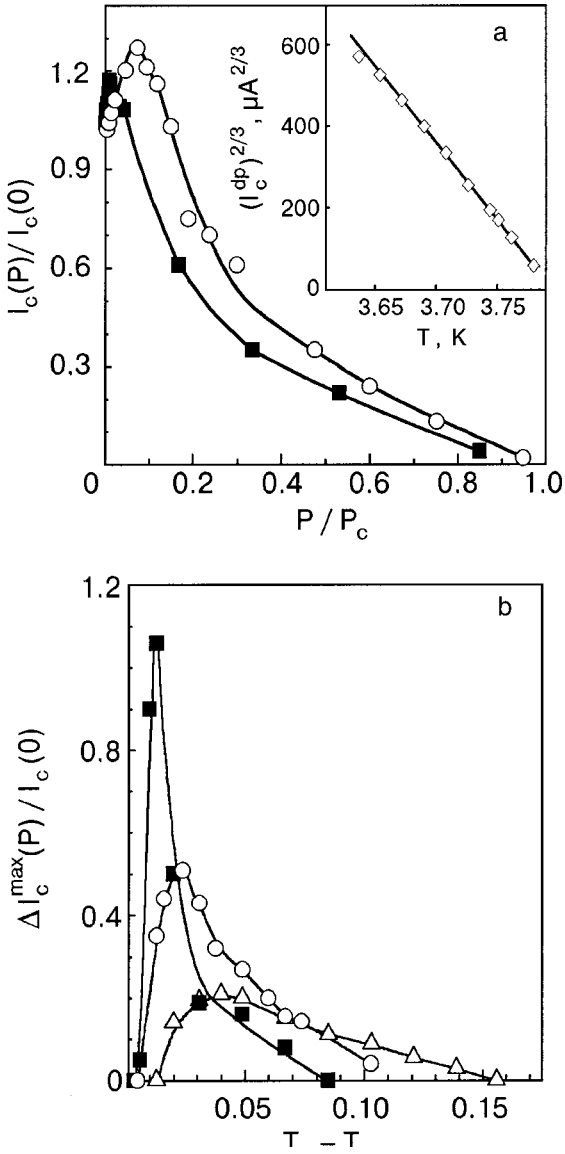

FIG. 2. Dependence of the relative increase of the critical current $I_c(P)/I_c(0)$ on the microwave irradiation power P/P_c at $T=3.744$ K (a) and the dependence of the maximum relative increment of the critical current $\Delta I_c^{max}(P)/I_c(0)=[I_c^{max}(P)-I_c(0)]/I_c(0)$ on the temperature of the sample (Sn-W4) (b) for different irradiation frequencies f [GHz]: 9.3 (■), 12.9 (○), 15.2 (△) [$I_c(0)$ is the critical current of the film at $P=0$; P_c is the minimum power of the electromagnetic radiation at which $I_c(P)=0$]. The inset shows the dependence of the depairing current I_c^{dp} on the temperature of the sample.

Analysis of the stepped I–V characteristics in Fig. 1 leads us to the following conjecture as to the mechanism of formation of the PSLs. When the transport current reaches the value I_c at which the edge barrier is suppressed, the intrinsic magnetic flux vortices begin to enter the film and creep toward the center. This process corresponds to the nonlinear region on the I–V characteristic for $I_c<I<I_c^{dp}$. When the current reaches the depairing value I_c^{dp} it become distributed uniformly over the width of the film, as is evidenced by the temperature dependence of the depairing current (see the inset in Fig. 2a). This corresponds to the critical state of the film, which from the standpoint of the current distribution is no different from the state of a narrow channel at a current equal to the critical. Here the role of the vortices ends. It is at this juncture that the formation of the dc PSL occurs in the sample. A dc PSL appears across the sample, and at all of the points of the dc PSL the order parameter oscillates in phase at the Josephson frequency, at certain points in time vanishing simultaneously along the whole line. A quasinormal region is formed across the film and acts as a source of nonequilibrium quasiparticles. Precisely this scenario of events, based on a numerical solution of the Ginzburg–Landau equations, was discussed in Ref. 5. Upon further increase in the current new PSLs arise, just as in the case of new PSCs in narrow channels. Here the I–V characteristics do not show any signs of the creep or flow of magnetic flux. The question of why a sample with PSLs is able to pass a significantly higher current than the value of I_c at which flux creep starts in the initial stage of the process remains an open question, just as the analogous question does in a system with PSCs:

why does the channel outside the PSCs withstand a current higher than the critical?

PHASE-SLIP LINES DUE TO THE ac CURRENT

The I–V characteristics of the tin film sample Sn-W4 measured at high levels of irradiation power (curves *5–11* in Fig. 1) have a completely different qualitative form than at low power levels (curves *1–4*). It is seen that I–V curves *9* and *10* have a common initial linear segment, the length of which decreases as the irradiation power increases, while its differential resistance R remains constant. In a narrow channel this is explained by the onset of rf PSCs.[4] In the wide film this is evidence of the formation of rf ac PSLs. Since l_E is a function of frequency, at high frequencies $l_E(f) > l_E(0)$ (Ref. 4). The dynamic resistance R of the ac PSL, as in the dc case, depends on $l_E(f)$. For the wide tin film Sn-W4 the resistance R of the common linear segment of I–V curves *9* and *10* is equal to 0.086 Ω. On I–V curves *5–8* the depinning action of the microwave irradiation has a noticeable effect, causing an appreciable decrease in the creep, and the form of the I–V characteristics approaches that corresponding to ''ideal'' flux flow. As the power is increased further the sample passes into the critical state, but now it is an rf one. An ac PSL arises with a dynamic resistance R_1 less than the normal resistance R_n (see I–V characteristics *9* and *10*).

The authors thank T. V. Salenkova for preparing the films.

[a)]E-mail: dmitriev@ilt.kharkov.ua

[1] V. G. Volotskaya, I. M. Dmitrenko, L. E. Musienko, and A. G. Sivakov, Fiz. Nizk. Temp. **7**, 383 (1981) [Sov. J. Low Temp. Phys. **7**, 188 (1981)].
[2] G. M. Éliashberg, JETP Lett. **11**, 114 (1970).
[3] V. M. Dmitriev and E. V. Khristenko, Fiz. Nizk. Temp. **4**, 821 (1978) [Sov. J. Low Temp. Phys. **4**, 387 (1978)].
[4] V. M. Dmitriev, I. V. Zolochevskii, and E. V. Khristenko, Fiz. Nizk. Temp. **27**, 227 (2001) [Low Temp. Phys. **27**, 165 (2001)].
[5] A. Weber and L. Kramer, J. Low Temp. Phys. **84**, 289 (1991.)

Translated by Steve Torstveit